

## Plasmonic nanopores for single molecule sensing

Verschueren, Daniel

**DOI**

[10.4233/uuid:a0099c3d-3244-4789-baa7-4819d7a429fa](https://doi.org/10.4233/uuid:a0099c3d-3244-4789-baa7-4819d7a429fa)

**Publication date**

2018

**Document Version**

Final published version

**Citation (APA)**

Verschueren, D. (2018). *Plasmonic nanopores for single molecule sensing*. [Dissertation (TU Delft), Delft University of Technology]. <https://doi.org/10.4233/uuid:a0099c3d-3244-4789-baa7-4819d7a429fa>

**Important note**

To cite this publication, please use the final published version (if applicable).  
Please check the document version above.

**Copyright**

Other than for strictly personal use, it is not permitted to download, forward or distribute the text or part of it, without the consent of the author(s) and/or copyright holder(s), unless the work is under an open content license such as Creative Commons.

**Takedown policy**

Please contact us and provide details if you believe this document breaches copyrights.  
We will remove access to the work immediately and investigate your claim.

**PLASMONIC NANOPORES FOR SINGLE MOLECULE  
SENSING**



# **PLASMONIC NANOPORES FOR SINGLE MOLECULE SENSING**

## **Proefschrift**

ter verkrijging van de graad van doctor  
aan de Technische Universiteit Delft,  
op gezag van de Rector Magnificus prof. ir. T.H.J.J. van der Hagen,  
voorzitter van het College voor Promoties,  
in het openbaar te verdedigen op maandag 24 september 2018 om 15:00 uur

door

**Daniel Vincent VERSCHUEREN**

Master of Physics,  
University of Oxford, Oxford, Verenigd Koninkrijk,  
geboren te Nijmegen, Nederland.

Dit proefschrift is goedgekeurd door de

promotor: prof. dr. C. Dekker

Samenstelling promotiecommissie:

Rector Magnificus,  
Prof. dr. C. Dekker,

voorzitter  
Technische Universiteit Delft

*Onafhankelijke leden:*

Prof. dr. R. Quidant,  
Prof. dr. U.F. Keyser,  
Prof. dr. S.J.G. Lemay,  
Prof. dr. L. Kuipers,  
Dr. ir. J.P. Hoogenboom,  
Prof. dr. N.H. Dekker,

ICFO, Spanje  
University of Cambridge, Verenigd Koninkrijk  
Universiteit Twente  
Technische Universiteit Delft  
Technische Universiteit Delft  
Technische Universiteit Delft, reservelid

*Overige leden:*

Dr. M.P. Jonsson

Linköping University, Zweden



*Keywords:* Single molecule, solid-state nanopore, plasmonic nanoantenna, nanotweezing, proteins, DNA origami, and plasmon resonance sensing

*Printed by:* Gildeprint

*Front & Back:* Selma van Tartwijk

Copyright © 2018 by D.V. Verschueren

Casimir PhD Series, Delft-Leiden 2018-29

ISBN 978-90-8593-359-5

An electronic version of this dissertation is available at  
<http://repository.tudelft.nl/>.

# CONTENTS

<b>1 Introduction</b>	<b>1</b>
1.1 Solid-state nanopores . . . . .	4
1.2 Localized surface plasmons . . . . .	6
1.3 Advantages of plasmonic nanopores . . . . .	8
1.4 Nanofabrication . . . . .	9
1.5 Previous works on plasmonic nanopores . . . . .	11
1.6 In this thesis . . . . .	12
References . . . . .	13
<b>2 Lithography-based fabrication of nanopore arrays in freestanding SiN and graphene membranes</b>	<b>17</b>
2.1 Introduction . . . . .	18
2.2 Results and discussion . . . . .	19
2.3 Conclusions. . . . .	24
2.4 Supporting information. . . . .	25
References . . . . .	27
<b>3 Self-aligned plasmonic nanopores by optically controlled dielectric breakdown</b>	<b>31</b>
3.1 Introduction . . . . .	32
3.2 Results and discussion . . . . .	33
3.3 Conclusion . . . . .	39
3.4 Experimental methods . . . . .	40
3.5 Supporting information. . . . .	41
References . . . . .	46
<b>4 DNA translocations through solid-state plasmonic nanopores</b>	<b>51</b>
4.1 Introduction . . . . .	52
4.2 Results and discussion . . . . .	52
4.3 Conclusion . . . . .	62
4.4 Experimental methods . . . . .	62
4.5 Supporting information. . . . .	65
References . . . . .	72
<b>5 Active delivery of single DNA molecules into a plasmonic nanopore for label-free optical sensing</b>	<b>77</b>
5.1 Introduction . . . . .	78
5.2 Results . . . . .	79
5.3 Discussion . . . . .	86
5.4 Experimental methods . . . . .	87

5.5	Supporting information. . . . .	89
	References . . . . .	95
<b>6</b>	<b>Label-free optical detection of DNA translocations through plasmonic nanopores</b>	<b>99</b>
6.1	Introduction . . . . .	100
6.2	Results and discussion . . . . .	101
6.3	Conclusion and outlook. . . . .	110
6.4	Experimental methods . . . . .	111
6.5	Supporting information. . . . .	114
	References . . . . .	120
<b>7</b>	<b>Nano-optical tweezing of single proteins in plasmonic nanopores</b>	<b>125</b>
7.1	Introduction . . . . .	126
7.2	Results and discussion . . . . .	127
7.3	Discussion and conclusion . . . . .	137
7.4	Experimental methods . . . . .	138
7.5	Supporting information. . . . .	140
	References . . . . .	147
<b>8</b>	<b>Temperature dependence of DNA translocations through solid-state nanopores</b>	<b>151</b>
8.1	Introduction . . . . .	152
8.2	Materials and methods . . . . .	152
8.3	Results . . . . .	153
8.4	Discussion . . . . .	160
8.5	Conclusion . . . . .	160
8.6	Supporting information. . . . .	162
	References . . . . .	168
<b>9</b>	<b>Mechanical trapping of DNA in a double-nanopore system</b>	<b>173</b>
9.1	Introduction . . . . .	174
9.2	Results and discussion . . . . .	175
9.3	Conclusion . . . . .	183
9.4	Experimental details . . . . .	183
9.5	Supporting information. . . . .	185
	References . . . . .	199
<b>10</b>	<b>Towards flow-driven rotation of a DNA origami nanomotor</b>	<b>203</b>
10.1	Introduction . . . . .	204
10.2	Results . . . . .	204
10.3	Conclusion and outlook. . . . .	214
10.4	Supporting information. . . . .	217
	References . . . . .	222
	<b>Summary</b>	<b>225</b>
	<b>Samenvatting</b>	<b>229</b>

---

<b>Acknowledgements</b>	<b>235</b>
<b>Curriculum Vitæ</b>	<b>239</b>
<b>List of Publications</b>	<b>241</b>



# 1

## INTRODUCTION

*In this chapter, we will describe the relevant background and the basic concepts that underlie the research described in this dissertation, which explores the development of a plasmonic nanopore single-molecule sensor. Starting from their historic discovery, a brief description of DNA and proteins, the elements under investigation by the sensor, will be presented here and their relevance to modern day medicine will be briefly touched upon. Next the fundamental concepts of nanopore sensing and plasmonic sensing will be briefly introduced, and the advantages of combining both sensing techniques into one will be highlighted. The fabrication procedure to create such a device will be presented and the chapter concludes by describing some key studies on plasmonic nanopores that have been conducted in the past.*

Life's complexity and resilience are both fascinating and puzzling, and has been a topic of research for over centuries. Fueled by substantial progress in microscopy, Robert Hooke and Anthony van Leeuwenhoek realized in the 17th century that living systems contain small containers that they termed cells [1]. Using their microscopes, these scientists could reveal to the eye this structural feature of life that had never been observed before. It took almost 200 years before the connection was made by Theodor Schwann, Matthias Schleiden, and contemporaries that all living organisms like plants and animals were made up of these cells, that these are in fact the most basic units of life. It was discovered that when a cell creates a new cell, or divides, it splits into two, making two copies of itself, i.e. a cell can only emerge from pre-existing cells.

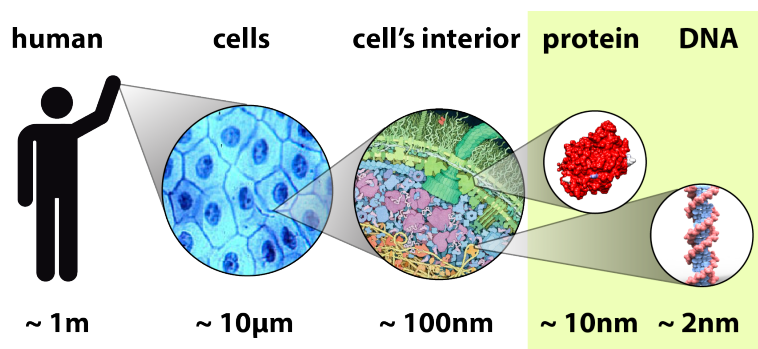


**Figure 1.1:** Illustration of size scale of cells, protein, and DNA, the essential working blocks of all present day life forms. The typical length scales are indicated. Figure adapted from [2, 3] and a design from Flaticon

Cells are made up of an intricate mesh of even smaller constituents that largely fall into two major classes: protein and DNA. Proteins were discovered as a distinct class of biological molecules that aggregate or coagulate under treatment of heat. Advances in chemistry by the end of the 19th and early 20th century showed that these proteins are chemical species essential for living organisms to thrive. Importantly, the fundamental discovery was made that these proteins can perform enzymatic or catalytic functions to modify or digest other chemical species and that these proteins are the working tools of the cell. Proteins, typically around 2-10 nm in size (see Fig. 1.1), are linear polymers that consist of a chain of amino acids that folds onto itself in a well-defined three-dimensional structure that gives each protein a highly specific function.

Famously, another biological molecule, DNA (deoxyribonucleic acid), chemically different from protein, was found inside cells. It consists of repeating units of 4 different nucleobases A, C, T and G, that each have a slightly different chemical structure and physical size. In the 1940's it was realized that this molecule contains the hereditary information that defines the cell and is passed on during cell division. After the discovery of the three-dimensional (3D) double-helical structure of DNA (see Fig. 1.1) by Watson and Crick [4], it became evident that this long polymer of 2.2 nm in diameter and up to a meter (!) in length, is a double chain of complementary nucleobases, where A pairs with T and C pairs with G. The sequence, with each nucleotide on a strand spaced 0.34 nm from another, encodes the information. DNA was identified as the blueprint of the cell,

encoding for proteins, while proteins are, amongst other functions, used to replicate the DNA. Hence, cells, the fundamental building units of all living tissues, have themselves fundamental building blocks in protein and DNA.

When one of these fundamental building blocks fail, a disease can develop that may severely affect the quality of life or even cause premature death. Misfolded proteins can, for example, lead to Alzheimer's disease that causes severe dementia. Mutations in DNA can cause cancer or a whole range of hereditary diseases like cystic fibrosis, which results in deteriorating lung function, or sickle-cell disease, which increases chances of blood anemia and strokes. Quick and reliable ways to detect and characterize these errors in DNA and proteins can lead to earlier diagnosis and better treatment of the diseases. Being able to screen for these errors per individual patient will be the next step in medicine, where better suited therapy and medication, specifically developed for particular categories of patients [5], will likely result in more effective treatment with less side effects.

Our current understanding of life has progressed a tremendous amount since the discovery of cells in the 17th century. Currently, scientists are using the acquired knowledge from proteins and DNA to create moving 3D nanostructures, reminiscent of protein, that have catalytic function [6, 7]. Moreover, researchers are pursuing efforts to make artificial cells that have functions such as division and growth similar to real living cells [8]. From all the way down at the smallest scale of life, scientists are now working back up in size and complexity, recreating what they discovered at the simpler steps, perhaps eventually creating a sentient artificial organism in a future far faraway.

Figure 1.1 illustrates this flow from living organism to protein and DNA and indicate the typical sizes involved. From a human (typical scale 1 m) to a typical cell ( $10\ \mu\text{m}$ ), one needs a magnification of around 100,000x. As your eye can see objects of about 1 mm, this magnification became feasible with Anthony van Leeuwenhoek's microscopes that had a maximum magnification of around 270x [1]. To really see the molecular constituents of the cell, i.e. the protein and DNA, another 100x (100 nm) to 10000x magnification (1 nm) is needed and, light microscopy is insufficient to achieve this. Nowadays, to look at these structures, we have a whole array of techniques, from x-ray crystallography to electron microscopy and super-resolution fluorescent imaging, at our disposal. However, investigating individual biomolecular objects remains challenging, in particular observing their function in their native environment.

Here we focus on developing a new technique to universally detect, investigate, and characterize single proteins and DNA molecules in liquid, and hence we focus on objects and structures of this length scale. By using solid-state nanostructures, we create optical and electrical forces that bring biomolecules into our sensor and keep them there. By reading out scattered light and ionic currents that interact with the biomolecule and our nanostructure, we aim to extract physical information, such as size and conformation, from that biomolecule to determine its identity. We will perform an initial investigation into these nanostructures from fabrication to initial tests on biomolecules. These novel single-molecule sensors can contribute to the understanding of the behavior of biomolecules [9] and eventually aid the advance of medical technology for more effective, more comfortable, and better patient care for all [10].

## 1.1. SOLID-STATE NANOPORES

Our sensor is a plasmonic nanopore that consists of two parts, a solid-state nanopore and a plasmonic nanostructure. A solid-state nanopore is a small hole of less than 100 nm in diameter that is pierced in a thin (less than 100 nm thick) solid-state membrane, typically made of silicon nitride or graphene. The application of these nanostructures for single-molecule sensing was initially inspired by biology. Naturally occurring toxins, such as alpha-hemolysin, are small protein nanopores, typically less than 2 nm in diameter, that insert into a cell membrane, or lipid bilayer, to deflate the cell. Their size allows them to be used to transport and investigate DNA [11] and later proteins [12].

Solid-state nanopores are made by electron beam [13], ion beam [14], lithographical (Chapter 2 of this thesis), or dielectric-breakdown techniques [15]. Each of these techniques aims to locally destroy the insulating membrane and leave behind a nanoscale-sized opening. The most commonly employed of these techniques is electron-beam sculpting, where an electron beam of a transmission electron microscope (TEM) is focused on the membrane to blast away the material with nanometer precision. However, the use of this technique requires very expensive machinery and is time consuming. The method of controlled dielectric breakdown is, in contrast, by far the cheapest, where the application of a large voltage (>10 V) over the membrane locally causes a fatigue in the material, leaving behind a nanopore.

The detection principle of nanopore sensing relies on an ionic current that flows through the nanopore, see Fig. 1.2A, where a DNA molecule and ions move through the nanopore simultaneously. The membrane containing the nanopore can be inserted as a separator between two containers filled with a salty solution, typically 1M KCl or 2M LiCl. Once an electrical bias voltage is applied between the two compartments, a strong electric field forms in the nanopore that moves ions in the solution through the pore, setting up a current that can be measured. The magnitude of the current depends on the size of the nanopore and an object that is smaller than the nanopore can enter and block part of the current. The size of the blockade current depends on the size of the molecule and the duration of the signal depends on its passage time. This principle has been used in the past on larger pores by Coulter to detect and size cells, and this sensing technique on these larger objects is still employed today [16]. The current that flows through the pore is made up of ions, typically  $\text{Li}^+$  or  $\text{K}^+$  and  $\text{Cl}^-$ , but the current that runs in the amplifier and can be recorded by a computer is made up of electrons. To convert the ionic current to an electronic (electron) one, we use a silver/silver chloride redox reaction at electrodes inserted in the solution (see Fig. 1.2A). This chemical reaction creates free electrons in the silver electrode that can run through the amplifier and be recorded in real time.

By monitoring the ionic current in real time the translocation of biomolecules can be detected and investigated, see Fig. 1.2B. Biomolecules in solution are usually charged, so they too will feel the effect of the electric field from the nanopore and will be forced into, or expelled, from it, depending on the voltage polarity. In particular DNA is highly charged, with 2 electron charges per basepair, and even though a DNA is a long polymer coil, often over a 1000 times longer than the nanopore, the end of the coil can still insert into the nanopore [17]. For pores larger than twice the diameter of the DNA, the large electric field near the entrance of the pore can strongly bend the DNA and start the

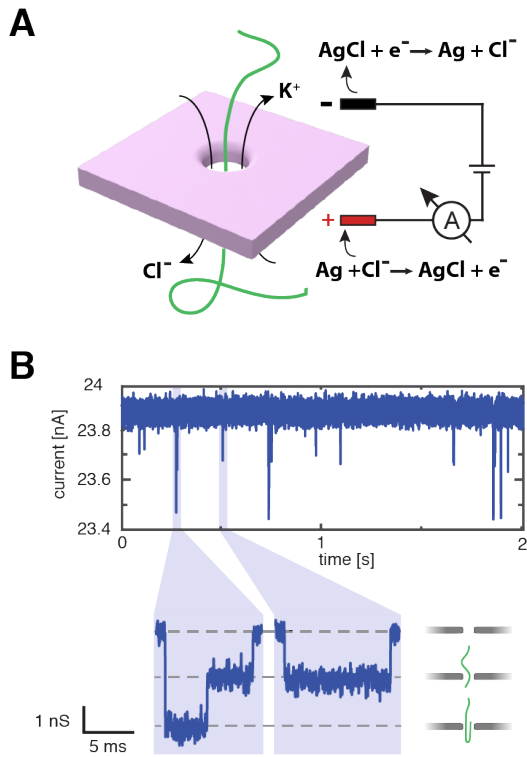


**Figure 1.2: Nanopore basics.** (A) Schematic illustration of a DNA (in green) translocation through a nanopore with an ionic current flowing simultaneously through the nanopore. At the electrodes, the ionic current is converted to an electronic one via silver/silver chloride chemistry. (B) Ionic current time trace with spikes indicative of DNA translocations. Closer inspection of the spikes (bottom) shows the two different conformations the DNA can adopt during translocation. The levels indicate how many double-strands of DNA are in the nanopore at one point in time, as indicated by the cartoons on the right.

traversing process somewhere along the length of the coil. This can be observed in the ionic current as now two parts of the same DNA coil, two double-strands of DNA, are simultaneously in the nanopore leading to twice the size of the current blockade, as indicated in the zoom by Fig. 1.2B.

Ionic current sensing and the electric field fields in the nanopore are great physical tools to investigate biomolecules and the transport thereof, but there is a major drawback. Even at typical driving voltages of 100 mV, which is required to set up the ionic current and insert the DNA, biomolecules pass through the pore so fast that hardly any information can be extracted from them, or that the molecules are even entirely missed [18]. To illustrate, a 10  $\mu\text{m}$  DNA molecule typically passes the nanopore in about 10 milliseconds (see Fig. 1.2B). Recalling that a nucleotide is spaced 0.34 nm from its neighbor, this means that 3 million nucleotides must be read per second if one were to read the DNA sequence. Even though this would be great in terms of speed, there is

currently no technology that can do this. To compare, this read-out speed would be the same as a train conductor on the platform accurately counting the number of people seated in a window seat, each window 1 m apart, while the train passes at 3000 km/s. Good luck, train conductor. Efforts have been undertaken to tackle this issue, and a successful strategy has been employed for protein nanopores. Here, on top of the nanopore, another protein, e.g. a helicase that is used to unwind the 2 DNA strands, slowly ratchets the DNA molecules, slowing the transport of DNA down by at least a factor 1000 or so, so that the different nucleobases on the DNA strand can be accurately read out using an ionic current. This principle has already brought us a commercial nanopore-based DNA sequencing device [19], but this method cannot easily be used to investigate proteins. Slowing down biomolecular transport in solid-state nanopores is still a major goal in the nanopore sensing field and will allow the use of nanopores for accurately detecting proteins, investigating their function, and for studying the interactions of protein with DNA.

## 1.2. LOCALIZED SURFACE PLASMONS

To provide additional functionality to the nanopore sensor and control the transport of the molecules through it, we equip the nanopore with a plasmonic nanoantenna. These nanoantennas are nanosized structures, or particles, made of inert metals like gold or silver that have a unique ability to highly concentrate visible light.

Metals can, if an electric field is applied, conduct electrical currents and they do so by electrons that can flow freely through the crystal structure of the metal. However, these conduction electrons not only move in the presence of a static electric field, but also respond to oscillating electric fields, or electromagnetic waves, such as radio waves or optical light. If the right oscillation frequency, or equivalently wavelength, is used, these electrons can oscillate collectively and this collective oscillation is called a plasmon. This is illustrated in Fig. 1.3A, where an oscillating electromagnetic field is incident from the left and induces an oscillation of the conduction electrons in the metal at the same frequency as the excitation light source. For metals the frequency at which plasmons are efficiently excited is typically near the wavelength of visible light.

Plasmons excited by light are by definition surface effects, as light cannot penetrate deeply into metals (which is why they are shiny and reflective). As a result, surface plasmons confine light waves to the surface of the metal and localize the optical field. The electron-cloud charge oscillation enhances the electromagnetic field at the surface and it quickly drops off away from the interface. Plasmons at metal/dielectric interfaces can be propagating or localized, depending on the topology of the metal interface, but nanostructures support exclusively localized surface plasmons [21]. This causes the optical light to be concentrated to local spots near the nanostructure, often a few nanometers in size, which makes them effective optical nanoantennas. Such extreme focusing of light cannot be achieved with free-space light, as the nature of the electromagnetic wave prevents its focusing to anything smaller than about half its wavelength, a fundamental limitation that is called the diffraction limit. The diffraction limit is exactly the reason why conventional microscopy cannot be used to visualize (unlabeled) single proteins or DNA molecules. In particular, nanoparticles with a small gap exhibit extreme field focusing and enhancement of the light intensity to the gap of

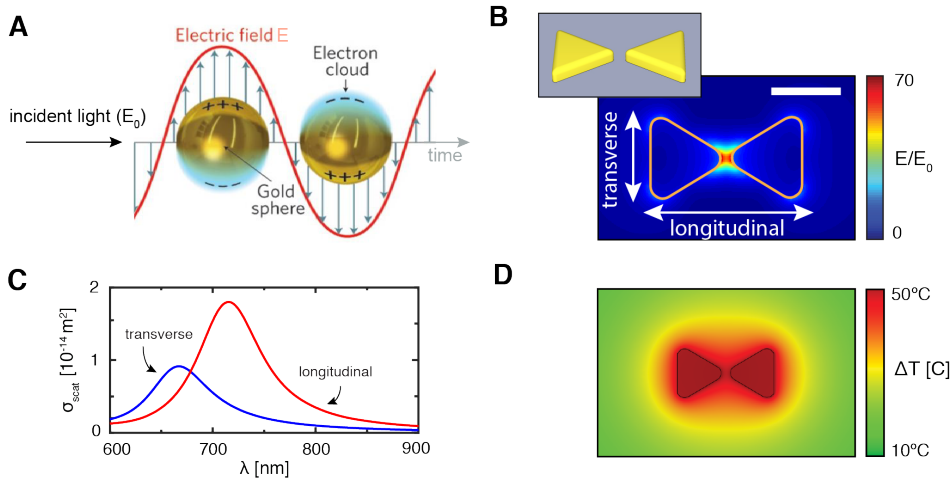


**Figure 1.3: The basics of plasmonics.** (A) Schematic illustration of plasmon excitation. Light is incident on the gold nanoparticle, and the oscillating nature of light, causes the electrons in the gold nanoparticle to oscillate coherently along with the electric field. (B) Perspective view of a bowtie nanoantenna: two small gold triangles facing each other tip to tip at a small separation. The simulated electric field distribution in longitudinal excitation (polarization of the light along the axis connecting the two triangles, as indicated in the figure) at the at the resonance of the antenna. Clear localization and enhancement in the gap can be observed. Scale bar is 50 nm. (C) Simulated scattering cross-section of the bowtie antenna in (B) at different wavelength for longitudinal and transverse polarization (in-plane perpendicular to the axis connecting the two triangles, see (B)). Clear peaks are observed, corresponding to efficient plasmon excitation at those frequencies. (D) Simulation of temperature distribution around the bowtie antenna in (B) at 1 mW of incident light power. A clear temperature increase of 50°C can be observed. Fig. 1.3A is adapted from [20].

the antenna, as is shown in Fig. 1.3B, where the simulated electric field density is plotted as a spatial map around the gold nanostructure, a bowtie antenna where two triangles are facing each other tip-to-tip at a small separation, as shown in the inset.

The plasmon excitation in small nanostructures is a resonance effect. In a simplified picture, the negatively-charged free-electron cloud in the metal is bound to the metal by the positive atomic cores, which are fixed. These cores act as a resorting force to the cloud, such that the oscillation is only efficiently excited at one particular resonance frequency, much like pushing a swing on a playground. This resonance frequency depends on the properties of metal, the geometry of the nanostructure, the properties of the dielectric around the nanostructure, and the polarization of the light with respect to the nanostructure. Figure 1.3C shows the scattering efficiency of the bowtie antenna in Fig. 1.3B at different wavelengths and different polarizations (as indicated in the Fig. 1.3B). For both cases a clear peak can be observed, at which the localized plasmons are most efficiently excited, but in each polarization the location of the spots at which the field will concentrate will be different.

Even though electrons in metals can flow rather freely through the metal, they still experience some resistance, or losses, which results in heating of the metal. This resistance leads to a decay of the plasmon oscillation and results in heating of the

nanostructure. Small metal nanoparticles, like the bowtie nanoantenna in Fig. 1.3B, cannot easily dissipate the generated heat, and this will cause a large temperature increase in the nanostructure and its surroundings. The temperature increase is rather local, as is shown in Fig. 1.3D for 1 mW of power of the incident light, and quickly resolves once the plasmon excitation is turned off. Because of this rapid and localized heating of the surrounding, plasmons can be used as localized heat sources and this has, for example, been employed to kill cancer cells [22]. However, heating is often considered a detrimental side effect since too much heating destroys the nanostructure and thus limits the input power that can be used.

The extreme electromagnetic field focusing ability and the resonance nature of localized surface plasmons are their most interesting properties. The extreme light focusing creates large gradients in the optical field intensity that can be used to trap small particles, such as biomolecules. Due to dielectric polarization, biomolecules in large optical gradients will move towards the region of highest intensity of the field, and when gradients are sufficient, will be maintained there. This has been used to trap 1000 nm size beads in the focus of a laser, in a so-called optical tweezer. Unfortunately, the diffraction limit prevents the laser from being focused tightly enough to do the same for single protein of only 10 nm in size. But plasmons can do the trick and this has been demonstrated in the past [23]. Furthermore, the resonance nature of the antenna can be used to detect the presence of biomolecules in the antenna. Since the resonance will change slightly as a protein sits near the antenna, protein can be detected, in so-called resonance sensing. Moreover, the field enhancement at the surface of the nanostructure allows the enhancement of light scattering from biomolecules, either by fluorescence or Raman scattering. The latter, termed surface enhanced Raman scattering (SERS), is particularly interesting, since Raman scattering probes vibrations of molecular bonds by exciting them and the energy at which this happens depends strongly on the chemical nature of the bond. In this way a Raman spectrum, where scattered light is collected at different frequencies (energies), serves as a fingerprint of a molecule and can be used to identify it.

These plasmonic nanoantennas can provide specific read-out and apply optical forces on biomolecules, all because of the plasmons that are excited in them. By fabricating these nanostructures next to a nanopore, we can bring these exciting functionalities to the nanopore and attempt to patch the drawbacks of nanopore sensing, the molecular translocation speed, with optical nanotrapping and furthermore complement the ionic-current read-out with a more specific spectroscopic read-out from a plasmonic nanostructure.

### 1.3. ADVANTAGES OF PLASMONIC NANOPORES

Figure 6.5 shows the advantages that plasmonic nanopores can bring to single-molecule sensing. The integration of a plasmonic nanoantenna with a nanopore allows, first of all, the efficient delivery of biomolecules to the most sensitive region of the nanoantenna. This is important to ensure that consistent signals can be observed from each biomolecule. The strong gradients in optical fields can optically trap molecules in the sensor and keep them there, so that there is more time to measure on each molecule. The advantage of acting both optical and electrical forces on the nanopore has been

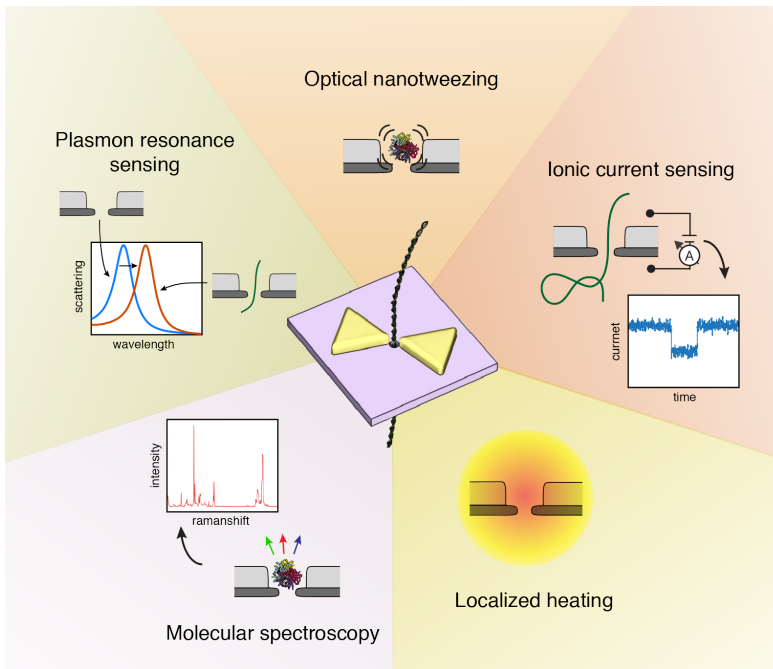


**Figure 1.4:** Plasmonic nanopores as single-molecule nanolabs. The plasmonic nanopore allows for multiple read-outs and forces to be applied to the single molecule. From the top, in clockwise direction: optical forces can nanotweeze or trap objects, ionic current flow can report on the presence and conformation of molecules, localized heating can perturb molecules rapidly and controllably, localized optical field enhancements create the possibility for single-molecule SERS, and plasmon resonance sensing can report on the presence of the biomolecule complementary to the ionic current sensing.

proposed to control the DNA translocation speed using a trap-release strategy where the optical field is cyclically turned off/on and the DNA can be read off one part at a time [24]. The ionic current sensing and resonance sensing can provide information about the size and conformation of the molecule in the antenna, while Raman signals from the molecule can provide information about the chemical identity of the molecule. Interestingly, dynamics can be observed as well. For example, when small substrates are added to the solution, a trapped enzyme can potentially be monitored while they perform their catalytic action, or the localized heating from the antenna can be used to heat shock a protein so that it unfolds or denatures, while it is trapped in the plasmonic nanopore. The plasmonic nanopore can thus be considered a versatile single-molecule nanolaboratory.

## 1.4. NANOFABRICATION

Before we discuss earlier work done on plasmonic nanopores, we'll briefly introduce our plasmonic nanopore fabrication process. The work flow for fabrication is illustrated in Fig. 1.5A. Plasmonic nanoantennas are fabricated on freestanding silicon-nitride membranes using standard electron-beam lithography processing. In our

electron-beam lithography processing, a 100 nm thick polymer resist is put on a sample using spin coating and exposed by rastering an electron bundle accelerated under 100 kV over the sample in a predefined pattern. Electrons are fired at the resist in vacuum conditions, destroying the polymer at specific locations dictated by the desired pattern and the mashed-up polymer is removed using a developer solution. Subsequently, the sample, with patterned resist, is taken to the gold evaporator. Here a gold target is heated up in vacuum to the point that gold atoms are released into the vacuum chamber. These atoms deposit on the sample, which is suspended above the gold target, to form a gold layer of around 30 nm thick in our case. After the evaporation, the remaining resist can be stripped with an aggressive solvent which removes the resist and gold film on top of it, leaving behind the nanostructures on the sample.

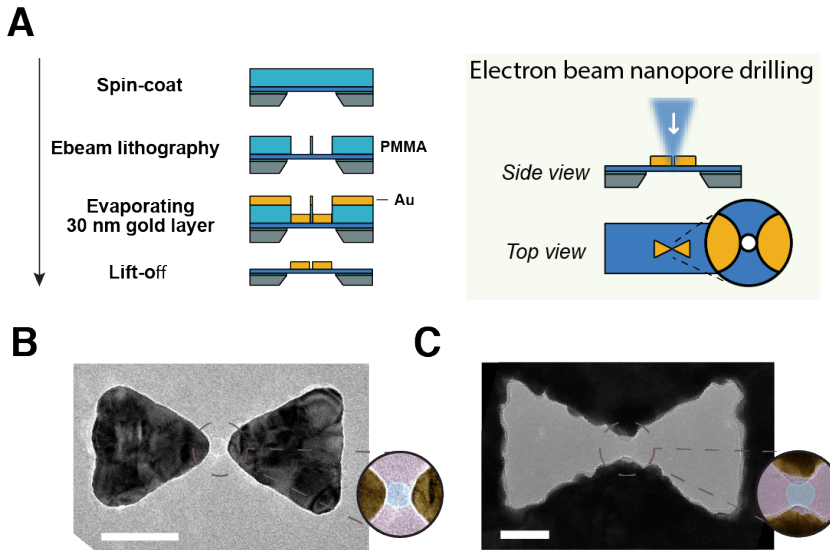


**Figure 1.5: Plasmonic nanopore fabrication.** (A) (left) A layer of resist is spin coated on a freestanding membrane, exposed by an electron beam and developed, and subsequently gold is evaporated on the sample whereupon the remaining resist is stripped. Finally, a nanopore is drilled in that gap of the structure using a TEM (right). The arrow guides the process flow. (B) TEM image of a plasmonic bowtie nanoantenna, with a nanopore in the gap (highlighted by a false colored zoom). (C) TEM image of an inverted-bowtie plasmonic nanopore, with a nanopore in its gap (highlighted by a false colored zoom). Scale bars are 50 nm.

Finally, to create a plasmonic nanopore, the sample is taken to the transmission electron microscope (TEM) (although dielectric breakdown can also be used, as we will show in this thesis in Chapter 3), where an operator picks a suitable nanostructure and drills a small hole in the membrane near the nanostructure using a large number of high-energy electrons. TEM images of the result for two different kinds of antennas is shown in Fig. 1.5, with false-colored zooms of the nanopore: Fig. 1.5B shows the bowtie antenna, as discussed before in Fig. 1.3. Fig. 1.5C shows its inverted counterpart, the inverted-bowtie nanoantenna, which allows for better heat conduction and can sustain larger input laser powers. The antenna is a bowtie-shaped aperture in a gold film, and

is made slightly differently than the regular bowtie antenna. For the inverted bowtie we use electron-beam patterning on a thick stack of resists. After patterning and gold evaporation, the resist is stripped from the substrate and the gold layer on top of the resist is kept intact, picked up from solution, and placed manually onto a membrane using micromanipulation under a microscope. After sealing the gold layer, the sample is taken to the TEM and a nanopore is drilled into it.

## 1.5. PREVIOUS WORKS ON PLASMONIC NANOPORES

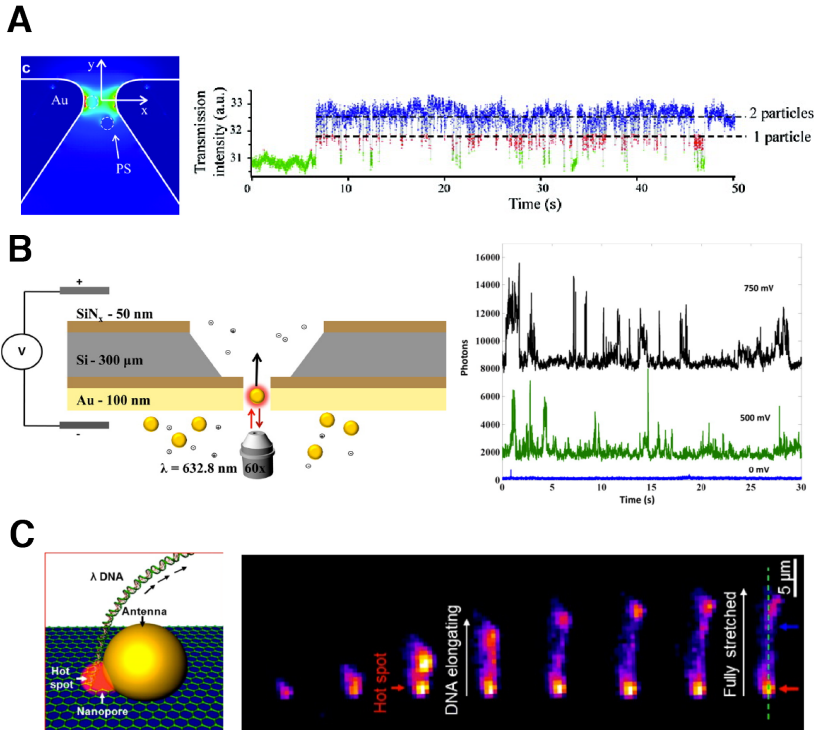


**Figure 1.6: Previous works on plasmonic nanopores.** (A) Optical trapping of two 22 nm polystyrene beads in a plasmonic nanoslit [25]. Left: sideview of a simulation of the optical field intensity in the slit with two particles present. Right: time trace of transmitted light through the slit during particle trapping. (B) SERS detection of translocating 40 nm gold nanospheres coated with a Raman active dye molecule [26]. Left: schematic of experiment. Right: SERS intensities at one chosen Raman active vibration of the dye molecule at different driving voltages. (C) Fluorescent detection of DNA translocating through a plasmonic nanopore made on graphene [27]. Left: schematic illustration of the DNA translocation process. Right: snapshots of a video of fluorescently labeled DNA that is translocating through the nanopore and gets stretched out

We are not the first to explore plasmonic nanopores for single-molecule sensing. Here, we briefly describe some of the work on plasmonic nanopores that has been done in the past, in particular on plasmonic nanotrapping, SERS, and fluorescence enhancement. Figure 1.6A shows an example of single-particle trapping in a 40x170 nm

nanoslit plasmonic nanopore [25]. Time traces of the transmitted light intensity, which is a measure for the scattered light intensity of the plasmonic nanoantenna that can be used for resonance sensing, show two 22 nm nanoparticles that were trapped in the plasmonic nanoslit. Figure 1.6B shows Raman signals from 40 nm gold nanoparticles that were coated with malachite green isothiocyanate, a molecule that exhibits particularly strong Raman signals, translocating through a circular plasmonic nanopore [26]. Another example of a plasmonic nanopore is shown in Fig. 1.6C. Here, a nanopore is made in graphene, a single-atom layer thick material, next to a gold nanoparticle. Fluorescently labeled lambda-DNA, which is about 50,000 nucleotides or 16  $\mu\text{m}$  long, can optically be observed to translocate through the nanopore [27].

These pioneering early studies have shown the capability of sensing and optical manipulation of small objects in plasmonic nanopores. Yet, it has not been shown to work for single molecules in a label-free manner. This thesis aims to explore the opportunities these plasmonic nanopore present for single-molecule biosensing. The main focus is on optical nanotrapping of biomolecules and using the ionic current and plasmonic resonance sensing to monitor the behavior of molecules in the plasmonic nanopore.

## 1.6. IN THIS THESIS

This thesis is an account of the development and study of plasmonic nanopore sensors, with a focus on single-biomolecule manipulation and heating effects in plasmonic nanopores. The first two chapters after this introduction describes two different kinds of new nanopore fabrication methods that we have developed. **Chapter 2** describes the fabrication of nanopore arrays using single-shot electron-beam lithography in both silicon-nitride and graphene freestanding membranes. Nanopores down to about 15 nm can be created in this way, and the dose per shot was found to control the nanopores size. We show that single nanopores created in this way can be used to detect DNA translocations. In **Chapter 3** we report on the fabrication of nanopores right in the gap of a plasmonic bowtie nanoantennas on freestanding SiN membranes using controlled dielectric breakdown. Plasmon excitation in longitudinal mode of the bowtie antenna during voltage stressing of the membrane, localizes the position of the dielectric breakdown to the gap to the antenna. TEM imaging confirms the nanopore is drilled in the gap and we demonstrate the plasmonic nanopore to work identically to their TEM drilled counterparts.

The next four chapters focus on using plasmonic nanopores for biosensing. **Chapter 4** describes the observation of DNA translocations through a plasmonic nanopore and characterizes the local heating in these nanopores. We observe a strong increase in the rate at which molecules translocate the sensor. We attribute this effect to the strongly localized heating from the plasmonic bowtie nanoantenna at the nanopore in combination with the thermophilic properties of DNA in high concentration LiCl solutions, which increases the local DNA concentration near the heated nanopore. In **Chapter 5** we show that the plasmonic nanopore can also be used to optically monitor the DNA translocation process by light that is backscattered from the antenna through plasmon resonance sensing. We demonstrate that the nanopore can be used efficiently to deliver molecules into the antenna hotspot and can be used to regenerate the sensing

volume, allowing for much higher sensor throughput and read-out speeds. **Chapter 6** demonstrates that an inverted-bowtie plasmonic nanopore can be used to detect DNA translocations optically through plasmon resonance sensing, simultaneously with their detection in the ionic current, but this time via the optical transmission through the antenna. We show that the optical detection scheme decouples the signal strength from the bias voltage and show that it has advantages over the ionic current detection in terms of acquisition speed and buffer conditions used for experiments. In **Chapter 7**, we demonstrate optical trapping of single protein in an inverted-bowtie plasmonic nanopore assisted by protein-surface interactions. We demonstrate optical tweezing of 20 nm polystyrene beads in the inverted-bowtie apertures, explain the polarity of the signal from the trapped protein by the simulated resonance of the nanostructures, and show that optical trapping of single protein in these plasmonic nanopores is dominated by surface-protein interactions. The remaining three chapters discuss the manipulation of DNA and DNA nanostructures in nanopores. **Chapter 8** investigates the behavior of DNA translocations through nanopores at different (global) temperatures. We demonstrate the nanopore can be used as a temperature sensor and show that the changes observed in characteristics of the DNA translocations can be explained using simple models, where the buffer viscosity plays a dominant role. **Chapter 9** studies a system with two in-plane nanopores, separate a few 100 nanometers apart, where long DNA molecules insert themselves in both nanopores and get stalled, some even indefinitely. About 1% of all DNA translocation events become trapped in both nanopores and analysis of the corresponding current blockades allows us to determine that the DNA remains inclined at an angle inside the pore and helps us to characterize the molecules' escape. **Chapter 10** outlines the status of an exciting new project, where we aim to dock 3D nanomotors made from DNA origami in an array of nanopores, to create autonomously driven DNA nanomotors that can convert free energy into rotational motion. We discuss the planned observation strategy of the motor by dark-field detection and discuss the strategy for labeling of the motors arm with a gold nanoparticle.

## REFERENCES

- [1] H. Gest, *The discovery of microorganisms by robert hooke and antoni van leeuwenhoek, fellows of the royal society*, Notes and Records of the Royal Society **58**, 187 (2004).
- [2] Y.-J. Kim and D.-N. Kim, *Structural basis for elastic mechanical properties of the dna double helix*, PloS one **11**, e0153228 (2016).
- [3] D. S. Goodsell, *The machinery of life* (Springer Science & Business Media, 2009).
- [4] J. D. Watson, F. H. Crick, *et al.*, *Molecular structure of nucleic acids*, Nature **171**, 737 (1953).
- [5] D. G. De Castro, P. Clarke, B. Al-Lazikani, and P. Workman, *Personalized cancer medicine: molecular diagnostics, predictive biomarkers, and drug resistance*, Clinical Pharmacology & Therapeutics **93**, 252 (2013).

- [6] S. E. Boyken, Z. Chen, B. Groves, R. A. Langan, G. Oberdorfer, A. Ford, J. M. Gilmore, C. Xu, F. DiMaio, J. H. Pereira, *et al.*, *De novo design of protein homo-oligomers with modular hydrogen-bond network-mediated specificity*, *Science* **352**, 680 (2016).
- [7] C. Teller and I. Willner, *Functional nucleic acid nanostructures and dna machines*, *Current opinion in biotechnology* **21**, 376 (2010).
- [8] C. Xu, S. Hu, and X. Chen, *Artificial cells: from basic science to applications*, *Materials Today* **19**, 516 (2016).
- [9] H. Craighead, *Future lab-on-a-chip technologies for interrogating individual molecules*, in *Nanoscience And Technology: A Collection of Reviews from Nature Journals* (World Scientific, 2010) pp. 330–336.
- [10] J. J. Gooding and K. Gaus, *Single-molecule sensors: Challenges and opportunities for quantitative analysis*, *Angewandte Chemie International Edition* **55**, 11354 (2016).
- [11] D. Deamer, M. Akeson, and D. Branton, *Three decades of nanopore sequencing*, *Nature biotechnology* **34**, 518 (2016).
- [12] G. Oukhaled, J. Mathe, A.-L. Biance, L. Bacri, J.-M. Betton, D. Lairez, J. Pelta, and L. Auvray, *Unfolding of proteins and long transient conformations detected by single nanopore recording*, *Physical review letters* **98**, 158101 (2007).
- [13] A. Storm, J. Chen, X. Ling, H. Zandbergen, and C. Dekker, *Fabrication of solid-state nanopores with single-nanometre precision*, *Nature materials* **2**, 537 (2003).
- [14] J. Li, D. Stein, C. McMullan, D. Branton, M. J. Aziz, and J. A. Golovchenko, *Ion-beam sculpting at nanometre length scales*, *Nature* **412**, 166 (2001).
- [15] H. Kwok, K. Briggs, and V. Tabard-Cossa, *Nanopore fabrication by controlled dielectric breakdown*, *PloS one* **9**, e92880 (2014).
- [16] M. D. Graham, *The coulter principle: foundation of an industry*, *JALA: Journal of the Association for Laboratory Automation* **8**, 72 (2003).
- [17] M. Wanunu, W. Morrison, Y. Rabin, A. Y. Grosberg, and A. Meller, *Electrostatic focusing of unlabelled dna into nanoscale pores using a salt gradient*, *Nature nanotechnology* **5**, 160 (2010).
- [18] C. Plesa, S. W. Kowalczyk, R. Zinsmeister, A. Y. Grosberg, Y. Rabin, and C. Dekker, *Fast translocation of proteins through solid state nanopores*, *Nano letters* **13**, 658 (2013).
- [19] M. Jain, H. E. Olsen, B. Paten, and M. Akeson, *The oxford nanopore minion: delivery of nanopore sequencing to the genomics community*, *Genome biology* **17**, 239 (2016).
- [20] M. L. Juan, M. Righini, and R. Quidant, *Plasmon nano-optical tweezers*, *Nature Photonics* **5**, 349 (2011).
- [21] V. Giannini, A. I. Fernández-Domínguez, S. C. Heck, and S. A. Maier, *Plasmonic nanoantennas: fundamentals and their use in controlling the radiative properties of nanoemitters*, *Chemical reviews* **111**, 3888 (2011).

- [22] S. Jain, D. Hirst, and J. O'sullivan, *Gold nanoparticles as novel agents for cancer therapy*, *The British journal of radiology* **85**, 101 (2012).
- [23] Y. Pang and R. Gordon, *Optical trapping of a single protein*, *Nano letters* **12**, 402 (2011).
- [24] M. Belkin, S.-H. Chao, M. P. Jonsson, C. Dekker, and A. Aksimentiev, *Plasmonic nanopores for trapping, controlling displacement, and sequencing of dna*, *ACS nano* **9**, 10598 (2015).
- [25] C. Chen, M. L. Juan, Y. Li, G. Maes, G. Borghs, P. Van Dorpe, and R. Quidant, *Enhanced optical trapping and arrangement of nano-objects in a plasmonic nanocavity*, *Nano letters* **12**, 125 (2011).
- [26] M. P. Cecchini, A. Wiener, V. A. Turek, H. Chon, S. Lee, A. P. Ivanov, D. W. McComb, J. Choo, T. Albrecht, S. A. Maier, *et al.*, *Rapid ultrasensitive single particle surface-enhanced raman spectroscopy using metallic nanopores*, *Nano letters* **13**, 4602 (2013).
- [27] S. Nam, I. Choi, C.-c. Fu, K. Kim, S. Hong, Y. Choi, A. Zettl, and L. P. Lee, *Graphene nanopore with a self-integrated optical antenna*, *Nano letters* **14**, 5584 (2014)



# 2

## LITHOGRAPHY-BASED FABRICATION OF NANOPORE ARRAYS IN FREESTANDING SiN AND GRAPHENE MEMBRANES

*We report a simple and scalable technique for the fabrication of nanopore arrays on freestanding SiN and graphene membranes based on electron-beam lithography and reactive ion etching. By controlling the dose of the single-shot electron-beam exposure, circular nanopores of any size down to 16 nm in diameter can be fabricated in both materials at high accuracy and precision. We demonstrate the sensing capabilities of these nanopores by translocating dsDNA through pores fabricated using this method, and find signal-to-noise characteristics on par with TEM-drilled nanopores. This versatile lithography-based approach allows for the high-throughput manufacturing of nanopores and can in principle be used on any substrate, in particular membranes made out of transferable 2D materials.*

---

This chapter has been published as: Daniel V. Verschuere, Wayne Yang, and Cees Dekker. Lithography-based fabrication of nanopore arrays in freestanding SiN and graphene membranes. *Nanotechnology*, 29(14):145302, 2018

## 2.1. INTRODUCTION

Solid-state nanopores drilled in a thin membrane are unique tools that allow for label-free high-throughput single-molecule investigation of biomolecules such as DNA, proteins, and peptides chains [1]. Their robustness, versatility, and ease of integration in CMOS processing are paramount to the sustained interest this class of biosensors has received over the past 15 years [2]. The principle of interrogation for nanopore sensing derives elegance from its simplicity: a nanopore, typically drilled in a 20 nm thick membrane, defines a nanoscale sensing volume through which biomolecules can be probed on passage, usually via an ionic-current readout [3]. More recently, nanopores in single-layer materials like graphene and MoS<sub>2</sub> have received a great deal of attention, as the two-dimensional (2D) nature of these materials drastically reduces the sensing volume and helps to enhance the signal [4, 5]. Both SiN and 2D nanopores have been used to provide insight into many complex biophysical phenomena, such as DNA-protein interactions [4, 6–9], protein-protein interactions [10], and DNA polymer physics [11, 12]. However nanopore fabrication is typically slow and expensive, particularly in 2D materials, preventing large-scale use of solid-state nanopores in commercial applications, such as clinical sensors for the detection of biomolecules in diagnostics [13, 14].

Currently, there are several techniques for the production of nanopores. First and foremost is the use of the electron beam of a Transmission Electron Microscope (TEM) [15]. This technique provides sub-nanometer precise control over the pore's diameter, but is very low in throughput, especially for larger sized nanopores (>15 nm) [16], very expensive, and labor intensive. A single nanopore takes at least 30 mins to be loaded into the TEM, aligned and sculpted to the desired size in a TEM by a trained operator. Furthermore, nanopores are notoriously hard to fabricate in 2D materials with conventional TEM drilling due to their sensitivity to carbon deposition and membrane damage [17]. Hence, the method lacks scalability and cost efficiency which are both required for commercialization. Fabrication using Helium Ion Microscope (HIM) is a promising, more high-throughput alternative for the fabrication of nanopores, but also requires access to expensive and delicate instrumentation [18, 19]. An alternative cost-effective technique is nanopore fabrication by controlled dielectric breakdown, where a nanopore is created by the timed termination of a large transmembrane voltage stress (~10 V) [20, 21]. However, the stochastic nature of the breakdown process does not provide control over the position of the nanopore [22]. Other techniques use ion bombardment and subsequent chemical [23, 24] or electrochemical wet etching [25]. Whereas these techniques can be used at high throughput, challenges remain in the timed termination of the wet etching [16] and the associated uniformity of the pore size.

Chemical dry etching or reactive ion etching (RIE) is a more promising alternative for high-throughput fabrication of large nanopores. In this widely used technique a pattern is predefined in a resist by electron-beam lithography (EBL), which is the standard technique used to define high-resolution structure in microfabrication, and is transferred into a substrate by plasma etching using reactive ions [26]. The directionality of the RIE process preserves the resolution obtained in the EBL pattern and allows for the resolution to be defined on a wafer scale [26–29]. The chemical dry etching allows a range of substrates to be used as membrane material [27], notably including

2D materials that require a transfer step. To exploit the potential of this technique for transferable materials, the EBL patterning should be performed on a freestanding membrane. Furthermore, patterning on a thin membrane can improve resolution, because it eliminates electron backscatter [30]. Here, we present a novel and simple method for rapid nanopore fabrication based on electron-beam lithography with reactive ion etching. By patterning the nanopores as a last step in the fabrication process, in principle any (transferable) membrane material can be readily used. To demonstrate the flexibility of this technique, we create single nanopores and nanopore arrays in both 20 nm thick SiN and single-layer graphene membranes. TEM inspection shows that the fabricated nanopores are highly circular and uniform in size. We show that the nanopore diameter can be set with nanometer precision by controlling the electron-beam dose. Finally, we demonstrate  $\lambda$ -DNA translocations through nanopores fabricated using this method. Although applied here for single-molecule biosensing, we anticipate that this simple, high-throughput, and versatile nanopore fabrication technique will find applications in other domains of the nanopore research field such as filtration, power generation and chemical sensing [19, 31, 32].

## 2.2. RESULTS AND DISCUSSION

Figure 2.1A outlines a schematic of the fabrication protocol for the production of a nanopore array in SiN. First, a layer a 100 nm thick layer of poly(methyl methacrylate) (PMMA-A3, 495K) electron sensitive resist (MicroChem Corp) is spin-coated on top of the chip containing a freestanding SiN membrane. Subsequently, the layer is patterned by exposing the resist with a 100 keV electron bundle from the electron-beam pattern generator (EBPG5200, Raith), using one single shot of e-beam exposure per nanopore. Details about the fabrication of the support and E-beam patterning can be found in the Supporting Information (SI) Section 2.4.1. After exposure, the PMMA is developed in a 1:3 mixture of methyl isobutyl ketone (MIBK) and isopropyl alcohol (IPA) for 1 min. Finally, the pattern is transferred into the SiN membrane by reactive ion etching with  $\text{CHF}_3$  (100 sec, 50 W, 50 sccm of  $\text{CHF}_3$ , 2.5 sccm of  $\text{O}_2$ , 8.6  $\mu\text{bar}$ , Leybold) and the resist is stripped in hot acetone (50°C) for 2 hours.

The fabrication of the graphene nanopore array (Fig. 2.1B) is analogous to the fabrication of the SiN nanopores. First, a layer of graphene (Graphenea, single layer CVD graphene on copper) is transferred onto a SiN membrane pre-patterned with square windows 1  $\mu\text{m}$  in size, creating 1x1  $\mu\text{m}$  freestanding areas of graphene (see SI Section 2.4.1). Then, a 150 nm thick layer of PMMA is spin-coated on top of the chip and the resist is exposed by a single shot from the electron beam. We note that thicker PMMA is used in the graphene nanopore arrays because the graphene requires an oxygen etch which also etches the PMMA mask substantially. After the development of the resist in 1:3 MIBK:IPA for one minute, the pattern is transferred into the graphene layer by reactive ion etching with oxygen (20 sec, 50 W, 20 sccm of  $\text{O}_2$ , 3.3  $\mu\text{bar}$ , Leybold). The remaining resist is stripped for 20 min in hot m-xylene (85°C) and air-dried. To avoid collapsing the freestanding graphene layer, the sample is gently plunged vertically into the solution. After 20 mins, the sample is removed and placed at an angle ( $\sim 20$  degrees to the horizontal plane) to allow the remaining droplet of m-xylene to evaporate.

Figure 2.2 shows example TEM images of nanopore arrays fabricated in both SiN

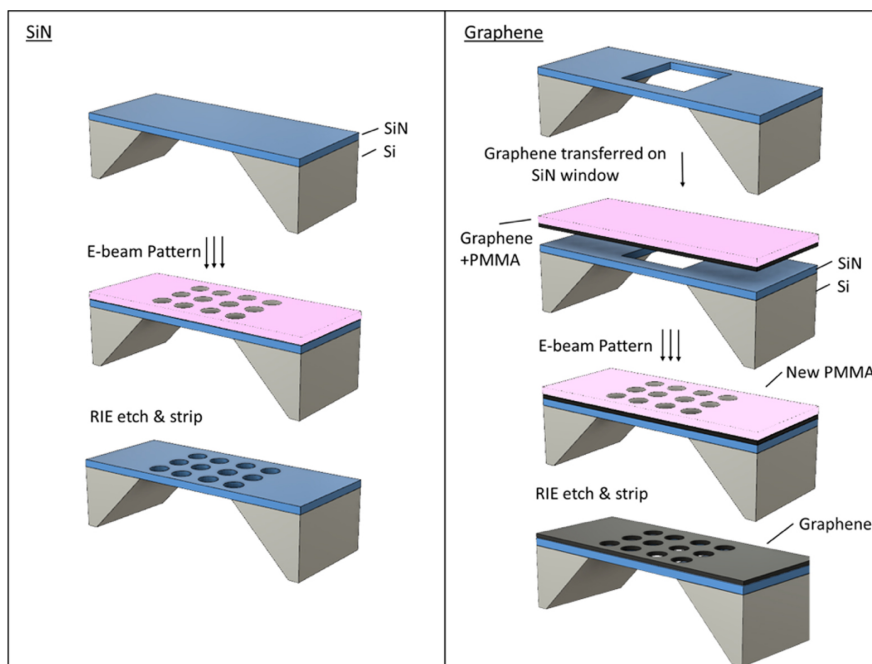


**Figure 2.1: Schematic of EBL assisted RIE nanopore fabrication. (A)** Fabrication process on SiN membrane. A 100 nm thick layer of PMMA is spin-coated on a SiN membrane prior to e-beam patterning. The pattern is transferred into the SiN membrane by reactive ion etching in a  $\text{CHF}_3$  plasma. Finally, the remaining resist is stripped in hot acetone ( $50^\circ\text{C}$ ) leaving a functional nanopore array. **(B)** The same process on the graphene membrane. A graphene layer with a supporting PMMA layer is deposited on a pre-etched SiN window. The supporting layer of PMMA is stripped and a new 150 nm of PMMA is deposited prior to e-beam patterning. The pattern is transferred into the graphene membrane by reactive ion etching in an oxygen plasma. Finally, the remaining resist is stripped in m-xylene, leaving a functional nanopore array.

(Fig. 2.2A) and in freestanding graphene (Fig. 2.2B) using the protocol outlined above. The nanopores in these examples were  $29 \pm 3$  nm and  $38 \pm 2$  nm (average  $\pm$  standard deviation) in diameter, for the SiN and graphene respectively. The nanopores produced are highly circular; The average ratio between their major and minor axis (major/minor) is  $1.08 \pm 0.08$  for the SiN arrays and  $1.08 \pm 0.14$  for the graphene nanopore arrays. We note that the graphene pores fabricated through this method seem to exhibit much less carbon deposition around the edges of the pore than conventionally drilled TEM graphene pores [33].

By adjusting the electron dose used in the patterning, we are able to vary the size of the nanopores formed, as shown in Fig. 2.3, where resulting diameter of the nanopore is plotted against the electron-beam dose used per shot of e-beam exposure, for both the SiN (Fig. 2.3A) and graphene nanopores (Fig. 2.3B). The smallest nanopore made was approximately  $16 \pm 2$  nm, both for SiN and graphene. Nanopores fabricated show similar variation in size (standard deviation is  $<10\%$ ) in both SiN and graphene. Because these values are similar and close to the size of the beamspot used ( $\sim 15$  nm), we speculate that the electron-beam spot size limits the resolution and hence it may be possible to

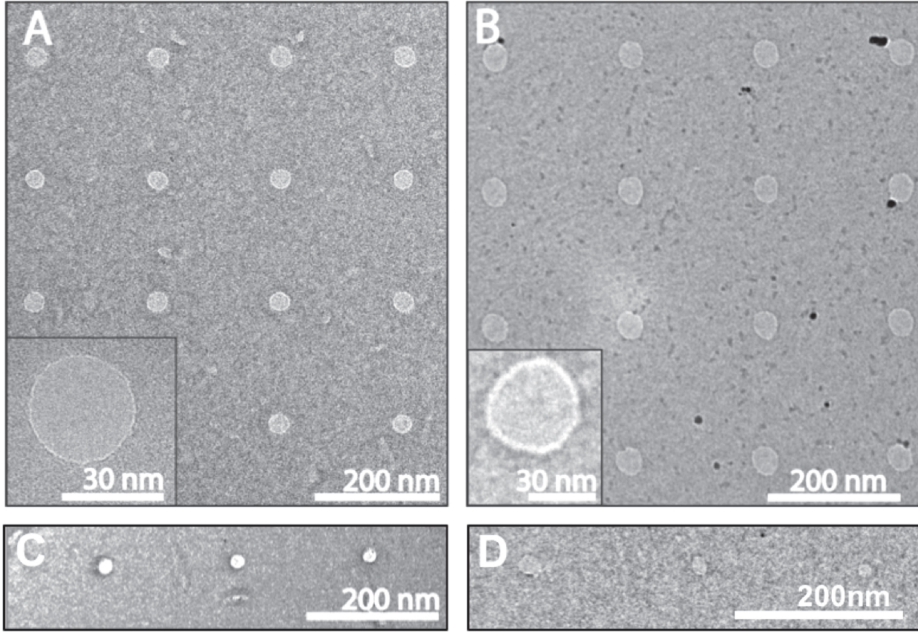


**Figure 2.2: TEM image of nanopore arrays fabricated using RIE.** (A) Nanopore array fabricated in a SiN membrane. The array was fabricated using a dose of 22 fC/shot, and the average pore diameter was  $29 \pm 3$  nm. (B) Nanopore array fabricated in free-standing graphene. The array was fabricated using a dose of 320 fC/shot, and the average pore diameter was  $38 \pm 2$  nm. The insets are zooms of a nanopore from each respective array, showing a circular nanopore. (C) An array of  $16 \pm 2$  nm size pores in SiN. (D) A dose test of nanopores on free-standing graphene. The nanopore diameters are, from left to right, 26 nm, 19 nm, and 17 nm. More examples of nanopore arrays can be found in the SI Section 2.4.4 and 2.4.3.

fabricate smaller pores using a smaller spot size. By varying the electron-beam dose only, we obtained a range of nanopore sizes from 16 to  $>100$  nm, though in principle even bigger sized pores can be produced by rasterizing a larger area with multiple shots of e-beam exposure. Interestingly, we find that the diameter of the resulting nanopore follows an empirical logarithmic relationship to the electron dose used for both SiN and graphene:

$$d = A \cdot \log(D) + B \quad (2.1)$$

where  $d$  is the nanopore diameter,  $D$  is the total electron dose, and  $A$  and  $B$  are fit parameters. A least-squares fit of Eqn. 2.1 to the red data points is plotted as a solid blue line in Fig. 2.3 and shows good agreement with the data (SiN:  $\chi_{red}^2 = 2.8$ , graphene:  $\chi_{red}^2 = 2.3$ ). The specific values of the fit parameters  $A$  and  $B$  are not universal and will depend on experimental factors, such as the membrane material, resist thickness and the electron accelerating voltage. For instance, a higher dose is needed to create the same size of nanopores in free standing graphene as compared to SiN. A different dependence results if patterning is performed on a thick substrate since electron backscatter from the substrate will be the dominant contribution to the

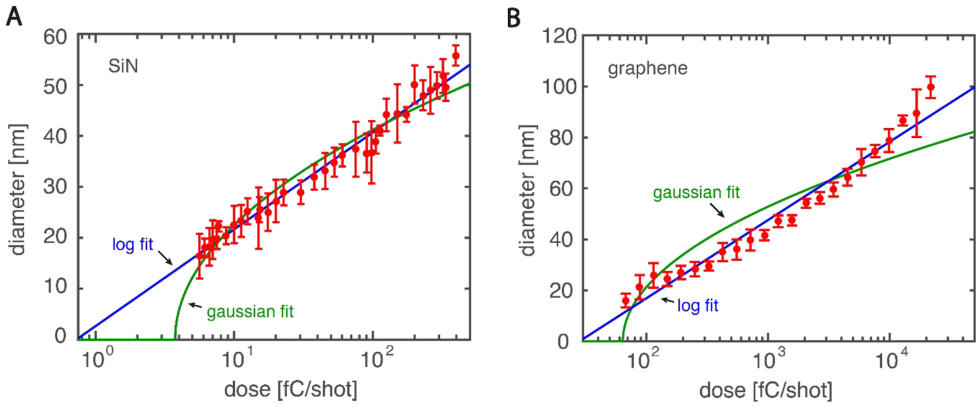


**Figure 2.3: Single-shot nanopore diameter versus electron-beam dose.** The solid blue line is an empirical logarithmic fit (A-SiN:  $\chi_{red}^2 = 2.8$ , B-Graphene:  $\chi_{red}^2 = 2.3$ ), the green curve is a fit assuming a Gaussian dependence of dose on diameter (A-SiN:  $\chi_{red}^2 = 7.2$ , B-Graphene:  $\chi_{red}^2 = 10.8$ ). Error bars are the standard deviation,  $\chi_{red}^2$  values are calculated using the standard error of the mean for each datapoint

exposure [29]. The agreement between the data and relationship is somewhat surprising as a more complex dependence is expected if one assumes that the nanopore size is merely set by the point spread function (PSF) of the electron beam [30]. This dependency can be modelled by assuming the resist only develops after receiving a local electron dose per unit area larger  $\tilde{D}$  than some threshold value of the dose  $D_T$ . Using a Gaussian PSF to describe the electron beam profile ( $\tilde{D} \propto De^{\gamma r^2}$ , where  $r$  is the distance from the center of the electron beam,  $D$  is the total dose, and  $\gamma$  is a fit parameter) and setting  $D_T = \tilde{D}(d)$ , a dependency of the diameter on the total dose can be extracted. This dependency is plotted as a green line in Fig. 2.3 and does not explain the trend well. Only moderate agreement between data (SiN:  $\chi_{red}^2 = 7.2$ , graphene:  $\chi_{red}^2 = 10.8$ ) is obtained. Hence the phenomenological model in Eqn. 2.1 should be used to determine the correct size of the nanopore from the dose.

One might wonder if the use of PMMA as a resist will set a maximum size for the nanopore size that can be fabricated, as it is known that PMMA will behave as a negative-tone resist at high doses [34] (>100 fC). This is however not the case, as at high-dose exposure, the resist in the tail of the beam will still be exposed to a low dose. This leads to a donut-shaped cut in the resist after development which will create a hole in the membrane after pattern transfer by RIE. Moreover, standard resist patterning (rastering) can be used for nanopores larger than 50 nm in diameter or for large nanopores of different shapes.

To show that the SiN and graphene nanopores created using this method can be used for the detection of DNA, we performed double-stranded DNA ( $\lambda$ -DNA, 48.5kbp) translocation experiments on these nanopores. A schematic of a typical nanopore experiment is shown in Fig. 2.4A, where DNA molecules added to the negatively-biased cis compartment of the flow cell are electrophoretically driven through the nanopore and detected by a change in ionic current through the pore. Fig. 2.4 shows examples of DNA translocations through a 18 nm graphene nanopore, fabricated using a dose of

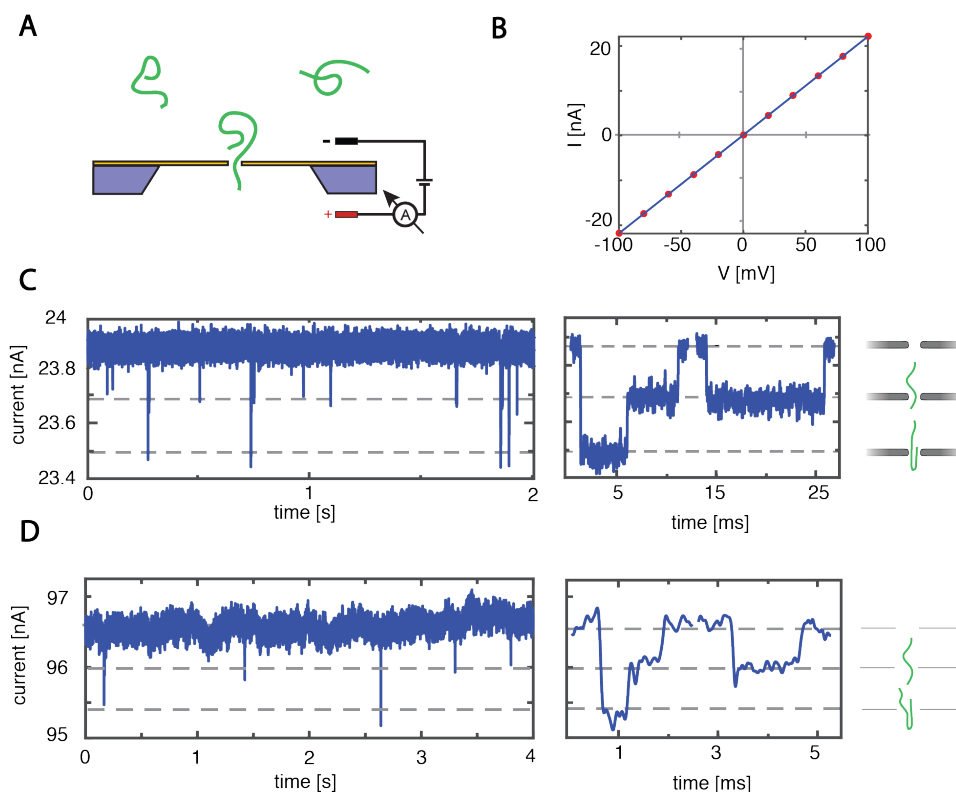


**Figure 2.4: DNA translocations through RIE-fabricated SiN and graphene nanopores.**(A) Schematic illustration of a DNA translocation experiment. (B) IV-curve of a 25 nm SiN nanopore with a resistance of 4.5 M $\Omega$ , with the corresponding linear fit. (C) Left: Current time trace through a SiN nanopore of 25 nm (4.5 M $\Omega$ ). Data was taken at 100 mV in 2M LiCl and low-pass filtered at 10 kHz. Right: zooms of DNA translocations, showing a folded and a linear translocation. (D) Left: Current time trace through a graphene nanopore of 18 nm (4.0 M $\Omega$ ). Data was taken at 500 mV in 2M LiCl and low-pass filtered at 5 kHz. The large driving voltage was used to enhance the DNA translocation rate. Right: zooms of DNA translocations, showing a folded and a linear translocation.

88 fC, and a 25 nm SiN nanopore, fabricated using a dose of 15 fC. DNA translocation experiments were done in a PEEK (Polyether ether ketone) flow cell in 2M LiCl (buffered with 20mM Tris-Cl, 2mM EDTA, pH 8) and we used Ag/AgCl electrodes and an Axopatch 200B amplifier (Molecular Devices) for current detection. To wet the graphene nanopore, we incubated the chip in the flow cell with a mixture of equal parts ethanol and water for 30 min. Figure 2.4B shows the linear IV curve of the SiN nanopore with a resistance of 4.5 M $\Omega$ . This compares well with the expected resistance of 3.9 M $\Omega$  for a 25 nm nanopore, calculated using a measured buffer conductivity of 13.8 nS/m and an effective membrane thickness of 6.7 nm. After adding  $\lambda$ -DNA to the cis chamber at a concentration of 10 ng/ $\mu$ L, transient current blockades could be clearly discerned, as shown in the first panel of Fig. 2.4C. The translocations show excellent signal-to-noise characteristics, illustrated by the zooms in the right panel of Fig. 2.4C of two such DNA

translocations, one molecule translocating in a linear fashion (right) and one in a folded conformation (left). The double-strand DNA conductance blockade of 1.8 nS ( $N = 580$ ) matches the expected value of 1.8 nS well. The normalized current power spectral density can be found in the SI Section 2.4.6.

2

Fig. 2.4D shows example DNA translocations through a 18 nm graphene nanopore. The nanopore had a resistance of 4.9 M $\Omega$ , which agrees reasonably well with the expected 4.2 M $\Omega$  using an effective membrane thickness of 0.6 nm [6, 35]. We used a high driving voltage of 500 mV, to enhance the low capture rates often observed in bare graphene nanopores [36]. The current time trace shows considerable low-frequency current noise, similar to what was observed for TEM-drilled graphene nanopores [6] (see SI Section 2.4.5). Analysis [37] of all detected events at 500 mV ( $N = 59$ ) show a blockade levels of  $\sim 1.0$  nS. This is markedly lower than the theoretically expected blockade of 5.6 nS from a dsDNA strand in a 18 nm graphene nanopore [38], but the discrepancy is consistent with previous work on TEM-drilled graphene nanopores which gave values of 1.5 nS for similar sized pores [33]. Graphene nanopores drilled using this RIE based method suffer from the same challenges as graphene nanopores drilled using TEM such as low fabrication yield. These challenges include limited statistics and current-signal resolving power caused by graphene-DNA interactions [39] and high  $1/f$  noise [6]. Overall about 10% of the graphene devices showed successful DNA translocation events compared to over 50% in SiN devices. Fortunately, these issues can be mitigated by reducing the freestanding area and using a molecular coating of the graphene [36].

Summarizing, these nanopores created using EBL with RIE show sensing characteristics that are on par with their TEM-drilled counterparts.

## 2.3. CONCLUSIONS

In conclusion, we have developed a facile method for rapid, flexible, and large-scale nanopore manufacturing in freestanding SiN and graphene membranes using electron-beam lithography with reactive ion etching which are very commonly available fabrication techniques. As the nanopore is created in the final step of the fabrication, our approach is extremely versatile and can in principle be used on any substrate, in particular 2D materials that require a transfer step. By adjusting the electron-beam dose, the diameter of the nanopore can accurately be controlled with a high-level of uniformity and precision. Furthermore, we demonstrate that the nanopores fabricated with this method show single-molecule sensing performances equivalent to their TEM drilled predecessors. The ease of the method allows for patterning large intact areas of freestanding 2D materials like graphene with a clearly defined array of nanopores. We expect that this technique will also find a range of applications beyond mere nanopore sensing, such as filtration with nano-sieves.

## 2.4. SUPPORTING INFORMATION

### 2.4.1. FABRICATION OF SiN MEMBRANE SUPPORTS WITH A 1X1 $\mu\text{M}$ SQUARE AND E-BEAM PATTERNING DETAILS

The silicon-nitride chips are fabricated using similar protocol as published in Janssen [40] to obtain 20 nm thick freestanding SiN membranes of 40x40  $\mu\text{m}$  wide. The top layers on the substrate are removed to create a flat SiN surface extending over the chip. Subsequently squares are etched in the SiN membrane which defined the area of freestanding graphene, in a similar procedure to making the nanopore arrays in SiN (see SI Section 2.4.2). For this, the chips are spincoated with a 100 nm thick layer of poly(methyl methacrylate) (PMMA, 495K) electron sensitive resist (MicroChem Corp). Then, the layer is patterned by exposing the resist with a 100 keV electron bundle from the electron-beam pattern generator (EBPG5200, Raith). Depending on the experiment, either a single square or an array of squares is patterned. For the dose test, we patterned an array of squares (1x1  $\mu\text{m}$ ). After exposure, the PMMA is developed in a 1:3 mixture of methyl isobutyl ketone (MIBK) and isopropyl alcohol (IPA) for 1 min. The pattern is transferred into the SiN by reactive ion etching (1 min 40 sec, 50 W, 50 sccm  $\text{CHF}_3$  and 2.5 sccm  $\text{O}_2$ , 8.5  $\mu\text{bar}$ , Leybold). The remaining resist is stripped using hot acetone (50°C) for 20 mins. For the nanopore experiments, a single 100x100 nm wide square is etched to define the freestanding graphene area. Electron-beam patterns are created in Layout-BEAMER (GenISys) from a gds file, where each nanopore is designed as a single 2x2 nm pixel size. The beam step size is set equal to the pixel size to ensure a single exposure per pixel and a mainfield size of 520x520  $\mu\text{m}$  is used. The pattern is subsequently imported into CJOB to generate a file compatible to the electron-beam pattern generator. Here an area dose is set and a beam is selected from a predefined list on the machine. The beam current used is 512 pA at an aperture size of 300  $\mu\text{m}$ . We note that using a different optimization marker on the sample holder did not reduce the optimized beam size of 16 nm. The dose per shot is calculated by multiplying the area dose by the beam step size.

### 2.4.2. GRAPHENE TRANSFER PROCESS

A supporting layer of 150 nm of PMMA is spin coated onto CVD graphene on copper (bought from Graphenea). The copper is etched away in a solution of 0.1M ammonium persulfate ( $(\text{NH}_4)_2\text{S}_2\text{O}_8$ , 5 g/100 ml). After 10 mins, the underside of the graphene-copper substrate is rinsed to strip the bottom layer of graphene. This is important to reduce the formation of graphene wrinkles. Subsequently, the graphene-copper substrate is placed back into the etching solution to fully etch the copper. The freely floating graphene-PMMA sample is scooped up by a clean glass slide and transferred into a beaker of clean deionized water. The sample was transferred to a second clean beaker of deionised water to completely remove all ammonium persulfate residues. In the final step, the graphene-PMMA sample is scooped up by the silicon nitride wafer sample (pre-etched with the freestanding window) and allowed to dry at an angle overnight. Finally, the PMMA is stripped by using a solution of hot acetone (45°C) or hot xylene (85°C) and the sample is ready for the patterning step.

### 2.4.3. TEM IMAGES OF GRAPHENE NANOPORE ARRAYS

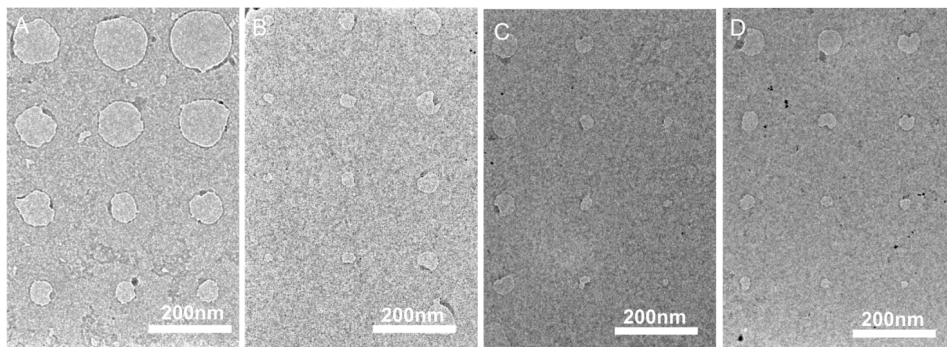


**Figure S2.5: Example TEM images of a nanopore arrays fabricated using RIE on graphene.** The electron dose was varied to produce different sized holes. (A) Graphene nanopore array with diameters ranging from 140 nm to 67 nm. (B-D) Graphene nanopore array with diameters ranging from (B) 69 nm to 23 nm, (C) 62 nm to 17 nm (D) 53 nm to 18 nm. The variance in size of hole produced at each of the respective dose is reported in the main text.

### 2.4.4. TEM IMAGES OF SiN NANOPORE ARRAYS

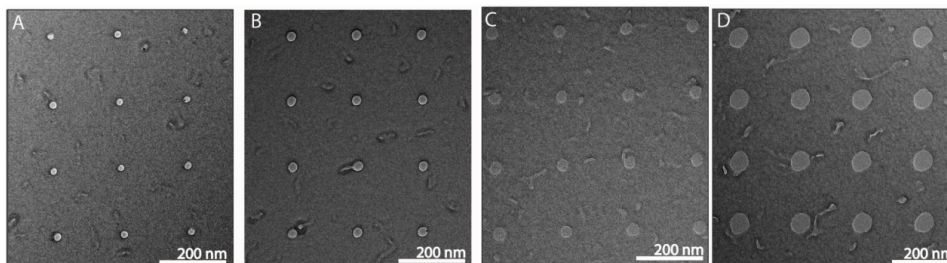


**Figure S2.6: Example TEM images of a nanopore arrays fabricated using RIE in SiN.** (A) Nanopore array with an average diameter of  $16 \pm 2$  nm. (B) Nanopore array with an average diameter of  $26 \pm 2$  nm. (C) Nanopore array with an average diameter of  $35 \pm 3$  nm. (D) Nanopore array with  $62 \pm 2$  nm.

### 2.4.5. NOISE SPECTRUM OF RIE FABRICATED GRAPHENE NANOPORE

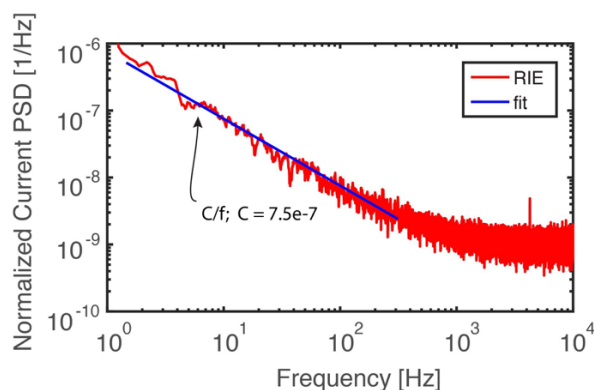


**Figure S2.7:** Normalized current power spectral density (PSD) ( $S_I/I^2$ ) of a 18 nm graphene nanopore fabricated using RIE using a dose of 88 fC and a fit to flicker noise contribution ( $S_I/I^2 = C/f$ ), where  $f$  is the frequency and  $C$  is low-frequency noise amplitude. The fit shows a value for the low-frequency noise amplitude of  $7.5 \cdot 10^{-7}$ , which is similar to values obtained from graphene nanopores drilled with the TEM ( $\sim 10^{-6}$ ) [6]. The PSDs are smoothed using a 20-point moving average.

### 2.4.6. NOISE SPECTRUM OF RIE FABRICATED GRAPHENE NANOPORE

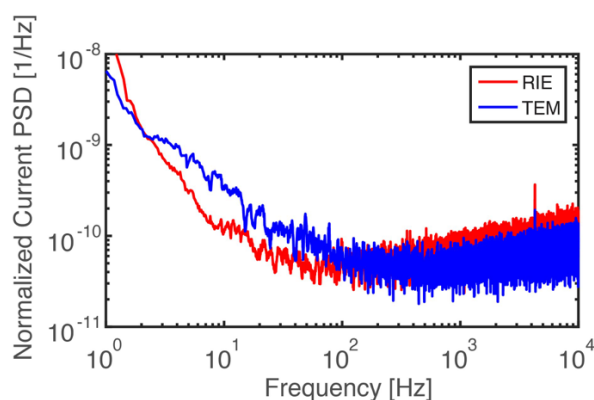


**Figure S2.8:** Normalized current power spectral density (PSD) ( $S_I/I^2$ ) of a 25 nm SiN nanopore fabricated using RIE with a dose of 15 fC and a 20 nm nanopore created using TEM drilling. The low frequency component of the noise (<1 kHz) is comparable between TEM drilled and RIE fabricated nanopores. The PSDs are smoothed using a 20-point moving average.

## REFERENCES

- [1] H. Arjmandi-Tash, L. A. Belyaeva, and G. F. Schneider, *Single molecule detection with graphene and other two-dimensional materials: nanopores and beyond*, Chemical Society Reviews **45**, 476 (2016).

- [2] B. N. Miles, A. P. Ivanov, K. A. Wilson, F. Doğan, D. Japrun, and J. B. Edel, *Single molecule sensing with solid-state nanopores: novel materials, methods, and applications*, Chemical Society Reviews **42**, 15 (2013).
- [3] M. Wanunu, *Nanopores: A journey towards dna sequencing*, Physics of life reviews **9**, 125 (2012).
- [4] J. Feng, M. Graf, K. Liu, D. Ovchinnikov, D. Dumcenco, M. Heiranian, V. Nandigana, N. R. Aluru, A. Kis, and A. Radenovic, *Single-layer mos2 nanopores as nanopower generators*, Nature **536**, 197 (2016).
- [5] S. J. Heerema and C. Dekker, *Graphene nanodevices for dna sequencing*, Nature nanotechnology **11**, 127 (2016).
- [6] S. J. Heerema, G. F. Schneider, M. Rozemuller, L. Vicarelli, H. W. Zandbergen, and C. Dekker, *If noise in graphene nanopores*, Nanotechnology **26**, 074001 (2015).
- [7] J. Chen, C. Li, and G. Shi, *Graphene materials for electrochemical capacitors*, The journal of physical chemistry letters **4**, 1244 (2013).
- [8] D.-e. Jiang, V. R. Cooper, and S. Dai, *Porous graphene as the ultimate membrane for gas separation*, Nano letters **9**, 4019 (2009).
- [9] C. Raillon, P. Cousin, F. Traversi, E. Garcia-Cordero, N. Hernandez, and A. Radenovic, *Nanopore detection of single molecule rnap-dna transcription complex*, Nano letters **12**, 1157 (2012).
- [10] G. Goyal, Y. B. Lee, A. Darvish, C. W. Ahn, and M. J. Kim, *Hydrophilic and size-controlled graphene nanopores for protein detection*, Nanotechnology **27**, 495301 (2016).
- [11] M. M. Marshall, J. Ruzicka, O. K. Zahid, V. C. Henrich, E. W. Taylor, and A. R. Hall, *Nanopore analysis of single-stranded binding protein interactions with dna*, Langmuir **31**, 4582 (2015).
- [12] D. Japrun, A. Bahrami, A. Nadzeyka, L. Peto, S. Bauerdick, J. B. Edel, and T. Albrecht, *Ssb binding to single-stranded dna probed using solid-state nanopore sensors*, The Journal of Physical Chemistry B **118**, 11605 (2014).
- [13] K. Chen, M. Juhász, F. Gularek, E. Weinhold, Y. Tian, U. F. Keyser, and N. A. Bell, *Ionic current-based mapping of short sequence motifs in single dna molecules using solid-state nanopores*, Nano letters **17**, 5199 (2017).
- [14] J. Y. Sze, A. P. Ivanov, A. E. Cass, and J. B. Edel, *Single molecule multiplexed nanopore protein screening in human serum using aptamer modified dna carriers*, Nature Communications **8**, 1552 (2017).
- [15] M. J. Kim, M. Wanunu, D. C. Bell, and A. Meller, *Rapid fabrication of uniformly sized nanopores and nanopore arrays for parallel dna analysis*, Advanced materials **18**, 3149 (2006).
- [16] T. Deng, M. Li, Y. Wang, and Z. Liu, *Development of solid-state nanopore fabrication*

- technologies*, Science bulletin **60**, 304 (2015).
- [17] Q. Xu, M.-Y. Wu, G. F. Schneider, L. Houben, S. K. Malladi, C. Dekker, E. Yucelen, R. E. Dunin-Borkowski, and H. W. Zandbergen, *Controllable atomic scale patterning of freestanding monolayer graphene at elevated temperature*, Acs Nano **7**, 1566 (2013).
- [18] J. Yang, D. C. Ferranti, L. A. Stern, C. A. Sanford, J. Huang, Z. Ren, L.-C. Qin, and A. R. Hall, *Rapid and precise scanning helium ion microscope milling of solid-state nanopores for biomolecule detection*, Nanotechnology **22**, 285310 (2011).
- [19] Y. Deng, Q. Huang, Y. Zhao, D. Zhou, C. Ying, and D. Wang, *Precise fabrication of a 5 nm graphene nanopore with a helium ion microscope for biomolecule detection*, Nanotechnology **28**, 045302 (2016).
- [20] H. Kwok, K. Briggs, and V. Tabard-Cossa, *Nanopore fabrication by controlled dielectric breakdown*, PloS one **9**, e92880 (2014).
- [21] A. T. Kuan, B. Lu, P. Xie, T. Szalay, and J. A. Golovchenko, *Electrical pulse fabrication of graphene nanopores in electrolyte solution*, Applied physics letters **106**, 203109 (2015).
- [22] A. Zrehen, T. Gilboa, and A. Meller, *Real-time visualization and sub-diffraction limit localization of nanometer-scale pore formation by dielectric breakdown*, Nanoscale **9**, 16437 (2017).
- [23] S. R. Park, H. Peng, and X. S. Ling, *Fabrication of nanopores in silicon chips using feedback chemical etching*, Small **3**, 116 (2007).
- [24] T. Deng, J. Chen, C. Wu, and Z. Liu, *Fabrication of inverted-pyramid silicon nanopore arrays with three-step wet etching*, ECS journal of solid state science and technology **2**, P419 (2013).
- [25] K. Yasuda, A. Ghicov, T. Nohira, N. Kani, R. Hagiwara, and P. Schmuki, *Preparation of organized ti nanorods by successive electrochemical processes in aqueous solution and molten salt*, Electrochemical and Solid-State Letters **11**, C51 (2008).
- [26] A. Han, M. Creus, G. Schürmann, V. Linder, T. R. Ward, N. F. de Rooij, and U. Staufer, *Label-free detection of single protein molecules and protein-protein interactions using synthetic nanopores*, Analytical chemistry **80**, 4651 (2008).
- [27] J. Bai, D. Wang, S.-w. Nam, H. Peng, R. Bruce, L. Gignac, M. Brink, E. Kratschmer, S. Rossnagel, and P. Waggoner, *Fabrication of sub-20 nm nanopore arrays in membranes with embedded metal electrodes at wafer scales*, Nanoscale **6**, 8900 (2014).
- [28] A. G. Ahmadi and S. Nair, *Geometry of nanopore devices fabricated by electron beam lithography: Simulations and experimental comparisons*, Microelectronic Engineering **112**, 149 (2013).
- [29] R. Wei, D. Pedone, A. Zürner, M. Döblinger, and U. Rant, *Fabrication of metallized nanopores in silicon nitride membranes for single-molecule sensing*, Small **6**, 1406 (2010).

- [30] I. Adesida, T. Everhart, and R. Shimizu, *High resolution electron-beam lithography on thin films*, Journal of Vacuum Science and Technology **16**, 1743 (1979).
- [31] A. Aghigh, V. Alizadeh, H. Y. Wong, M. S. Islam, N. Amin, and M. Zaman, *Recent advances in utilization of graphene for filtration and desalination of water: a review*, Desalination **365**, 389 (2015).
- [32] S. Howorka and Z. Siwy, *Nanopore analytics: sensing of single molecules*, Chemical Society Reviews **38**, 2360 (2009).
- [33] G. F. Schneider, S. W. Kowalczyk, V. E. Calado, G. Pandraud, H. W. Zandbergen, L. M. Vandersypen, and C. Dekker, *Dna translocation through graphene nanopores*, Nano letters **10**, 3163 (2010).
- [34] H. Duan, D. Winston, J. K. Yang, B. M. Cord, V. R. Manfrinato, and K. K. Berggren, *Sub-10-nm half-pitch electron-beam lithography by using poly (methyl methacrylate) as a negative resist*, Journal of Vacuum Science & Technology B, Nanotechnology and Microelectronics: Materials, Processing, Measurement, and Phenomena **28**, C6C58 (2010).
- [35] R. C. Rollings, A. T. Kuan, and J. A. Golovchenko, *Ion selectivity of graphene nanopores*, Nature communications **7** (2016).
- [36] G. F. Schneider, Q. Xu, S. Luik, S. Hage, J. N. Spoor, S. Malladi, H. Zandbergen, and C. Dekker, *Tailoring the surface chemistry and hydrophobicity of graphene nanopores*, Nature communications **4**, 2619 (2013).
- [37] C. Plesa and C. Dekker, *Data analysis methods for solid-state nanopores*, Nanotechnology **26**, 084003 (2015).
- [38] A. T. Carlsen, O. K. Zahid, J. Ruzicka, E. W. Taylor, and A. R. Hall, *Interpreting the conductance blockades of dna translocations through solid-state nanopores*, Acs Nano **8**, 4754 (2014).
- [39] Y. Kabiri, A. N. Ananth, J. van der Torre, A. Katan, J.-Y. Hong, S. Malladi, J. Kong, H. Zandbergen, and C. Dekker, *Distortion of dna origami on graphene imaged with advanced tem techniques*, small **13**, 1700876 (2017).
- [40] X. J. Janssen, M. P. Jonsson, C. Plesa, G. V. Soni, C. Dekker, and N. H. Dekker, *Rapid manufacturing of low-noise membranes for nanopore sensors by trans-chip illumination lithography*, Nanotechnology **23**, 475302 (2012)

# 3

## SELF-ALIGNED PLASMONIC NANOPORES BY OPTICALLY CONTROLLED DIELECTRIC BREAKDOWN

*We present a novel cost-efficient method for the fabrication of high-quality self-aligned plasmonic nanopores by means of optically controlled dielectric breakdown. Excitation of a plasmonic bowtie nanoantenna on a dielectric membrane localizes the high-voltage-driven breakdown of the membrane to the hotspot of the enhanced optical field, creating a nanopore that is automatically self-aligned to the plasmonic hotspot of the bowtie. We show that the approach provides precise control over the nanopore size and that these plasmonic nanopores can be used as single molecule DNA sensors with a performance matching that of TEM-drilled nanopores. The principle of optically controlled breakdown can also be used to fabricate non-plasmonic nanopores at a controlled position. Our novel fabrication process guarantees alignment of the nanopore with the optical hotspot of the nanoantenna, thus ensuring that pore-translocating biomolecules interact with the concentrated optical field that can be used for detection and manipulation of analytes.*

---

This chapter has been published as: Sergii Pud, Daniel V. Verschueren, Nikola Vukovic, Calin Plesa, Magnus P. Jonsson, and Cees Dekker. Self-aligned plasmonic nanopores by optically controlled dielectric breakdown. Nano Letters, 15(10):7112-7117, 2015

### 3.1. INTRODUCTION

Solid-state nanopores [1–3] are biologically inspired sensors for label-free detection of single-biomolecules that show great promise for a large variety of applications, such as the investigation of proteins [4, 5], DNA-protein interactions [6–8], protein-receptor binding [9], and DNA sequencing [10, 11]. The elegance of nanopore biosensing relies in its robustness, versatility and simple working principle: the passage of biomolecules through a nanopore sensor modulates the nanopore ionic conductance, which serves as a means for detection and investigation of the target analyte [12, 13]. Yet, solid-state nanopores face challenges. For example, control over the translocation speed of the biomolecule [14–17] is crucial for base-pair recognition on a DNA polymer, as already demonstrated using biological nanopores [18, 19]. Furthermore, it would be advantageous to expand the nanopore approach with new measuring modalities (e.g. optical detection) beyond mere electrical probing.

Recently, plasmonic solid-state nanopores were introduced, [20–24] which present new opportunities for biomolecular sensing. Here, a plasmonic nanoantenna enhances and focuses electromagnetic radiation to a nanoscale volume (hotspot) right at the nanopore through which biomolecules can be translocated. Reports on plasmonic nanopores have so far mostly focused on nanoplasmonic heating [25–27]. However, great promise lies in also exploiting the capabilities of these plasmonic nanostructures for extreme light-concentration to local nm-sized hotspots. Indeed, first examples of plasmon-enhanced optical detection of translocating analytes are already at hand [22, 24]. For these applications it is of paramount importance that the nanopore is precisely aligned with the optical hotspot to ensure that biomolecules pass the region of highest field localization. Fabrication of plasmonic nanopores thus requires accurate positioning of the nanopore with respect to the plasmonic hotspot. Currently this is achieved by means of transmission electron microscopy (TEM) drilling or ion milling, where a beam of highly energetic charged particles locally ablates the membrane material to form a nanosized aperture [28–31]. While providing nanometer-precise control of the nanopore size and shape, [29] these drilling techniques have significant drawbacks: they are labor-intensive and not scalable, as fabrication is sequential and the constant presence of a machine operator is required. These issues make milling approaches for nanopore fabrication expensive and low-throughput. Recently however, an alternative method of in situ nanopore fabrication was introduced, based on the effect of dielectric breakdown [32, 33]. In this technique, a nanopore is rapidly formed upon local failure in the dielectric membrane, induced by applying a high transmembrane voltage that creates a large electric field (on the order of MV/cm) in the membrane [34]. The size of the nanopore can be determined by monitoring the ionic transmembrane current that flows through the newly formed pore. Once the nanopore has reached a certain size, a lowering of the applied voltage can stop the breakdown process. Subsequently, the nanopore can be enlarged to any desired diameter by applying short voltage pulses [35]. While the simple and inexpensive method of dielectric breakdown can provide high-quality nanopores [32, 33], its use has so far been limited to applications that do not require control of the nanopore position.

Here, we demonstrate a method for self-aligned fabrication of plasmonic nanopores based on the promotion and localization of the dielectric breakdown by plasmonic

excitation. By simultaneously electrically biasing the freestanding silicon-nitride membrane close to its critical field and applying laser excitation of a gold bowtie plasmonic nanostructure, we are able to induce the formation of a nanopore in the optical field hotspot of the bowtie nanoantenna. These fabricated plasmonic nanopores show a performance that is competitive with TEM-fabricated plasmonic nanopores [20, 27], as demonstrated by optical beam profiling and detection of DNA translocations through the pores. The approach is cost-efficient, high-throughput and ensures that the nanopore is formed right in the gap of the bowtie antenna, which is essential for future applications of plasmonic nanopores for label-free biomolecule manipulation.

### 3.2. RESULTS AND DISCUSSION

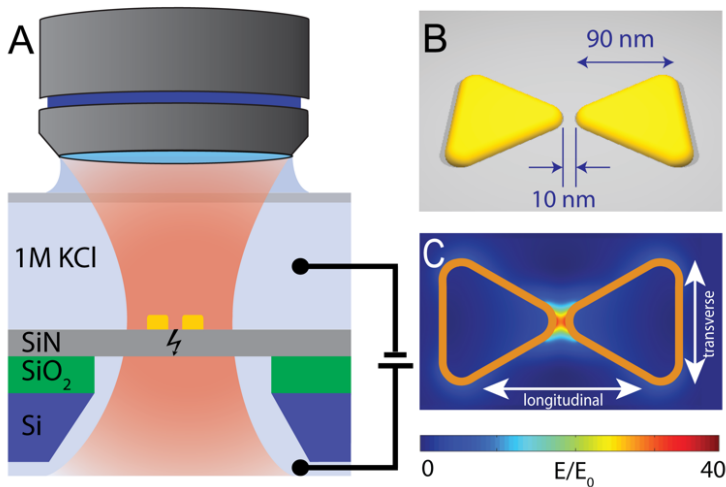


**Figure 3.1: Schematic of plasmonic nanopore fabrication experiment** (A) Side-view sketch of the experimental layout. The membrane is exposed to a DC electric field and to the optical field that is locally enhanced by the plasmonic antenna. (B) Sketch of the plasmonic bowtie antenna on top of the freestanding silicon-nitride membrane. Typical sizes are indicated. (C) Result of a simulation of the electric field distribution ( $E$ ) compared to the incident electric field amplitude ( $E_0$ ) at longitudinal excitation at a wavelength of 785 nm. Orange frames outline the position of the plasmonic structures in the model. The different polarization directions (longitudinal and transverse) of the excitation light is indicated with an arrow.

Figure 3.1A shows the concept of the plasmonic nanopore formation process, where a gold plasmonic bowtie antenna on a 20 nm thick low-stress silicon nitride-membrane is illuminated with a focused laser beam while a large transmembrane bias is applied. The gold bowtie nanoantenna (Fig. 3.1B) consists of two 30 nm thick gold equilateral triangles of 90 nm size (tip-to-base) that face each other tip-to-tip with a 10 nm separation gap, fabricated using lift-off (see Experimental section 3.4 for fabrication details). Fig. 3.1C shows the results of a finite-difference time domain (FDTD) simulation for the optical field distribution around the bowtie at 785 nm incident wavelength. The structures can be illuminated at different polarizations of the laser beam, as indicated

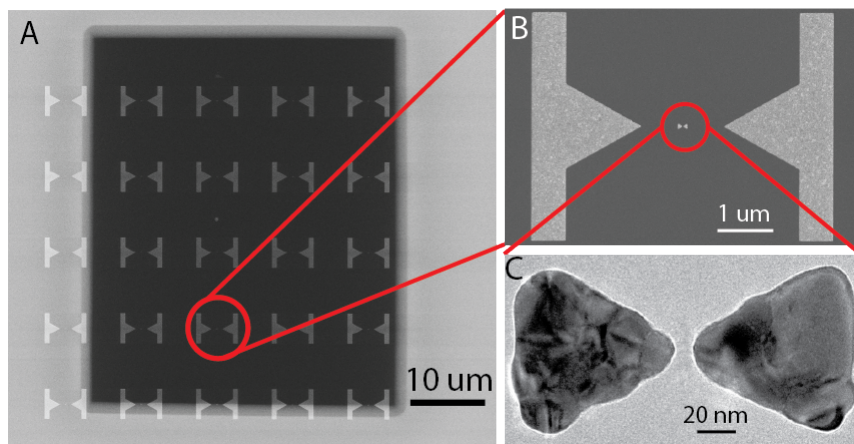


**Figure 3.2: Plasmonic nanopore device before breakdown.** (A) SEM image of a freestanding silicon-nitride membrane and gold marker structures. (B) SEM image of the gold plasmonic nanostructure (in the center) and two gold markers used to optically align the laser focus with the nanostructures. (C) Close-up TEM image of a plasmonic bowtie antenna on the membrane (without a pore yet).

on Fig. 3.1C: one along the main axis of the structures, termed the longitudinal mode of excitation, and one perpendicular to this axis, termed the transverse mode. For a longitudinal polarization of the incident light (Fig. 3.1C), the optical field is clearly localized to the center of the bowtie structure (see Section 3.4.2). The hotspot of the evanescent field between the gold structures produces field enhancements up to 40 times compared to the incident field strength at the illumination wavelength. We used large metal markers to align the plasmonic nanostructure with our focused 785 nm wavelength laser. Figure 3.2A shows a scanning electron microscopy (SEM) image of a freestanding silicon nitride membrane with these metal markers. The separation between the metal markers and the plasmonic bowtie antenna is more than 500 nm (see Fig. 3.2B), to prevent optical coupling of the nanoantenna to the metal markers. Fig. 3.2C shows a transmission electron microscopy (TEM) image of the nanostructure. The triangles have slightly rounded tips resulting from the fabrication process, which was accounted for in the optical field simulations (Fig. 3.1C).

Fabrication of a nanopore using plasmonic dielectric breakdown starts with assembling the sample in an optically accessible flow cell as described in [36] and flushing in 1M KCl or 2M LiCl electrolyte solution. The electrolyte solution was buffered to pH 8 with 10mM Tris-Cl and 1mM EDTA to provide better control over the breakdown process [33]. After aligning the diffraction-limited laser spot ( $\sim 0.5 \mu\text{m}$  in size) with the plasmonic nanostructure, the membrane bias voltage is applied using Ag/AgCl electrodes (see Experimental Section 3.4.1 for details). Figure 3.3 shows an example time-trace of the current through the membrane during a breakdown experiment. First, applying a transmembrane voltage of  $V_m = 6 \text{ V}$  results in a leakage current due to trap-assisted tunneling. [37]. No pore formation occurs with these settings, even after long times, as discussed in more detail below. Next, we keep the applied voltage and

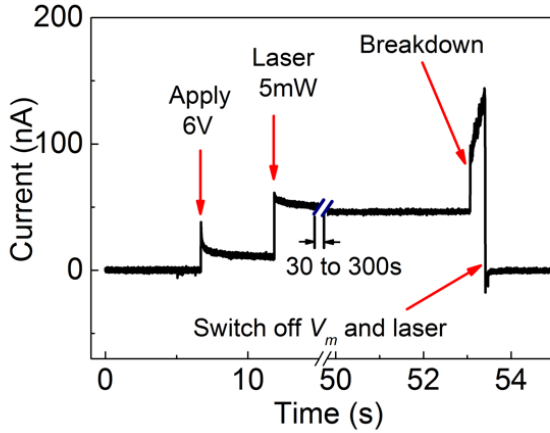


**Figure 3.3:** Time trace of the transmembrane current during the formation of a plasmonic solid-state nanopore by dielectric breakdown.

add illumination of the selected plasmonic bowtie structure with 5 mW laser power in longitudinal mode. This often increases the leakage current (see Fig. 3.3), although quantitatively this varies from sample to sample. Then, within the next 30 s to 300 s, we suddenly discern a very rapid increase of the current across the membrane. This signifies the plasmonic dielectric breakdown event, which is associated with the formation of a nanopore (Fig. 3.3). After reaching a certain preset threshold (130 nA in this case), both the bias voltage and the laser illumination are switched off to allow further control over the size of the nanopore. The resulting nanopores have a 70 to 130 M $\Omega$  resistance, corresponding to a nanopore diameter smaller than 4.5 nm using the model of Kowalczyk et al. for the nanopore conduction with the effective pore length taken as 8.6 nm [38]. Such a small pore can be further enlarged to any desired diameter by subsequent applying moderate voltage pulses [35]. After sizing the breakdown pore to the desired diameter, it is left overnight in 4M LiCl solution to equilibrate as in [32] before DNA translocation experiment. Equilibration is thought to occur as the nanopore surface slowly rearranges over time into a energetically more favorable shape [28].

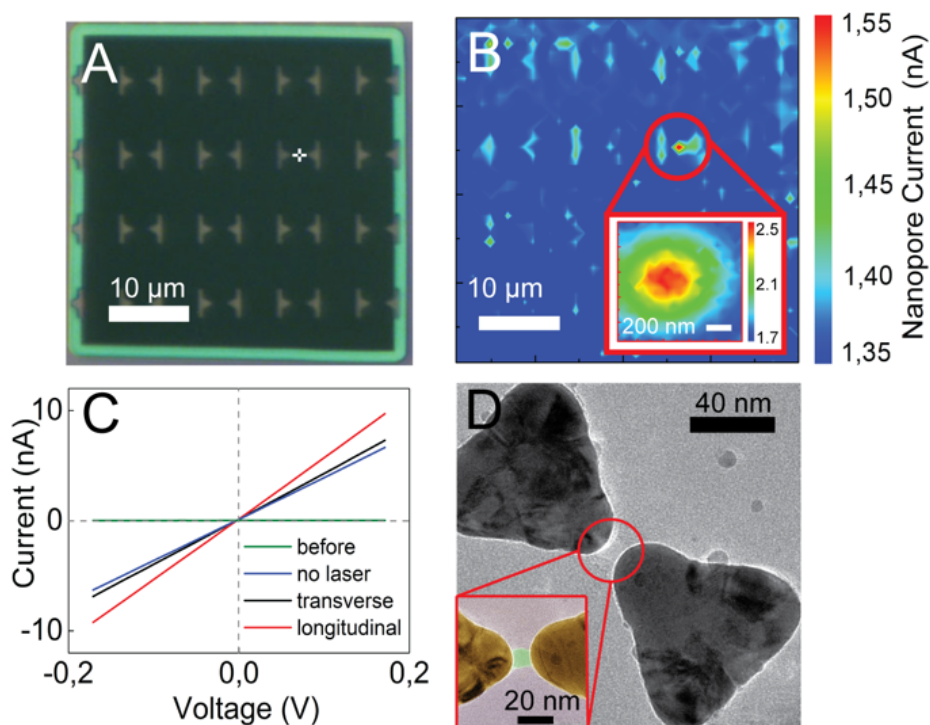


**Figure 3.4: Characterization of plasmonic nanopore form by controlled dielectric breakdown** (A) Optical image of the freestanding silicon-nitride membrane with gold markers indicating the positions of the plasmonic nanostructures. The position of the laser spot that is used to induce the formation of the nanopore, and hence the desired nanopore location, are indicated by a white cross. (B) Ionic current map of the membrane at 100 mV bias at low (0.5 mW) laser power after pore formation. The inset is a higher resolution scan of the area near the nanopore. (C) Current-voltage characteristics of the fabricated pore acquired with and without laser excitation of the plasmonic bowtie antenna. Green line corresponds to the current-voltage characteristic of the freestanding membrane before breakdown event. (D) Typical TEM image of a nanopore fabricated using plasmonic dielectric breakdown. The zoom in the inset shows a false-colored image of the gap of the gold bowtie structure that more clearly visualizes the nanopore.

We are able to locate the nanopore in the plasmonic nanopore setup directly after its formation and enlargement. Figure 3.4A shows the freestanding silicon nitride membrane where the white cross indicates the point where we intended to create a plasmonic nanopore by illuminating a bowtie that was located at that position. After the breakdown, the pore location was determined by scanning the membrane with a low-power (0.5 mW) laser beam and simultaneous monitoring of the nanopore current at 100 mV transmembrane voltage (Fig. 3.4B). When the laser focus illuminates the plasmonic nanostructure in the vicinity of the fabricated nanopore, localized heating of the plasmonic structure causes a local increase of the electrolyte conductivity [27], and hence an increase in the ionic current through the pore, which results in an absolute maximum on the current map. The location of the maximum in Fig. 3.4B confirms that the nanopore was indeed successfully formed at the position of the

plasmonic bowtie that was illuminated with the laser during pore formation (Fig. 3.4A). The inset of Fig. 3.4B shows a higher-resolution membrane scan of the area in the vicinity of the nanopore. To characterize the located nanopore we measure the I-V curves of the formed pore under transverse and longitudinal laser polarizations, as shown in Fig. 3.4C. Linear I-V curves are observed. The creation of the pore drastically changed the resistance from  $>1\text{ G}\Omega$  before breakdown to a value of  $26.6\text{ M}\Omega$ . Upon laser illumination, the pore resistance changes to  $24.3\text{ M}\Omega$  and  $18.1\text{ M}\Omega$  for transverse and longitudinal excitation respectively, which indicates that the fabricated pore is in close proximity to a plasmonic nanostructure and that the absorption cross-section of the bowtie nanoantenna in longitudinal mode is higher than in transverse mode.

TEM microscopy allowed for a careful visualization of the nanopore. Figure 3.4D shows a typical TEM image of a plasmonic nanopore that was fabricated by means of plasmonic dielectric breakdown in longitudinal mode. In agreement with our hypothesis, the nanopore has formed right in the gap of the bowtie structure, where the hotspots of the optical field are located (clear from the false-colored inset in Fig. 3.4D). Whereas a temperature elevation is known to promote dielectric breakdown [39], this would cause the pore to form anywhere around the nanostructure, as the temperature profile over the  $\sim 100\text{ nm}$  nanostructure is nearly uniform [40]. Instead, we observe that pores form consistently at the center of the bowtie (see additional examples in Supporting Information (SI) Section 3.5.1), confirming that the plasmonic optical field enhancement plays an essential role in the localization of the breakdown effect.

In order to set proper conditions for plasmonic dielectric breakdown we selected an applied voltage of  $V_m = 6\text{ V}$ . This was the highest attainable voltage that was insufficient to generate a dielectric breakdown in absence of plasmonic excitation, within at least 30 min of observation. Such a  $V_m$  creates an electric field strength of  $3\text{ MV/cm}$  in the  $20\text{ nm}$  thick dielectric membrane, which is at least 3 times lower than the breakdown field of low-stress silicon-nitride films as reported in the literature [41, 42]. Staying below the breakdown field safeguards us against the occurrence of a regular breakdown event [33], which would result in the formation of a nanopore in a random location on the membrane. Notably, the optical field in the hotspot of the bowtie antenna at  $5\text{ mW}$  of laser power is estimated to produce an optical field of  $1.5\text{ MV/cm}$  in the plasmonic hotspot (see SI Section 3.5.5) that is spatially localized to a small volume of a few nanometers. While providing an additional electromagnetic field at the position for pore formation, this highly nonuniform optical field has a different nature than the applied DC electric field.

A number of control experiments confirm that the plasmonic dielectric breakdown is the result of synergetic influence of the DC electric field and the plasmonic optical field on the membrane. First, we verified that the pores made by regular dielectric breakdown, without laser illumination, at  $V_m$  higher than  $7\text{ V}$  did indeed form in a random location on the freestanding membrane, unaffected by the presence of the plasmonic nanostructures. Using higher laser powers, the pore can be located by scanning the membrane as described above (See SI Section 3.5.3). Second, we demonstrate that, interesting in itself, the optical field of the laser is capable of localizing the breakdown event also without plasmonic structures, provided that a much higher laser power ( $45\text{ mW}$ ) is used (See SI Section 3.5.2). This confirms that it is the optical nature of

the excitation that promotes the dielectric breakdown rather than mere temperature elevation. In passing, we note that this also provides a novel means to control the position of nonplasmonic nanopores using dielectric breakdown.

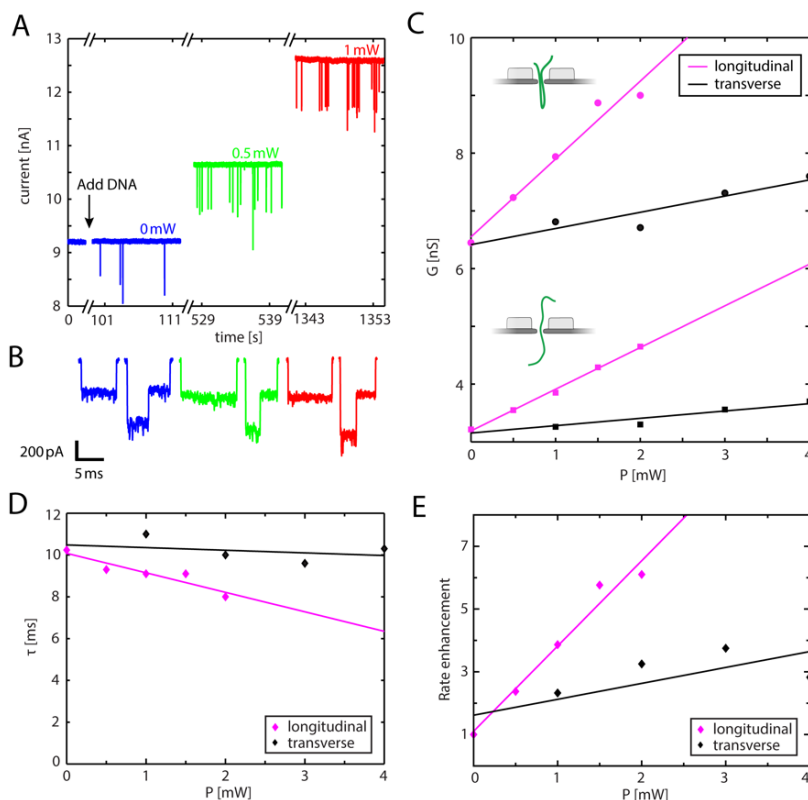


**Figure 3.5: DNA translocations through plasmonic nanopore** (A) Time trace of the ionic current through a dielectric-breakdown-fabricated plasmonic nanopore, during DNA translocations under 100 mV bias voltage at 0 mW (blue), 0.5 mW (green) and 1 mW (red) plasmonic excitation in longitudinal polarization. (B) Sample events for a linear translocation and a folded translocation at 0 mW (blue), 0.5 mW (green) and 1 mW (red) low-pass filtered at 10 kHz. (C) Conductance blockade levels  $\Delta G$ , for the single blockade-level (squares, one double strand of DNA inside the nanopore) and the double blockade level (circles, two double strands of DNA inside the nanopore) as a function of illumination power for longitudinal (magenta) and transverse (black) polarization. The full lines are linear fits. (D) DNA translocation times  $\tau$  as a function of illumination power for longitudinal (magenta) and transverse (black) polarization. Lines are linear fits. (E) Event rate enhancement versus laser power for both longitudinal (magenta) and transverse excitation (black). Lines are linear fits. Standard errors of the mean were in all cases smaller than the marker symbols and hence error bars are omitted in the plots.

To demonstrate that plasmonic nanopores drilled by controlled dielectric breakdown can be used as high-quality single molecule biosensors, we performed DNA translocation experiments on such nanopores with and without laser excitation of the plasmonic nanostructures. Under application of a bias voltage across the membrane, DNA molecules are electrophoretically attracted to the nanopore and then driven through it, thus leading to a transient reduction of the ionic current, as the passing molecule obstructs part of the ion flow through the nanopore.

Figure 3.5A shows 3 typical time traces of the current at 100 mV during a DNA translocation experiment through a 11.0 M $\Omega$  nanopore, equivalent to an effective diameter of 10.6 nm in 2M LiCl at 0 mW, 0.5 mW, and 1 mW of excitation power in longitudinal mode (see SI Section 3.5.7). After the addition of 5 ng/ $\mu$ L  $\lambda$ -DNA (48.5 kbp), transient current blockades can clearly be observed for all 3 illumination conditions. Figure 3.5B shows zooms of 6 DNA translocation events in a linear (left) and folded fashion (right). The clear distinct conductance levels reflect that the fabricated plasmonic nanopore exhibits excellent signal-to-noise characteristics, at least on-par with nanopores drilled using TEM (see SI Section 3.5.6) [20, 33, 43]. Figure 3.5C displays the conductance blockade levels  $\Delta G$  change with laser power in longitudinal and transverse excitation. The blockade levels rise linearly with increasing laser power, in quantitative agreement with data for the TEM-drilled plasmonic nanopores [20], which can be explained by plasmonic heating. Figure 3.5D shows the translocation times of the DNA molecules. While, based on a locally heated nanopore, no significant dependence on the laser power is expected [20], the translocation times decrease slightly with laser power for longitudinal polarization, but not for transverse polarization. Finally, Fig. 3.5E shows a strong enhancement of the rate at which the DNA molecules are captured into the nanopore with increasing of the laser power, where the longitudinal mode shows a stronger enhancement than the transverse mode of excitation. This rate enhancement in LiCl is in good agreement with the results obtained in TEM drilled plasmonic nanopores and can be explained by plasmon-induced thermophoretic capture of DNA [20].

### 3.3. CONCLUSION

In summary, we have developed a novel method for self-aligned formation of nanopores in plasmonic hotspots by means of controlled dielectric breakdown. The breakdown event is initiated at the optical field hotspot of the plasmonic nanostructure by applying a large DC electric field applied across a thin membrane while simultaneously optically illuminating the plasmonic nanostructure on the membrane. This ensures that the nanopore is automatically positioned at the location of highest field intensity. Interestingly, this makes the method particularly suitable also for plasmonic systems where the position of the most intense hot spot is not previously known or difficult to predict [44]. We have demonstrated DNA translocations through these nanopores and have shown that they perform on-par with TEM-drilled plasmonic nanopores in both their noise and DNA-translocation characteristics. The method presented is cost-efficient and high-throughput. Since the approach results in a nanopore that is automatically aligned with the optical hotspot of the plasmonic nanostructure, the method is perfectly suited for high-yield fabrication of plasmonic nanopores, promising for applications such as fluorescence detection, Raman characterization,

DNA sequencing, and trapping of single biomolecules.

## 3.4. EXPERIMENTAL METHODS

### 3.4.1. SAMPLE FABRICATION

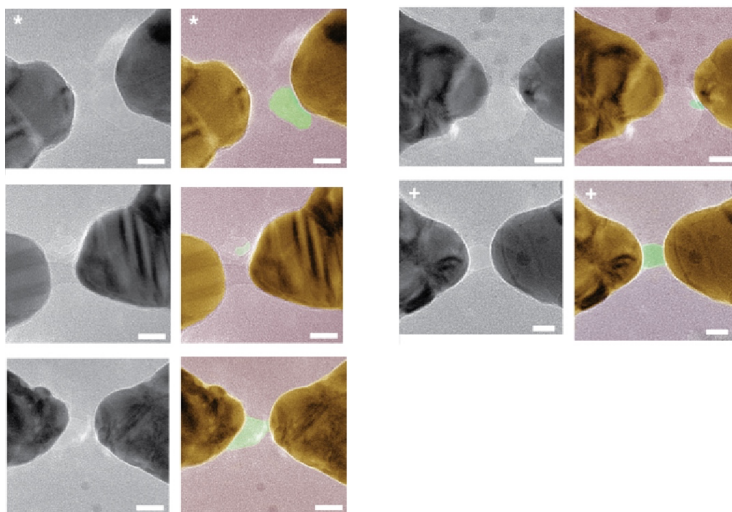
Chips with  $30 \times 30 \mu\text{m}$  20 nm thick free-standing silicon-nitride membranes were fabricated as described in [45], where transmembrane patterning was omitted to expose the full silicon-nitride surface. Plasmonic nanostructures and alignment marker structures were fabricated on top of the free-standing membranes using e-beam lithography patterning of a single-layer PMMA 950K resist. After development, an adhesion layer of 1 nm Ti was evaporated on the sample followed by evaporation of 30 nm of gold. Then the PMMA layer was subsequently removed using lift-off. Alignment of laser focus with plasmonic structure before breakdown: The position of the laser focus was aligned to the plasmonic nanostructure using the large metal markers and a piezoelectric positioning stage (PI GmbH), while being imaged using a 60x 1.2 NA water-immersion objective (Olympus). The same objective was used to focus the 785 nm wavelength laser to a diffraction-limited laser spot size of about  $0.5 \mu\text{m}$ , which was enough for sufficiently accurate alignment of the laser focus and the plasmonic nanostructure using the markers. The plasmonic nanostructures were not exposed to laser illumination during the alignment procedure. Electronic Instrumentation: For plasmonic dielectric breakdown, we used a custom-build current amplifier, capable of applying  $\pm 20$  V and recording sub-nA currents, as described in more detail in [33]. I-V and ionic current measurements during nanopore localization and DNA translocations are recorded using a commercial amplifier, Axopatch 200B (Molecular Devices, LLC) with a four-pole Bessel filter set at 100 kHz.

### 3.4.2. FDTD SIMULATIONS

We used FDTD Solutions (Lumerical Solutions, Inc., Canada) to model the optical properties of the plasmonic bowtie nanoantenna. The bowtie antenna was modeled as two 30 nm thick gold equilateral triangles of 90 nm in size (tip-to-base) that face each other tip- to-tip with a 10 nm separation. The corners of the triangles were rounded (15 nm-in-radius rounding) to better resemble the fabricated structures. The antenna was positioned on a 20 nm thin silicon-nitride membrane with a refractive index (RI) of 2 and 1 nm native oxide layer of RI = 1.4. The surrounding medium was modeled as water with a RI of 1.33. Symmetry was used to reduce the computational time. The plasmonic antenna was excited by a pulse from a total-field scattered-field source incident normal to the membrane, and with the polarization in either the longitudinal or the transverse mode. The optical absorption cross section was calculated by the net power flux through a box surrounding the antenna.

### 3.5. SUPPORTING INFORMATION

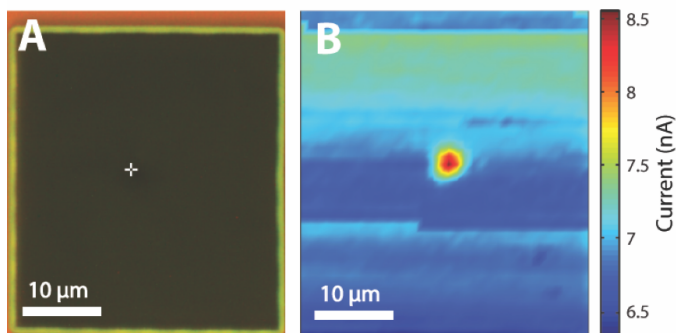
#### 3.5.1. TEM IMAGES OF PLASMONIC NANOPORES FABRICATED USING PLASMONIC DIELECTRIC BREAKDOWN IN LONGITUDINAL POLARIZATION



**Figure S3.6:** Examples of original and false colored TEM images of plasmonic nanopores drilled using plasmonic promoted dielectric breakdown in longitudinal mode. Scale bars are 10 nm. The TEM image of the nanopore used for the DNA translocations is indicated with a star: the image used in Fig. 3.5 in the main text is indicated with a plus sign.

#### 3.5.2. NANOPORE FABRICATED USING LASER-PROMOTED (NON-PLASMONIC) DIELECTRIC BREAKDOWN

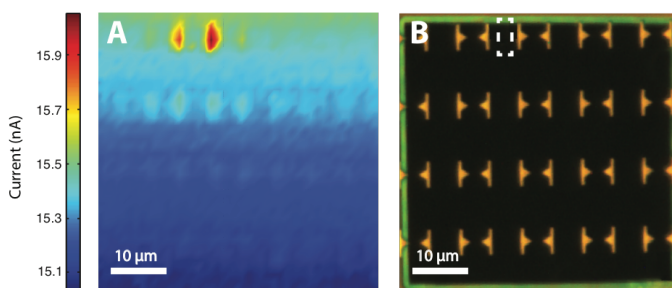
To show that the plasmonic dielectric breakdown is promoted by the optical field rather than heating from the plasmonic nanostructure, we fabricated a nanopore using dielectric breakdown promoted using the laser only (i.e. without the presence of any plasmonic structure). Figure S3.7A shows the optical image of a membrane before dielectric breakdown, where the white cross is indicating the laser location. Directly after the formation of a nanopore, drilled at  $V_m = 6$  V in 2 M LiCl and 45 mW, we scanned the membrane at 45 mW to visualize the location of the nanopore [46] (Fig. S3.7B). A clear current increase was observed at the location the laser was initially placed, indicating the laser illumination localized the dielectric breakdown to the desired position.



**Figure S3.7: Laser-promoted dielectric-breakdown-fabricated nanopore.** (A) Position of laser focus before dielectric breakdown. (B) Ionic current map of the membrane, scanned at 100 mV bias and 45 mW of laser power in 1  $\mu\text{m}$  size steps.

### 3.5.3. NANOPORE FABRICATED USING REGULAR DIELECTRIC BREAKDOWN (NO LASER) IN PLASMONIC MEMBRANE

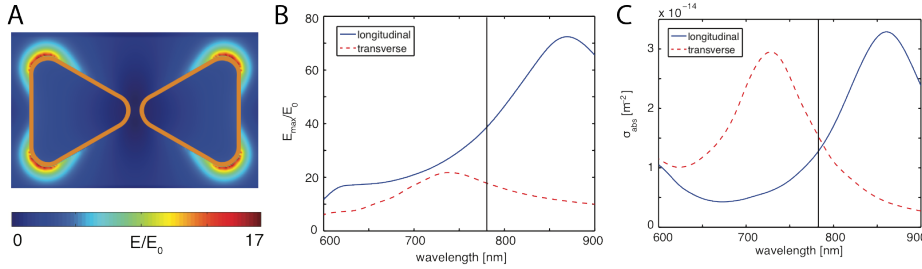
To show that the plasmonic dielectric breakdown localizes nanopore formation due to plasmon excitation, we fabricated a nanopore in a plasmonic membrane using regular dielectric breakdown, i.e. without any laser illumination. Figure S3.8A shows the result of a membrane scan after nanopore formation, drilled at  $v_m=7$  V in 2M LiCl. Two regions of small current enhancement are clearly distinguishable. In each of these regions a gold alignment-marker structure is located, which heats up its immediate surroundings when illuminated with the laser. This heating will cause a measurable current increase through the nanopore, if the pore has formed in the proximity of the marker structure. Since laser illumination of two markers leads to a current increase, we infer that the nanopore is located in between both alignment-markers. Figure S3.8B shows an optical image of the membrane, where the region of expected pore location (in between 2 marker structures) is indicated. Note that direct illumination of the nanopore at low laser power will cause



**Figure S3.8: Regular dielectric breakdown in plasmonic membrane.** (A) Ionic current map of the membrane, scanned in 1  $\mu\text{m}$  size steps at 50 mV bias and 1 mW of laser power in longitudinal mode. (B) Optical image of the membrane, where the region of expected pore location is indicated.

an insufficient current increase to be observed, as no plasmonic structures are present on top of it.

### 3.5.4. FDTD SIMULATIONS OF FIELD ENHANCEMENTS AND ABSORPTION CROSS-SECTIONS OF THE BOWTIE



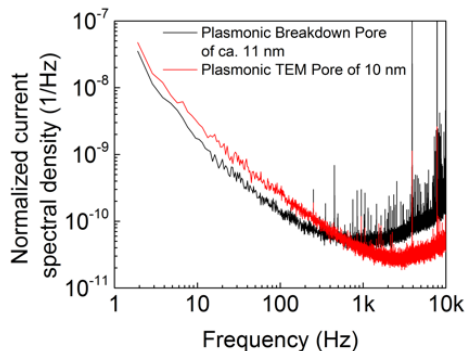
**Figure S3.9:** FDTD simulation of bowtie nanoantennas (A) FDTD simulation of the electric field  $E_{max}/E_0$  at 785 nm wavelength for the bowtie antenna as described in the main text, illuminated in transverse polarization. The bowtie is indicated by the orange frame. (B) FDTD simulation of the maximum electric field enhancement  $E_{max}/E_0$  as a function of wavelength for bowtie nanoantennas as described in the main text. The blue solid line and the red dashed line show the results for longitudinal and transverse excitation. The excitation wavelength (785 nm) as used in our setup is indicated with a vertical black line. (C) Absorption cross-section  $\sigma_{abs}$  as a function of wavelength for bowtie nanoantennas as described in the experimental section of the main text.

Figure S3.9 a show the simulated spectral response of the bowtie nanoantenna, respectively for the maximum field enhancement  $E_{max}/E_0$  and the absorption cross-section  $\sigma_{abs}$  in both excitation modes. It is clear from both figures that the laser wavelength used in our experiments (785 nm, indicated with the solid black line) is not on the resonance of the nanostructures (which, however, is unimportant for all the effects reported in this chapter).

### 3.5.5. ESTIMATION OF THE OPTICAL FIELD

We here present a calculation for the maximum optical electric field strength present in the plasmonic hotspot, based on results from our FDTD simulations (see SI Section 3.5.4). For a focused laser beam of power  $P$  and diameter  $D$ , we approximate the intensity in the laser beam as  $I_0 = \frac{4P}{\pi D^2}$ . The intensity subsequently can be converted to an electric field strength  $E_0$  by assuming  $I_0 = \frac{1}{2} c n_e \epsilon_0 |E_0^2|$ , where  $n_e$  is the refractive index of the medium,  $c$  is the speed of light in vacuum, and  $\epsilon_0$  is the electric permittivity of the vacuum. Using 1.33 as the refractive of the surrounding medium, we estimate the incident optical electric field strength at 5 mW to be 0.038 MV/cm. This leads to a maximum optical field strength in the gap of the bowtie antenna to be 1.5 MV/cm, using 40 as the electric field enhancement for longitudinal polarization. This is far below the threshold for pure optical breakdown [47], when no DC transmembrane bias would be applied.

### 3.5.6. NOISE-SPECTRA OF PLASMONIC-BREAKDOWN-FABRICATED NANOPORE



**Figure S3.10:** Normalized noise spectra of a plasmonic nanopore made using plasmonic dielectric breakdown (black) and using TEM drilling (red). The figure shows that the low frequency noise of both nanopores is comparable.

### 3.5.7. CONDUCTANCE VERSUS DIAMETER OF PLASMONIC-BREAKDOWN-FABRICATED NANOPORES

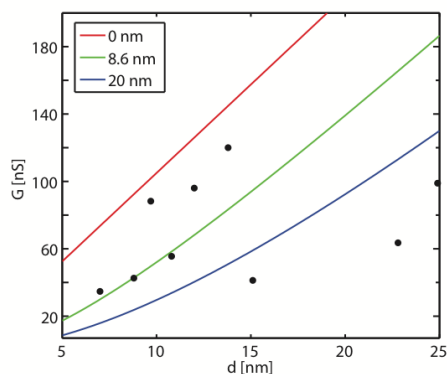


**Figure S3.11:** Conductance  $G$  of plasmonic breakdown nanopores versus diameter  $d$  as determined from TEM images (black circles). The equation of Kowalczyk *et al.* has been plotted for different values of the effective length  $l_{eff} = 0$  nm (red, lower limit), 8.6 nm (green, estimated value for TEM-drilled pores) and 20 nm (blue, full membrane thickness, upper limit).

Figure S3.11 shows the measured nanopore conductance plotted versus the nanopore diameter, as determined from the TEM pore images. In the same plot, the hourglass model for nanopore conductance from Kowalczyk *et al.* is shown, using values for the effective pore length of 20 nm (perfect cylindrical pore), 8.6 nm (TEM hourglass-shaped pore) and 0 nm (extremely thin pore). The effective nanopore length

corrects for the pore having an hourglass shape, i.e., not being a perfect cylinder that crosses the 20 nm thick membrane.

The measured values deviate quite strongly from the model's prediction for a given value of effective pore length, where no single effective pore length fits the data well. The discrepancies might arise because of several reasons. First of all, the model used assumes a cylindrically symmetric hourglass-shaped nanopore and a good fit of the model requires all pores to have a similar nanopore wall profile. However, the plasmonic breakdown method in general does not lead to cylindrically symmetric nanopores (as is already clear from the TEM images in Fig. S3.6), nor will the wall profile of each pore be necessarily similar from pore to pore. Hence, expecting a good fit using from the model might be too optimistic. Second, the nanopore conductance was measured right after pore formation. Afterwards, pores were stored in an 1:1 ethanol:water mixture until TEM imaging up to 1 week later. In the mean time, pores could have grown in size, which could lead to larger pore sizes on the TEM images. Thus, the TEM-determined size will not accurately reflect the size at the time of the conductance measurement. Third, the nanopore diameter was determined from TEM imaging by approximating the area of the nanopore as a circle. The area often clearly did not resemble a circle, and hence this method might have led to additional errors.

### **3.5.8. DIAMETER AND CONDUCTANCE DETERMINATION OF PLASMONIC NANOPORE USED IN DNA TRANSLOCATIONS**

The estimated value for the diameter of the nanopore used for DNA translocations was 14.2 nm and 10.6 nm, as determined from the TEM image in Fig. S3.6 (image indicated with a star) and the hourglass model for the nanopore conductance, respectively. To determine the diameter and effective length (4.3 nm) of the nanopore using the model, we used the measured pore conductance of 91 nS, the measured DNA conductance blockade of 3.2 nS conductance blockade (both measured at the start of the translocation experiment), and the 12.6 S/m conductivity of the 2M LiCl (measured using Zetasizer Nano ZS (Malvern)). During the experiment, pore growth was observed for illumination powers above 2 mW, which resulted in an increased pore conductance of 120 nS and a DNA conductance blockade of 2.9 nS at the end of the translocation experiment. The latter values predict a pore diameter of 12.8 nm (and effective pore length of 2.9 nm), which is much closer to the 14.2 nm as measured from the TEM image.

### 3.5.9. RELATIVE CURRENT INCREASE VERSUS LASER POWER

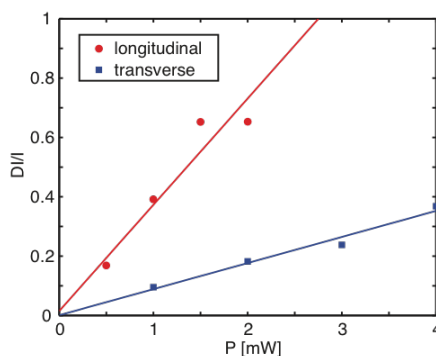


**Figure S3.12:** Relative current increase  $\frac{DI}{I} = \frac{I_{laser} - I_{nolaser}}{I_{nolaser}}$  in longitudinal (blue) and transverse excitation (red) for nanopore used in DNA translocation experiment versus laser power  $P$  and linear fits.

The current through the nanopore can be used as an indication for the temperature near the nanopore. In the hourglass-shape geometrical model for the nanopore conductance, the only temperature dependent parameter is the buffer conductivity. Hence the relative conductance increase  $\frac{DI}{I} = \frac{I_{laser} - I_{nolaser}}{I_{nolaser}}$  is solely determined by buffer conductivity [27]. Here  $I_{laser}$  is the current through the nanopore at a give laser power and  $I_{nolaser}$  is the current in absence of laser illumination. Hence, using Figure S3.12, we can deduce that laser illumination of this bowtie antenna in longitudinal mode leads to a temperature increase in 26 C/mW and 7.1 C/mW for the transverse mode.

## REFERENCES

- [1] C. Dekker, *Solid-state nanopores*, Nature nanotechnology **2**, 209 (2007).
- [2] M. Wanunu, *Nanopores: A journey towards dna sequencing*, Physics of life reviews **9**, 125 (2012).
- [3] M. Muthukumar, C. Plesa, and C. Dekker, *Single-molecule sensing with nanopores*, Physics Today **68**, 40 (2015).
- [4] E. L. Bonome, R. Lepore, D. Raimondo, F. Cecconi, A. Tramontano, and M. Chinappi, *Multistep current signal in protein translocation through graphene nanopores*, The Journal of Physical Chemistry B **119**, 5815 (2015).
- [5] B. Cressiot, A. Oukhaled, L. Bacri, and J. Pelta, *Focus on protein unfolding through nanopores*, BioNanoScience **4**, 111 (2014).
- [6] D. Japrun, A. Bahrami, A. Nadzeyka, L. Peto, S. Bauerdick, J. B. Edell, and T. Albrecht, *Ssb binding to single-stranded dna probed using solid-state nanopore sensors*, The Journal of Physical Chemistry B **118**, 11605 (2014).
- [7] M. M. Marshall, J. Ruzicka, O. K. Zahid, V. C. Henrich, E. W. Taylor, and A. R.

- Hall, *Nanopore analysis of single-stranded binding protein interactions with dna*, *Langmuir* **31**, 4582 (2015).
- [8] C. Plesa, J. W. Ruitenber, M. J. Witteveen, and C. Dekker, *Detection of individual proteins bound along dna using solid-state nanopores*, *Nano letters* **15**, 3153 (2015).
- [9] R. Wei, V. Gatterdam, R. Wieneke, R. Tampé, and U. Rant, *Stochastic sensing of proteins with receptor-modified solid-state nanopores*, *Nature nanotechnology* **7**, 257 (2012).
- [10] G. Ando, C. Hyun, J. Li, and T. Mitsui, *Directly observing the motion of dna molecules near solid-state nanopores*, *ACS nano* **6**, 10090 (2012).
- [11] A. T. Carlsen, O. K. Zahid, J. Ruzicka, E. W. Taylor, and A. R. Hall, *Interpreting the conductance blockades of dna translocations through solid-state nanopores*, *ACS Nano* **8**, 4754 (2014).
- [12] M. Muthukumar, *Mechanism of dna transport through pores*, *Annu. Rev. Biophys. Biomol. Struct.* **36**, 435 (2007).
- [13] H. Chang, F. Kosari, G. Andreadakis, M. Alam, G. Vasmatzis, and R. Bashir, *Dna-mediated fluctuations in ionic current through silicon oxide nanopore channels*, *Nano letters* **4**, 1551 (2004).
- [14] D. Fologea, J. Uplinger, B. Thomas, D. S. McNabb, and J. Li, *Slowing dna translocation in a solid-state nanopore*, *Nano letters* **5**, 1734 (2005).
- [15] R. M. Smeets, U. F. Keyser, D. Krapf, M.-Y. Wu, N. H. Dekker, and C. Dekker, *Salt dependence of ion transport and dna translocation through solid-state nanopores*, *Nano letters* **6**, 89 (2006).
- [16] U. F. Keyser, *Controlling molecular transport through nanopores*, *Journal of The Royal Society Interface* , rsif20110222 (2011).
- [17] C. Plesa, N. van Loo, P. Ketterer, H. Dietz, and C. Dekker, *Velocity of dna during translocation through a solid-state nanopore*, *Nano letters* **15**, 732 (2014).
- [18] J. Clarke, H.-C. Wu, L. Jayasinghe, A. Patel, S. Reid, and H. Bayley, *Continuous base identification for single-molecule nanopore dna sequencing*, *Nature nanotechnology* **4**, 265 (2009).
- [19] E. A. Manrao, I. M. Derrington, A. H. Laszlo, K. W. Langford, M. K. Hopper, N. Gillgren, M. Pavlenok, M. Niederweis, and J. H. Gundlach, *Reading dna at single-nucleotide resolution with a mutant mspa nanopore and phi29 dna polymerase*, *Nature biotechnology* **30**, 349 (2012).
- [20] F. Nicoli, D. Verschueren, M. Klein, C. Dekker, and M. P. Jonsson, *Dna translocations through solid-state plasmonic nanopores*, *Nano letters* **14**, 6917 (2014).
- [21] M. Belkin, S.-H. Chao, M. P. Jonsson, C. Dekker, and A. Aksimentiev, *Plasmonic nanopores for trapping, controlling displacement, and sequencing of dna*, *ACS nano* **9**, 10598 (2015).

- [22] M. P. Cecchini, A. Wiener, V. A. Turek, H. Chon, S. Lee, A. P. Ivanov, D. W. McComb, J. Choo, T. Albrecht, S. A. Maier, *et al.*, *Rapid ultrasensitive single particle surface-enhanced raman spectroscopy using metallic nanopores*, *Nano letters* **13**, 4602 (2013).
- [23] C. Chen, M. L. Juan, Y. Li, G. Maes, G. Borghs, P. Van Dorpe, and R. Quidant, *Enhanced optical trapping and arrangement of nano-objects in a plasmonic nanocavity*, *Nano letters* **12**, 125 (2011).
- [24] S. Nam, I. Choi, C.-c. Fu, K. Kim, S. Hong, Y. Choi, A. Zettl, and L. P. Lee, *Graphene nanopore with a self-integrated optical antenna*, *Nano letters* **14**, 5584 (2014).
- [25] Y. Li, F. Nicoli, C. Chen, L. Lagae, G. Groeseneken, T. Stakenborg, H. W. Zandbergen, C. Dekker, P. Van Dorpe, and M. P. Jonsson, *Photoresistance switching of plasmonic nanopores*, *Nano letters* **15**, 776 (2014).
- [26] C. R. Crick, P. Albella, B. Ng, A. P. Ivanov, T. Roschuk, M. P. Cecchini, F. Bresme, S. A. Maier, and J. B. Edel, *Precise attoliter temperature control of nanopore sensors using a nanoplasmonic bullseye*, *Nano letters* **15**, 553 (2014).
- [27] M. P. Jonsson and C. Dekker, *Plasmonic nanopore for electrical profiling of optical intensity landscapes*, *Nano letters* **13**, 1029 (2013).
- [28] M. Van den Hout, A. R. Hall, M. Y. Wu, H. W. Zandbergen, C. Dekker, and N. H. Dekker, *Controlling nanopore size, shape and stability*, *Nanotechnology* **21**, 115304 (2010).
- [29] A. Storm, J. Chen, X. Ling, H. Zandbergen, and C. Dekker, *Fabrication of solid-state nanopores with single-nanometre precision*, *Nature materials* **2**, 537 (2003).
- [30] A. G. Ahmadi, Z. Peng, P. J. Hesketh, and S. Nair, *Wafer-scale process for fabricating arrays of nanopore devices*, *Journal of Micro/Nanolithography, MEMS, and MOEMS* **9**, 033011 (2010).
- [31] Y. H. Lanyon, G. De Marzi, Y. E. Watson, A. J. Quinn, J. P. Gleeson, G. Redmond, and D. W. Arrigan, *Fabrication of nanopore array electrodes by focused ion beam milling*, *Analytical chemistry* **79**, 3048 (2007).
- [32] K. Briggs, H. Kwok, and V. Tabard-Cossa, *Automated fabrication of 2-nm solid-state nanopores for nucleic acid analysis*, *Small* **10**, 2077 (2014).
- [33] H. Kwok, K. Briggs, and V. Tabard-Cossa, *Nanopore fabrication by controlled dielectric breakdown*, *PloS one* **9**, e92880 (2014).
- [34] S. Sze, *Current transport and maximum dielectric strength of silicon nitride films*, *Journal of Applied Physics* **38**, 2951 (1967).
- [35] E. Beamish, H. Kwok, V. Tabard-Cossa, and M. Godin, *Precise control of the size and noise of solid-state nanopores using high electric fields*, *Nanotechnology* **23**, 405301 (2012).
- [36] S. Van Dorp, U. F. Keyser, N. H. Dekker, C. Dekker, and S. G. Lemay, *Origin of the*

- electrophoretic force on dna in solid-state nanopores*, Nature Physics **5**, 347 (2009).
- [37] K. Briggs, M. Charron, H. Kwok, T. Le, S. Chahal, J. Bustamante, M. Waugh, and V. Tabard-Cossa, *Kinetics of nanopore fabrication during controlled breakdown of dielectric membranes in solution*, Nanotechnology **26**, 084004 (2015).
- [38] S. W. Kowalczyk, A. Y. Grosberg, Y. Rabin, and C. Dekker, *Modeling the conductance and dna blockade of solid-state nanopores*, Nanotechnology **22**, 315101 (2011).
- [39] M. Kimura, *Field and temperature acceleration model for time-dependent dielectric breakdown*, IEEE Transactions on Electron Devices **46**, 220 (1999).
- [40] G. Baffou and R. Quidant, *Thermo-plasmonics: using metallic nanostructures as nano-sources of heat*, Laser & Photonics Reviews **7**, 171 (2013).
- [41] S. Habermehl, R. Apodaca, and R. Kaplar, *On dielectric breakdown in silicon-rich silicon nitride thin films*, Applied Physics Letters **94**, 012905 (2009).
- [42] S. Lombardo, J. H. Stathis, B. P. Linder, K. L. Pey, F. Palumbo, and C. H. Tung, *Dielectric breakdown mechanisms in gate oxides*, Journal of Applied Physics **98**, 12 (2005).
- [43] S. W. Kowalczyk, D. B. Wells, A. Aksimentiev, and C. Dekker, *Slowing down dna translocation through a nanopore in lithium chloride*, Nano letters **12**, 1038 (2012).
- [44] J. Langer, S. M. Novikov, and L. M. Liz-Marzán, *Sensing using plasmonic nanostructures and nanoparticles*, Nanotechnology **26**, 322001 (2015).
- [45] X. J. Janssen, M. P. Jonsson, C. Plesa, G. V. Soni, C. Dekker, and N. H. Dekker, *Rapid manufacturing of low-noise membranes for nanopore sensors by trans-chip illumination lithography*, Nanotechnology **23**, 475302 (2012).
- [46] U. F. Keyser, D. Krapf, B. N. Koeleman, R. M. Smeets, N. H. Dekker, and C. Dekker, *Nanopore tomography of a laser focus*, Nano letters **5**, 2253 (2005).
- [47] M. Lenzner, J. Krüger, S. Sartania, Z. Cheng, C. Spielmann, G. Mourou, W. Kautek, and F. Krausz, *Femtosecond optical breakdown in dielectrics*, Physical review letters **80**, 4076 (1998)



# 4

## DNA TRANSLOCATIONS THROUGH SOLID-STATE PLASMONIC NANOPORES

*Nanopores enable label-free detection and analysis of single biomolecules. Here, we investigate DNA translocations through a novel type of plasmonic nanopore based on a gold bowtie nanoantenna with a solid-state nanopore at the plasmonic hot spot. Plasmonic excitation of the nanopore is found to influence both the sensor signal (nanopore ionic conductance blockade during DNA translocation) and the process that captures DNA into the nanopore, without affecting the duration time of the translocations. Most striking is a strong plasmon-induced enhancement of the rate of DNA translocation events in lithium chloride (LiCl), already tenfold enhancement at a few mW of laser power). This provides a means to utilize the excellent spatiotemporal resolution of DNA interrogations with nanopores in LiCl buffers, which is known to suffer from low event rates. We propose a mechanism based on plasmon-induced local heating and thermophoresis as explanation of our observations.*

---

This chapter has been published as: Francesca Nicoli, Daniel V. Verschuere, Misha Klein, Cees Dekker, and Magnus P. Jonsson. DNA translocations through solid-state plasmonic nanopores. *Nano Letters*, 14(12):6917-6925, 2014

## 4.1. INTRODUCTION

Solid-state nanopores have emerged as a versatile concept for label-free detection and investigation of biomolecules at the single-molecule level [1]. In brief, molecules that translocate through a small pore in a thin membrane can be electrically detected one by one, because they temporarily modulate the ionic conductance of the pore. The concept has proven useful for many applications, including molecular size discrimination [2], investigation of biomolecular interactions at the single-molecule level [3], and investigation of local structures along elongated molecules, such as protein bound to DNA [4]. Several variations and extensions of the nanopore concept have recently been explored, to a large extent motivated by a common goal to achieve nanopore-based DNA sequencing. Examples include nanopores systems with integrated tunneling detectors [5], and nanopore sensors combined with optics [6–9]. Besides direct optical detection [6, 7, 9] illuminating a nanopore with light was recently shown to be useful for modulation of the nanopore's surface charge density, thereby enabling optical control of the electroosmotic flow through the pore [10]. The integration of metal nanostructures close to a nanopore generates additional possibilities, including light-induced local heating, as recently explored for both biological [11] and solid-state [8] nanopores. Such optical heating is a result of the strong interaction of light and metal nanoparticles through excitation of plasmons (collective charge oscillations in the particles) [12].

In addition to heating, plasmonic systems enable control and manipulation of optical fields at the nanoscale. Optical nanoantennas that are made of two closely spaced and optically coupled plasmonic nanoparticles are particularly interesting in this respect. They can be used to focus optical fields to the sub-diffraction-limited gap region between the individual structures, typically referred to as the hot spot, where the optical field can be very intense [13]. A common example is the bowtie antenna, consisting of two metal nanotriangles that face each other, as depicted in Fig. 4.1A [13, 14]. Here we demonstrate label-free detection of single DNA molecules with a solid-state plasmonic nanopore. The sensor device is based on a nanopore that is placed right at the hot spot of a gold bowtie nanoantenna [8]. We explore the effects of plasmon excitation on the essential parameters in nanopore sensing experiments, primarily the sensor signal (changes in the pore conductance due to DNA translocation); the translocation time (the time a DNA molecule occupies the pore during translocation); and the event rate (the number of translocated DNA molecules per unit time). In order to gain a better understanding of plasmonic effects on DNA nanopore translocations and, in particular, the role of plasmonic heating, we also provide complementary control measurements where the temperature of conventional (nonplasmonic) nanopores was regulated by heating the whole flow cell with a Peltier element (referred to as temperature-control measurements).

## 4.2. RESULTS AND DISCUSSION

### 4.2.1. SOLID-STATE PLASMONIC NANOPORE SENSOR

Figure 4.1A depicts the geometry of the solid-state plasmonic nanopore. The bowtie antenna consists of two 30 nm thick equilateral gold triangles (that measure 60 nm from one tip to the opposite flat side), separated by a 10 nm gap. A 1 nm thick titanium layer

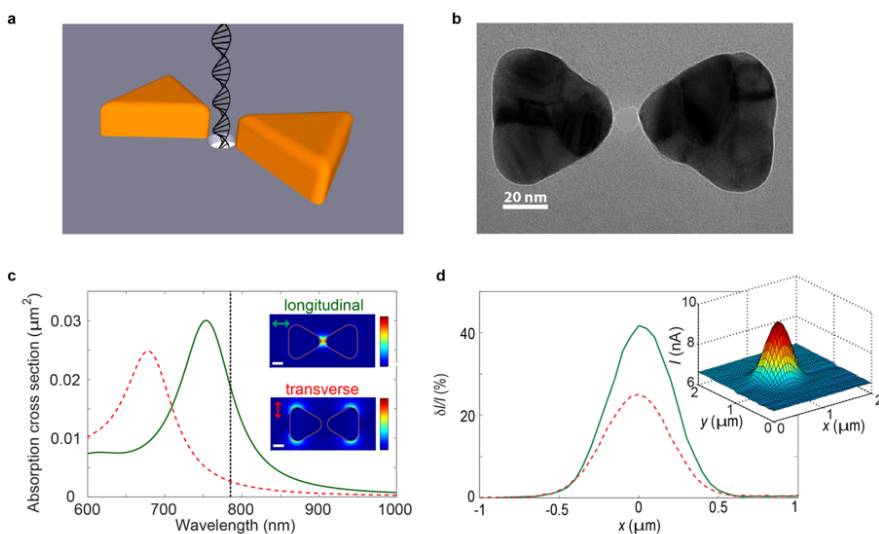


**Figure 4.1: Plasmonic nanopore concept and basic characteristics.** (A) Schematic illustration of a DNA molecule translocating through a plasmonic nanopore that consists of a gold bowtie antenna with a 10 nm nanopore at the gap center (not to scale) (B) TEM top-view image of a plasmonic nanopore device. (C) Simulated absorption cross sections of the plasmonic nanopore in longitudinal (green full line) and transverse (red dashed line) excitation. The black dotted line indicates the laser wavelength of 785 nm that was used in our experiments. The insets show color plots of the simulated electrical field intensity enhancement at 785 nm in the plane of the antenna and through the middle of the gold triangles (color map from 0 to 1200 and 0 to 65 for longitudinal and transverse mode, respectively). Scale bars are 20 nm. (D) Change in current,  $\delta I$ , relative to the base line current,  $I$ , for line scans of the pore through the laser focus for longitudinal (green full line) and transverse (red dashed line) mode at 0.5 mW. The inset shows a 2D scan of the variation in current along the focal plane (longitudinal mode, 100 mV bias voltage).

under the gold ensured good adhesion to the underlying 20 nm thick silicon nitride (SiN) membrane. Right at the gap of the plasmonic antenna, we drill a 10 nm-in-diameter nanopore through the membrane using a transmission electron microscope (TEM). Figure 4.1B shows a TEM image of a plasmonic nanopore. As mentioned above, the gold bowtie antenna can focus incident light to the small gap region right at the pore mouth. This is illustrated in the upper inset of Fig. 4.1C, which shows a finite-difference time-domain (FDTD) simulation of the enhancement in the electric field intensity (compared with the incident field) when the sensor is excited with 785 nm light polarized along the direction of the antenna (longitudinal excitation, illustrated in the figure). As expected, the optical field is enhanced by many orders of magnitude in a  $\sim 10$  nm hot spot in the gap between the two gold triangles. The lower inset instead shows the simulated enhancement in the electric field intensity upon excitation with light polarized in the transverse direction. While the hot spot at the pore mouth is not excited in transverse mode, there is still a considerable amount of light absorption (red dashed line in Fig. 4.1C) and corresponding local heating. As a result, we expect effects related to local heating to appear in both longitudinal mode and in transverse mode, although to a lesser extent for transverse excitation. In contrast, effects that require intense optical

fields close to the pore are expected to appear for longitudinal excitation only.

Plasmonic excitation modulates the ionic conductance of the pore [8], which enables us to accurately align the plasmonic nanopore with the focal spot of a 785 nm laser in our custom-made microscope setup (see Experimental Section 4.4 for details). Briefly, the ionic current flowing through the pore is measured at a constant bias voltage (100 mV) while the pore is scanned through the laser focus. Figure 4.1D shows the relative change in current for a plasmonic pore that is scanned across the focal spot, for both longitudinal (full green line) and transverse (red dashed line) excitation, at 0.5 mW. The signal is strongest when the bowtie is excited in the longitudinal mode, as predicted from the FDTD simulations. The observed difference between longitudinal and transverse mode is smaller than predicted, which is likely due to small deviations in the actual nanopore-bowtie geometry from the simulated structure. Scanning in all three dimensions provides the coordinates of the laser focus as the position of highest plasmon-induced change in the nanopore conductance, at which the pore is positioned for further experiments. When the nanopore is fixed at a given position, the nanopore current varies linearly with voltage, both with and without laser excitation, as shown in Fig. S4.7.

#### 4.2.2. DNA SENSING WITH PLASMONIC NANOPORES

We demonstrate the potential of the plasmonic nanopore for single-molecule sensing using doubled-stranded DNA (dsDNA, 48.5 kilobase pairs). The DNA molecules were added at a concentration of 10 ng/ $\mu$ L in a 1M KCl buffer on one side of the membrane (opposite from the plasmonic antenna, unless stated otherwise) and pulled through the pore electrophoretically by a 100 mV potential applied across the membrane. The blue curve in Fig. 4.2A shows the ionic nanopore current without plasmonic excitation, before and after adding DNA to the flow cell. Translocation of DNA molecules leads to the downward spikes in the current. The green and red curves in Fig. 4.2A show the sensor signal during plasmon excitation. The separation of the time traces demonstrates a significant increase in the open nanopore current (base line) upon laser excitation. The increase in the open nanopore current for a given laser power varied significantly between different plasmonic nanopores, which likely is due to differences in alignment and the exact nanopore-bowtie geometry. Importantly, the noise level upon plasmon excitation remains sufficiently low to allow for detection of single DNA molecules with high signal-to-noise ratio. Details of two DNA translocation events at 5 mW laser excitation are shown to the right in Fig. 4.2A. The upper panel is an example of a dsDNA molecule translocating in a linear fashion, while the bottom panel corresponds to a partially folded molecule [15].

We construct conductance blockade histograms to investigate in detail how plasmonic excitation affects the sensor signal. The histograms in Fig. 4.2B represent the two main conductance blockade levels from more than 700 DNA translocation events. The peaks at 0 nS correspond to the open pore conductance at each laser power. The middle peaks at about -2 nS correspond to one DNA strand blocking the pore, and the peaks near -4 nS to -5 nS arise from DNA molecules that are partially folded when moving through the pore (i.e., two strands blocking the pore). The results clearly show that the conductance blockade and hence, the sensor signal, increases with plasmonic

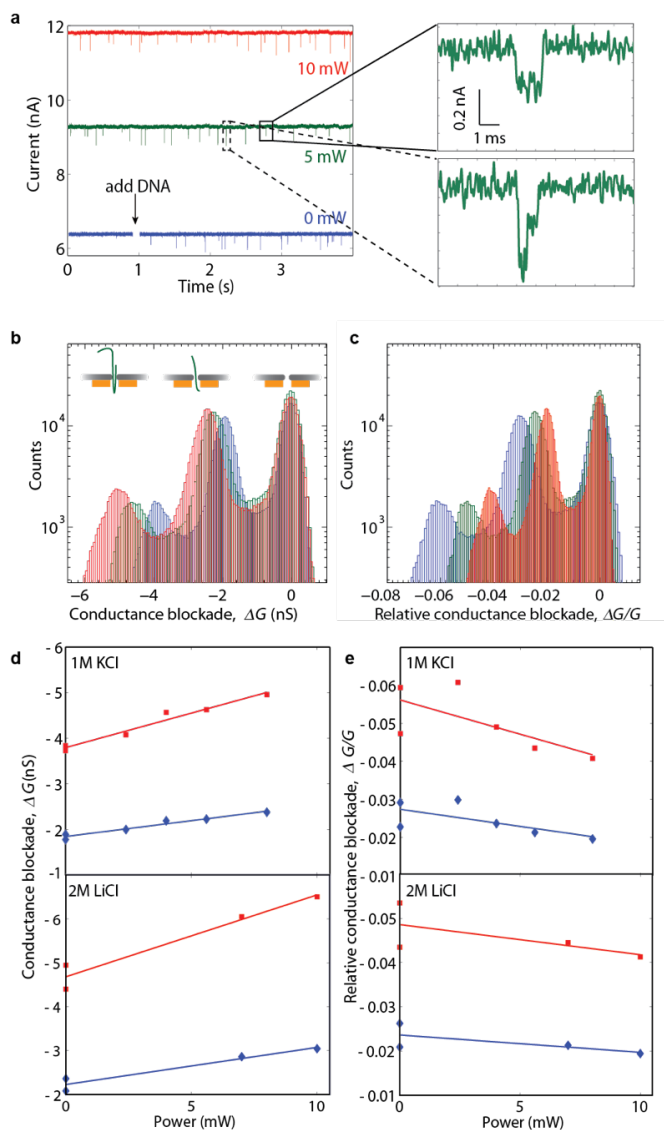


**Figure 4.2: DNA translocations through a plasmonic solid-state nanopore.** (A) Examples of current traces in 1M KCl without (blue) and with (green, red) plasmon excitation (longitudinal mode). The panels to the right show the details of one linear (top) and one partially folded (bottom) translocation event upon 5 mW laser excitation. (B) Conductance blockade histograms for DNA translocations in 1M KCl at 0 mW (blue), 5 mW (green) and 10 mW (red) laser excitation. (C) Same as in (B), but for relative conductance blockades (blockades normalized with the open pore conductance at each power). (D) Position of the conductance blockade peaks versus power for measurements in 1M KCl (top) and 2M LiCl (bottom). Diamonds and squares correspond to the first and the second translocation peak, respectively. (E) Same as in (D), but for the relative conductance blockade. The lower points (lower absolute values) at 0 mW corresponds to the last acquisition during the experiments.

excitation. Plasmonic excitation sometimes also resulted in an increase in the noise level (e.g. see Fig. 4.2A), which exemplifies that an increase in signal does not always lead to an increase in the signal-to-noise ratio of a sensor. We repeated the measurements using 2M LiCl as buffer medium, which has similar bulk conductivity as 1M KCl (see Fig. S4.6 in the Supporting Information, SI) while providing significantly lower translocation speeds [16]. The results are presented in Fig. 4.2D, showing conductance blockades versus laser power for DNA translocations in 1M KCl (top) and 2M LiCl (bottom). The trend of increasing conductance blockade with laser excitation is clear at both buffer conditions. These observations can be explained by plasmonic heating of the nanopore. Plasmons in the optical antenna are excited by the laser illumination and decay either through re-emission of photons or through non-radiative absorption [12]. The absorption results in local heating of the nanopore and a corresponding temperature increase of the buffer in and around the nanopore. In turn, an increase in temperature increases the buffer conductivity, thereby enhancing both the open pore conductance and the magnitude of the blockades [17]. A clear increase in the conductance blockades with temperature was indeed confirmed by our temperature-control measurements (see Fig. S4.14A).

Histograms of the relative conductance blockades,  $\Delta G/G$  (where  $G$  is the open pore conductance at the given laser power and  $\Delta G$  is the magnitude of the conductance blockade) are shown for different laser powers in Fig. 4.2C for the 1M KCl experiment. The corresponding peak positions are plotted versus laser power for both 1M KCl and 2M LiCl in Fig. 4.2E. The graphs show that the relative conductance blockades decrease slightly with increasing laser power.

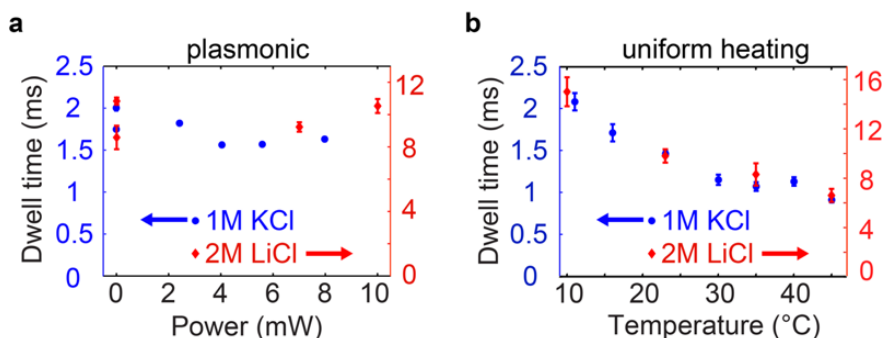


**Figure 4.3: Comparison of dwell times for local and global heating (A)** Dwell times for  $\lambda$ -DNA translocations through plasmonic nanopores upon plasmon excitation at different powers (longitudinal) in 1M KCl (blue circles, left axis) and in 2M LiCl (red diamonds, right axis). **(B)** Dwell times at different temperatures for  $\lambda$ -DNA translocations through 10 nm in diameter conventional nanopores in 1M KCl (blue circles, left axis) and in 2M LiCl (red diamonds, right axis). All error bars were calculated as the standard error of the mean (and are smaller than the symbols for 1M KCl in (A)).

Interestingly, we see a similar decrease in the relative conductance blockades also upon uniform heating of a nanopore (see Fig. S4.14B). However, we cannot exclude additional effects, other than heating, that could contribute to the observed decrease in relative conductance blockades. For example, light-induced changes in the surface charge density at the pore wall would primarily affect the open pore conductance and not the conductance blockade during DNA translocation [10]. We also note that part

of the decrease was often non-reversible (did not go back when the laser excitation was switched off), which is likely caused by small changes in the nanopore geometry during measurements.

The translocation time,  $\Delta t$ , is another essential parameter in nanopore sensing experiments. Interestingly, we find that the translocation time stays approximately constant upon plasmon excitation, both in 1M KCl and in 2M LiCl (Fig. 4.3A). This suggests that plasmon excitation in our device is capable of modulating both the open pore conductance and the conductance blockades, as shown above, without significantly affecting the force balance during DNA translocation, which sets the translocation time. This is a nontrivial result, because the force balance and hence, the translocation time, typically depends on the same parameters that affect the nanopore ionic current, including temperature and surface charge. Indeed, our temperature-control measurements show a considerable decrease in the translocation time with increasing temperature (more than 50% shorter translocation time at 45°C compared to at 10°C, see Fig. 4.3B). An increase in the negative surface charge density of the nanopore, which was reported for laser-illuminated conventional nanopores [10], would instead create an electroosmotic flow that opposes the DNA translocation, thereby leading to an increase in the translocation time. Hence, the fact that we do not observe a significant change in the translocation time upon plasmonic excitation may result from a coincidental balance between the competing effects from heating and a change in the surface charge of the nanopore.

However, an alternative, and in our opinion more likely, explanation of the insensitivity of the translocation time to plasmon excitation is based on the fact that plasmonic heating is highly local. The gold bowtie antenna acts as a local nanoscale heat source and causes a temperature increase that is strongest at the gold surface and drops to below half already at a 100 nm distance from the structure (see Fig. 4.5A) [12]. Although a local temperature increase and corresponding decrease in buffer viscosity acts to reduce the drag coefficient on the DNA inside the pore, this effect is counteracted by an enhancement of the electroosmotic flow through the pore that opposes the DNA movement (also due to the temperature-induced change in viscosity, a more detailed discussion is provided in SI Section 4.5.6) [18, 19]. As a result, local heating of the nanopore is not expected to significantly affect the translocation time. By contrast, the decrease in translocation time that we observe upon uniform heating is dominated by temperature-induced changes in the viscous drag on the untranslocated part of the DNA that is farther away from the pore (where local heating would be low) [20]. Hence, plasmon-induced local heating may indeed affect both the open pore conductance and conductance blockades without significantly affecting the translocation time, in agreement with our observations.

### 4.2.3. PLASMON-INDUCED ENHANCEMENT OF THE EVENT RATE

The most noticeable effect of plasmon excitation on the DNA translocation behavior through plasmonic nanopores is a dramatic increase in the event rate in LiCl buffers. Figure 4.4A shows typical consecutive current traces of DNA translocations in 2M LiCl without (blue) and with (red) laser excitation. The increase in noise that is observed upon plasmonic excitation in Fig. 4.4A was not always present and is not fully

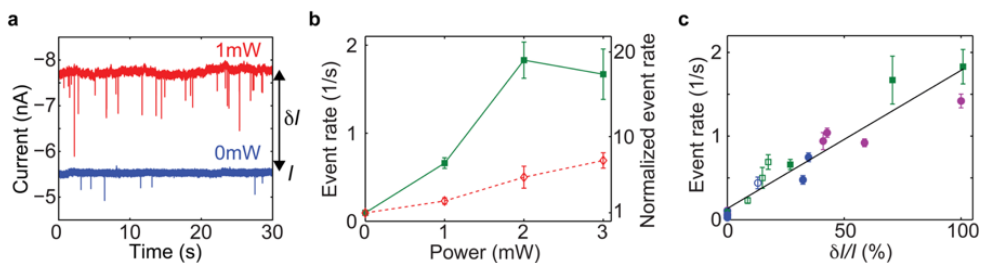


**Figure 4.4: Plasmon-induced event rate enhancement in 2M LiCl.** (A) Examples of current traces at 0 mW (blue) and 1 mW laser excitation in longitudinal mode. The DNA was added to the side of the antenna, therefore the negative currents. (B) Event rate (left y-axis) and event rate normalized with the initial value at 0 mW (right y-axis) versus laser power for the same plasmonic nanopore as in (A), excited in longitudinal mode (green filled squares) and in transverse mode (red open diamonds). The error bars correspond to the statistical error of the mean. (C) Event rate versus relative increase in the open pore current upon laser excitation,  $\delta I/I$ . Different colors correspond to different plasmonic nanopores. Filled and open symbols are for longitudinal and transverse polarization, respectively. Squares and circles correspond to DNA added from the side of the bowtie antenna and the other side, respectively. The black full line is a linear fit to all data. The green markers correspond to the data in (B).

understood at this stage.

The event rate at different laser powers for both longitudinal and transverse excitation is shown in Fig. 4.4B for the same sample. At longitudinal excitation, the enhancement in the event rate exceeds one order of magnitude already at about 2 mW. The effect is significant also in transverse mode (amounting to around 30% of the enhancement in longitudinal mode for the same laser power). This shows that the effect is not exclusively dependent on the optical hot spot at the plasmonic nanopore, because the hot spot is only excited in the longitudinal mode (see Fig. 4.1C). The two data points at 0 mW were acquired between measurements at the different polarizations, demonstrating that the effect is reversible and directly related to plasmon excitation. Interestingly, while also observed for 1M LiCl (Fig. S4.10), the rate enhancement effect was never observed for DNA in KCl buffer. Instead, for KCl we typically observe a decrease in the event rate upon laser excitation (Fig. S4.8). We also note that the event rate was found to be linearly dependent on the bias voltage (Fig. S4.11), demonstrating the event rate is limited by transport of molecules to the nanopore rather than by the barrier involved in the DNA entering the pore [21].

We performed a systematic study of the event rate in 2M LiCl at different conditions in order to gain a better understanding of the plasmon-induced enhancement. The main results are presented in Fig. 4.4C (while results from additional experiments can be found in Fig. S4.9). On the x-axis of Fig. 4.4C, we use the relative increase in the open pore current upon laser excitation,  $\delta I/I$  (not to be confused with the relative conductance blockade,  $\Delta G/G$ ). We find  $\delta I/I$  to be a suitable parameter in describing the optical response of the plasmonic nanopore, and particularly useful for comparing results obtained for different plasmonic nanopore chips and results acquired at different polarizations. Each color in Fig. 4.4C corresponds to a different plasmonic nanopore. Filled and open symbols correspond to longitudinal and transverse excitation, respectively. Finally, round markers correspond to DNA being

translocated from the opposite side of the bowtie antenna, while squares correspond to DNA added at the same side as the nanoantenna.

Remarkably, the results for all combinations of these different conditions together collapse to display a clear, approximately linear, dependence of the event rate on  $\delta I/I$ . The implications of this are multifold. First, when compared using  $\delta I/I$  instead of laser power, the enhancement is of similar strength for both polarizations. This indicates that the strength of plasmon excitation and optical absorption is essential, while the effect does not require excitation of the plasmonic hot spot. We can therefore exclude explanations of the effect that are based on optical forces resulting from the strong field gradients in the hot spot. The independence on translocation direction shows that the effect can neither be ascribed to any vertical asymmetry of the plasmonic nanopore (i.e. from having the plasmonic antenna only on one side of the membrane). Also, the effect is quantitatively the same for different sensor chips, showing that small changes in the plasmonic nanopore geometry do not significantly modulate the effect.

The clear dependence of the event rate on  $\delta I/I$ , and the insensitivity to other experimental conditions like polarization, indicates that the event rate enhancement is caused by plasmon-induced heating, which for a given  $\delta I/I$  is the same for longitudinal and transverse excitation. Our temperature-control measurements show some increase in the event rate with temperature. However, this increase is fairly moderate, from around  $0.1 \text{ s}^{-1}$  at  $20^\circ\text{C}$  to around  $0.15 \text{ s}^{-1}$  at  $45^\circ\text{C}$ , while the plasmon-induced enhancement exceeds one order of magnitude already at very low laser powers. In order to enable a direct comparison between the temperature-control measurements and the plasmonic measurements, we convert  $\delta I/I$  to an upper limit of the temperature increase caused by plasmon excitation. This is done using the measured temperature-dependence of the bulk conductivity of our 2M LiCl buffer (Fig. S4.6) and by assuming that  $\delta I/I$  is caused only by a change in temperature. From this (Fig. S4.15), it is clear that the plasmon-induced enhancement is significantly stronger than expected from uniform heating. Furthermore, the temperature-regulated measurements show enhancements for both 2M LiCl and 1M KCl (Fig. S4.15), while the plasmon-induced rate enhancement only appears for LiCl. Based on these results we can exclude a simple increase in temperature as the main cause of the observed plasmon-induced rate enhancement.

Instead, we suggest that the effect is related to the localized nature of plasmonic heating and the associated strong thermal gradients around the plasmonic nanopore. DNA and other biomolecules are known to move along thermal gradients through thermophoresis [22], which has previously been proposed to influence the translocation dynamics of polymers through nanopores [11, 23, 24]. Thermophoresis is a complex process, and both the magnitude and the direction of thermophoretic forces depend on multiple variables, including temperature, size and charge of the moving molecule, type of salt and ionic strength [22]. Interestingly, LiCl is known to result in negative thermophoresis, for which molecules move from cold to warm regions [25–27]. This was recently demonstrated for DNA at high concentrations of LiCl [28]. We propose that negative thermophoresis aid the capture process in our experiments, by moving DNA molecules towards the warm nanopore and into the small region close the pore within which they are electrophoretically captured and translocated (i.e. they are moved

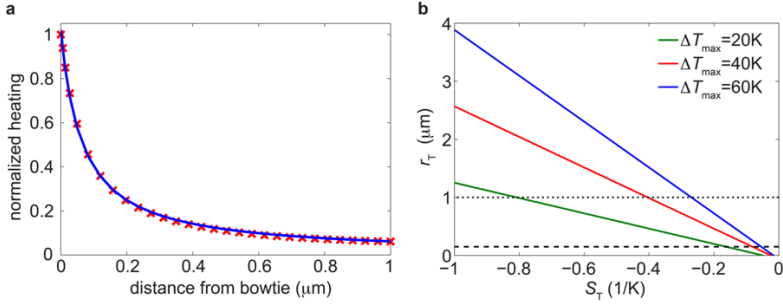


**Figure 4.5: Analysis of thermophoretic effects in plasmonic nanopores.** (A) Normalized heating profile from the top of the bowtie nanoantenna along the  $z$  axis perpendicular to the membrane and at the center position of the pore. The red markers are results from the finite-element simulation and the blue full curve is a fit to Eq. 4.2, using  $a = 0.06581 \mu\text{m}$  and  $b = 0.06425 \mu\text{m}$ . (B) Estimated thermophoretic capture distance ( $r_T$ ) versus the Soret coefficient ( $S_T$ ) for local heating of the nanopore at different temperatures. The dashed and dotted lines correspond to the estimated electrophoretic capture radii in 2M LiCl and 1M KCl, respectively.

to within the electrophoretic capture distance). We adopt the theoretical model by He *et al* [24] to evaluate if thermophoretic capture of DNA is consistent with the observed plasmon-enhanced event rate. The thermophoretic capture distance  $r_T$  describes the distance from the pore below which thermophoresis start to dominate over diffusion. Whether or not thermophoretic effects are likely to affect the capture process of DNA can then be evaluated by comparing  $r_T$  with the electrophoretic capture distance. We can estimate  $r_T$  from [24]

$$\Delta T(r_T) = -\frac{1}{S_T}, \quad (4.1)$$

where  $\Delta T(r)$  is the plasmon-induced temperature increase at distance  $r$  from the structure and  $S_T$  is the Soret coefficient that describes both direction and magnitude of thermophoresis of  $\lambda$ -DNA in the buffer medium. In order to determine  $r_T$  for a given  $S_T$ , we need the temperature distribution around the illuminated plasmonic nanopore, which was calculated by finite-element simulations (see Experimental Section 4.4 for details). The normalized temperature profile away from the bowtie antenna along the pore direction is presented in Fig. 4.5A. As expected, the temperature can be accurately fitted as inversely proportional to the distance from the structure [12],

$$\frac{\Delta T(r)}{\Delta T_{\max}} = -\frac{a}{r+b}, \quad (4.2)$$

where  $a$  and  $b$  are fit parameters and  $\Delta T_{\max}$  is the maximum temperature increase close to the pore. Although the plasmonic heating is local, the temperature is still significantly increased at distances outside the electrophoretic capture distance, which is very short for 2M LiCl ( $\sim 150$  nm at our experimental conditions, see SI Section 4.5.5 in SI). Combining Eq. 4.1 and Eq. 4.2 gives

$$r_T = -\Delta T_{\max} S_T a - b. \quad (4.3)$$

Equation 4.3 predicts that local heating combined with a negative Soret coefficient will result in a positive thermophoretic capture distance. The relation also predicts that

$r_T$ , and therefore also the event rate [21], increases linearly with the local temperature increase at the nanopore. This is in agreement with the experimental trend shown in Fig. 4.4C and Fig. S4.15.

We plot  $r_T$  versus  $S_T$  for different values of  $\Delta T_{\max}$  in order to evaluate if the model can explain the experimentally observed rate enhancements for realistic values of  $S_T$  (Fig. 4.5B). For 60 K heating of the nanopore, the estimated thermophoretic capture distance exceeds the electrophoretic capture distance (dashed line in the figure) already for  $S_T \approx -0.06 \text{ K}^{-1}$ . Experimentally, 60 K local heating increased the event rate around 16 times (see the linear trend in Fig. S4.15). Using the theoretical model, this enhancement yields a predicted value of  $S_T \approx -0.6 \text{ K}^{-1}$ , for which  $r_T \approx 2.4 \text{ }\mu\text{m}$  (16 times larger than the estimated electrophoretic capture distance in 2M LiCl).

In order to evaluate if  $S_T \approx -0.6 \text{ K}^{-1}$  is a reasonable value for our experimental conditions, we can compare it with the estimated value obtained by extrapolation from reported values of  $S_T$  for short single stranded DNA (ssDNA) at high LiCl concentrations (short Debye lengths,  $r_D$ ) [28].  $S_T$  was reported to be around  $-0.01 \text{ K}^{-1}$  for 80 bp ssDNA at LiCl concentrations corresponding to  $r_D \approx 1 \text{ nm}$ , and the fitted curve in the same report suggests that the magnitude increases to at least  $-0.015 \text{ K}^{-1}$  when increasing the concentration to 2M LiCl ( $r_D \approx 0.2 \text{ nm}$ ). Using an approximate scaling of  $S_T$  as the square root of the DNA length, as reported for dsDNA in low ionic strength KCl [22], we estimate  $S_T$  to be on the order of  $-0.4 \text{ K}^{-1}$  for 48.5 kbp DNA at 2M LiCl. Given the many uncertainties involved in order to reach this value, we find it remarkably close to the predicted value of  $S_T \approx -0.6 \text{ K}^{-1}$ , for which our thermophoretic model quantitatively agrees with the experimentally observed rate enhancements. Hence, the analysis corroborates that thermophoresis can have significant effects on molecules at micrometer distances from a locally heated nanopore and that negative thermophoresis is a highly plausible mechanism for the observed plasmon-enhanced event rate.

If thermophoresis plays the major role in the event-rate enhancement, the effect should also appear for a locally heated nonplasmonic nanopore. We tested this by positioning a conventional nanopore at the diffraction-limited focal spot of the laser in our setup. While this approach should provide less localized heating than plasmonic heating (and correspondingly lower temperature gradients), we note that Eq. 4.1 predicts  $r_T$  to be determined by the temperature increase at  $r_T$  and not by the temperature gradient at  $r_T$ . This, perhaps nonintuitive, prediction is in perfect analogy with the model for electrophoretic capture by Grosberg and Rabin [21], which predicts the electrophoretic capture distance to be determined by the electric bias potential and not by the gradient in the potential (the electric field), although the electrophoretic force arise from the latter. Indeed, although a much higher laser power was required (50 mW increased  $\delta I/I$  by around 23%) to get a similar current increase as for the plasmonic nanopores, we observed a significant event rate enhancement in 2M LiCl also for the locally heated nonplasmonic nanopore (Fig. S4.13).

The small plasmon-induced decrease in event frequency that is observed in 1M KCl may be related to positive thermophoresis in KCl [22, 28], and a corresponding decrease in the DNA concentration close to the pore. Considering the much larger capture distance in 1M KCl compared with in 2M LiCl ( $\sim 1 \text{ }\mu\text{m}$ , see dotted line in Fig. 4.5B and SI Section 4.5.5), this effect is expected to be less pronounced, which is

in good agreement with our observations. We finally note that thermophoretic motion of the salt ions in the solution may also play a role by affecting the spatial distribution of the ionic concentration close to the nanopore. While  $K^+$  ions are thermophobic above room temperature [29],  $Li^+$  ions are typically thermophilic [26] and may thus accumulate around the nanopore. This could affect both the capture process as well as the effective nanopore conductance. However, the magnitude of the Soret coefficient is highly dependent on particle size [22], and it is expected to be very small for the  $Li^+$  ions (on the order of  $10^{-3} - 10^{-2} K^{-1}$ ) [25]. We therefore think such effects at most play a minor role for our observations.

### 4.3. CONCLUSION

This article presents a systematic investigation of plasmonic effects on DNA translocations through solid-state plasmonic nanopores. We were able to characterize the response of the sensor device to translocating dsDNA molecules by quantifying the most important parameters such as conductance blockades, translocation time, and event rate. All observed plasmonic effects on these parameters are consistent with plasmonic local heating of the nanopore. The most significant plasmonic effect that we observe is a dramatic enhancement of the event rate in LiCl buffer, which is attributed to negative thermophoresis in the strong thermal gradients caused by plasmonic heating. It should be stressed that this plasmon-induced rate enhancement is of high relevance for nanopore sensing, because measurements in LiCl buffers typically suffer from very low event rates at suitable molecular concentrations, but provide other important advantages such as low translocation speeds and a corresponding high spatiotemporal resolution.

Plasmonic excitation and local heating of our solid-state plasmonic nanopore also increased the sensor signal (larger conductance blockades) without a corresponding decrease in the translocation time that one obtains for uniform heating. With respect to sensor signals, we note that the addition of plasmonic functionalities to nanopores also opens up for optical detection schemes, including monitoring shifts in plasmonic resonances [30–34], plasmon-enhanced fluorescence [35], and surface-enhanced Raman scattering [6]. The two latter are based on the strong optical fields around plasmonic nanostructures and are particularly suitable for our system that provides a plasmonic hot spot right at the nanopore. Furthermore, optical forces based on the strong optical field gradients in the plasmonic hot spot may be useful for trapping and controlling the motion of biomolecules through nanopores [36, 37].

## 4.4. EXPERIMENTAL METHODS

### 4.4.1. SAMPLE FABRICATION

Plasmonic nanopore chips were fabricated from pre-fabricated 4-inch wafers containing multiple (256) individual silicon (Si) chips with freestanding SiN membranes (approximately  $40 \times 40 \mu m$  and 20 nm thick). The chips were designed to have a 500 nm insulating silicon dioxide layer between the silicon (Si) and the nanopore membrane to minimize capacitive noise [38, 39]. This layer was removed from membrane regions using a 7 min buffered oxide wet etch. Arrays of plasmonic bowtie nanoantennas were

defined on top of the membranes using conventional electron beam lithography, as described in our earlier work [8]. Finally, a TEM (Philips CM300UT-FEG or FEI Tecnai TF20) was used to drill a single 10 nm-in-diameter pore through the SiN membrane right at the gap position of a suitable optical nanoantenna. The plasmonic nanopore chips were stored in a water-ethanol (1:1) mixture until usage.

#### 4.4.2. DNA TRANSLOCATIONS THROUGH PLASMONIC NANOPORES

After a short oxygen plasma treatment, the plasmonic nanopore chip was mounted in a custom-made flow cell such that it separated two compartments containing buffer solution (1M KCl or 2M LiCl buffer, each containing 10mM Tris (tris(hydroxymethyl)aminomethane) and 1mM EDTA (Ethylenediaminetetraacetic acid) at pH 8). The ionic current flowing through the nanopore was monitored using Ag/AgCl electrodes connected to a patch clamp amplifier (Axon Axopatch 200B, Molecular Devices, US) and the measured signals were transferred to a computer via a DAC card (USB-6251, National Instruments, US). A 100 mV bias voltage was used in all experiments unless stated otherwise. We used light from a 785 nm diode laser (Omicron-Laserage Laserprodukte GmbH, Germany) for plasmon excitation. The laser beam was expanded to about 7 mm using two lenses and focused into the flow cell through a water-immersion objective (60X, Olympus, The Netherlands) in a custom-built inverted microscope. A rotatable quarter wave plate was used to control the polarization. A piezo stage (P-545, Physik Instrumente, Germany) enabled accurate control of the position of the plasmonic nanopore with respect to the focused laser beam. Experiments were performed using a custom-designed LabView program (National Instruments, US) that controlled our instruments. For translocation experiments, unmethylated  $\lambda$  DNA (Promega, US) was first heat treated at 65°C for ten minutes and then stored on ice before it was added to the flow cell.

#### 4.4.3. OPTICAL FDTD SIMULATIONS

FDTD Solutions (Lumerical Solutions, Inc., Canada) was used to model the optical properties of the plasmonic nanopore. The bowtie antenna was modeled as two 30 nm thick and 60 nm long (tip to end) gold triangles separated by a 10 nm gap on a 20 nm thin SiN membrane (refractive index (RI) = 2), and with a 10 nm in diameter pore through the membrane at the gap center. The upper corners of the triangles were slightly rounded (15 nm-in-diameter rounding) to better resemble the fabricated structures. The RI of the surrounding medium was set to 1.33. Symmetry was used to reduce the computational time. The plasmonic antennas were excited by a pulse from a total-field scattered-field source with the optical axis perpendicular to the membrane and the polarization in either the longitudinal or the transverse mode. The optical absorption cross section was calculated through the net power flow into a box surrounding the antenna.

subsectionCombined optical and thermal simulations The temperature distribution around a plasmonic nanopore illuminated with 785 nm light was calculated using the finite-element method (Comsol Multiphysics). The same geometry was used as for the FDTD simulations, but with rounded corners only in the plane of the membrane. We also excluded the nanopore to reduce the simulation time. The total simulation region was a cube with a side length of 2  $\mu\text{m}$ . Refractive indices for the membrane, the surrounding

medium and the gold antenna were 2, 1.33, and taken from Johnson and Christy [40], respectively. The thermal conductivity of the SiN membrane was set to  $3 \text{ W}/(\text{m}\cdot\text{K})$  [41] and we used values from the built-in library for gold and for the surrounding medium (using values for water for the latter). A tetrahedral mesh was used (maximum element size far from the antenna set to  $1/10$  of the wavelength).

Maxwell's equations were solved in the wave optics module in Comsol and used to calculate the optical absorption and corresponding heat source of the nanoantenna upon illumination by a plane wave at  $785 \text{ nm}$ , polarized in the longitudinal direction. Perfectly matched layers were used to avoid back scattering at the outer boundaries. The two-fold symmetry of the nanoantenna allowed us to calculate only one quadrant of the simulation region by using a perfect electric conductor boundary plane (orthogonal to the polarization and to the membrane) and a perfect magnetic conductor boundary plane (parallel to polarization and orthogonal to the membrane), both going through the center of the antenna. The steady-state temperature distribution of the system could then be calculated by solving the heat equation (heat transfer module) using the total power dissipation obtained above as the heat source. Newton's cooling law was imposed on the outer boundaries of the simulation,

$$\phi = \text{Nu} \cdot \frac{\kappa}{L} (T - T_{\text{inf}}) \quad (4.4)$$

where  $\phi$  is the heat flux over the boundary,  $\kappa$  is the thermal conductivity of the material at the boundary,  $L = 2 \mu\text{m}$  is the typical length scale,  $T$  is the temperature at the boundary and  $T_{\text{inf}}$  is the set temperature of the surrounding far away. The Nusselt number (Nu) was set to 1.4 after optimization using simulations for a spherical heat source and comparison with the corresponding known analytical solution. The use of Newton's cooling law as boundary condition provided significantly more accurate temperature distributions compared with using a fixed temperature at the boundary.

## 4.5. SUPPORTING INFORMATION

### 4.5.1. TEMPERATURE-DEPENDENCE OF BUFFER CONDUCTIVITY

The buffer conductivity at different temperatures was measured using a zeta potential analyzer (Zetasizer Nano, Malvern Instruments Ltd, UK) and fitted to linear curves, as shown below.

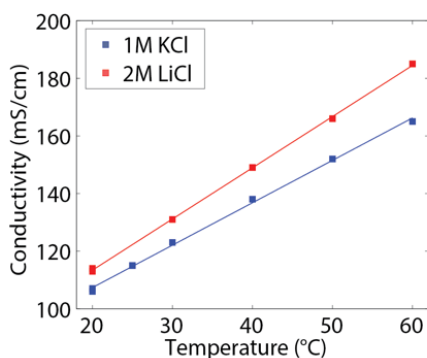


**Figure S4.6:** Measured bulk conductivity,  $\sigma_{bulk}$ , of 1M KCl (blue squares) and 2M LiCl (red squares) as a function of temperature. In this temperature range, the experimental values fit well to a linear model,  $\sigma_{bulk}(T) = a + bT$  for both buffers. The fits give  $a = 77.9$  mS/cm,  $b = 1.47$  mS/(cm°C) for 1M KCl and  $a = 77.9$  mS/cm,  $b = 1.78$  mS/(cm°C) for 2M LiCl.

### 4.5.2. CURRENT-VOLTAGE CHARACTERISTICS

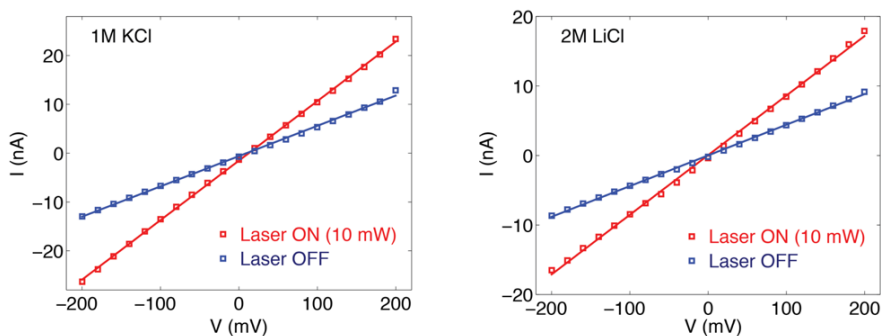


**Figure S4.7:** Current versus voltage with (red) and without (blue) laser excitation, in 1M KCl (left) and 2M LiCl (right).

### 4.5.3. RESULTS FROM ADDITIONAL EXPERIMENTS

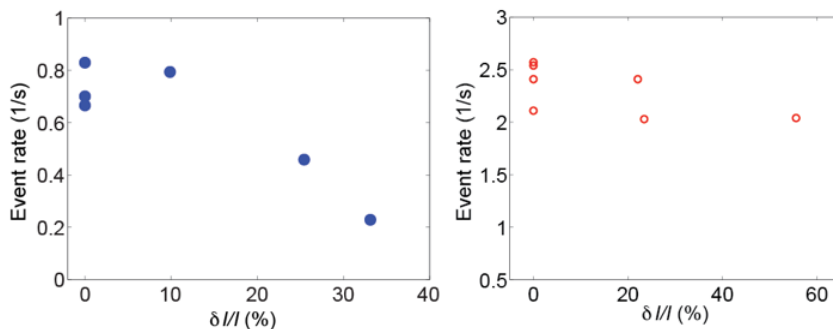


**Figure S4.8: Event rate upon plasmon excitation in 1M KCl.** Examples of event rate measurement for a plasmonic nanopore in 1M KCl versus  $\delta I/I$ . The plots on the left and on the right correspond to measurements where plasmons were excited with longitudinal and transverse polarization, respectively. For both measurements, DNA molecules were translocated from the side of the bowtie antenna at a concentration of 10 ng/ $\mu$ L.

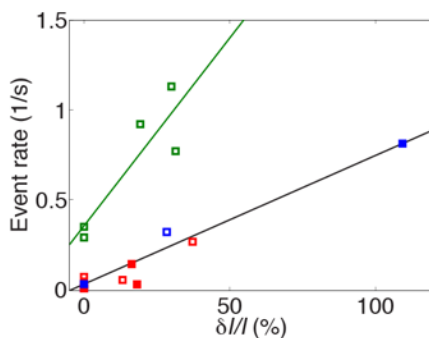


**Figure S4.9: Plasmon-induced rate enhancement in 2M LiCl for different initial rates.** Event rate in 2M LiCl as a function of current increase upon laser illumination for experiments with significantly different initial rates at 0 mW. Different colors correspond to different samples. Filled and open symbols correspond to laser illumination in longitudinal and transverse polarization respectively. The full lines are guides to the eye.

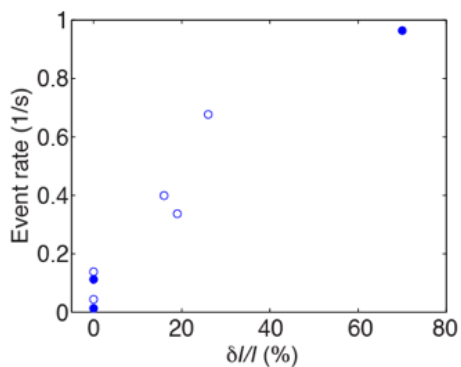


**Figure S4.10: Plasmon-induced rate enhancement in 1M LiCl.** Event rate as a function of the increase in open pore current upon laser illumination in 1M LiCl buffer. The open and filled symbol correspond to laser illumination in transverse and longitudinal polarization, respectively.

4

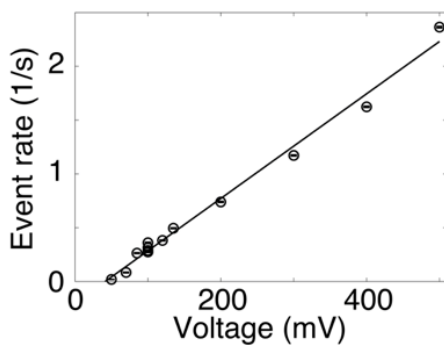
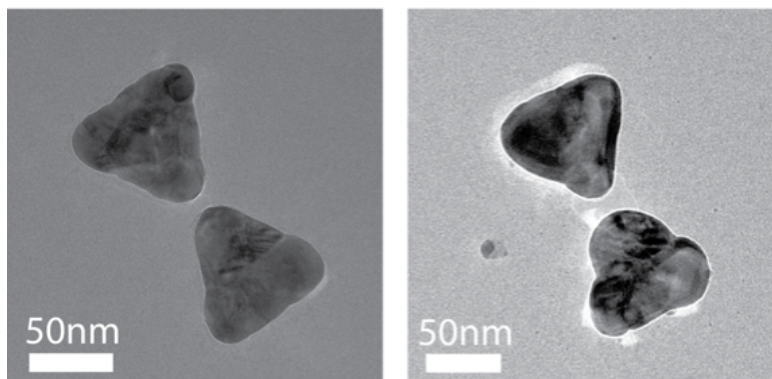


**Figure S4.11: Voltage-dependence on the event rate** Dependence of bias voltage on event rate of  $\lambda$ -DNA translocations in 2M LiCl.



4

**Figure S4.12: TEM images of plasmonic nanopores before and after measurement for a relatively unstable device.** TEM images before (left) and after (right) plasmon excitation in longitudinal mode at XmW in 1M KCl for a plasmonic sample. This particular chip showed very significant nanopore growth during experiment. Small changes in the rounding of the gold triangles can also be observed. Most samples are much more stable.

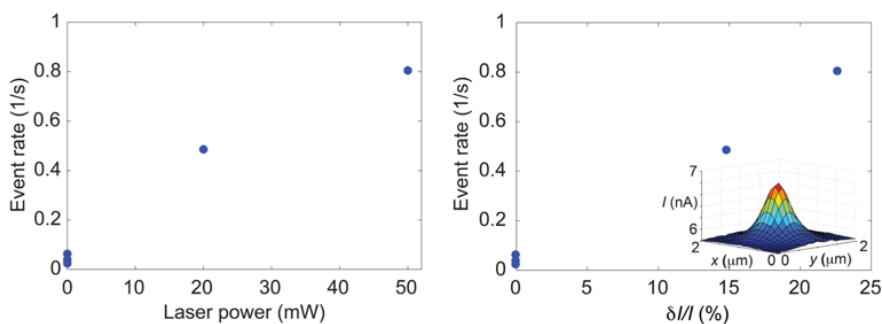


**Figure S4.13: Event rate-enhancement in 2M LiCl for a locally heated conventional nanopore.** Event rate as a function of laser power (left) and relative increase in the open pore current (right) upon focused laser illumination for a conventional nanopore in 2M LiCl. The inset shows a 2D current scan through the focal plane obtained at 20 mW and at 100 mV bias voltage.

#### 4.5.4. TEMPERATURE-REGULATED NANOPORE EXPERIMENTS

Temperature effects on DNA translocations through a conventional nanopore were investigated in a measurement setup that provides control of the temperature of the whole flow cell using a Peltier heater/cooler. The nanopore current was monitored in the same way as for the plasmonic measurements. The nanopores also had the same dimensions (10 nm in diameter, 20 nm thick SiN membrane) as in the plasmonic measurements, but without the gold nanoantennas and a slightly different geometry of the chip in the region outside the membrane (where instead of a SiO<sub>2</sub> layer between the membrane and the Si, we used two SiO<sub>2</sub> and SiN layers above the nanopore membrane). All measurements were acquired using a 100 mV bias voltage.

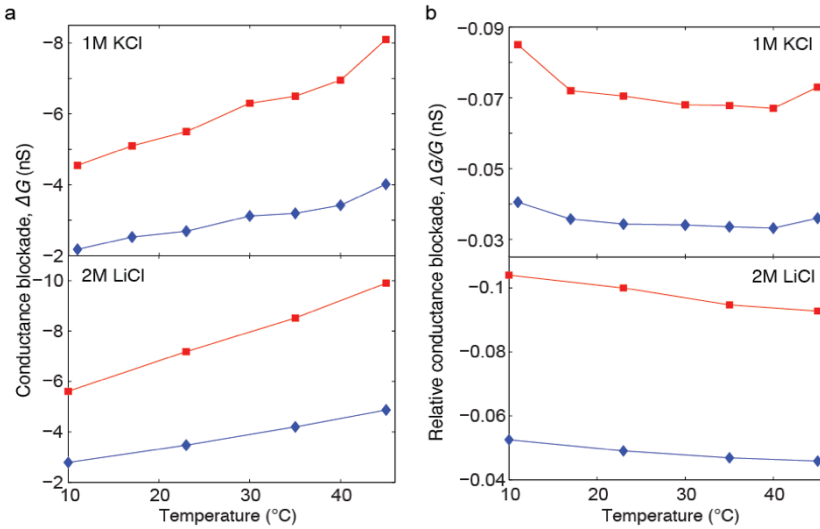


**Figure S4.14: Temperature-dependence of absolute and relative conductance blockades.** (A) Conductance blockade versus temperature for  $\lambda$ -DNA in 1M KCl (top) and 2M LiCl (bottom). Blue diamonds and red squares correspond to the first and the second peak of the conductance histograms, respectively, similar to the plasmonic measurements. (B) Same as in (A), but for the relative conductance blockade.

#### 4.5.5. ESTIMATION OF ELECTROPHORETIC CAPTURE DISTANCES

Here we estimate the capture distance, i.e. the typical distance from the pore at which DNA molecules are electrophoretically captured and pulled through the nanopore. The different parameters are approximated at 25°C for 1M KCl and 2M LiCl and are stated in parentheses when introduced. According to Grosberg and Rabin [21] the capture distance,  $r_C$ , can be estimated as:

$$r_C = \Delta V \frac{d^2 \mu}{8lD} \quad (\text{S4.5})$$

where  $\Delta V$  is the applied voltage over the membrane (0.1 V),  $d$  is the diameter of the nanopore (10 nm),  $l$  is the effective length of the pore (8.6 nm, adopted from Kowalczyk *et al.* [17] for the same membrane thickness),  $\mu$  is the electrophoretic mobility of the

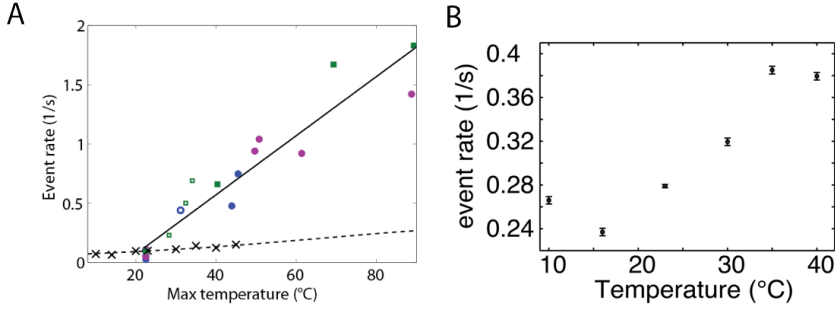


**Figure S4.15: Comparison of temperature-induced and plasmon-induced enhancement of the event rate.** (A) Comparison between event rate for plasmonic excitations (colored symbols and black full line) and uniform heating (black x symbols and dashed line). All experiments were performed in 2M LiCl. Different colors correspond to different plasmonic nanopores. Filled and open symbols are for longitudinal and transverse polarization, respectively. Squares and circles correspond to DNA added from the side of the bowtie antenna and the other side, respectively. The x-axis shows the measured temperature for the temperature-regulated measurements and the estimated maximum temperature for the plasmonic measurements, assuming that  $\delta I/I$  can be fully ascribed to plasmonic heating and using the temperature dependence of the buffer conductivity, as shown in Fig. S4.6. (B) Temperature dependence of event rate in 1M KCl for a uniformly heated pore

DNA molecule in the particular electrolyte and  $D$  is the DNA diffusion coefficient. The diffusion coefficient can be estimated using [42]:

$$D = \frac{8\sqrt{3}\pi k_B T}{18\pi\eta\sqrt{l_p l_C}} \quad (\text{S4.6})$$

where  $k_B$  is the Boltzmann constant ( $1.38 \cdot 10^{-23} \text{ kgm}^2\text{s}^{-2}\text{K}^{-1}$ ),  $T$  is the absolute temperature (298.15 K),  $\eta$  is the viscosity of the electrolyte (0.88mPa · s for 1M KCl [43] and 1.2 mPa·s for 2M LiCl) [44],  $l_p$  is the DNA persistence length (48.5 nm) [45] and  $l_C$  is the DNA contour length (16  $\mu\text{m}$ ). This gives estimated diffusion coefficients of 2.3  $\mu\text{m}^2/\text{s}$  and 1.7  $\mu\text{m}^2/\text{s}$  in 1M KCl and 2M LiCl, respectively. The electrophoretic mobility can be estimated using:

$$\mu = \frac{2\alpha e r_D}{\pi\eta f d} \quad (\text{S4.7})$$

where  $e$  is the elementary charge ( $1.6 \cdot 10^{-19} \text{ kgm}^2/(\text{Vs}^2)$ ),  $r_D$  is the Debye length, (0.3 nm for 1M KCl and 0.2 nm for 2M LiCl) [46],  $f = 0.34 \text{ nm}$  is the distance between base pairs and  $d$  is the diameter of the DNA molecule (2 nm). The numerical factor  $\alpha$  accounts for the fact that the effective charge of the DNA is lowered due screening by counterions. We use  $\alpha = 0.5$  for 1M KCl, and estimate  $\alpha = 0.07$  in 2M LiCl, which is 7 times lower than in 1M KCl, based on a stronger binding of  $\text{Li}^+$  ions than  $\text{K}^+$  ions to the DNA, resulting in a much higher screening [16]. Using these values, the electrophoretic mobilities can be estimated to 1.7 · 10<sup>-8</sup> m<sup>2</sup>/(V·s) and 0.17 · 10<sup>-8</sup> m<sup>2</sup>/(V·s) for 1M KCl and 2M LiCl, respectively. Finally, we estimate the capture distances to be 1.0 m and 150 nm for 1M KCl and 2M LiCl, respectively. While being rough estimations, based on treating the

DNA molecule as a point particle (which particularly may not hold for small capture distances), we conclude that the capture distance is almost one order of magnitude smaller for 2M LiCl compared with 1M KCl. As a result, local heating effects will play a significantly larger role in measurements in 2M LiCl, in agreement with the effects we observe on the event rate.

#### 4.5.6. DISCUSSION ON TEMPERATURE EFFECTS ON TRANSLOCATION TIMES

In this section we consider how the DNA translocation times depend on a localized temperature change near the pore. The DNA translocation times are determined by a force balance between a forward electrophoretic drive and a retracting viscous drag on the DNA. The viscous drag force consists of two parts: a viscous drag force on the DNA strand residing in the pore and a viscous drag on the untranslocated part of the DNA away from the pore (on the order of the radius of gyration, roughly 500 nm) [20]. Drag forces in general can be described as:

$$f_d = \xi \eta v_d \quad (\text{S4.8})$$

where  $v_d$  is the relevant velocity,  $\eta$  is the buffer viscosity (locally in the pore or at the region of the untranslocated DNA), and  $\xi$  is a geometrical factor characterizing the size of the object that the drag force is exerted on (hence, different for the two drag contributions). The viscosity decreases with increasing temperature for our buffer conditions [43, 44]. While this may indicate that the drag forces decrease with temperature, we also need to consider how the relevant velocities depend on temperature.

Importantly, the relevant velocity is different for the untranslocated DNA and for the DNA inside the pore. In a simplified model, the velocity scale that determines the drag on the untranslocated part of the DNA is set by the DNA translocation speed, whereas the velocity scale that determines the drag in the pore is set by the electroosmotic flow (EOF) in the pore [24]. The EOF arises from a net charge flow in the mobile Debye layer near the pore walls and is, at the center of the pore, given by [18, 19]:

$$v_{EOF} = \frac{\Delta V \epsilon_0 \epsilon_r \Phi_0}{l \eta} \quad (\text{S4.9})$$

Here,  $\Delta V$  is the applied voltage bias,  $\epsilon_0 \epsilon_r$  is the electric permittivity of water,  $l$  is the pore length and  $\Phi_0$  is the zeta-potential at the pore wall. The Grahame equation connects the surface charge density and the potential on the pore wall [47]:

$$\sigma_{surf}(\Phi_0) = \frac{2\epsilon_0 \epsilon_r k_B T}{e r_D} \sinh\left(\frac{e\Phi_0}{2k_B T}\right) \quad (\text{S4.10})$$

Here,  $\sigma_{surf}$  is the surface charge density on the pore wall,  $k_B$  is the Boltzmann constant,  $T$  is the temperature,  $e$  the electron charge, and  $r_D$  is the Debye length (which has a negligible dependence on temperature in this case). Upon linearizing Eq. S4.10 for small zeta-potential, the EOF will be given by

$$v_{EOF} = \frac{\Delta V \sigma_{surf} r_D}{l \eta} \quad (\text{S4.11})$$

where an appreciable temperature dependence of the EOF is enclosed in the viscosity only.

The EOF will exert a drag force on the DNA if the pore surface is negatively charged (as is the case for SiN at pH 8). We note that the EOF is typically much faster than the DNA translocation speed (on the order of  $10^{-1}$  m/s compared to  $10^{-3}$  m/s for the DNA translocation speed for a typical surface charge density of  $-60$  mC/m<sup>2</sup>) [47]. As a result, the EOF dominates and determines the drag force on the DNA inside the pore. In turn, the inverse proportionality of this flow to the buffer viscosity cancels the initial dependence of the drag force on viscosity (Eq. S4.8). Hence, the drag force in the pore due to the EOF will be unaffected by a change in viscosity and in turn, this force will be largely unaffected by a change in temperature.

Based on this reasoning, we conclude that local heating of the nanopore is not expected to significantly affect the translocation time. By contrast, uniform heating affects the viscosity also in the region of the untranslocated DNA, and the resulting decrease in the drag force on the untranslocated DNA will thus be compensated by an increase in the relevant velocity scale, which in this case is the DNA translocation speed. Hence, uniform heating, but not local heating, is expected to result in decreased translocation times, which is in agreement with our observations.

## REFERENCES

- [1] M. Wanunu, *Nanopores: A journey towards dna sequencing*, Physics of Life Reviews **9**, 125 (2012).
- [2] G. V. Soni and C. Dekker, *Detection of nucleosomal substructures using solid-state nanopores*, Nano Letters **12**, 3180 (2012).
- [3] R. S. Wei, V. Gatterdam, R. Wieneke, R. Tampe, and U. Rant, *Stochastic sensing of proteins with receptor-modified solid-state nanopores*, Nature Nanotechnology **7**, 257 (2012).
- [4] S. W. Kowalczyk, A. R. Hall, and C. Dekker, *Detection of local protein structures along dna using solid-state nanopores*, Nano Letters **10**, 324 (2010).
- [5] A. P. Ivanov, E. Instuli, C. M. McGilvery, G. Baldwin, D. W. McComb, T. Albrecht, and J. B. Edel, *Dna tunneling detector embedded in a nanopore*, Nano Letters **11**, 279 (2011).
- [6] M. P. Cecchini, A. Wiener, V. A. Turek, H. Chon, S. Lee, A. P. Ivanov, D. W. McComb, J. Choo, T. Albrecht, S. A. Maier, and J. B. Edel, *Rapid ultrasensitive single particle surface-enhanced raman spectroscopy using metallic nanopores*, Nano Letters **13**, 4602 (2013).
- [7] G. A. T. Chansin, R. Mulero, J. Hong, M. J. Kim, A. J. Demello, and J. B. Edel, *Single-molecule spectroscopy using nanoporous membranes*, Nano Letters **7**, 2901 (2007).
- [8] M. P. Jonsson and C. Dekker, *Plasmonic nanopore for electrical profiling of optical intensity landscapes*, Nano Letters **13**, 1029 (2013).

- [9] G. V. Soni, A. Singer, Z. L. Yu, Y. J. Sun, B. McNally, and A. Meller, *Synchronous optical and electrical detection of biomolecules traversing through solid-state nanopores*, Review of Scientific Instruments **81** (2010), 10.1063/1.3277116.
- [10] N. Di Fiori, A. Squires, D. Bar, T. Gilboa, T. D. Moustakas, and A. Meller, *Optoelectronic control of surface charge and translocation dynamics in solid-state nanopores*, Nature Nanotechnology **8**, 946 (2013).
- [11] J. E. Reiner, J. W. F. Robertson, D. L. Burden, L. K. Burden, A. Balijepalli, and J. J. Kasianowicz, *Temperature sculpting in yoctoliter volumes*, Journal of the American Chemical Society **135**, 3087 (2013).
- [12] G. Baffou and R. Quidant, *Thermo-plasmonics: using metallic nanostructures as nano-sources of heat*, Laser & Photonics Reviews **7**, 171 (2013).
- [13] A. Kinkhabwala, Z. F. Yu, S. H. Fan, Y. Avlasevich, K. Mullen, and W. E. Moerner, *Large single-molecule fluorescence enhancements produced by a bowtie nanoantenna*, Nature Photonics **3**, 654 (2009).
- [14] R. D. Grober, R. J. Schoelkopf, and D. E. Prober, *Optical antenna: Towards a unity efficiency near-field optical probe*, Applied Physics Letters **70**, 1354 (1997).
- [15] A. J. Storm, J. H. Chen, H. W. Zandbergen, and C. Dekker, *Translocation of double-strand dna through a silicon oxide nanopore*, Physical Review E **71** (2005), 10.1103/PhysRevE.71.051903.
- [16] S. W. Kowalczyk, D. B. Wells, A. Aksimentiev, and C. Dekker, *Slowing down dna translocation through a nanopore in lithium chloride*, Nano Letters **12**, 1038 (2012).
- [17] S. W. Kowalczyk, A. Y. Grosberg, Y. Rabin, and C. Dekker, *Modeling the conductance and dna blockade of solid-state nanopores*, Nanotechnology **22** (2011), 10.1088/0957-4484/22/31/315101.
- [18] S. Ghosal, *Effect of salt concentration on the electrophoretic speed of a polyelectrolyte through a nanopore*, Physical Review Letters **98** (2007), 10.1103/PhysRevLett.98.238104.
- [19] C. T. A. Wong and M. Muthukumar, *Polymer capture by electro-osmotic flow of oppositely charged nanopores*, Journal of Chemical Physics **126** (2007), 10.1063/1.2723088.
- [20] L. Chen and A. T. Conlisk, *Forces affecting double-stranded dna translocation through synthetic nanopores*, Biomedical Microdevices **13**, 403 (2011).
- [21] A. Y. Grosberg and Y. Rabin, *Dna capture into a nanopore: Interplay of diffusion and electrohydrodynamics*, Journal of Chemical Physics **133** (2010), 10.1063/1.3495481.
- [22] S. Duhr and D. Braun, *Why molecules move along a temperature gradient*, Proceedings of the National Academy of Sciences of the United States of America **103**, 19678 (2006).
- [23] M. Belkin, C. Maffeo, D. B. Wells, and A. Aksimentiev, *Stretching and controlled*

- motion of single-stranded dna in locally heated solid-state nanopores*, *ACS Nano* **7**, 6816 (2013).
- [24] Y. H. He, M. Tsutsui, R. H. Scheicher, F. Bai, M. Taniguchi, and T. Kawai, *Thermophoretic manipulation of dna translocation through nanopores*, *ACS Nano* **7**, 538 (2013).
- [25] J. Colombani, J. Bert, and J. Dupuy-Philon, *Thermal diffusion in (licl,rh2o)*, *Journal of Chemical Physics* **110**, 8622 (1999).
- [26] T. Ikeda and H. Kimura, *Relative determination of soret coefficients of electrolytes*, *Journal of Physical Chemistry* **69**, 41 (1965).
- [27] S. A. Putnam and D. G. Cahill, *Transport of nanoscale latex spheres in a temperature gradient*, *Langmuir* **21**, 5317 (2005).
- [28] M. Reichl, M. Herzog, A. Gotz, and D. Braun, *Why charged molecules move across a temperature gradient: The role of electric fields*, *Physical Review Letters* **112** (2014), 10.1103/PhysRevLett.112.198101.
- [29] F. Romer, Z. L. Wang, S. Wiegand, and F. Bresme, *Alkali halide solutions under thermal gradients: Soret coefficients and heat transfer mechanisms*, *Journal of Physical Chemistry B* **117**, 8209 (2013).
- [30] F. Eftekhari, C. Escobedo, J. Ferreira, X. B. Duan, E. M. Giroto, A. G. Brolo, R. Gordon, and D. Sinton, *Nanoholes as nanochannels: Flow-through plasmonic sensing*, *Analytical Chemistry* **81**, 4308 (2009).
- [31] M. P. Jonsson, A. B. Dahlin, L. Feuz, S. Petronis, and F. Hook, *Locally functionalized short-range ordered nanoplasmonic pores for bioanalytical sensing*, *Analytical Chemistry* **82**, 2087 (2010).
- [32] S. Kumar, N. J. Wittenberg, and S. H. Oh, *Nanopore-induced spontaneous concentration for optofluidic sensing and particle assembly*, *Analytical Chemistry* **85**, 971 (2013).
- [33] F. Mazzotta, F. Hook, and M. P. Jonsson, *High throughput fabrication of plasmonic nanostructures in nanofluidic pores for biosensing applications*, *Nanotechnology* **23** (2012), 10.1088/0957-4484/23/41/415304.
- [34] A. A. Yanik, M. Huang, A. Artar, T. Y. Chang, and H. Altug, *Integrated nanoplasmonic-nanofluidic biosensors with targeted delivery of analytes*, *Applied Physics Letters* **96** (2010), 10.1063/1.3290633.
- [35] A. G. Brolo, S. C. Kwok, M. G. Moffitt, R. Gordon, J. Riordon, and K. L. Kavanagh, *Enhanced fluorescence from arrays of nanoholes in a gold film*, *Journal of the American Chemical Society* **127**, 14936 (2005).
- [36] S. Nam, I. Choi, C. C. Fu, K. Kim, S. Hong, Y. Choi, A. Zettl, and L. P. Lee, *Graphene nanopore with a self-integrated optical antenna*, *Nano Letters* **14**, 5584 (2014).
- [37] Y. J. Pang and R. Gordon, *Optical trapping of a single protein*, *Nano Letters* **12**, 402

- (2012).
- [38] X. J. A. Janssen, M. P. Jonsson, C. Plesa, G. V. Soni, C. Dekker, and N. H. Dekker, *Rapid manufacturing of low-noise membranes for nanopore sensors by trans-chip illumination lithography*, *Nanotechnology* **23** (2012), 10.1088/0957-4484/23/47/475302.
- [39] M. Wanunu, T. Dadoosh, V. Ray, J. M. Jin, L. McReynolds, and M. Drndic, *Rapid electronic detection of probe-specific micrnas using thin nanopore sensors*, *Nature Nanotechnology* **5**, 807 (2010).
- [40] P. B. Johnson and R.-W. Christy, *Optical constants of the noble metals*, *Physical review B* **6**, 4370 (1972).
- [41] H. Jianqiang, L. Yan, L. Senlin, and L. Qing, *Thermal conductivity of pecvd silicon-rich silicon nitride films measured with a sio2/sixny bimaterial microbridge test structure*, *Journal of Semiconductors* **35**, 046002 (2014).
- [42] C. Plesa, S. W. Kowalczyk, R. Zinsmeister, A. Y. Grosberg, Y. Rabin, and C. Dekker, *Fast translocation of proteins through solid state nanopores*, *Nano letters* **13**, 658 (2013).
- [43] M. Afzal, M. Saleem, and M. T. Mahmood, *Temperature and concentration dependence of viscosity of aqueous electrolytes from 20. degree. c to 50. degree. c chlorides of (sodium (1+), potassium (1+), magnesium (2+), calcium (2+), barium (2+), strontium (2+), cobalt (2+), nickel (2+), copper (2+) and chromium (3+)*, *Journal of Chemical and Engineering Data* **34**, 339 (1989).
- [44] I. M. Abdulagatov, A. B. Zeinalova, and N. D. Azizov, *Experimental viscosity b-coefficients of aqueous licl solutions*, *Journal of molecular liquids* **126**, 75 (2006).
- [45] S. Geggier, A. Kotlyar, and A. Vologodskii, *Temperature dependence of dna persistence length*, *Nucleic acids research* **39**, 1419 (2010).
- [46] J. N. Israelachvili, *Intermolecular and surface forces* (Academic press, 2011).
- [47] S. H. Behrens and D. G. Grier, *The charge of glass and silica surfaces*, *The Journal of Chemical Physics* **115**, 6716 (2001)



# 5

## ACTIVE DELIVERY OF SINGLE DNA MOLECULES INTO A PLASMONIC NANOPORE FOR LABEL-FREE OPTICAL SENSING

*Plasmon resonance biosensors are able to provide ultimate sensitivity at the single-molecule level. This exceptional sensitivity is, however, associated with a nanometer-sized confined sensing volume where the electromagnetic field is extremely enhanced, and accordingly molecules are only detected upon inefficiently drifting into these optical hotspots by diffusion, without any positional control. Here, we combine a plasmonic nanoantenna with a solid-state nanopore and demonstrate that single DNA molecules can be efficiently delivered to the plasmonic hot spot. By monitoring the backscattered light intensity from the plasmonic nanoantennas, single DNA molecules can be detected in a label-free manner at sub-millisecond acquisition rates. Our method realizes an event detection rate of 10 molecules per second with better than 200  $\mu$ s temporal resolution, both orders of magnitude better than for any reported plasmonic single-molecule sensing method. Furthermore, the DC electric field applied to the nanopore can, in contrast to previous surface-binding-based plasmonic biosensors, both capture and release biomolecules from the hotspot, allowing efficient reuse of the sensor for subsequent molecules. The plasmonic nanopore sensor reported here significantly outperforms conventional single-molecule plasmon resonance sensors and opens opportunities for high-throughput optical single-molecule-sensing assays.*

---

This chapter has been submitted as: Xin Shi, Daniel V. Verschueren, and Cees Dekker. Active delivery of single DNA molecules into a plasmonic nanopore for label-free optical sensing.

## 5.1. INTRODUCTION

Plasmon resonance sensing is a promising technique for high-throughput, high-speed, high-sensitivity, and label-free biosensing based on optical read-out [1]. Biomolecule detection follows from a shift in the plasmon resonance of a plasmonic nanoantenna that results from changes in the refractive index of the local environment of the antenna induced by the presence of the analyte. This concept has been used extensively in bulk sensing [2, 3], and has been integrated into a variety of biological and chemical sensing devices [4]. Recently, impressive developments in plasmonic sensing has pushed the sensitivity of these devices to the ultimate detection level of single molecules. This advance has been achieved through engineering the hotspot, the nanoscale volume into which the plasmonic nanoantenna strongly concentrates the incident optical field [5–7].

Despite the substantial progress over the past years, single-molecule plasmon resonance sensing faces severe challenges. As the extreme increase in sensitivity requires the nanoscale electromagnetic (EM) hotspot to become exceedingly more confined, the probability that a biomolecule will be diffusing into the hot spot becomes vanishing small for any practical analyte concentrations [8–10]. Furthermore, molecules interact with the plasmonic sensor at many positions on the nanoantenna, not merely at its most sensitive region. Also, most plasmon resonance sensors employ surface binding to bind the analyte molecule to the hotspot of the antenna, and accordingly the sensing area saturates very quickly and cannot be reused, thus limiting throughput. Hence, a technique that would be able to deliver single molecules to a hotspot, position them there, as well as eject them from the spot again, would greatly enhance the sensing performance of plasmonic sensors.

A solid-state nanopore is a biosensor that enables single biomolecules to be driven through a nanometer-sized aperture in a free-standing membrane. Acting as a gateway between two electrically biased reservoirs, the nanopore is at the focus of a DC electric field that delivers and translocates charged biomolecules such as DNA or proteins across the membrane [11]. The nanopore simultaneously can be used as a detector, as the passage of the molecules through the pore can be measured through a temporary blockade of the ionic current that is running through the pore by the same electric bias voltage. Although the ionic-current-based nanopore sensing has been employed for single-molecule analysis with considerable success [12, 13], in particular for DNA and protein sensing, the current-based read-out has its own limitations. An optical read-out would be beneficial for nanopore sensing [14–18], as it could be employed at large measurement bandwidth, it could be operated irrespective of the chosen buffer conditions, and it does hold excellent potential for high sensor integration densities.

Here we demonstrate the high-throughput and label-free plasmonic-resonance sensing of individual DNA molecules by integrating a nanopore with a plasmonic nanoantenna. The nanopore serves as an active element that electrophoretically drives biomolecules into the nanopore, thus forcing them exactly into the hotspot of the plasmonic sensor. We use top-down fabricated plasmonic nanostructures with sub-10-nm gaps to create highly localized and enhanced electromagnetic field hotspots that are excited by single-wavelength continuous-wave (CW) laser illumination of the nanoantenna. We show that the translocation of a single unlabeled DNA molecule through the nanopore in the gap can be monitored from a transient intensity change of

the light that is elastically backscattered from the antenna (Fig. 5.1A). We demonstrate that the optical signal originates from a shift in the resonance of the plasmonic antenna and show that there is an excellent correlation between the backscattered signals from the antenna and the ionic current signals as DNA molecules traverse the nanopore. By integrating a nanopore with a plasmonic nanoantenna, single molecules can thus be actively transported toward the sensor, be precisely positioned at will into the hotspot, and subsequently be read out optically in a label-free manner.

## 5.2. RESULTS

### 5.2.1. PLASMONIC NANOPORE DEVICES FOR LABEL-FREE SINGLE MOLECULE SENSING

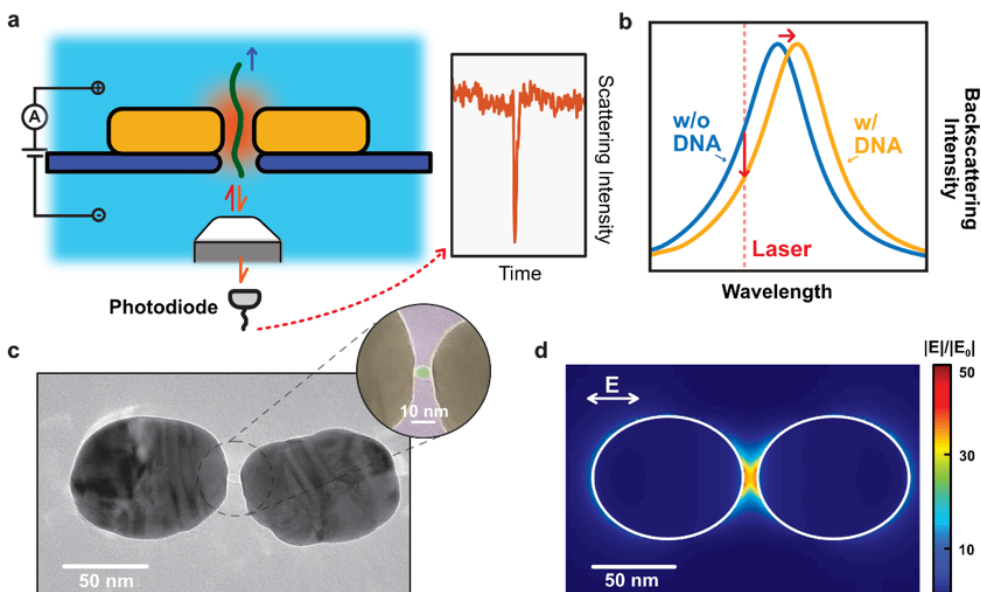


**Figure 5.1: Plasmonic nanopores for single molecule optical sensing.** (A) Schematic side-view illustration of a DNA molecule that is electrophoretically driven through a plasmonic nanopore and detected by optical backscattering from the plasmonic antenna. (B) Illustration of the sensing principle. The temporary presence of the DNA in the hotspot region of the plasmonic antenna induces a shift of the resonance wavelength of the antenna, hence decreasing the scattering intensity that is detected at the excitation laser wavelength. (C) Typical TEM image of the plasmonic nanopore pore devices used in our experiments. The plasmonic nanopore consists of a gold dimer antenna with a  $\sim 5$  nm nanopore at the gap center. The inset shows a false colored TEM image of a zoom of the nanogap region, highlighting the nanopore. (D) Simulated electromagnetic field distribution of the plasmonic nanopore in longitudinal excitation (i.e., with a polarization of the  $E$  along the long axis of the structure, cf. image) with a wavelength of 785 nm, as used in our experiments. The simulation shows the extremely enhanced and confined electromagnetic field within the gap of the dimer antenna, which is required for label-free optical sensing of single molecules.

The principle for optical sensing with plasmonic nanopores relies on a refractive index change that is induced as an analyte molecule enters the hotspot of the plasmonic nanoantenna, i.e., the region where the electromagnetic field is most strongly

localized. The DNA translocation will induce a redshift of the plasmon resonance of the entire nanostructure, that can be observed through monitoring the backscattered light intensity from the antenna (Fig. 5.1B). This shift can either be detected through tracking the plasmon resonance peak of the antenna [5], which is inevitably slow (tens of milliseconds), or by monitoring the scattered light intensity at a fixed excitation wavelength, which can be done at microsecond speeds. Note that, in the latter case, which is clearly advantageous for high-speed readouts, the presence of a biomolecule in the hotspot will produce either an increase in intensity (if the excitation wavelength is shorter than the peak of the plasmon resonance, Fig. 5.1B) or a decrease (if the excitation wavelength is longer than the plasmon resonance peak). We adopted this detection principle by light excitation with a CW laser at 785 nm and collecting the elastically backscattered light from the plasmonic nanostructure with a balanced photodiode detector, which thus allows for fast monitoring of the hotspot region. Details on the experimental setup can be found in the SI Section 5.5.1 and Fig. S5.5.

Our plasmonic nanopore devices are fabricated using a top-down approach based on two-step electron-beam lithography (EBL) to create an array of plasmonic nanoantennas combined with subsequent electron-beam sculpting to create a nanopore in the feed gap of a single antenna [19]. Fig. 5.1C shows a TEM image of a typical plasmonic nanopore used in our experiments. Each nanoantenna consists of two elongated gold nanodiscs, positioned on a 20 nm thin free-standing silicon-nitride membrane, each with a 90 nm length and a 70 nm width, that are facing tip-to-tip and are separated by a  $\sim 8$  nm gap. A  $\sim 5$  nm diameter nanopore is drilled through the SiN membrane in the center of the nanogap (see inset Fig. 5.1C). Details of the device fabrication can be found in Methods section and more TEM images of example devices can be found in SI Fig. S5.6.

If the two elongated nanodiscs are separated by only a few-nanometer-sized gap, they do generate an extremely enhanced EM field when the gap-mode plasmon resonance is excited. We used Finite-Difference Time-Domain (FDTD) simulations to estimate the strength of the field enhancement as well as the spatial localization of the EM field in the nanostructure. Fig. 5.1D shows the resulting simulated normalized electric field distribution for a nanostructure of two  $90 \times 70 \times 30$  nm (length  $\times$  width  $\times$  height) gold cylindroids with an 8 nm gap that is excited in longitudinal (i.e. along the longest direction of the nanostructure, see Fig. 5.1A) polarization of the illumination light at 785 nm. The result shows that the magnitude of the electric field in the nanogap is strongly enhanced, over 50 times, and closely is localized to the nanometer-sized gap region. SI Section 5.5.5 shows simulation results under transverse (i.e. along the shortest direction of the nanostructure) polarization, where no field enhancement occurs in the gap. Details of the FDTD simulations are provided in Section 5.4.

Before performing the single-molecule experiments, we characterize the devices and select a fitting nanoantenna for measurements. During the fabrication, we make an array of the nanoantennas with slightly different gap sizes, from which we chose one structure that is deemed most suitable to our experimental requirements, in which we drill a nanopore in its gap by use of a TEM. The device is then assembled as a separator between two compartments of a custom-made flow cell that are filled with electrolyte (2M LiCl buffered to pH 8 with tris-EDTA buffer), leaving the nanopore as the only

connection between the two reservoirs. This flow cell is mounted on a piezo stage on an optical detection setup with an 60x 1.2NA objective (see SI Section 5.5.1), and the membrane is scanned with a 100  $\mu\text{W}$  longitudinally polarized 785 nm laser beam that is focused to a  $\sim 0.5 \mu\text{m}$  spot. During scanning, both the backscattered light intensity and the ionic current are simultaneously recorded at each position. Fig. 5.2 shows a typical back-scattering and corresponding ionic-current map resulting from such a scan. The scattering map (Fig. 5.2A) shows an array of dots, where several antennas in the array scatter the focused laser beam significantly differently than the background (Fig. 5.2C and SI Section 5.5.3). The ionic current map (Fig. 5.2B) invariably shows only a single current maximum that is produced by local heating of the nanoantenna at the nanopore location [20]. The heating from plasmonic nanostructures locally creates a temperature increase [21], and an associated increase in current will only be observed if the excited nanoantenna contains a nanopore. In this fashion, the plasmonic structure with a nanopore can easily be identified from the array and get aligned to the laser.

The typical structures we choose for these experiments are aimed to have a gap-mode resonance wavelength close to, but slightly longer than, the illumination laser wavelength (785 nm), see simulation results in SI Section 5.5.3. Indeed, as illustrated by the scattering map of Fig. 5.2, the antenna containing the nanopore has an excellent (but not the highest) backscattering baseline signal indicating that the antenna has a plasmon resonance close to the excitation wavelength. Moreover, excitation close to resonance will lead to significant absorption and heat generation. Indeed, a substantial temperature increase of about 40°C [21, 22] can be estimated from the ionic-current increase of 50% at a mere 100  $\mu\text{W}$  of excitation power in Fig. 5.2B. Such a temperature elevation is acceptable for these experiments with double stranded DNA. If desired, one may use alternative designs for plasmonic nanodevices that yield a much reduced temperature increase [23] and that recently were also implemented for optical transmission detection of DNA translocation [18]. Fig. 5.2D illustrates the strong difference in scattering strength if a transverse polarization is used. The scattering signal is weak from all antennas, as expected since the transverse mode does not excite the gap mode and has a peak resonance far off from the excitation wavelength. The observations clearly support the fact that backscattering in the longitudinal polarization is dominated by the gap-mode resonance excitation.

### 5.2.2. LABEL-FREE OPTICAL DETECTION OF DNA MOLECULE TRANSLOCATIONS

Next, we show the label-free detection of DNA molecules as they translocate through the nanopores. After locating and aligning the plasmonic nanopore to the focused laser spot, 10 kbp dsDNA molecules are flushed into the *cis*-side of the membrane (the bare SiN side without the gold nanostructures). Subsequently a bias voltage (300 mV) is applied across the membrane while the laser excites the plasmonic nanostructure, and both the ionic current and the back-scattering optical intensity are recorded simultaneously (details of the single-molecule experiments are described in Methods). Typical trajectories of both channels are shown in Fig. 5.3A. Numerous concurrent transients can be clearly discerned in both the ionic current and backscattered light intensity. These signals can be immediately recognized as single DNA molecules passing freely both the

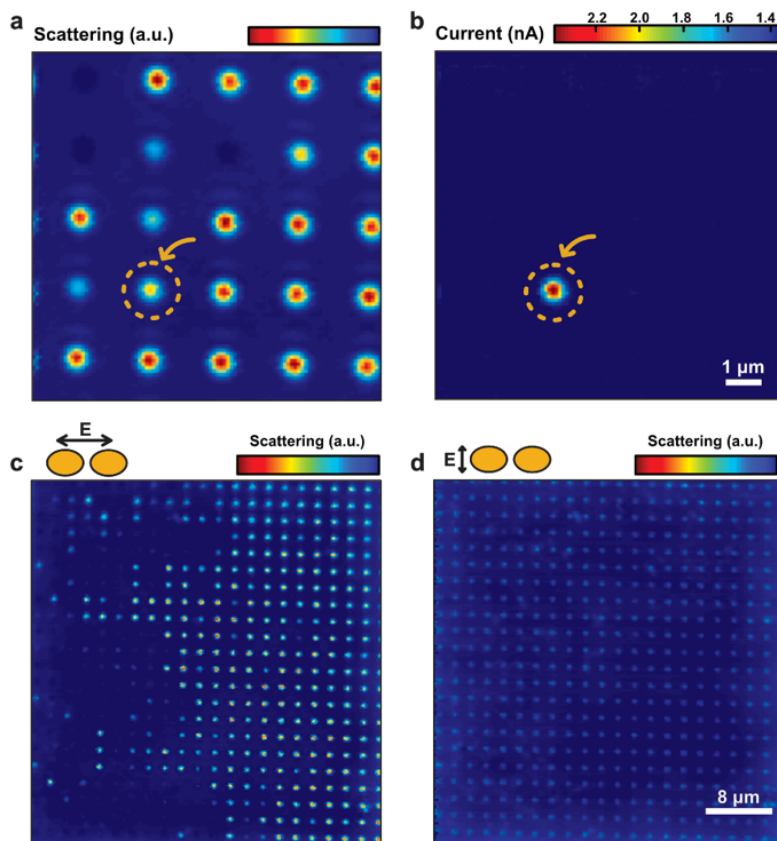


**Figure 5.2: Backscattering and ionic-current mapping from a plasmonic antenna array.** (A) Backscattering intensity map from scanning a focused laser with longitudinal polarization across the plasmonic antenna array. Each of the nanoantennas in this image has a slightly different gap size, leading to varying scattering intensities. The one structure that had a nanopore drilled in the gap is marked with the yellow arrow/dashed circle. (B) Ionic current map to the scan corresponding to panel (A). A clear current increase can be observed when the longitudinally polarized laser hit the plasmonic structure with a nanopore in the gap. The structure with a nanopore drilled in the gap is marked with the yellow arrow/ dashed circle. (C) and (D), Backscattering intensities across an array of plasmonic nanoantennas with different gap sizes under longitudinal (C) and transverse (D) polarizations, respectively. Only under longitudinal polarization, we observe backscattering that is strong and sensitive to the gap size of the antenna, while the scattering in transverse excitation is weak and almost invariant to the gap size of the nanostructures.

optical and electrical detection volumes of the plasmonic nanopore. We observe the archetypical electrical transients that are exemplary for DNA translocations, with signals exhibiting excellent signal-to-noise characteristics due to the small pore (5 nm) and the large electrolyte concentration used (2M LiCl). More importantly, the signals in the optical channel also display good signal-to-noise ratio characteristics and they correlate excellently with the signals from the ionic current channel, confirming that these optical signals derive from single-DNA translocation events. This demonstrates that, remarkably, our plasmonic nanoantenna can be used for high-throughput label-free

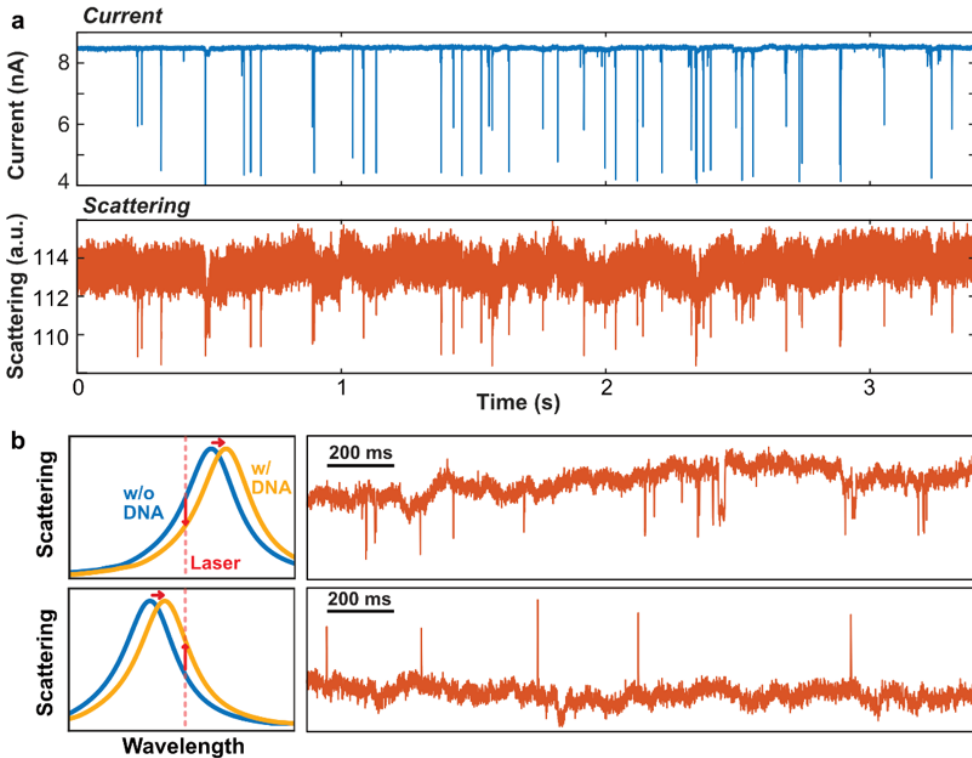


**Figure 5.3: Optical detection of single DNA translocations through plasmonic nanopores.** (A) Example of corresponding ionic-current (blue) and backscattering (orange) time traces during a DNA translocation experiment. Single-molecule events appear as blockades in both the ionic current, where the ion flow is blocked by DNA, and the optical signals, where transient decreases in the backscattering intensity of nanoantenna are induced by DNA molecules that traverse the hotspot region. Traces are filtered with a 5 kHz low-pass filter. (B) Examples of single-molecule optical events that, remarkably, display different signal polarities. The top and bottom traces are obtained for two different devices with a different plasmonic resonance peak wavelength. The schematics in the left panel illustrate the mechanism that explains the decrease or increase of the scattering intensity induced by single DNA molecules. As the DNA molecules always induce a red shift of the antenna's resonance wavelength, a decrease will be observed if the resonance wavelength is longer than the 785 nm excitation laser wavelength, while an increase will be observed if the resonance wavelength is shorter than the excitation wavelength

optical detection of single DNA molecules that are electrically driven through the hotspot.

The assertion that the optical signals arise from a shift of the plasmon resonance is corroborated by Fig. 5.3B, where the backscattering signals for DNA translocations are displayed for two different devices with slightly different geometries. The top trace of Fig. 5.3B shows that the scattering intensity reduces during DNA translocation events, whereas the bottom trace, from a different device, shows increases in the scattering intensity for translocation events. These different signal polarities are caused by the different plasmon resonance peak wavelength in both devices. Since the refractive index of DNA is larger than water at optical frequencies (1.8 - 2.5 [24] vs 1.3), insertion of a

DNA molecule into the hotspot will induce a redshift of the plasmon resonance of the gold antenna [25]. Subsequently, as illustrated on the left of Fig. 5.3, the backscattering intensity reduces when the resonance peak wavelength is longer than the wavelength of excitation, but increases when it is shorter. The observation of these different signal polarities serves as a clear hallmark of the plasmonic-resonance origin of the DNA signals.

### 5.2.3. MICROSCOPIC INSIGHT OF THE DNA TRANSLOCATION THROUGH A PLASMONIC NANOPORE

Figure 5.4A shows a closer inspection of the typical signals from both the optical and electrical channels. The ionic current signals (blue traces) display the characteristic levels that are typical for DNA translocations: before translocation, an open pore current runs through the pore, which is subsequently partially reduced when a molecule is inserted into the nanopore. The DNA molecule can traverse the pore in a linear head-to-tail fashion (where it enters the pore with one of its ends and only one double strand of DNA resides in the nanopore during the translocation), or in a folded mode [26] (where it enters the pore in a folded fashion with at first two double strands of DNA residing in the nanopore) that is distinctive for electrophoretically driven DNA translocations through a solid-state nanopore. Surprisingly, however, in our plasmonic devices, we observe that the current after translocation does not immediately recover to the baseline value, but remains at a very shallow current blockade level that lasts for a few milliseconds. This signal strength is too shallow to be attributed to DNA that is inserted in the nanopore. Instead, it indicates that the DNA remains near the nanopore without inserting exactly in it, i.e., it suggests that part of the nearby DNA molecule contributes to an additional access resistance that slightly lowers the current [27]. The simultaneously acquired signals in the optical channel further illuminate these translocation events (Fig. 5.4A, orange traces). Initially a strong reduction of the backscattered light intensity from the baseline can be observed, which correlates well with the translocation of the DNA molecule through the nanopore, albeit that the optical signal does not seem to distinguish strongly between linear and folded translocation modes. Remarkably, the signal strength after DNA translocation through the pore reduces only slightly (if at all), indicating that the DNA molecule remains present in the hotspot region. The duration of the extended signal matches well with the shallow level observed in the current channel, implying a close proximity of the DNA molecule near the nanopore while it resides in the hotspot.

The data lead to a physical picture of the translocation process as sketched in Fig. 5.4B. Once a DNA molecule diffuses into the capture region of the nanopore, the negatively charged molecule is driven towards the nanopore prior to translocation. Next, the single DNA molecule enters the nanopore in either a linear or folded fashion, blocking part of the ion flow and producing a distinctive blockade current signal. Directly after the DNA molecule traverses through the 20-nm short nanopore, it enters the hotspot region of the gold nanoantenna, incurring a clear change in the scattered light intensity. The DNA polymer continues to be reeled through the pore and eventually exits the nanopore, but at that point it remains present in the optical hotspot (as well in the electrical access region) by virtue of the interactions between the DNA molecule

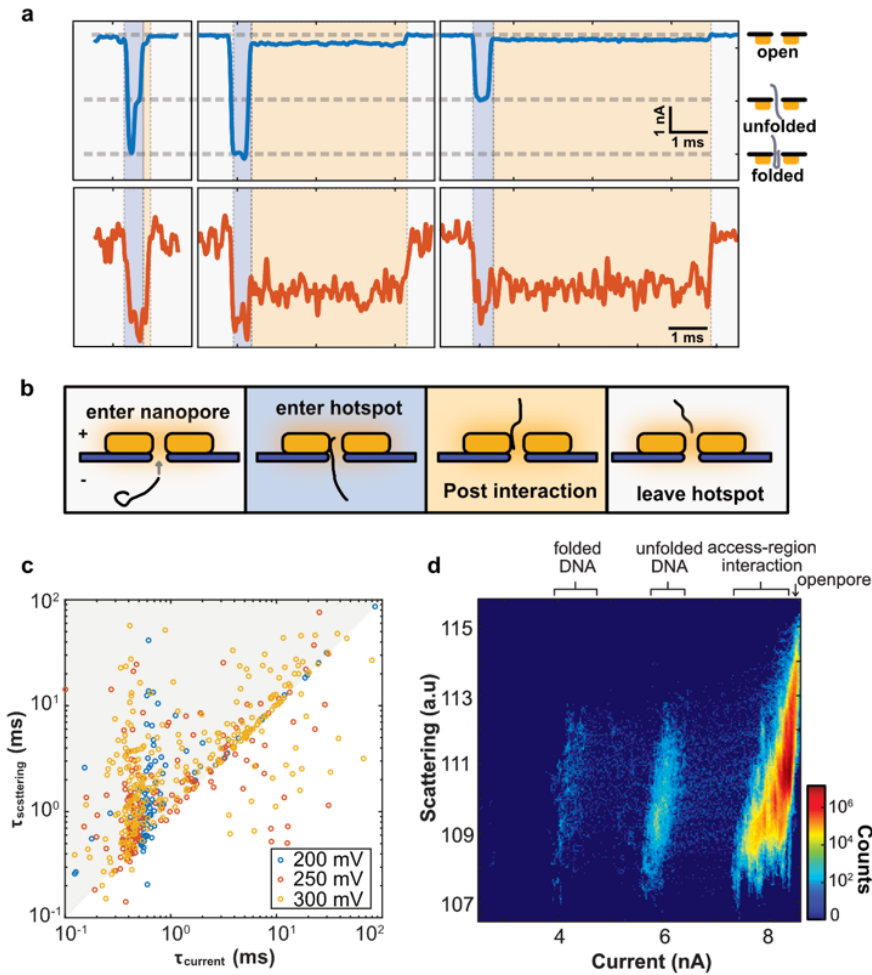


**Figure 5.4: Comparison of optical and current-blockade single-molecule signals.** (A) Examples of single-molecule DNA translocations. Top traces (blue) are ionic current signals; bottom traces (orange) are optical backscattering signals. The ionic current reports on different folding conformations during translocation (cf. insets on the right). Interestingly, a clear post-translocation optical signal and shallow current blockade signal can be observed, indicating the presence of the molecule in the hotspot of the plasmonic antenna on the exit access region of the nanopore. (B) Cartoons for illustrating the different phases of DNA translocation of plasmonic nanopores (background colors correspond to panel (A)). A DNA molecule enters the nanopore, inducing a blockade of the ionic current. It then moves virtually instantaneously into the hotspot, resulting in optical detection of the molecule. After the DNA molecule has translocated, post-translocation DNA-gold interactions maintain an extended presence of the DNA molecule in the hotspot that is located in the exit access region of the nanopore, leading to a pronounced optical and weak ionic current signal. Finally, the molecule is unloaded from the nanopore. (C) Comparison of the signal duration  $\tau$  (the time taken between two baseline crossings) of the optical and electrical signals under 200 mV, 250 mV and 300 mV bias voltages. (D) Comparison of ionic current and scattering intensity for all data points at 300 mV bias. Events with anomalously long (integral of current signal  $>20$  nA $\cdot$ ms) sticking of the DNA are ruled out from this analysis.

and the surface of gold nanoantenna. Finally, the DNA molecule also escapes from this region.

This picture is further supported by an in-depth analysis of the signals. Fig. 5.4C provides a log-log scatter plot that compares the signals durations  $\tau$  from both channels for all translocation events at different driving voltages. The events along the diagonal have an identical optical and electrical dwell time (as in the examples in Fig. 5.4A). A large number of events is however observed above the diagonal in the diagram, representing events with a longer signal duration in the optical channel than in the electrical channel. Since the post-translocation interaction cannot always be discerned in the ionic current, as the blockade is shallow and its strength depends on the position of the molecule in the electrical access region [27], optical signals typically last longer than the associated electrical ones. The signal strengths of both the electrical and optical channels is compared in Fig. 5.4D. This all-points heatmap of the current and scattering intensities for all translocation events shows a strong clustering of data points around the current blockade levels corresponding to the folded and linear translocation events (near 6 and 4 nA, respectively), consistent with the ionic current examples shown in Fig. 5.4A. However, most of the data points cluster at the access-region contribution to the electrical signals (near 8 nA), since the molecules typically spend a much longer time in the hotspot region than in the nanopore (see SI, Fig. S5.12). In the optical channel, no tight clustering is observed, which can, as discussed in SI Section 5.5.4 be attributed to inhomogeneities in the EM field distribution along the gold nanoantenna gap.

### 5.3. DISCUSSION

Method	Time resolution	Waiting time	Max # of events	Ref
<b>Photothermal microscopy</b>	100 ms (integration time)	Tens to hundreds of seconds (100 nM protein)	<10 (streptavidin)	[5]
<b>Dark-field spectroscopy</b>	24 ms (exposure time + cycle time)	50 s (average, 1.25 $\mu\text{g}/\text{mL}$ fibronectin)	~10-20 (fibronectin)	[4]
<b>Scattering from nanorods</b>	100 ms (integration time)	~10-100 s (25 nM - 2.5 nM antibody)	~10 (antibody)	[6]
<b>Plasmonic nanopores</b>	<200 $\mu\text{s}$ (5 kHz low pass filter, higher cutoff possible)	~100 ms (1 $\mu\text{g}/\text{ml}$ dsDNA, capture rate ~10/s, multiplexing is possible)	>500 (Typical dsDNA experiments, no binding site is consumed)	This work

**Table 5.1:** Comparison of plasmon resonance biosensing strategies

Our plasmonic nanopores significantly outperform previous plasmonic biosensors in a number of aspects. Table 5.1 provides a detailed comparison between our results and those from pioneering methods such as photothermal microscopy, dark-field spectroscopy, and scattering from plasmonic nanorods. The integration of nanopore

in the hotspot provides the plasmonic nanostructure with the capability of actively attracting biomolecules into the sensing region as well as releasing the molecules after acquisition of the sensor signals. This provides clear advantages on time resolution, waiting time, and maximum number of events for each nanoantenna over these previously reported plasmonic single-molecule sensing approaches. The limited signal-to-noise ratio of the previous methods typically requires long integration time for obtaining distinguishable signals. In our method, the detection bandwidth can easily be set to 5 kHz or higher, an improvement of more than a factor of 500, while further improvements can be achieved by optimizing the nanoantenna geometry. In our nanopore approach, molecules are actively captured and delivered into the sensing region, which reduces the waiting time between events from hundreds of seconds down to the millisecond regime, e.g. again an improvement of 3 orders of magnitude from conventional techniques. Finally, previous methods can at most detect  $\sim 10$  molecules per antenna because of a saturation of the sensing region. In our plasmonic nanopore approach, the applied electrophoretic force actively releases the analyzed molecules from the sensing region, and hence the hotspot of the nanoantenna is not consumed, removing any limit to the maximum number of molecules that can be detected by a single nanoantenna.

In conclusion, we have introduced a new method to optically detect single DNA molecules in solution. Plasmonic nanoantennas are used to create a well-defined and highly EM field-enhanced plasmonic hotspot into which molecules are precisely delivered via a solid-state nanopore. The backscattered light from the antenna enables to detect, in a label-free manner, the presence of single DNA molecules in the hotspot. The nanopore in the plasmonic gap actively captures analyte molecules from the bulk, and ejects them after signal acquisition, so that the most sensitive hotspot region can be reused for probing next molecules. The plasmonic nanopores provide orders of magnitude improvements on the time resolution, waiting time, and maximum number of events over previously reported plasmon-resonance-based single-molecule sensing methods. Improved antenna design and lower-noise optical detectors can yield yet higher sensitivities and detection bandwidth than reported in these first proof-of-principle experiments. We anticipate plentiful applications and extensions of the technique. For example, additional selectivity can be provided to the sensor through modification of the gold surface, akin to previous plasmonic resonance sensing schemes. Moreover, the plasmonic-resonance nanopore sensing approach is easily applicable to other biomolecules such as proteins, as the refractive index sensing mechanism will apply generally to any analyte. Finally, these plasmonic nanopores can be fabricated in massively parallel arrays, where each nanoantenna is simultaneously read out, which will allow the development of high-throughput single-molecule optical assays for sensing a variety of analytes.

## 5.4. EXPERIMENTAL METHODS

### 5.4.1. FABRICATION OF PLASMONIC NANOPORES

The plasmonic nanopore devices were fabricated using an electron-beam-lithography (EBL) based top-down approach, as we reported before [2]. In brief, an array of

plasmonic bowtie nanoantennas, each consisting of two elongated nanodiscs with a length of 90 nm and width of 70 nm, was defined using EBL in two steps. The pattern from each step contains on dimer half, such that alignment of the two patterns will provide a variety of gap spacings between adjacent dimers. For each EBL step, ~100 nm PMMA resist layer (950K MW, 3% in anisole) was spin coated on the SiN membranes and then exposed using a Raith EBPG 5200 EBL system, at an accelerating voltage of 100 kV, with pressure below  $5 \cdot 10^{-7}$  mbar, and with e-beam doses ranging from 2000 to 2500  $\mu\text{Ccm}^{-2}$ . The EBL-defined patterns were developed in methyl isobutyl ketone (MIBK) and isopropanol (IPA) mixture (a volume ratio 1:3, MIBK: IPA) for 60 s. Then, a 30 nm gold layer with 1 nm titanium as adhesion layer were deposited using electron beam evaporation and the lift-off was performed by immersing the samples in 80°C PRS-3000 solution overnight. The nanodiscs arrays defined in the first ebeam step were manually aligned to the center of the freestanding membranes, and the second-step patterns were aligned by an automatic mark search routine on markers defined in the first step. Finally, a single nanopore was drilled using a TEM (FEI Tecnai 200S, 200 kV) in the gap of a single nanoantenna on each freestanding membrane.

#### 5.4.2. FDTD SIMULATIONS

FDTD Solutions (Lumerical Solutions, Inc., Canada) was used to model the electric field distribution around the plasmonic nanopore. The elongated gold discs dimer was modeled as two 70x90x30 nm (width x length x thickness) cylindroids separated by a 8 nm gap on a 20 nm thin SiN membrane (refractive index, RI = 2) with 1 nm Ti layer under the gold. A 6 nm in diameter nanopore through the SiNx membrane is placed at the gap center. The RI of the surrounding medium was set to 1.33. Symmetry on the boundaries was used to reduce the computational time. The modeled antenna was excited by a total-field scattered-field source propagating along the axis perpendicular to the membrane. Figures S5.8, S5.9, and S5.10 show the FDTD simulation results.

## 5.5. SUPPORTING INFORMATION

### 5.5.1. EXPERIMENTAL SETUP

The simultaneous scattering light intensity and current detection was performed using a custom-built setup. A schematic of the setup is shown in Fig. S5.5. The 785 nm polarized laser beam was expanded and passed through a non-polarizing beam splitter where 50% of the incident light was focused into the flow cell with a water-immersion objective (60x, 1.2NA, Nikon), while the other 50% of the laser was partly coupled into a fiber and sent to one of the input channels of a balanced photodetector. The backscattered light from the plasmonic nanopore structures was collected through the same objective and then sent to the complementary input channel of the photodetector. The difference between the photocurrents in the two photodiodes was amplified and sent into a DAQ board (USB-6251, National Instruments). A white-light LED is used to illuminate the sample during the sample alignment, and a camera was employed to acquire video images for sample alignment.

The DC voltage was applied by a patch clamp amplifier (Axopatch 200B, Molecular Devices) via a pair of Ag/AgCl electrodes. The ionic current is acquired, amplified, send to the the DAC board and read-out together with the amplified photocurrent using a synchronous call. The entire setup is operated with a custom-designed LabVIEW program and the digitized signals of both channels were recorded by a computer.

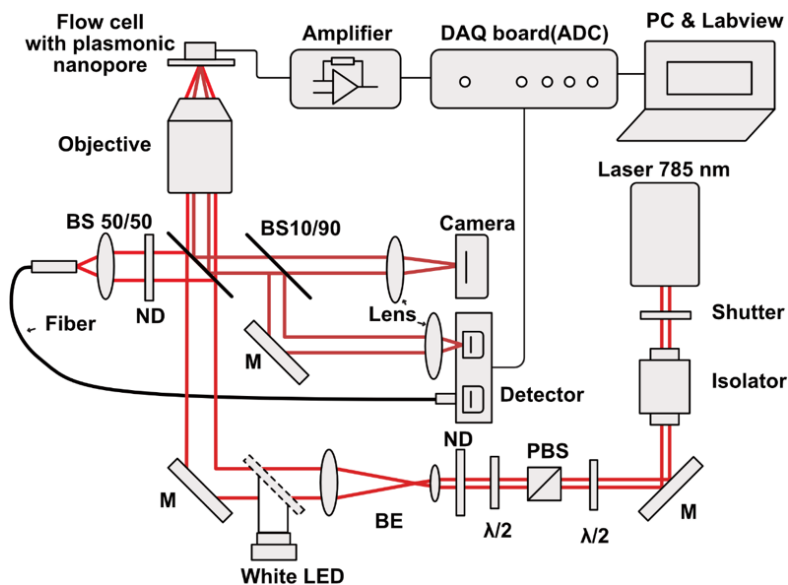


**Figure S5.5: Experimental setup for label-free single molecule plasmonic nanopore sensing.** M: mirror; BS: non-polarizing beam splitter; PBS: polarizing beam splitter; ND: neutral density filter; BE: beam expander.

### 5.5.2. ADDITIONAL EXAMPLES OF PLASMONIC NANOPORE DEVICES USED IN THE EXPERIMENTS

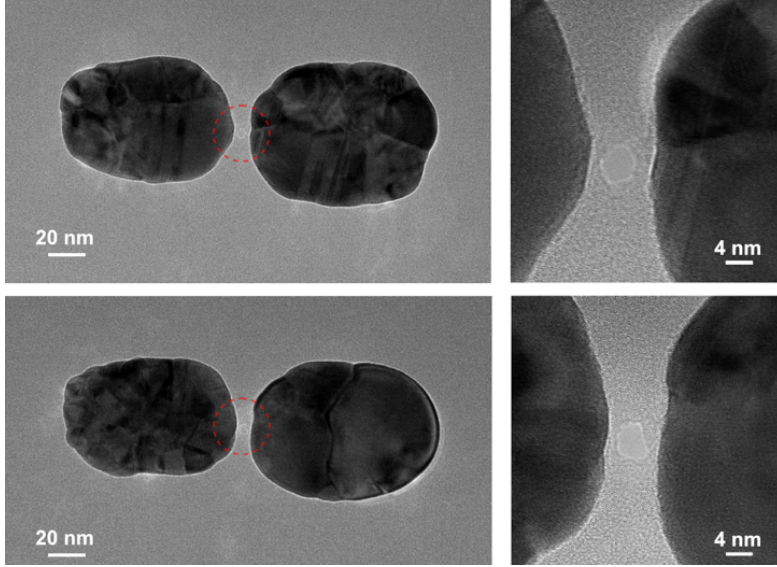


**Figure S5.6: Additional examples of plasmonic nanopore devices used in the experiments.** Right panels are close-up TEM images of the corresponding structures in the left panels.

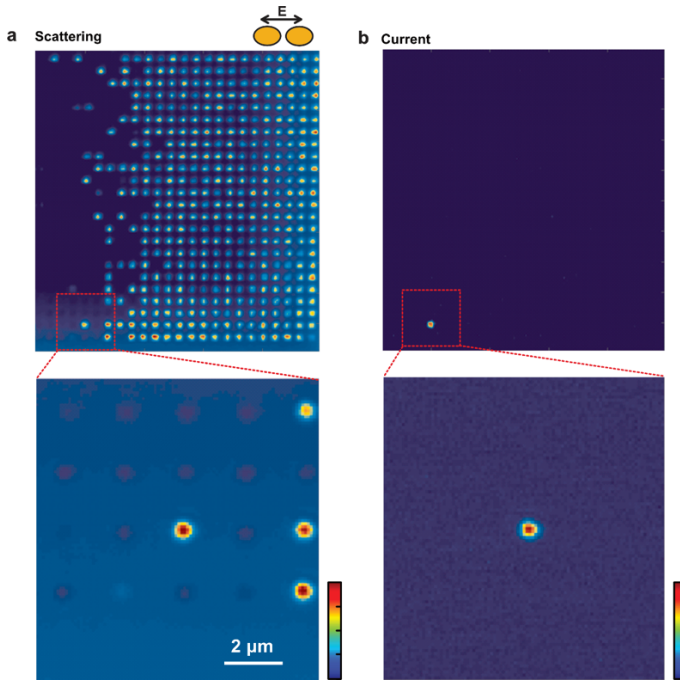
### 5.5.3. BACKSCATTERING MAPPING OF DIMER ANTENNA ARRAY

Figure 5.2 (Main text) and Fig. S5.7 show backscattering maps of our plasmonic antenna arrays excited with a laser. Within the array, the dimer antennas have slightly different gap sizes between two particles, and accordingly show different backscattering intensities under longitudinal polarized excitation. Some of them even show lower light signal than the background (the reflection of the membrane). Here we briefly discuss the mechanism of such intensity variations.

In our experiments, the backscattering light is collected by the same objective used for focusing the incident laser light. The detected light intensity reaching the photodiode  $I_d$  can be written as follows [28]:

$$I_d = |E_r + E_s|^2 = E_i^2 (r^2 + |s|^2 - 2r|s|\cos(\theta)), \quad (\text{S5.1})$$

where  $E_r$ ,  $E_s$ , and  $E_i$  are the reference field (arising mainly from the reflection from the membrane surface), the scattering field (scattered field from the particle of interest), and the incident field, respectively,  $r$  is a real reference amplitude,  $s$  is a complex scattering amplitude, and  $\theta$  is the phase difference between these two fields at a large distance. This phase difference contains contributions from the path length difference between the two fields, the Gouy shift, and phase shift due to the polarizability of the antennas. The first term on the right,  $E_i^2 r^2$ , in our case, is chiefly the specularly reflected light from the SiN membrane, the second term,  $E_i^2 s^2$ , is the pure scattering intensity from



**Figure S5.7:** Additional example of scattering (A) and ionic current (B) mappings over a large area on the free-standing membrane containing an array of plasmonic nanoantennas.

the nanoantenna, and the third term,  $2r|s|\cos(\theta)$ , is the interferometric scattering term that expresses the interference of the reflected and the scattered light. The scattering amplitude,  $s$ , is the quantity of interest and is strongly dependent on the material, size, and geometry of the nanoparticle.

From our FDTD simulation results, shown in Fig. S5.8, we learn that the magnitude of scattering cross section of dimer antennas under longitudinal excitation at our laser wavelength varies with gap size and changes drastically if the structure is merged. During the EBL fabrication, we fabricate an array of dimers with various gap sizes on each free-standing membrane, including some without gap (i.e. two merged particles). Therefore, the array contains a variety of nanostructures with strongly varying scattering cross-sections.

The scattering maps can thus be interpreted as follows. The peaks in the maps correspond to excitation of plasmonic nanostructures with a gap. For these structures the backscattering cross-sections are large and the backscattered light intensities will be dominated by the pure scattering term (middle term Eqn. S5.1). The exact intensities of these peaks vary somewhat because of the different gaps the nanostructures in the array possess. The areas in between the nanostructures will just show a small background scattering intensity from the light reflected weakly at the membrane (first term Eqn. S5.1). The dips, that may look puzzling at first, can be explained by interferometric scattering (last term Eqn. S5.1). When the scattering is weak, as is the

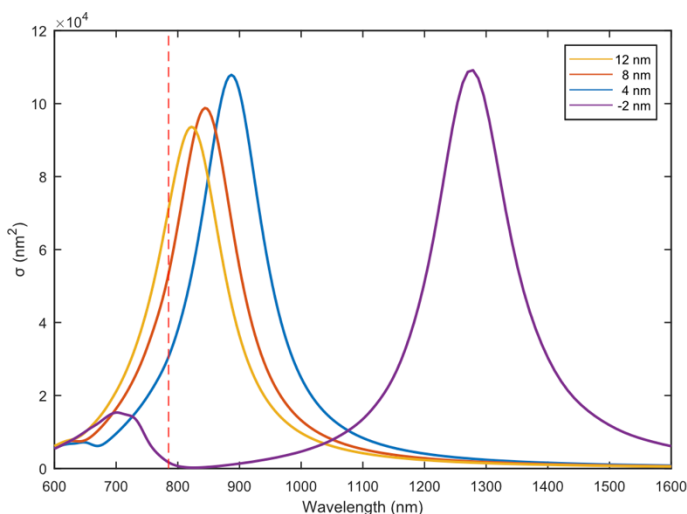


**Figure S5.8: Simulated scattering cross section versus wavelength for plasmonic dimer antennas (disks of 90 by 70 nm) with various gap sizes under longitudinal excitation.** For small variations in the gap size, the resonance peaks shift moderately, until the dimers merge when a dramatic shift occurs. At the wavelength of excitation (dashed line), the scattering will be almost minimal in that case.

5

case for antennas without gaps, the pure scattering term in Eqn. S5.1 will negligible, but the interferometric term might not be. Depending on the phase difference between reference and scattering fields, the backscattered intensity can either show a reduction or increase from the background intensity. In our case, the phase difference between the two beams is such that the scattered and reference beam are in antiphase and thus we observe dips when the merged structures are illuminated.

#### 5.5.4. SPATIAL FIELD DISTRIBUTION OF THE ELECTROMAGNETIC HOTSPOT IN THE PLASMONIC GAPS

The scattering signals do not show consistent multiple levels originating from the different conformations of the DNA assumes during translocation. We attribute this to the inhomogeneity of the EM field distribution in the plasmonic gaps. To illustrate this, we plot the simulated normalized EM field intensity distribution under 785 nm excitation in the XZ cross section, along the longitudinal axis of the dimer, in Fig. S5.9. As the simulation result shows, the squared electric field strength in the gap shows a distinct spatial inhomogeneity. The squared field strength near to the gold surface appears to be more than 4 times stronger than the squared field strength in the center of the gap. Since the plasmon shift produced by biomolecules in the hotspots is proportional to the local squared electric field intensity integrated over the molecule volume [8, 25] molecules positioned at the surface of the sensor will produce stronger signals than molecules residing in the middle of the gap. As an advantage, such an extremely enhanced and confined EM field could in principle provide extraordinarily high spatial resolution [24] and could be used to determine substructure of biomolecules and biopolymers in future applications. For other applications where such confinement becomes limiting,

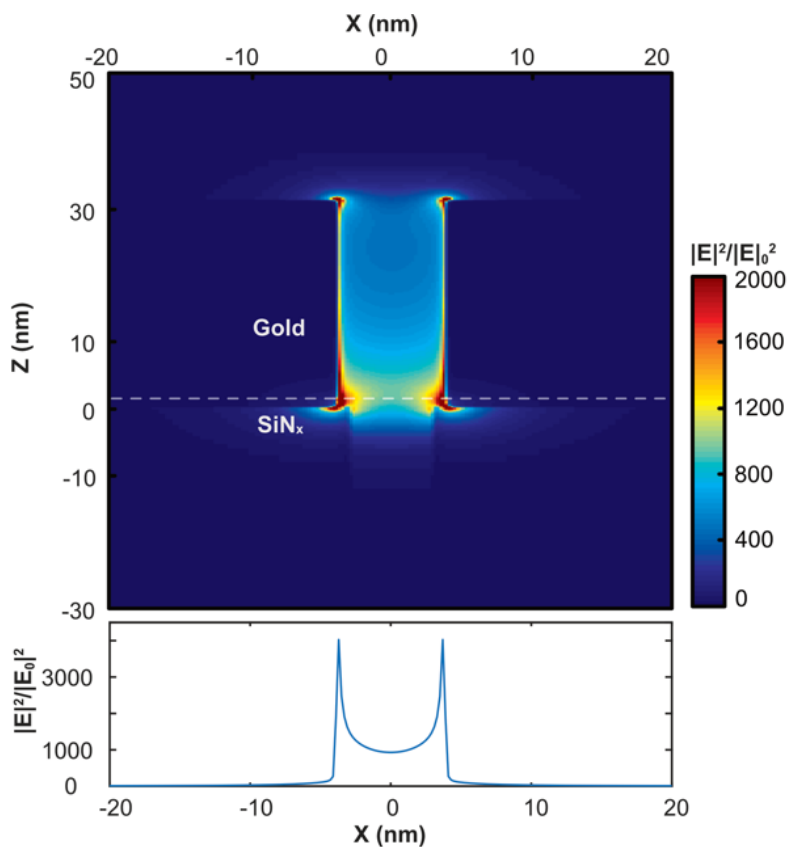


**Figure S5.9: The inhomogeneity of the optical field distribution in the gap of plasmonic antenna.** The upper panel shows an XZ cross section of the squared electric field strength at the plasmonic antenna along the longitudinal axis. The squared field strength shows an extremely enhanced field around the lower corner of the antenna and decays very quickly away from the gold surface to the center of the gap. The lower panel shows a profile of the squared field at 1 nm above the upper surface of the SiN<sub>x</sub> (dash line) demonstrating a 4 times difference in squared intensity  $|E|^2/|E_0|^2$  between the surface of the gold and the center of the gap.

it can be improved by changing the design of the plasmonic structures to create more homogeneous EM field.

### 5.5.5. SIMULATED ELECTROMAGNETIC FIELD AROUND THE PLASMONIC ANTENNA EXCITED WITH TRANSVERSE POLARIZED LIGHT

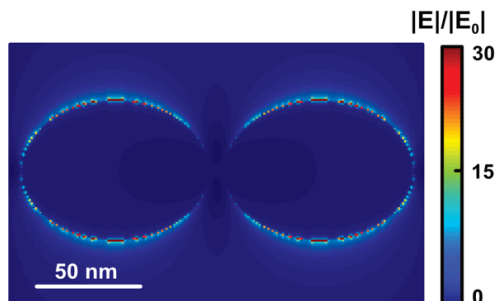


Figure S5.10: Simulated electromagnetic field around the plasmonic antenna excited with transverse polarized light. Note the absence of any increased field intensity in the gap

5

### 5.5.6. HEATING EFFECT ON PLASMONIC NANOPORES

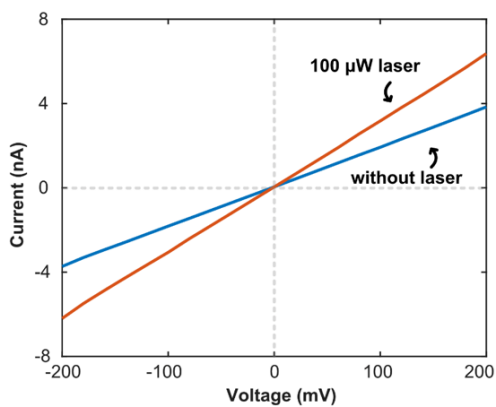
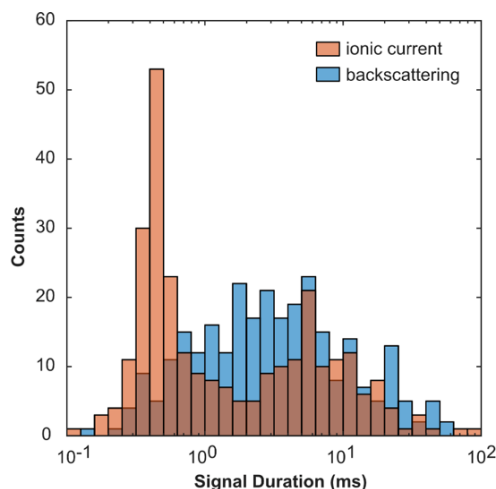


Figure S5.11: Heating effect on plasmonic nanopores. Typical IV curve of a plasmonic nanopore device with (orange) and without (blue) laser illumination (785 nm, 100  $\mu$ W, focused into a diffraction-limited spot).

### 5.5.7. COMPARISON OF THE SIGNAL DURATIONS OF CORRESPONDING IONIC CURRENT EVENTS AND BACKSCATTERING EVENTS



**Figure S5.12: Comparison of the signal durations of corresponding ionic current events (orange) and backscattering events (blue) under 300 mV bias.** Two peaks of ionic current events can be observed, which can be attributed to translocation where post-translocation interaction is (peak at longer durations) or is not (peak at shorter durations) detected from the access region current blockade. On the contrary, the optical scattering data show a single broad peak that signals the prolonged presence of DNA molecules in the hotspots.

## REFERENCES

- [1] K. A. Willets and R. P. Van Duyne, *Localized surface plasmon resonance spectroscopy and sensing*, *Annu. Rev. Phys. Chem.* **58**, 267 (2007).
- [2] H. Xin, B. Namgung, and L. P. Lee, *Nanoplasmonic optical antennas for life sciences and medicine*, *Nature Reviews Materials* (2018), 10.1038/s41578-018-0033-8.
- [3] K. M. Mayer and J. H. Hafner, *Localized surface plasmon resonance sensors*, *Chemical Reviews* **111**, 3828 (2011).
- [4] A. G. Brolo, *Plasmonics for future biosensors*, *Nature Photonics* **6**, 709 (2012).
- [5] I. Ament, J. Prasad, A. Henkel, S. Schmachtel, and C. Sönnichsen, *Single unlabeled protein detection on individual plasmonic nanoparticles*, *Nano Letters* **12**, 1092 (2012).
- [6] P. Zijlstra, P. M. Paulo, and M. Orrit, *Optical detection of single non-absorbing molecules using the surface plasmon resonance of a gold nanorod*, *Nature Nanotechnology* **7**, 379 (2012).
- [7] M. A. Beuwer, M. W. Prins, and P. Zijlstra, *Stochastic protein interactions monitored by hundreds of single-molecule plasmonic biosensors*, *Nano Letters* **15**, 3507 (2015).
- [8] A. B. Taylor and P. Zijlstra, *Single-molecule plasmon sensing: current status and*

- future prospects*, ACS Sensors **2**, 1103 (2017).
- [9] E. J. Blackie, E. C. Le Ru, and P. G. Etchegoin, *Single-molecule surface-enhanced raman spectroscopy of nonresonant molecules*, Journal of the American Chemical Society **131**, 14466 (2009).
- [10] E. C. Le Ru and P. G. Etchegoin, *Single-molecule surface-enhanced raman spectroscopy*, Annual Review of Physical Chemistry **63**, 65 (2012).
- [11] S. Van Dorp, U. F. Keyser, N. H. Dekker, C. Dekker, and S. G. Lemay, *Origin of the electrophoretic force on dna in solid-state nanopores*, Nature Physics **5**, 347 (2009).
- [12] K. Chen, M. Juhasz, F. Gularek, E. Weinhold, Y. Tian, U. F. Keyser, and N. A. Bell, *Ionic current-based mapping of short sequence motifs in single dna molecules using solid-state nanopores*, Nano Letters **17**, 5199 (2017).
- [13] P. Waduge, R. Hu, P. Bandarkar, H. Yamazaki, B. Cressiot, Q. Zhao, P. C. Whitford, and M. Wanunu, *Nanopore-based measurements of protein size, fluctuations, and conformational changes*, ACS Nano **11**, 5706 (2017).
- [14] O. N. Assad, T. Gilboa, J. Spitzberg, M. Juhasz, E. Weinhold, and A. Meller, *Light-enhancing plasmonic-nanopore biosensor for superior single-molecule detection*, Advanced Materials **29**, 1605442 (2017).
- [15] T. Gilboa and A. Meller, *Optical sensing and analyte manipulation in solid-state nanopores*, Analyst **140**, 4733 (2015).
- [16] A. Ivankin, R. Y. Henley, J. Larkin, S. Carson, M. L. Toscano, and M. Wanunu, *Label-free optical detection of biomolecular translocation through nanopore arrays*, ACS Nano **8**, 10774 (2014).
- [17] F. Pulizzi, *Building a better nanopore*, Nature Nanotechnology **11**, 105 (2016).
- [18] D. Verschueren, S. Pud, X. Shi, L. De Angelis, K. Kuipers, and C. Dekker, *Label-free optical detection of dna translocations through plasmonic nanopores, in preparation*.
- [19] X. Shi, D. Verschueren, S. Pud, and C. Dekker, *Integrating sub-3 nm plasmonic gaps into solid-state nanopores*, Small **14**, 1703307 (2018).
- [20] M. P. Jonsson and C. Dekker, *Plasmonic nanopore for electrical profiling of optical intensity landscapes*, Nano Letters **13**, 1029 (2013).
- [21] F. Nicoli, D. Verschueren, M. Klein, C. Dekker, and M. P. Jonsson, *Dna translocations through solid-state plasmonic nanopores*, Nano Letters **14**, 6917 (2014).
- [22] D. V. Verschueren, M. P. Jonsson, and C. Dekker, *Temperature dependence of dna translocations through solid-state nanopores*, Nanotechnology **26**, 234004 (2015).
- [23] M. Belkin, S.-H. Chao, M. P. Jonsson, C. Dekker, and A. Aksimentiev, *Plasmonic nanopores for trapping, controlling displacement, and sequencing of dna*, ACS Nano **9**, 10598 (2015).

- [24] R. Chikkaraddy, V. Turek, N. Kongsuwan, F. Benz, C. Carnegie, T. Van De Goor, B. de Nijs, A. Demetriadou, O. Hess, and U. F. Keyser, *Mapping nanoscale hotspots with single-molecule emitters assembled into plasmonic nanocavities using dna origami*, *Nano Letters* **18**, 405 (2017).
- [25] J. Yang, H. Giessen, and P. Lalanne, *Simple analytical expression for the peak-frequency shifts of plasmonic resonances for sensing*, *Nano Letters* **15**, 3439 (2015).
- [26] A. J. Storm, J. Chen, H. Zandbergen, and C. Dekker, *Translocation of double-strand dna through a silicon oxide nanopore*, *Physical Review E* **71**, 051903 (2005).
- [27] A. T. Carlsen, O. K. Zahid, J. Ruzicka, E. W. Taylor, and A. R. Hall, *Interpreting the conductance blockades of dna translocations through solid-state nanopores*, *Acs Nano* **8**, 4754 (2014).
- [28] V. Jacobsen, P. Stoller, C. Brunner, V. Vogel, and V. Sandoghdar, *Interferometric optical detection and tracking of very small gold nanoparticles at a water-glass interface*, *Optics express* **14**, 405 (2006)



# 6

## LABEL-FREE OPTICAL DETECTION OF DNA TRANSLOCATIONS THROUGH PLASMONIC NANOPORES

*Solid-state nanopores are single-molecule sensors that hold great potential for rapid protein and nucleic-acid analysis. Despite their many opportunities, the conventional ionic current detection scheme that is at the heart of the sensor suffers inherent limitations. This scheme intrinsically couples signal strength to the driving voltage, requires the use of high-concentration electrolytes, suffers from capacitive noise, and impairs high-density sensor integration. Here, we propose a fundamentally different detection scheme based on the enhanced light transmission through a plasmonic nanopore. We demonstrate that translocations of single DNA molecules can be optically detected, without the need of any labeling, in the transmitted light intensity through an inverted-bowtie plasmonic nanopore. Characterization and the cross-correlation of the optical signals with their electrical counterparts verify the plasmonic basis of the optical signal. We demonstrate DNA translocation event detection in a regime of driving voltages and buffer conditions where traditional ionic current sensing fails. This novel label-free optical detection scheme opens opportunities to probe native DNA-protein interactions at physiological conditions.*

---

This chapter has been submitted as: Daniel V. Verschuereen, Sergii Pud, Xin Shi, Lorenzo De Angelis, L. Kuipers, and Cees Dekker. Label-free optical detection of DNA translocations through plasmonic nanopores.

## 6.1. INTRODUCTION

Nanopores are an emergent class of label-free single-molecule biosensors that are projected to significantly impact the multibillion dollar markets of diagnostics and medicine [1, 2] by providing a starting point on the roadmap to personalized medicine [3]. The simple concept of shrinking the sensor down to the size of the molecule that it is probing has already brought a commercial DNA sequencing device [4] and new applications in diagnostics and biophysics are currently being explored. Example applications include the analysis of blood serum [5], the classification of proteins in solution [6–8], and characterization of DNA-protein binding [9, 10]. To date, nanopore-based detection schemes rely almost exclusively on the modulation of an ionic current to report on the small changes in physical size of the analyte during its passage through the nanopore [11]. However, the ionic current is set up by a transmembrane driving voltage that controls the translocation speed of the molecules, thus inextricably linking the signal strength and the translocation time. Furthermore, the ionic current strongly depends on the electrolyte concentration, characteristically high-molar ( $\sim 1$  M) salt solutions, rendering sensing at physiological conditions impractical. Finally, the requirement for individual current amplifiers for read-out of each nanopore limits the sensors density in scalable integration on chip [12]. Alternative read-out strategies based on silicon nanowire FETs [13], calcium fluorescence [14, 15], tunneling junctions [16], and even graphene nanoribbons [17–19] have been developed to address these issues. While some of these approaches are more permissive for sensor parallelization, these schemes have not demonstrated full independence of ion flow or electrolyte composition to mediate and amplify the signal of interest. Completely decoupling the biomolecular signal from the driving voltage and buffer conditions will increase the versatility and scalability of nanopore sensing.

To overcome these challenges, we propose a radically different, purely optical, nanopore read-out mechanism based on single-molecule plasmonic resonance sensing through enhanced light transmission [20, 21]. In this scheme, changes in light intensity transmitted through a resonant nanoscale aperture report on the presence and conformation of biomolecules. The plasmonic excitations of the metal's electron gas can mediate the propagation of light through sub-diffraction-limit apertures, enhancing its light transmission [22, 23]. The magnitude of the light transmission is strongly dependent on the wavelength and polarization of the excitation light, the geometry of the nanostructure and its dielectric environment [24]. The latter strong sensitivity of the resonance of nanoaperture to the local environment allows for the optical sensing of molecules [21] that reside in the optical near-field of the aperture. The near-fields can be highly concentrated in the aperture by using small nanogaps [25] that focus the plasmon oscillation into this gap, creating intense optical hotspots. These hotspots have been used to study non-linear optical effects [26], perform molecular spectroscopy [27], and trap single-molecules through nanotweezing [28, 29]. The resonance that excites the gap is extremely sensitive to the local refractive index in the hotspot and the presence of biomolecules in the gap is thus communicated to the far field by variations in the light transmission intensity.

By integrating a nanopore right at the feed gap of the plasmonic nanoantenna, biomolecules can be directly delivered to the nanogap, ensuring interaction of the

analyte with the hotspot [30] and bypassing the otherwise diffusion-limited arrival times of biomolecules to the sensor [31]. Several experimental accounts have been published on plasmonic nanopores for single-molecule biosensing, but so far these focused on nanoplasmonic heating [32, 33], Raman scattering [34], and fluorescence detection [35], while plasmon resonance sensing has remained unexplored. Because plasmon resonance sensing is purely optical, the signal from a translocating biomolecule is without any fluorescent labels and entirely independent of the buffer conditions and driving voltage used, creating a versatile and more powerful nanopore sensor that naturally allows for high-density integration on a device [36].

Here, we experimentally show simultaneous ionic-current and optical-transmission-based detection of single-molecule DNA translocations through a nanopore integrated in the gap of a bowtie-shaped gold plasmonic nanoaperture. By characterizing the optical signal, we verify the plasmonic origin of the effect and show that the amplitude of the optical transients is driving-voltage and buffer independent. We demonstrate that the optical detection scheme outperforms the ionic-current detection at high measurement bandwidth and can detect translocations of DNA molecules in e.g. physiological buffer conditions where the traditional ionic-current detection loses its sensitivity.

## 6.2. RESULTS AND DISCUSSION

### 6.2.1. FABRICATION AND CHARACTERIZATION OF THE INVERTED-BOWTIE PLASMONIC NANOPORE

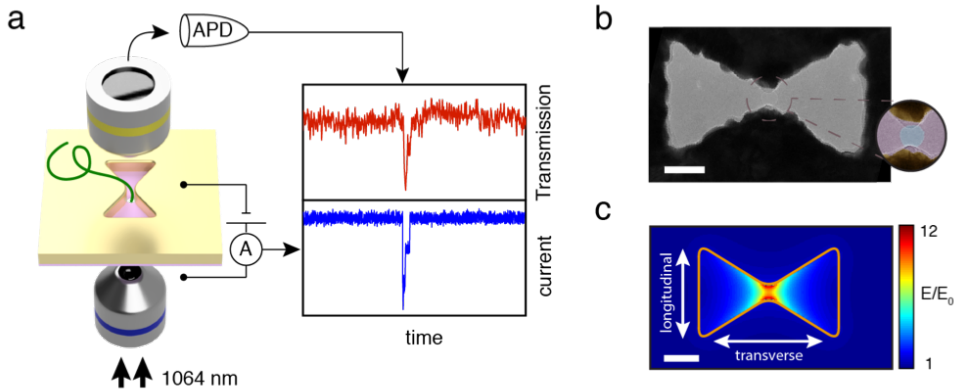


**Figure 6.1: Inverted-bowtie plasmonic nanopore.** (A) Schematic of the plasmonic nanopore experimental setup. (B) Transmission electron microscope image of a plasmonic inverted-bowtie with a nanopore drilled in its gap. The zoom shows a false-colored TEM image of the nanopore in the gap. (C) Normalized electric-field density distribution simulated for the idealized geometry (outlined in orange) of the nanoantenna in (B), clearly revealing optical-field localization and field enhancement up to 12 times in the gap region of the antenna. Scale bars are 50 nm.

Figure 6.1 shows a schematic of the experimental setup. Light transmission is monitored by sandwiching a plasmonic nanopore device in between two objectives, one

for excitation and one for collection of the transmitted light (Fig. 6.1A). The plasmonic antenna is a bowtie-shaped nanoaperture in a 100 nm thick gold film. The apertures, fabricated using electron-beam lithography on a thick PMMA/MMA-MAA/PMGI resist layer, are placed on a 20 nm thin freestanding silicon-nitride (SiN) membrane by wedging transfer (for fabrication details, see Section 6.4). Figure 1b shows a transmission electron microscopy (TEM) image of a typical nanoantenna with a feed gap of 20 nm, a width of 160 nm across, and a side length of 100 nm. More images can be found in the Supportin Information (SI) Section 6.5.1. The nanopore is drilled right in the center of the feed gap of the antenna using TEM drilling, as shown in the false-colored zoom in Fig. 6.1B.

We illuminate the inverted bowtie with an infrared 1064 nm laser while an electrical bias is applied across the supporting SiN membrane. The DC electrical bias serves to drive biomolecules through the nanopore sensor by electrophoresis. The light transmitted through the nanoantenna is monitored using an avalanche photodetector (APD) and the ionic current is simultaneously observed using a conventional current amplifier (see Methods Section 6.4). When illuminated with light that is polarized across the feed gap direction of the antenna (longitudinal polarization, see Fig. 6.1C), a plasmon resonance is excited that enhances and concentrates the electromagnetic field to the hotspot in the gap of the antenna. Figure 6.1C shows the spatial distribution of the normalized electric-field strength in the antenna at 1064 nm wavelength excitation resulting from a finite-difference time-domain (FDTD) simulation. The light is clearly concentrated in the gap and an electric field enhancement up to a factor 12 compared to the incident light can be achieved (see Methods section 6.4 for simulation details). The simulations are validated through a comparison of experimental transmission spectra with simulated ones, see SI Section 6.5.2. Importantly, the gap resonance is not excited when illuminating the antenna with light polarized in the orthogonal orientation (transverse polarization), and hence the field localization is absent and light transmission through the nanoaperture is minimal in that case (see SI Section 6.5.3). The approach presented here aims to optically sense single DNA molecules as they traverse through a plasmonic nanopore, where the presence of the DNA in the hotspot may affect the resonance of the nanoantenna, hence modulating the optical transmission intensity (Fig. 6.1A).

Before adding DNA, we first test and characterize the plasmonic nanopore. After mounting the sample in a custom-made flow cell, electrolyte is flushed in, a bias voltage of 100 mV is applied using a pair of Ag/AgCl electrodes to induce an ionic current flow, and the membrane is scanned with a 1064 nm wavelength laser focused to a diffraction-limited spot ( $\sim 0.8 \mu\text{m}$  in size). Excitation of the plasmonic nanopore by the laser focus will lead to localized plasmonic heating. This, in turn, creates a small temperature increase at the nanopore that can be observed by monitoring the temperature-sensitive ionic current through the pore [37] and allows for accurately aligning the nanopore with the laser focus. 7.5 milliwatts of excitation power, for example, resulted in a measured temperature increase of  $\Delta T$  at the nanopore, in good agreement with predictions from simulations (see SI Section 6.5.4). Please note that the temperature increase observed in the inverted antenna is very significantly lower than that observed for a typical freestanding dimer antenna [32], due to a much more efficient

heat dissipation by the 100 nm thick surrounding gold film and the slight off-resonant excitation of the plasmonic gap mode.

### 6.2.2. OPTICAL LIGHT TRANSMISSION EXHIBITS TRANSIENT SIGNALS CAUSED BY DNA TRANSLOCATIONS

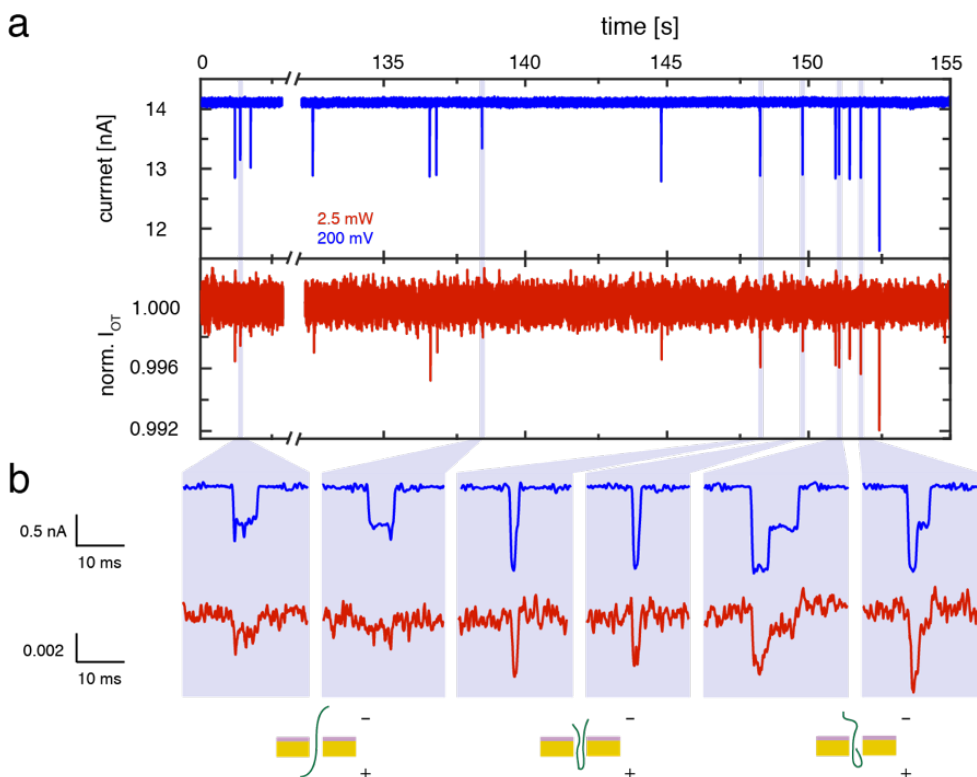


**Figure 6.2: Simultaneous detection of DNA translocation in the ionic current and transmitted light.** (A) Time trace of both the ionic current (blue) and normalized optical light transmission (norm.  $I_{OT}$ , red) in 2M LiCl after the addition of  $\lambda$ -DNA, at a bias voltage of 200 mV and 2.5 mW laser power. Clear transients due to DNA translocation can be observed concurrently in both traces. (B) Zooms and schematic interpretation of the events observed in (A), for two linear DNA translocation (left), two fully folded DNA translocations (middle) and two partially folded DNA translocations (right). For display purposes, electrical traces are low-pass filtered with a 1 kHz Gaussian filter, optical traces are band-pass filtered using 2-pole Butterworth filter with a 4 Hz to 1 kHz window.

Next, we test the use of these plasmonic nanopores as optical single-molecule sensors. After adding  $\lambda$ -DNA and applying a 200 mV bias, transient decreases characteristic for DNA translocations can be clearly observed in the time traces of the ionic current, as shown in blue in Fig. 6.2A. Gratifyingly, concurrent spikes are also observed in the time traces of the normalized optical transmission intensity ( $I_{OT}$ ), as shown in red in Fig. 6.2A. This demonstrates that the nanoantenna can be used to optically detect DNA translocations through a nanopore in a label-free manner.

Inspection of the two traces shows that the transient signals are very closely correlated, i.e., each time that an optical spike is observed, there is a concurrent spike in the ionic current signal, which demonstrates that the signals in the optical transmission are induced by translocating DNA molecules.

Closer examination of the spikes in the ionic current (blue, Fig. 6.2B) reveals current blockade signatures that are typical of DNA translocations: for large nanopores (>5 nm) DNA molecules can either enter in a linear fashion (blue, left two examples Fig. 6.2B), with one double-strand of DNA in the nanopore, or it can traverse the pore in a folded fashion (blue, remaining examples Fig. 6.2B) with two double-stands of DNA temporarily residing in the nanopore [38]. The use of 2M LiCl electrolyte produces excellent signal-to-noise characteristics in the electrical trace ( $\frac{\Delta I_{ionic}}{I_{rms,ionic}} \sim 50$ ) and allows these folds to be easily identified. Interestingly, inspection of the optical traces reveals very similar characteristics, where the folds detected in the ionic current are also discernible in the optical channel (red, right two examples Fig. 6.2B), albeit at a clearly lower signal-to-noise level ( $\frac{\Delta I_{OT}}{I_{rms,EOT}} \sim 3$ ). Whereas with the current signal-to-noise ratio, linear translocations may occasionally escape our optical detection (red, second example from the left in Fig. 2b), folded events are systematically detected (red, remaining examples on the right of Fig. 6.2B). Notably, the excellent correlation of electrical and optical signals as well as the observation of folded events in the optical signal immediately leads to the conclusion that the optical signal arises from the nanoscale localized region of the nanoaperture, and is not due to modulation of the light by the large ( $\sim 1 \mu\text{m}$ ) DNA polymer blob that resides above or below the pore before or after the molecule translocates through the pore.

### 6.2.3. DNA SIGNALS IN OPTICAL LIGHT TRANSMISSION ARISE FROM A PLASMONIC RESONANCE SHIFT

Next, we verify that our optical transmission signals originate from the plasmonic gap resonance of the nanoantenna. First, we confirm that the signal from translocating DNA molecules is mediated by the excitation of the plasmonic gap resonance. For this, we perform DNA translocations under different illumination conditions. When the incident laser light is polarized in the longitudinal direction (cf. inset to Fig. 6.3A), it excites the gap resonance and concurrent transient signals from translocating DNA molecules are observed in both the electrical and optical channel (Fig. 6.3A). For the transverse polarization (inset Fig. 6.3B), on the contrary, no optical transients are observed whatsoever, whereas DNA translocations are clearly discerned in the ionic current (Fig. 6.3B). This confirms expectations since changing the polarization of the incident light to the transverse orientation should remove the field localization in the gap of the antenna and hence the light transmission should no longer be sensitive to changes in dielectric environment of the gap region. Typically, the light transmission through the antenna under the transverse illumination is significantly lower than under longitudinal excitation. To make a fair comparison, we increase the detector gain and the incident laser power from 7.5 mW to 20 mW such that the absolute transmission baseline during transverse illumination is matched to the transmission baseline during longitudinal excitation. Still, no optical transients can be detected. The absence of signatures from translocating DNA molecules in the transverse illumination condition

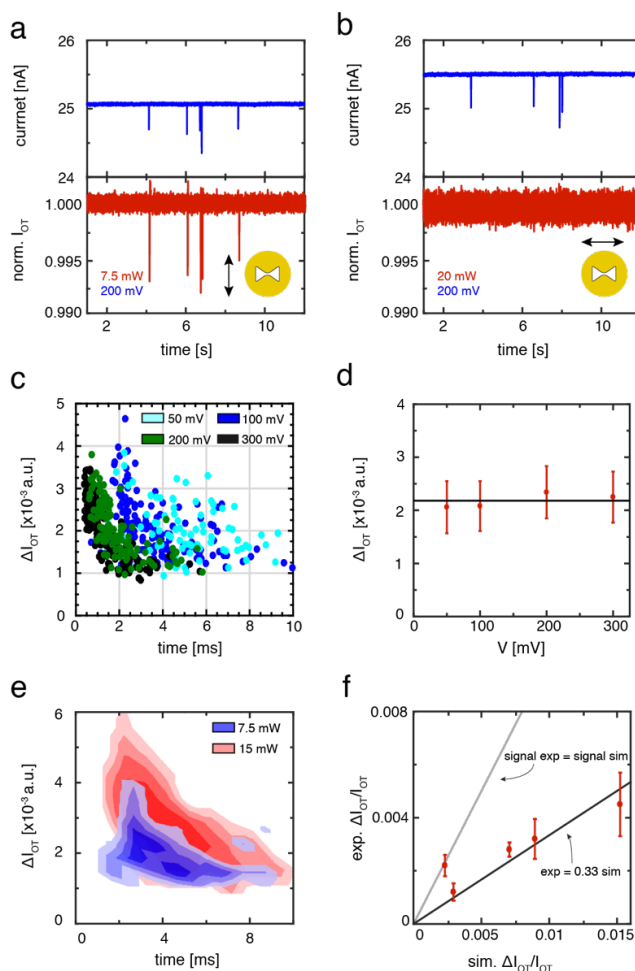


**Figure 6.3: Characterization of the optical signal for DNA translocations.** (A)  $\lambda$ -DNA translocations in 2M LiCl under longitudinal polarization. Translocations produce clear transients in both the electrical trace (top, blue) and in the transmitted light trace when longitudinal excitation is used (bottom, red). (B)  $\lambda$ -DNA translocations in 2M LiCl under transverse polarization. No transients are produced in the optical signal, whereas they are clearly discerned in the ionic current trace. (C) Scatter plot of average optical event amplitude versus the signal duration for 20 kbp DNA at 7.5 mW laser power and different driving voltages. A clear shift is observed towards short event durations at different driving voltages, but the average event amplitude remains unchanged. (D) Histogram peak of all optical events for 20 kbp DNA translocations as a function of driving voltage. The signal amplitude seems to be independent of applied voltage. The peak signal indicates the signal strength from a folded translocation. Error bars are the standard deviation in the normalized transmission baseline. (E) Heat map from the scatter plot of average optical event amplitude versus the signal duration for 20 kbp DNA for two different excitation powers. (F) Normalized experimental signal amplitude from all optical events versus the normalized simulated transmission change upon the insertion of two double strands of DNA in the gap of each individual nanoantenna (see SI Section 6.5.8). The experimental signals follow a linear trend through the origin as predicted by the simulations, albeit with a factor three lower signal amplitude (linear fit, blackline,  $\chi^2_{red} = 2.0$ ).

clearly shows that the signals in the optical channel indeed originate from the excitation of the plasmonic gap mode.

To assess whether or not the amplitude of the optical transients is independent from the electrical bias, we characterize the voltage dependence of the optical signal on the driving voltage. Figure 6.3C shows a scatter plot of average optical event amplitude  $\Delta I_{OT}$  versus the event duration for translocations of 20 kbp DNA molecules at different voltages (for details on the event detection and analysis, see Methods section 6.4). The scatters show a characteristic L-shape clustering of events (see SI Section 6.5.5) that is typically observed for ionic current events in nanopores that are wide enough to permit folded translocations [38]. Clearly, the clusters shift to shorter event duration times for higher driving voltages. Notably, however, the signal amplitude remains unchanged. This sharply contrasts the amplitude of the electrical signals which originates from the ionic current blockade and scales linearly with voltage (see SI Section 6.5.5). Figure 6.3D quantifies this independence of the transmission signal amplitude for folded events versus voltage (see SI Section 6.5.6 for details).

The fact that we observe a well-defined amplitude level of the optical signal from a dsDNA strand present in the gap, is actually striking in the light of extensive previous work that reported a strong heterogeneity of the signal strengths. Generally, molecules that approach a plasmonic nanostructure encounter a spatially inhomogeneous hotspot, producing varying signal strengths as a result [39]. In our case, the nanopore delivers the biomolecule directly into the hotspot by design, reducing uncertainties in the exact location for the interaction of the molecule with the hotspot of the nanoantenna, and furthermore the hotspot region is approximately homogeneous due to off-resonant excitation of the antenna (see Fig. 6.1 and SI Section 6.5.7).

Because the optical signals from translocating DNA molecules are only observed in longitudinal excitation and are voltage independent, we conclude that these signals originate from a shift of the plasmonic gap resonance that is temporarily induced by the translocating molecule. First, this explains the observed transient decreases in transmitted light as the presence of a molecule in the hotspot will induce a redshift of the antenna resonance, which results in a reduction in transmitted light intensity as the antenna is excited at a wavelength shorter than the peak of the resonance of the nanoantenna. Second, this predicts that the signal strength should depend linearly on the excitation power, since the transmitted light intensity through the nanoaperture  $I_{OT}$  will scale linearly with the excitation power of the 1064 nm wavelength laser. Figure 6.3E shows a heat map of the absolute event amplitude  $\Delta I_{OT}$  versus event duration for 7.5 mW and 15 mW of laser power. An increase in signal strength is indeed observed, indicated by a shift of the event population towards higher signal amplitude. The average signal amplitude for two double strands of DNA increased from  $\Delta I_{OT} = 2.0 \pm 0.7 \cdot 10^{-3}$  a.u. to  $\Delta I_{OT} = 3.4 \pm 0.7 \cdot 10^{-3}$  a.u. (mean values and standard deviations of the distribution). We note that the larger incident power produces a slightly higher temperature increase at the nanopore (7.0°C increase at 15 mW, compared to 3.6°C at 7.5 mW), but we do not expect this to have an impact of the optical signal strength, contrary to what is observed for the ionic current signal [32].

Finally, we compare the signal amplitude from DNA translocations with predictions from FDTD simulations. Here, we examine the resonance of the fabricated

nanoantennas with and without two double strands of DNA present in the center of the nanopore, and we extract the DNA signal amplitude by subtracting the two simulated transmission values at  $\lambda = 1064$  nm (details in SI Section 6.5.8 and Methods section 6.4). Figure 6.3F shows the normalized experimental signal amplitude for two double strands of DNA versus the normalized simulated signal amplitude. The simulated and experimental signal intensities correlate very well, and follow a linear trend through the origin, though quantitatively the simulations overestimate the signal strength by a factor of three. The good correlation between the experimental and simulated results is quite striking, considering the crudeness of the simplified DNA modelling [40, 41] and it further corroborates that the optical transients arise from a shift of the plasmonic gap resonance.

#### 6.2.4. THE OPTICAL SENSING VOLUME IS LOCATED IN THE GAP OF THE NANOANTENNA.

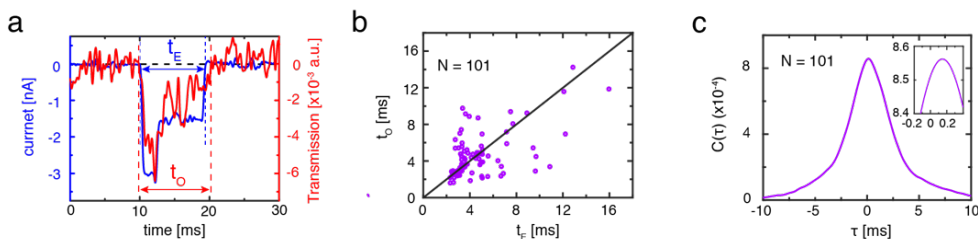


**Figure 6.4: Electrical and optical signal time correlation analysis.** (A) Overlay of the optical (red) and electrical signal (blue) for one DNA translocation event;  $t_E$  and  $t_O$  indicate the event duration for an electrical and optical signal, respectively. Signal duration is defined as the time taken between two consecutive baseline crossings before and after the spike that is detected by thresholding (see Methods section 6.4). (B) Correlation plot of the electrical and optical signal duration of all simultaneously detected events (63% from all ionic current events, conducted in 2 M LiCl and 200 mV, 2.5 mW) showing a correlation between both signal durations ( $r = 0.58$ ). The deviations from  $t_E = t_O$  (black line) arise from inaccurate determination of the optical signal duration due to its lower signal-to-noise ratio. (C) Cross-correlation between all events in (B). A broad peak emerges around 0. The zoom shows a closer inspection of the peak, which reveals a small delay in the optical signal of around  $140 \pm 190$   $\mu$ s.

The transit times for moving the DNA through the plasmonic nanopore are very similar for the optical and electrical signals. Figure 6.4A displays an example of the electrical signal and the optical signal for the same DNA-translocation event. Using simple thresholding, the duration of an event is defined as the time in between the baseline crossings prior and posterior to the spike. Figure 6.4B shows the scatter of the signal duration for the electrical ( $t_E$ ) and optical channels ( $t_O$ ), for events that are simultaneously well resolved in both channels (63% of all events) for  $\lambda$ -DNA translocations at 200 mV. The data shows a clear linear correlation ( $r = 0.58$ ), but display an appreciable scatter as the low signal-to-noise levels for one double strand of DNA in the optical channel troubled the correlation. The observed passage times are similar to the passage times observed in a normal solid-state SiN nanopore under these conditions, indicating that plasmonic trapping forces [42] and DNA gold-surface interactions [43] do not play a major role here.

Even though the optical and electrical signals both probe the DNA molecule at the nanopore during the translocation, the sensing regions of both signals are not exactly identical. For the ionic current, the sensing region largely comprises of the nanopore volume [44] that spans the 20 nm thickness of the SiN membrane. For the optical signal, however, the sensing region is confined to the hotspot region with the increased optical field, which is localized within the gap of the inverted-bowtie antenna and which spans roughly uniformly across the total thickness of the 100 nm gold film on top of the nanopore (SI Section 6.5.7). Modifying the nanostructure design will allow for the engineering of the field localization to create even more focused sensing regions, for example by using tapering of the sidewall of the gold structure [45]. From a detailed analysis of the signals, we can deduce a subtle timing difference between these sensing regions. Due to the design of the plasmonic nanopore, the electrical and optical sensing regions are stacked vertically. Since the analyte is added to the SiN side of the chip, the translocating molecules are first inserted in the nanopore, passing its electrical sensing region, before they subsequently enter the optical sensing region in the gold nanoaperture. Figure 6.4C shows the lumped cross-correlation of all simultaneously detected signals from Fig. 6.4B. A broad peak (full-width half-maximum 4.3 ms) is observed around a time delay of zero, as is expected for signals that originate from the same translocation events. However, a closer inspection (see inset Fig. 6.4C) reveals that the correlation function  $C(\tau)$  peaks at  $\tau = 140 \pm 190 \mu\text{s}$  (mean and standard error of the mean), i.e., the onset of the optical signal is measured slightly later than the electrical signal. This delay time corresponds to roughly  $560 \pm 760 \text{ nm}$  distance travelled for a translocating DNA molecule, using an average translocation time of  $\sim 4 \text{ ms}$  for a linear  $16 \mu\text{m}$  long  $\lambda$ -DNA molecule (Fig. 6.3C). The very large error bar prevents an accurate comparison to the expected offset of  $\sim 100 \text{ nm}$ , viz., the vertical distance between the electrical and optical sensing volumes.

### 6.2.5. ADVANTAGES OF OPTICAL TRANSMISSION SENSING OVER CONVENTIONAL IONIC CURRENT SENSING

After validating the reliability of the optical sensing method, we demonstrate some of the advantages that the method offers over traditional ionic current sensing. The first and foremost benefit is the decoupling of the driving voltage from the signal strength. Signals in ionic current sensing rely on the physical obstruction of an ion flow by the volume of the biomolecule and better signals are obtained if larger currents are present, which intrinsically requires the application of a larger driving voltage. In sharp contrast, the optical signals rely on a change in plasmon resonance that is independent of the bias voltage. The decoupling of the signal from the driving allows the translocation process to be studied at any driving voltage, even in the absence of any bias. Figure 6.5A demonstrates this by showing time traces of 20 kbp DNA molecules translocating a 20 nm nanopore at 500mM LiCl at different driving voltages. DNA translocation events can clearly be observed in both the electrical and optical channels at 200 mV bias voltage (left, Fig. 6.5A). At 100 mV bias, the signal strength from the events in the current channel is decreased significantly (center, Fig. 6.5A), and at 50 mV it completely disappears in the noise floor (right, Fig. 6.5A). On the contrary, the signal in the optical channel remains the same at each bias voltage and translocations can still be well resolved at 50 mV

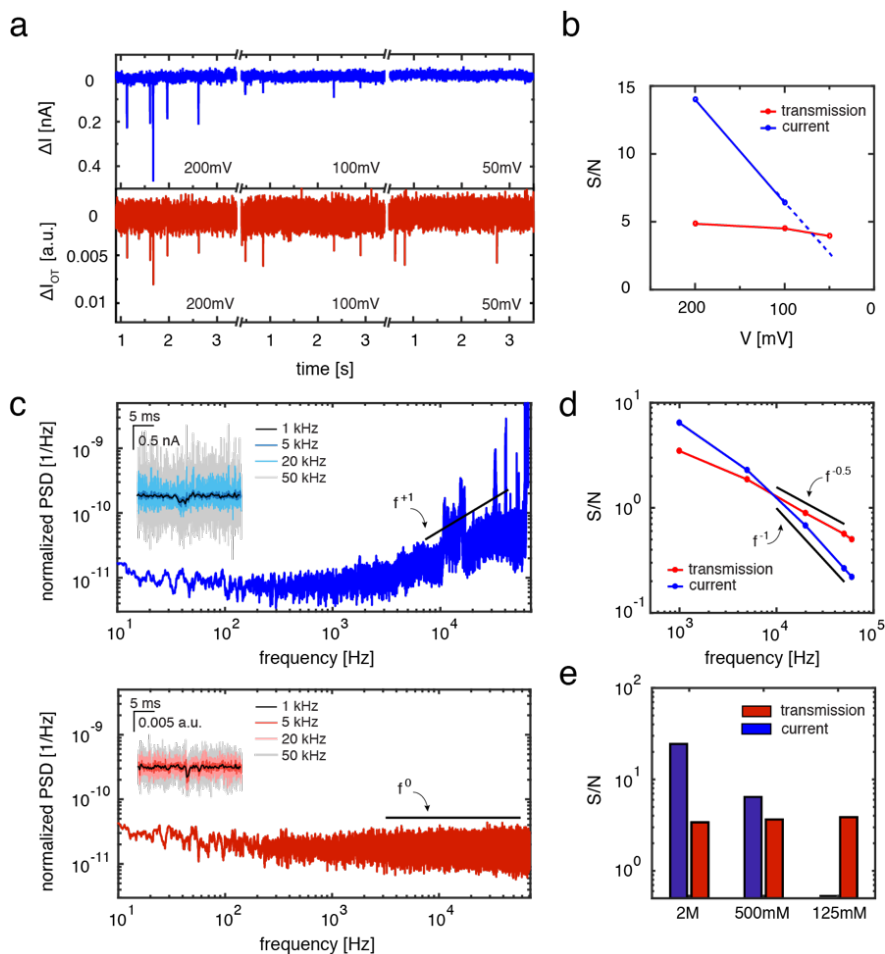


**Figure 6.5: Advantages of optical light transmission over traditional ionic current sensing.** (A) Electrical (blue) and optical (red) time trace during a 20 kbp DNA translocation experiment at 500 mM LiCl at different driving voltages. Whereas the ionic current signal decreases with driving voltage and disappears at 50 mV bias, the optical signal remains unchanged and translocations can still be detected. (B) The signal-to-noise level as a function of decreasing voltage for both electrical and optical signals displayed in (A). (C) Normalized PSD (PSD divided by the square of the average baseline signal) of the ionic current (top, blue) and optical transmission (bottom, red). For the ionic current a clear  $f^{-1}$  scaling is present at high frequencies due to dielectric noise, and interference peaks are present. Contrary to the electrical channel, the power spectrum of the optical channel is flat ( $f^0$ ) and free of interference. The insets show a typical event (taken from a measurement conducted at 500mM, 100 mV, and 7.5 mW using 20 kbp DNA) filtered using various low-pass cut-off filter frequencies. (D) Log-log plot of the signal-to-noise ratio (S/N) versus low-pass cut-off filtering frequency, assuming a fixed signal strength for each. A scaling can be observed for the optical S/N, versus a scaling for the electrical S/N. (E) S/N for both the optical and electrical signal of 20 kbp DNA translocations at 100 mV and 7.5 mW in different LiCl concentrations. A clear decrease can be observed for the electrical signal, preventing DNA translocations to be detected electrically at 125mM LiCl. The optical signal-to-noise ratio remains unchanged with different LiCl concentrations and DNA translocations can still be discerned at 125mM.

bias. This is also demonstrated in Fig. 6.5B, where the optical signal-to-noise ratio stays constant versus applied bias voltage, whereas the electrical signal-to-noise ratio decreases steeply.

As a second advantage, optical detection schemes offer, in principle, much higher-bandwidth data acquisition, as was also pointed out by others [14]. Figure 6.5C shows the normalized power spectral density (PSD) versus frequency plot the electrical (top, blue) and optical channels (bottom, red). The ionic current channel displays  $1/f$  type noise in the low-frequency region as well as dielectric noise [46] in the high-frequency region, manifested as a linear dependence of the PSD on  $f$  (see Fig. 6.5C). Moreover, the channel suffers from electrical interference pick-up in the high frequency part of the spectrum, indicated by the strong peaks in this region. By contrast, the PSD from the optical transmission channel is flat at high frequencies (indicated by the horizontal line in Fig. 6.5C) and is free of any electric interference. It implies that the signal-to-noise ratio will decrease more rapidly for the electrical signals than for the optical signals if the larger acquisition bandwidth is used. This is illustrated by the insets in Fig. 6.5C, where the same translocation event (500 mM LiCl, 100 mV) is shown at full bandwidth in the electrical (inset in top panel) and optical channel (inset in bottom panel), but subsequently filtered at different low-pass cut-off frequencies. It is clear that the noise levels increase much more strongly with higher cut-off frequencies for the electrical compared to the optical channel, resulting more quickly in the onset of signal loss. Figure 6.5D quantifies this assertion by plotting the signal-to-noise ratio as a function of frequency. The signal-to-noise levels for the ionic current scale as  $f^{-1}$  for high frequencies (blue, Fig. 6.5D). On the other hand, the spectrally flat frequency dependence of the background fluctuations in the optical channel leads to a  $f^{-0.5}$  dependence in the signal-to-noise ratio (red in Fig. 6.5D), meaning that the optical signal will be more tolerant to increasing measurement bandwidth than the electrical signal.

Finally, the signal strength from plasmon resonance changes is independent of buffer conditions, contrary to the ionic current sensing which requires high concentrations of ions, thus allowing experiments to be conducted at any buffer composition and electrolyte concentration. Figure 6.5E shows the signal-to-noise level for translocation experiments at different electrolyte concentrations for the electrical signal (blue) and optical signal (red). A clear decrease in the electrical signal-to-noise ratio can be observed for lower salt concentrations. Importantly, at a physiological salt concentration of 125mM LiCl the electrical signal completely disappears in the noise floor. This decrease can be attributed to a decrease in signal strength, as the current noise does not lower significantly upon lowering the electrolyte concentrations [47]. By contrast, the optical signal-to-noise ratio remains unchanged, as expected, and translocations can still be observed even at 125mM LiCl. This demonstrates that, importantly, the optical sensing technique alleviates the restriction to high-salt concentrations which often limits nanopore sensing if physiological conditions are required.

### 6.3. CONCLUSION AND OUTLOOK

In conclusion, we have demonstrated a label-free optical sensing technique using plasmonic nanopores that allows to probe translocating biomolecules independently from the applied driving voltage and electrolyte concentrations used. The detection

is based on the enhanced light transmission through an inverted bowtie nanoantenna with a nanopore drilled in its feed gap, and relies on a plasmon resonance shift induced by the presence of the molecule in the gap of the nanoantenna. We have shown that the transmitted light through the nanoantenna produces an optical signal that can report on the conformation of translocating DNA molecules. Our observations indicate that the optical sensing region lies within the gap of the plasmonic nanoantenna and that the noise for this optical sensing scheme increases with measurement bandwidth more favorably than for ionic current detection. In future work, it will be advantageous to improve the signal in our detection scheme, for example by bringing the resonance of the plasmonic nanoantennas closer to the excitation laser or by modifying the antenna layout.

This new label-free optical detection scheme may open up new directions in biosensing. The optical observation of DNA in such wide (20 nm) plasmonic nanopores naturally allows to be extended to the detection of protein-DNA complexes and large proteins in native salt conditions. Moreover, optical detection schemes are well suited for high-density nanopore device integration, which are challenging to be achieved when ionic current sensing is employed. Finally, the decoupling of the signal and driving voltage allows for novel measurement modes. For instance, polymers that are electrophoretically inserted in the nanopore can be studied under the application of only a very weak bias, and their escape can be studied in absence of any bias, all without any loss of signal. Alternatively, this sensing technique can be used the study of thermophoretically or pressure driven polymer translocations, omitting an electrical bias all together. Finally, this detection scheme will aid the development of plasmonic nanopores as a platform for label-free nanotweezing and single-molecule Raman spectroscopy.

## 6.4. EXPERIMENTAL METHODS

### 6.4.1. SAMPLE FABRICATION

Inverted-bowtie nanoapertures are fabricated using electron-beam lithography. First, a trilayer stack of (from substrate to top) PMGI/MMA-MAA copolymer/PMMA is spincoated at 400 nm/1000 nm/100 nm thickness on a piece of a silicon wafer. The multilayer stack is essential to allow the gold layer on top of the stack to be stripped and the resulting gold flake to be handled. The resist is patterned with an array of bowties at a dose of  $2500 \mu\text{C}/\text{cm}^2$  using a 100 keV electron bundle from an electron-beam pattern generator (EBPG5200, Raith) and developed in MIBK:IPA 1:3 for 1 min followed by a 15 second dip into MF321 to transfer pattern also to PMGI layer. Next, 100 nm of gold is evaporated onto the layers using an electron-beam evaporator (Temescal 2000) at a rate of  $3 \text{ \AA}/\text{s}$ , without the use of any adhesion layers. The MMA/PMMA/gold flake is then stripped from the substrate by submerging the sample in a 3% KOH solution for 15 min to dissolve the PMGI. Subsequently, the PMMA/MMA-MAA is removed using acetone and the flake is transferred into an isopropanol solution. Using a wedging technique [48], the flake is picked up from the solution and placed onto a freestanding SiN membrane. After drying, the flake is sealed onto the sample by covering the edge of the gold flake with PDMS. The sample is then cleaned in  $\text{O}_2$  plasma (50 W) for 1 hr to

prevent carbon contamination in the TEM chamber. Finally, a TEM is used to select a suitable nanostructure and a nanopore is drilled in the feed gap of the nanoaperture.

#### 6.4.2. EXPERIMENTAL SETUP

Prior to the experiment, the sample is rinsed in ethanol and ddH<sub>2</sub>O and cleaned in O<sub>2</sub> plasma for 30 sec (50 W). The sample is mounted in a custom-made PEEK flow cell that allows the plasmonic nanopore to be illuminated and the transmission light to be collected. Next, electrolyte, 2 M LiCl buffered to pH 8 with 20 mM Tris and 2 mM EDTA unless otherwise stated, is flushed in. Current through the plasmonic nanopore is measured using a pair of Ag/AgCl electrodes and acquired using a Axopatch 200B (Molecular Devices), and analog filtered at 100 kHz using a low-pass 4-pole Bessel filter. The laser (M9-A64-0200 laser-diode, Thorlabs) is operated in constant injection-current mode and focused to a diffraction-limited spot on the sample using a 60x 1.2 NA water-immersion objective (Olympus) in an inverted microscope setup. The transmission light is collected using a 10x 0.3 NA objective (Nikon) and projected onto an Avalanche Photo Diode (APD410C/M, Thorlabs). Subsequently, the position of the laser focus is aligned to the plasmonic nanopore by scanning the membrane through the focus of the laser using a piezoelectric positioning stage (MadCity Labs, Inc) and maximizing the current increase that is induced by plasmonic heating. Data acquisition is performed using custom-made Labview software through a NI DAQ (NI USB-6251, National Instruments) at a sampling rate of 200 kHz, where both the current amplifier and photodiode are read-out simultaneously to ensure synchronized signal acquisition.

#### 6.4.3. EVENT DETECTION AND ANALYSIS

Event detection and analysis is performed using Tranzalyser [49], a custom-made MATLAB-based software package developed in our lab. All traces, both electrical and optical, are low-pass filtered using a Gaussian filter with a cut-off at 1 kHz for analysis. Event detection is done in both channels by using a 5-sigma-threshold spike detection, using a baseline and sigma value calculated from a moving average window of 30000 data points for the electrical traces and 5000 data points for the optical traces. For display purposes, electrical traces are low-pass filtered using 1 kHz cut-off and optical traces are band-pass filtered using a 2-pole Butterworth filter between 4 Hz and 1 kHz.

#### 6.4.4. FDTD SIMULATIONS

We use FDTD Solutions (Lumerical Solutions, Inc., Canada) to model the optical properties of the inverted-bowtie plasmonic nanoantennas. The inverted bowtie is modeled as a bowtie-shaped aperture in a 100 nm thick gold film with a width of 160 nm, a side length of 100 nm, a 20 nm gap, and 30 nm-in-radius in-plane tip rounding to resemble the fabricated structures. The antenna is positioned on a 20 nm thin silicon-nitride membrane with a refractive index (RI) of 2. The surrounding medium is modeled as water with a RI of 1.33. Symmetry is used to reduce the computational time. The plasmonic aperture is excited by a pulse from a total-field scattered-field source incident normal to the gold surface, and with the polarization in either the longitudinal or the transverse mode. The fractional light transmission through the nanostructure is calculated by integrating the far-field power flux through a screen placed 350 nm below

the membrane and normalized to the total incident power at each frequency.

The optical response of fabricated nanostructures is simulated by extracting the planar geometry from a TEM image, using the image import function of the FDTD Solutions program. The planar geometry is extruded 100 nm perpendicular to model an aperture in the gold film. The optical response with and without DNA inserted into the gap is calculated using the far-field power flux, where the DNA molecule is simulated as a 200 nm long rod of 2.2 nm in diameter and a refractive index of 2.5 [41].

## 6.5. SUPPORTING INFORMATION

### 6.5.1. ADDITIONAL TEM IMAGES OF INVERTED-BOWTIE PLASMONIC NANOPORES

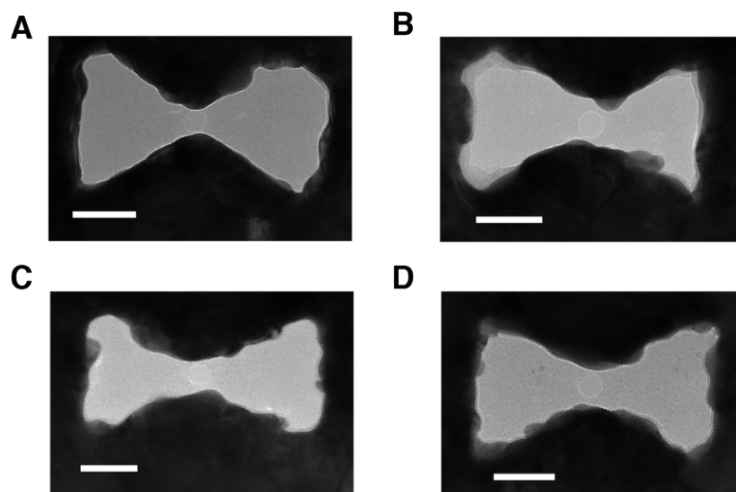


**Figure S6.6:** Additional TEM images of plasmonic nanopores. Scale bars are 50 nm.

### 6.5.2. EXPERIMENTAL AND SIMULATED SPECTRUM OF PLASMONIC NANOPORE

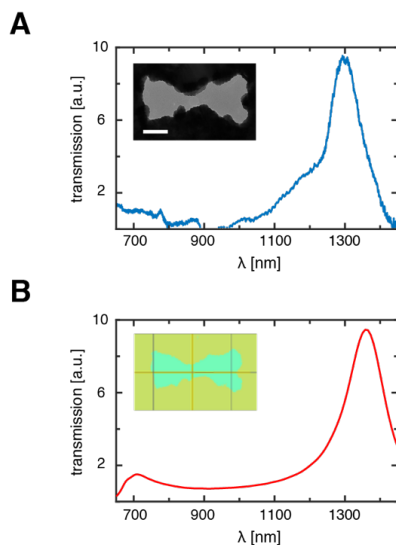


**Figure S6.7: Experimental and simulated transmission spectrum.** (A) Experimental transmission spectrum from the nanostructure shown in the inset (scale bar is 50 nm). (B) Simulated transmission spectrum from the nanostructure in (A). The inset shows a top down view of the geometry that was simulated, which was extracted from the TEM image in (A).

Figure S7.8 shows the experimental (A) and simulated (B) transmission spectrum of the nanoantenna, which is shown in the inset of (A). A clear resonance peak can be observed experimentally around 1300 nm (Fig. S7.8A) and around 1350 nm in the simulated spectrum (Fig. S7.8B), demonstrating good agreement. Experimental spectra are obtained by inserting the plasmonic nanopore chip in a custom-made flow cell that exposes the nanostructure to ddH<sub>2</sub>O and leaves the opposite site exposed to air. The sample is then illuminated by a broadband lamp and a region of interest of 2  $\mu\text{m}$  in size is selected on the sample using a 40  $\mu\text{m}$  circular pinhole in a conjugate image plane. Subsequently, the transmission light collected through the pinhole is focused onto a spectrometer (Acton SP500i, Princeton Instruments). A spectrum from the nanostructure is obtained by subtracting the averaged background from 8 locations surrounding the nanoantenna from the raw sample spectrum and dividing the result by the spectral intensities of the lamp.

### 6.5.3. SIMULATION OF IDEALIZED INVERTED-BOWTIE NANOANTENNA IN TRANSVERSE POLARIZATION

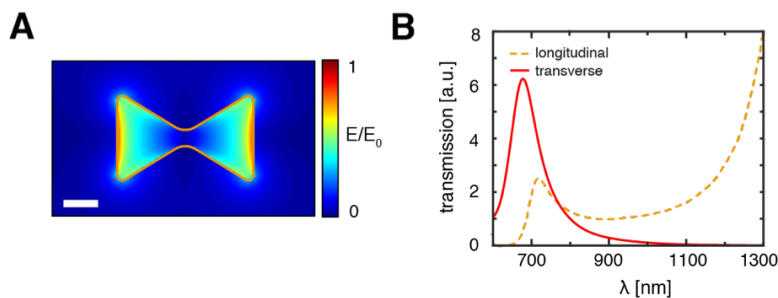


**Figure S6.8: Simulated optical response of the inverted-bowtie nanoantenna.** (A) Normalized electric field density distribution under transverse illumination. No strong optical field enhancement is observed, and in a field density minimum can be found in the gap region. Scale bar is 40 nm, (B) Simulated light transmission spectra of the nanostructure under longitudinal and transverse illumination.

### 6.5.4. EXPERIMENTAL AND SIMULATED TEMPERATURE INCREASE IN A PLASMONIC NANOPORE

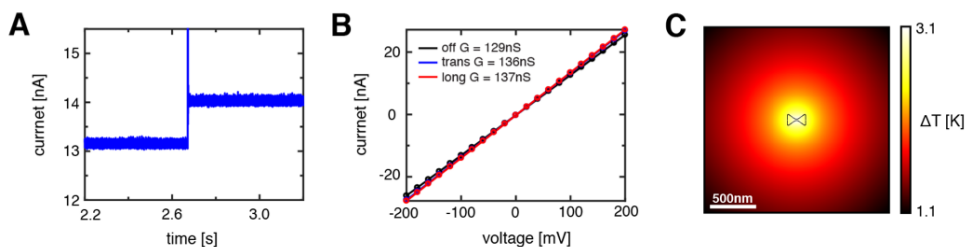


**Figure S6.9: Heating in a plasmonic nanopore** (A) Ionic current increase upon 7.5 mW of laser power in longitudinal mode through a 20 nm plasmonic nanopore at 100 mV and 2M LiCl. (B) IV characteristics of the same nanopore without laser illumination ( $G = 129$  nS) transverse illumination of 7.5 mW ( $G = 136$  nS) and longitudinal illumination of 7.5 mW ( $G = 137$  nS). (C) Simulated spatial temperature distribution for a heat input equivalent to 7.5 mW of laser illumination in longitudinal mode. Note that the temperature increase amounts to only a modest 3.6°C.

Plasmonic heating due to resistive losses in the metal are a common side effect from plasmon excitation. The plasmonic nanopore naturally allows for the heating to be quantified experimentally, as the nanopore can serve as a local temperature probe [50]. A temperature increase leads to an increase in the buffer conductivity, which can be monitored through the nanopore current and as such the nanopore serves as a local thermometer. Indeed, upon laser illumination of a plasmonic nanopore, an increase in the ionic current can be readily observed (see Fig. S6.9A). Figure S6.9B shows the IV characteristics of the plasmonic nanopore under different illumination conditions. In longitudinal mode under 7.5 mW of illumination power at 1064 nm, a

relative current increase of 5.7% is observed, corresponding to a temperature increase of 3.6 K [50]. The temperature increase in a plasmonic nanopore can be modeled using simple finite element modeling. We used COMSOL Multiphysics 4.0 to simulate the heating in plasmonic nanoantenna and calculated the resulting temperature increase by setting a fixed total heat power on the surface of the nanoantenna (absorption of plasmonic nanoantenna) and the top gold surface (absorption by gold film). Details on the COMSOL simulation setup can be found elsewhere [32]. Using an absorption cross-section of  $10^{-14}\text{m}^2$  for the antenna at 1064 nm, as determined through FDTD simulations, a diffraction limited laser spot size (objective NA 1.2) and a transmission efficiency through the objective of 50%, 64  $\mu\text{W}$  of laser power is converted to heat in the plasmonic nanoantenna. This leads to a predicted temperature increase of 3.1 K, which is in good agreement of the 3.6 K observed experimentally. We note that this temperature increase is significantly less than is observed for a nanoantenna dimer, such as the plasmonic bowtie [32] which can be attributed to the good heat conductive properties of the gold film.

### 6.5.5. BLOCKADE CURRENT VERSUS DWELL TIME SCATTER PLOTS

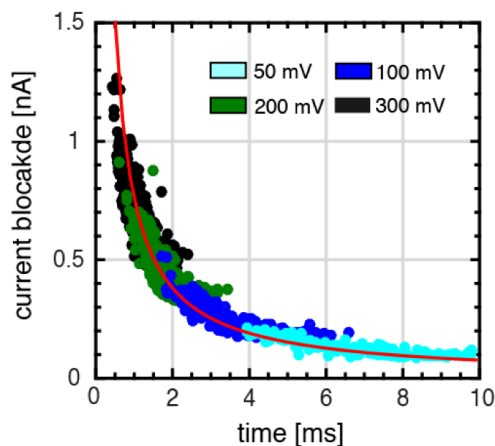


**Figure S6.10:** Blockade current versus dwell times scatter plots at 50, 100, 200, and 300 mV. The red line is the constant charge deficit contour: average event amplitude  $\times$  dwell time = 0.76 ms-nA, as determined from the charge deficit peak of all data points. The data points per voltage scatter in a characteristic L-shape, that follows the constant charge deficit contour. A clear shift in both amplitude and dwell time can be observed.

6

### 6.5.6. ALL POINT HISTOGRAMS OF OPTICALLY DETECTED EVENTS AT DIFFERENT BIAS VOLTAGES

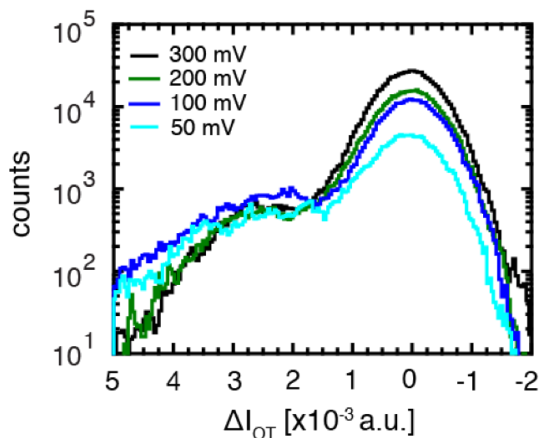


**Figure S6.11:** All point histogram from all optically detected events used to determine signal amplitude at various voltages (Fig. 6.3C in the main text). Two peaks can be observed, one around 0 (open pore) and one around  $\sim 2.3$  (where two dsDNA strands are inserted into the pore).

### 6.5.7. SIMULATION OF NORMALIZED ELECTRIC FIELD MAP ACROSS GOLD THICKNESS

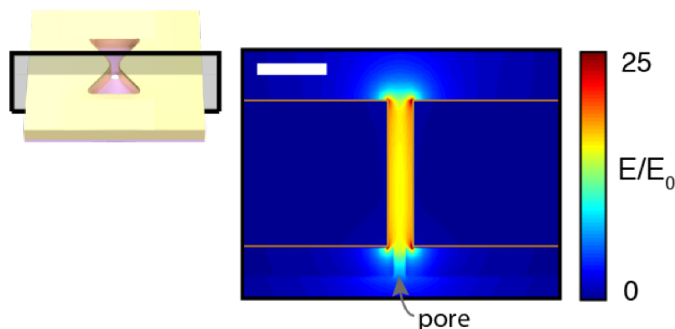


**Figure S6.12:** Normalized electric field map of the inverted bowtie excited in longitudinal mode at 1064 nm in the plane indicated in the inset (i.e. the cross section through the thickness of the gold). The electric field localization extends along the entire thickness of the gold, and is approximately uniform in the gap. Scale bar is 50 nm.

### 6.5.8. DETAILS ON DETERMINATION OF RELATIVE SIMULATED SIGNAL AMPLITUDE

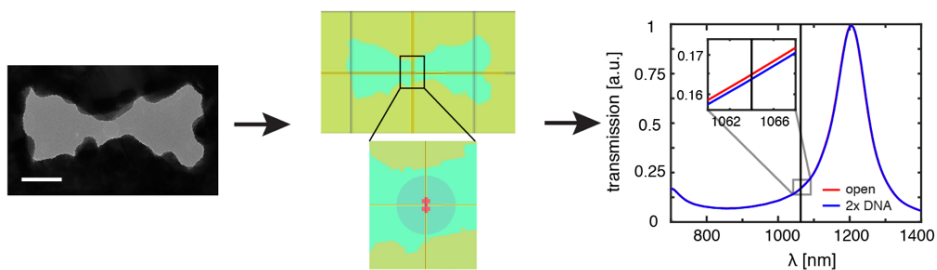


**Figure S6.13:** Workflow in determining the simulated signal amplitude. A TEM image is converted into a model shape and the difference in simulated transmission with and without two double strands of DNA is extracted at 1064 nm. The scale bar is 50 nm.

To extract a simulated signal amplitude, we directly simulated the nanoantenna as deduced from the TEM image. First a TEM image of the nanostructure is imported into Lumerical FDTD software using image import. Using thresholding the image is converted into a 2D geometry that can be used in the simulation and the geometry is perforated through a 100 nm thick gold layer to create a gold nanoaperture. Subsequently the structure is aligned with a 20 nm nanopore (shown in the middle zoom) in the simulation. Two simulations are done: one for an that contains two strands of dsDNA, simulated as a 200 nm two long rods of 2.2 nm in diameter (as shown in

red) and a refractive index of 2.5. The strands are placed  $\pm 2$  nm from the center of the nanopore, in the longitudinal direction. The different simulation spectra for the structure with or without DNA are normalized to the peak transmission intensity, plotted, and the difference is extracted at 1064 nm and divided by the light transmission through the open nanostructure.

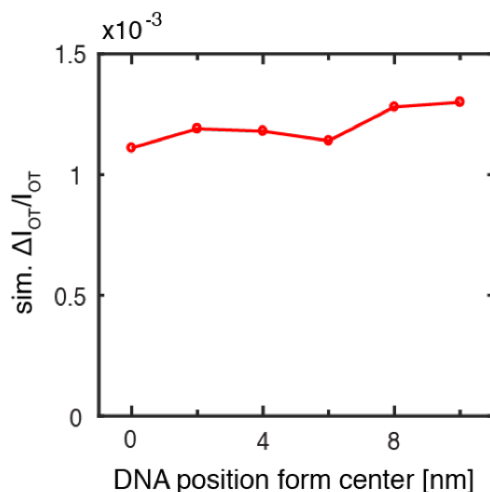


**Figure S6.14:** Normalized simulated signal amplitude of one double strand of DNA inserted in a 20 nm pore at different positions from the center. The signal strength is about 30% larger when the DNA strand touches the gold surface than when at the center.

We tested the dependence of the signal strength on the exact location of the DNA strand in the nanopore. For this we used the idealized geometry, as described in the main text. Figure S6.14 shows the resulting signal amplitude when a single DNA rod is at different locations in the nanopore. The DNA rod is moved from the center of the pore to the very edge of the gold surface. The signal amplitude increases when the DNA moves closer to the surface, but the amplitude increases only about 30% from the center to the edge. We thus assume that the exact position of the DNA is of minor influence to the simulation.

Furthermore, we tested the difference between one and two DNA double strands in the nanopore in the idealized geometry. The normalized amplitude for one DNA rod was 0.00115 at the center and 0.00193 for 2 rods in the configuration described above.

## REFERENCES

- [1] E. Pennisi, *Dna sequencers still waiting for the nanopore revolution*, *Science* **343**, 2 (2014).
- [2] Y. Feng, Y. Zhang, C. Ying, D. Wang, and C. Du, *Nanopore-based fourth-generation dna sequencing technology*, *Genomics, proteomics & bioinformatics* **13**, 4 (2015).
- [3] C.-S. Ku and D. H. Roukos, *From next-generation sequencing to nanopore*

- sequencing technology: paving the way to personalized genomic medicine*, Expert review of medical devices **10**, 1 (2013).
- [4] H. Lu, F. Giordano, and Z. Ning, *Oxford nanopore minion sequencing and genome assembly*, Genomics, proteomics & bioinformatics **14**, 265 (2016).
- [5] J. Y. Sze, A. P. Ivanov, A. E. Cass, and J. B. Edel, *Single molecule multiplexed nanopore protein screening in human serum using aptamer modified dna carriers*, Nature Communications **8**, 1552 (2017).
- [6] J. Larkin, R. Y. Henley, M. Muthukumar, J. K. Rosenstein, and M. Wanunu, *High-bandwidth protein analysis using solid-state nanopores*, Biophysical journal **106**, 696 (2014).
- [7] N. A. Bell and U. F. Keyser, *Digitally encoded dna nanostructures for multiplexed, single-molecule protein sensing with nanopores*, Nature nanotechnology **11**, 645 (2016).
- [8] E. C. Yusko, B. R. Bruhn, O. M. Eggenberger, J. Houghtaling, R. C. Rollings, N. C. Walsh, S. Nandivada, M. Pindrus, A. R. Hall, and D. Sept, *Real-time shape approximation and fingerprinting of single proteins using a nanopore*, Nature nanotechnology **12**, 360 (2017).
- [9] C. Plesa, J. W. Ruitenbergh, M. J. Witteveen, and C. Dekker, *Detection of individual proteins bound along dna using solid-state nanopores*, Nano letters **15**, 3153 (2015).
- [10] J.-S. Yu, M.-C. Lim, D. T. N. Huynh, H.-J. Kim, H.-M. Kim, Y.-R. Kim, and K.-B. Kim, *Identifying the location of a single protein along the dna strand using solid-state nanopores*, ACS nano **9**, 5289 (2015).
- [11] W. Shi, A. K. Friedman, and L. A. Baker, *Nanopore sensing*, Analytical chemistry **89**, 157 (2016).
- [12] R. D. Maitra, J. Kim, and W. B. Dunbar, *Recent advances in nanopore sequencing*, Electrophoresis **33**, 3418 (2012).
- [13] P. Xie, Q. Xiong, Y. Fang, Q. Qing, and C. M. Lieber, *Local electrical potential detection of dna by nanowire–nanopore sensors*, Nature nanotechnology **7**, 119 (2012).
- [14] A. Ivankin, R. Y. Henley, J. Larkin, S. Carson, M. L. Toscano, and M. Wanunu, *Label-free optical detection of biomolecular translocation through nanopore arrays*, ACS nano **8**, 10774 (2014).
- [15] B. N. Anderson, O. N. Assad, T. Gilboa, A. H. Squires, D. Bar, and A. Meller, *Probing solid-state nanopores with light for the detection of unlabeled analytes*, ACS nano **8**, 11836 (2014).
- [16] A. P. Ivanov, E. Instuli, C. M. McGilvery, G. Baldwin, D. W. McComb, T. Albrecht, and J. B. Edel, *Dna tunneling detector embedded in a nanopore*, Nano letters **11**, 279 (2010).

- [17] F. Traversi, C. Raillon, S. Benameur, K. Liu, S. Khlybov, M. Tosun, D. Krasnozhan, A. Kis, and A. Radenovic, *Detecting the translocation of dna through a nanopore using graphene nanoribbons*, *Nature nanotechnology* **8**, 939 (2013).
- [18] M. Puster, A. Balan, J. A. Rodríguez-Manzo, G. Danda, J. Ahn, W. Parkin, and M. Drndić, *Cross-talk between ionic and nanoribbon current signals in graphene nanoribbon-nanopore sensors for single-molecule detection*, *small* **11**, 6309 (2015).
- [19] S. J. Heerema, L. Vicarelli, S. Pud, R. N. Schouten, H. W. Zandbergen, and C. Dekker, *Probing dna translocations with inplane current signals in a graphene nanoribbon with a nanopore*, *ACS nano* **12**, 2623 (2018).
- [20] X. Shi, R. Gao, Y.-L. Ying, W. Si, Y.-F. Chen, and Y.-T. Long, *A scattering nanopore for single nanoentity sensing*, *ACS Sensors* **1**, 1086 (2016).
- [21] A. B. Dahlin, *Sensing applications based on plasmonic nanopores: The hole story*, *Analyst* **140**, 4748 (2015).
- [22] F. J. Garcia-Vidal, L. Martin-Moreno, T. Ebbesen, and L. Kuipers, *Light passing through subwavelength apertures*, *Reviews of Modern Physics* **82**, 729 (2010).
- [23] F. G. De Abajo, *Colloquium: Light scattering by particle and hole arrays*, *Reviews of Modern Physics* **79**, 1267 (2007).
- [24] S. A. Maier, *Plasmonics: fundamentals and applications* (Springer Science & Business Media, 2007).
- [25] M.-K. Kim, H. Sim, S. J. Yoon, S.-H. Gong, C. W. Ahn, Y.-H. Cho, and Y.-H. Lee, *Squeezing photons into a point-like space*, *Nano letters* **15**, 4102 (2015).
- [26] P. Genevet, J.-P. Tetienne, E. Gatzogiannis, R. Blanchard, M. A. Kats, M. O. Scully, and F. Capasso, *Large enhancement of nonlinear optical phenomena by plasmonic nanocavity gratings*, *Nano letters* **10**, 4880 (2010).
- [27] H. Wei and H. Xu, *Hot spots in different metal nanostructures for plasmon-enhanced raman spectroscopy*, *Nanoscale* **5**, 10794 (2013).
- [28] Y. Pang and R. Gordon, *Optical trapping of a single protein*, *Nano letters* **12**, 402 (2011).
- [29] A. A. Al Balushi and R. Gordon, *Label-free free-solution single-molecule protein-small molecule interaction observed by double-nanohole plasmonic trapping*, *ACS Photonics* **1**, 389 (2014).
- [30] M. Belkin, S.-H. Chao, M. P. Jonsson, C. Dekker, and A. Aksimentiev, *Plasmonic nanopores for trapping, controlling displacement, and sequencing of dna*, *ACS nano* **9**, 10598 (2015).
- [31] X. Shi, D. V. Verschueren, and C. Dekker, submitted .
- [32] F. Nicoli, D. Verschueren, M. Klein, C. Dekker, and M. P. Jonsson, *Dna translocations through solid-state plasmonic nanopores*, *Nano letters* **14**, 6917 (2014).

- [33] C. R. Crick, P. Albella, H.-J. Kim, A. P. Ivanov, K.-B. Kim, S. A. Maier, and J. B. Edel, *Low-noise plasmonic nanopore biosensors for single molecule detection at elevated temperatures*, ACS Photonics **4**, 2835 (2017).
- [34] M. P. Cecchini, A. Wiener, V. A. Turek, H. Chon, S. Lee, A. P. Ivanov, D. W. McComb, J. Choo, T. Albrecht, and S. A. Maier, *Rapid ultrasensitive single particle surface-enhanced raman spectroscopy using metallic nanopores*, Nano letters **13**, 4602 (2013).
- [35] S. Nam, I. Choi, C.-c. Fu, K. Kim, S. Hong, Y. Choi, A. Zettl, and L. P. Lee, *Graphene nanopore with a self-integrated optical antenna*, Nano letters **14**, 5584 (2014).
- [36] J. Korlach, P. J. Marks, R. L. Cicero, J. J. Gray, D. L. Murphy, D. B. Roitman, T. T. Pham, G. A. Otto, M. Foquet, and S. W. Turner, *Selective aluminum passivation for targeted immobilization of single dna polymerase molecules in zero-mode waveguide nanostructures*, Proceedings of the National Academy of Sciences **105**, 1176 (2008).
- [37] M. P. Jonsson and C. Dekker, *Plasmonic nanopore for electrical profiling of optical intensity landscapes*, Nano letters **13**, 1029 (2013).
- [38] A. J. Storm, J. Chen, H. Zandbergen, and C. Dekker, *Translocation of double-strand dna through a silicon oxide nanopore*, Physical review E **71**, 051903 (2005).
- [39] I. Ament, J. Prasad, A. Henkel, S. Schmachtel, and C. Sönnichsen, *Single unlabeled protein detection on individual plasmonic nanoparticles*, Nano letters **12**, 1092 (2012).
- [40] J.-S. Huang, V. Callegari, P. Geisler, C. Brüning, J. Kern, J. C. Prangma, X. Wu, T. Feichtner, J. Ziegler, and P. Weinmann, *Atomically flat single-crystalline gold nanostructures for plasmonic nanocircuitry*, Nature communications **1**, 150 (2010).
- [41] V. V. Thacker, L. O. Herrmann, D. O. Sigle, T. Zhang, T. Liedl, J. J. Baumberg, and U. F. Keyser, *Dna origami based assembly of gold nanoparticle dimers for surface-enhanced raman scattering*, Nature communications **5**, 3448 (2014).
- [42] M. L. Juan, R. Gordon, Y. Pang, F. Eftekhari, and R. Quidant, *Self-induced back-action optical trapping of dielectric nanoparticles*, Nature Physics **5**, 915 (2009).
- [43] R. Wei, D. Pedone, A. Zürner, M. Döblinger, and U. Rant, *Fabrication of metallized nanopores in silicon nitride membranes for single-molecule sensing*, small **6**, 1406 (2010).
- [44] S. W. Kowalczyk, A. Y. Grosberg, Y. Rabin, and C. Dekker, *Modeling the conductance and dna blockade of solid-state nanopores*, Nanotechnology **22**, 315101 (2011).
- [45] Y. Chen, A. Kotnala, L. Yu, J. Zhang, and R. Gordon, *Wedge and gap plasmonic resonances in double nanoholes*, Optics express **23**, 30227 (2015).
- [46] J. B. Edel and T. Albrecht, *Engineered nanopores for bioanalytical applications* (William Andrew, 2013).

- [47] R. M. Smeets, U. F. Keyser, D. Krapf, M.-Y. Wu, N. H. Dekker, and C. Dekker, *Salt dependence of ion transport and dna translocation through solid-state nanopores*, Nano letters **6**, 89 (2006).
- [48] G. F. Schneider, V. E. Calado, H. Zandbergen, L. M. Vandersypen, and C. Dekker, *Wedging transfer of nanostructures*, Nano letters **10**, 1912 (2010).
- [49] C. Plesa and C. Dekker, *Data analysis methods for solid-state nanopores*, Nanotechnology **26**, 084003 (2015).
- [50] D. V. Verschueren, M. P. Jonsson, and C. Dekker, *Temperature dependence of dna translocations through solid-state nanopores*, Nanotechnology **26**, 234004 (2015)

# 7

## NANO-OPTICAL TWEEZING OF SINGLE PROTEINS IN PLASMONIC NANOPORES

*Universal single-molecule biosensors should ideally be able to detect and characterize single biomolecules label-free and with high throughput. Current established single-molecule sensing technologies are low in throughput or cannot provide the extensive measurement times required for monitoring of single molecules. To address these issues, we developed a plasmonic nanopore single-molecule biosensor, with a nanopore that can deliver molecules towards the sensor, embedded in a plasmonic nanoantenna that is used to trap single molecules and provide ample measurement time. Employing the light transmission through the nanoantenna as the read out signal, we verified the optical trapping ability of the plasmonic nanopore by tweezing 20 nm-in-diameter polystyrene nanoparticles for seconds or longer. To prove that the plasmonic nanopore can function as a single molecule biosensor, we furthermore trapped single beta-amylase molecules, a 200 kDa protein, in the nanoantenna. Analysis of the trapping events revealed that trapping was assisted by protein-surface interactions and indicated that some trapped protein denatured on the surface. The application of an electrical bias voltage increased the event rate over an order of magnitude and shortened the residence time of the molecules in the plasmonic nanopore. The integration of these two established single-molecule sensors, a plasmonic nanoantenna and solid-state nanopore, provides the experimenter with two independent control handles at the single-molecule level, the optical trapping force and electrophoretic force, which helps to overcome the limitations that each sensor bears separately.*

---

This chapter is based on a manuscript in preparation as: Daniel V. Verschuere, Xin Shi, and Cees Dekker. Nano-optical tweezing of single proteins in plasmonic nanopores.

## 7.1. INTRODUCTION

The universal label-free detection and characterization of single biomolecules, in particular proteins, is a grand ambition in the development of diagnostic sensors [1]. Beyond the obvious advantage that single-molecule biosensors can perform detection at the fundamental limit of one single molecule, such sensors would be able to spot rare aberrant biomolecules in an abundant background of healthy ones [2], can probe substructure of single-molecules [3], and allow to study behavior of single-molecular interactions [4], all without the need for chemical labeling. Two main approaches that are being explored to achieve such sensors are nanopores, both biological [5] and solid-state nanopores [6], and plasmonic nanoantennas, both gold nanoparticles [7] and nanoapertures [8]. The basis of each of these single-molecule sensors is a nanoscale detection volume that approaches the size of biomolecule to be probed. This not only enhances the measurement signal, but also provides a way to eliminate background from other components in the solution [9]. However, challenges still remain in sensor specificity [7], sensor response time [10], temporal resolution [11], and the range of different analytes that can be probed [5].

Biological and solid-state nanopores are nanoscale openings in a thin membrane that have, in the past decade, proven themselves as versatile biosensors [3, 12]. Both types of nanopores have been used to detect and characterize protein [13, 14], DNA [15, 16], and protein-DNA interactions [17, 18], by virtue of an ionic current signal that transduces the information of analyte size and conformation to the experimenter. Whereas nanopore sensors have great sensor response times as biomolecules are actively transported into the sensor, the fixed size of a biological nanopore limits analyte versatility [5] and their solid-state nanopores counterparts suffer from fast translocation speeds and limited temporal resolution [11].

Single plasmonic nanoantennas have more recently entered the scene of single-molecule biosensing. These sensors rely on light-driven coherent electron oscillations at a metal-dielectric interface, also termed localized surface plasmon resonances, that enhance and focus electromagnetic fields into nanoscale volumes, so-called hotspots. These optical resonances are extremely sensitive to the immediate dielectric surrounding at the optical hotspot [19] and the geometry of the antenna. Proteins entering these hotspots change the local dielectric environment and induce a redshift in the plasmon resonance [7]. This shift can be detected by measuring the shift of the entire resonance [20, 21], or by monitoring the scattering properties of the antenna at a single frequency [22]. For nanoapertures, the latter can be easily monitored at high speeds by the optical transmission through the aperture, where plasmon excitation creates a much enhanced optical transmission (OT), through the sub-diffraction limit aperture [23].

Interestingly, these plasmon resonances provide much more to the sensor than just a read-out. The electromagnetic field concentration into nanoscale hotspots generates very strong spatial gradients in the optical field intensity that can be used to perform tweezing of nanoscale objects [22], providing ample measurement time to characterize the trapped molecule. This has been used in nanoapertures, supported on a glass surface, to tweeze single proteins, characterizing their size [24] and shape [25], and studying protein-DNA binding [26]. However, these plasmon sensors suffer from low

throughput, as they rely on molecular diffusion towards the sensor [10] and they lack a method to perturb the molecule under study and extract dynamic information from it.

Here, we propose a plasmonic nanopore to get the best of both worlds, by equipping a plasmonic nanoantenna for optical trapping with an electric force actuator. Here, the plasmonic nanopore is a nanoaperture not only spans across the gold film, but also penetrates the supporting membrane. A DC bias voltage can be applied across the nanoaperture to actively transport molecules towards the nanoaperture and provide an electrical force on the trapped biomolecules [27]. In the past, some first attempts to create a through-hole plasmonic nanotweezer were made that successfully demonstrated nanotweezing of 20 nm polystyrene beads [28]. However, a demonstration of protein detection as well as electrical biasing of such devices, essential for further development of these promising and versatile biosensors, has not been reported yet to our best knowledge.

Our plasmonic nanopore biosensor uses read-out based on optical transmission (OT) through the plasmonic nanoantenna (Fig. 7.1A). The sensor consists of an inverted-bowtie shaped opening in a gold covered silicon-nitride membrane, where the nanoaperture serves both as an optical antenna and a through hole, allowing simultaneous application of optical and electrokinetic forces. Using the OT through the nanoaperture as a read-out, we demonstrate the nanotweezing capability of the plasmonic nanopore by retaining 20 nm polystyrene nanoparticles inside the nanopore for seconds. We show that the plasmonic nanopore can be used to detect the protein beta-amylase, where the polarity of the detected signals is correctly predicted from the simulated plasmon resonance peak wavelength of the nanostructure. The extended residence times of the protein indicate optical nanotweezing, while the irreversible presence of the protein in the plasmonic nanopore suggests surface interactions to play a significant role in the process. Finally, we characterize the protein detection signal under the application of a transmembrane bias voltage and find that the residence times of the protein decrease and the event rates increase with increasing bias, demonstrating that the DC bias voltage can be used as an experimental force knob to alter the protein behavior in the nanopore.

## 7.2. RESULTS AND DISCUSSION

### 7.2.1. EXPERIMENTAL DESIGN OF THE PLASMONIC NANOPORE EXPERIMENT

Figure 7.1A shows a schematic description on how this is achieved in practice. A sample containing an inverted-bowtie plasmonic nanopore is sandwiched in between two objectives. We use a high NA 60x objective to focus incident 1064 nm wavelength laser light onto a single plasmonic nanopore sensor relies on the excitation of surface plasmons in the nanostructure for nano-optical tweezing and on the collection of optical transmission (OT) through the inverted-bowtie nanoantenna nanoantenna and a low NA 10x objective to collect light transmitted through the antenna and focus it onto an avalanche photo diode (APD). Near-field focusing of the incident optical field by the antenna permits optical nanotweezing of small nanoobjects, like single proteins, and changes in the light transmitted through the antenna report on the presence of the

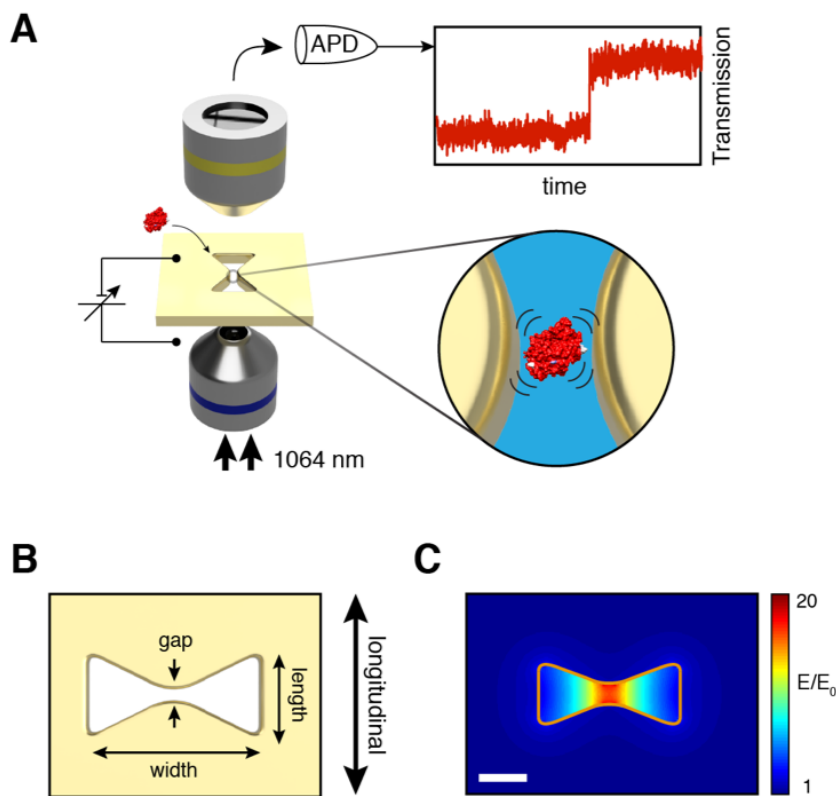


**Figure 7.1: Inverted-bowtie plasmonic nanopore system for optical protein trapping.** (A) Schematics of the plasmonic nanopore experimental setup, where a protein is optically trapped and monitored in a plasmonic nanopore during the application of a variable bias voltage. (B) schematic of a through-hole inverted-bowtie nanoantenna. The definition of the geometrical design parameters is indicated in the figure. (C) Simulated normalized electric-field distribution of the geometry outlined in orange. Field confinement and enhancement up to 20 to the gap region is clearly illustrated. Scale bar is 40 nm.

object. Furthermore, the plasmonic nanopore chip separates two fluidic reservoirs in a custom-made flow cell, which allows for a variable bias voltage to be applied across the membrane and an electrophoretic force to be acted on the object (see Experimental Section 7.4 for details).

Figure 7.1B show a schematic of the optical antenna, with the definition of various geometrical parameters indicated in the figure. The nanoantenna is an inverted-bowtie shaped aperture in a 100 nm/20 nm thick gold/silicon-nitride film, with typical dimensions of a 60 nm side length, 140 nm width, and 20 nm gap (see Fig. 7.1B). Its 20 nm gap is chosen to, at the same time, fit 20 nm-in-diameter nanoobjects and maximize the plasmon focusing of the optical field. Figure 7.1C shows a finite-difference time-domain (FDTD) simulation (see Experimental Section 7.4) of the amplitude of the

optical near field of the antenna excited in longitudinal polarization (as indicated in Fig. 7.1B). This clearly illustrates the field confinement to the gap and shows an electric field enhancement of up to 20 times the incident field strength. The chosen geometry slightly blue detunes the resonance of the antenna, which is purely plasmonic in origin [29]. Exciting the resonance using a longer wavelength than the resonance wavelength boosts the optical forces that can be exerted on the trapped object [30, 31]. Moreover, exciting the nanostructure at the steep edge rather than on resonance maximizes signal for read-out [19].

### 7.2.2. CHARACTERIZATION OF INVERTED-BOWTIE NANOANTENNAS

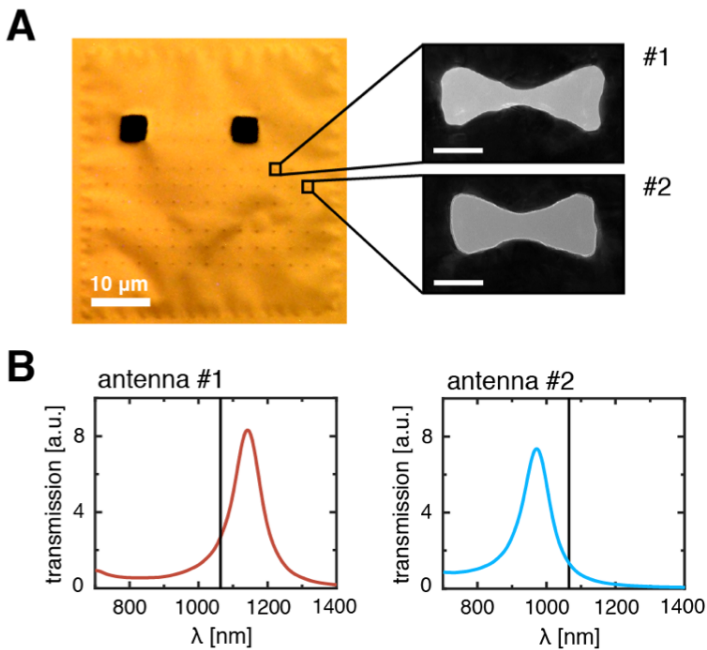


**Figure 7.2: Experimental plasmonic nanopores and simulated optical response.** (A) Optical image of a plasmonic nanopore membrane, with 2 larger apertures (black squares) for detector alignment. The nanoantennas are discernible as the small dots. Two zooms (TEM images) of inverted-bowtie plasmonic nanopores are shown on the right. Scale bars are 50 nm. (B) Simulated transmission spectra of the nanoantennas shown in (A). Antenna #1 has a peak in transmission at a longer wavelength than the excitation laser marked by the black vertical line (i.e. red detuned). Antenna #2 has a peak in transmission at a shorter wavelength than the excitation laser (i.e. blue detuned).

Plasmonic nanoantennas are fabricated using electron-beam lithography and reactive-ion etching on a freestanding SiN membrane. An array of nanoantennas is patterned into an electron-sensitive resist and transferred into the membrane using reactive-ion etching. This process creates an array of inverted-bowtie shaped holes into the membrane. Subsequent evaporation of 100 nm gold onto the membrane leads to

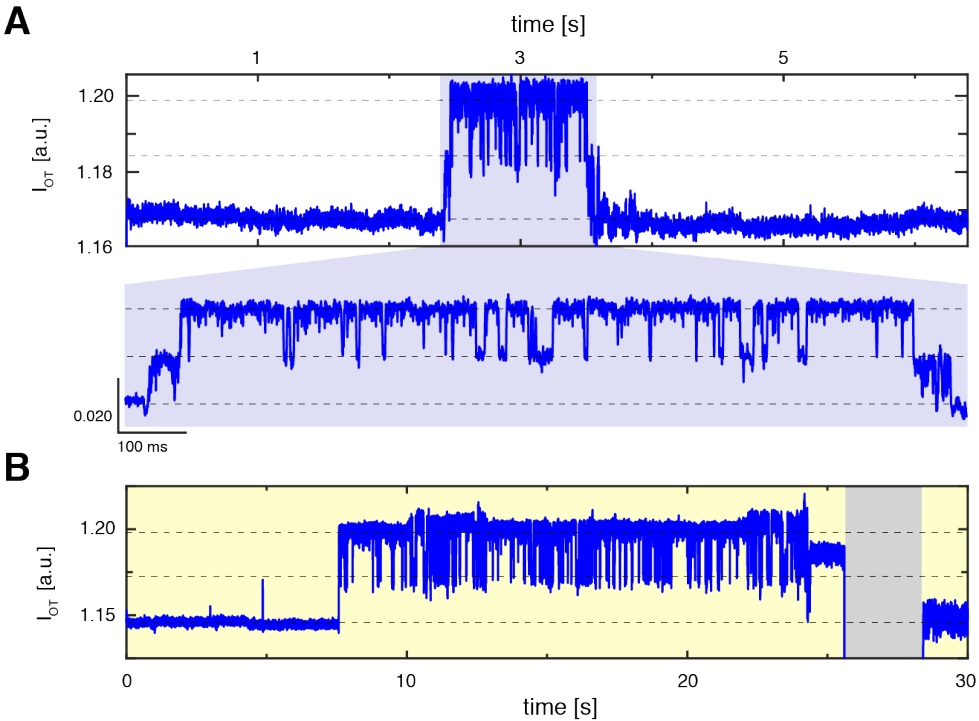
a SiN/gold film perforated with bowtie shaped apertures (see Experimental Section 7.4 for fabrication details). Note that in the fabrication process creates an array of large bowtie-shaped pores into the membrane, making single-molecule electrophysiological measurements on single pores infeasible.

Figure 7.2A shows a bright field image of a plasmonic nanopore membrane of around  $30 \times 30 \mu\text{m}$ , with two  $4 \times 4 \mu\text{m}$  square apertures clearly visible (see Experimental Section 7.4 for details). Some long-range membrane wrinkling is observed, which is due to residual stress release during fabrication in the SiN membrane, but we expect this to not affect the plasmon resonance properties of the individual antennas. The nanoantennas can be discerned as dots arranged in rows on the membrane. Each row has slightly different design parameters, resulting in slightly reduced scattering for rows that run through the large  $4 \times 4 \mu\text{m}$  apertures. Every antenna is spaced at least  $3 \mu\text{m}$  from its neighbor to prevent optical coupling or simultaneous excitation of multiple antennas. The zooms show TEM images of two antennas from this sample, clearly revealing the resulting geometries: antenna #1 (top zoom) with a side length of 61 nm, a width of 166 nm, and a gap of 15 nm, and antenna #2 (bottom zoom) with a side length of 64 nm, a width of 148 nm, and a gap of about 25 nm. Typical variations in resulting geometrical parameters within a row (i.e. with the same design parameters) are  $\pm 7$  nm (see additional images in SI Section 7.5.1). The large variation in geometrical parameters means that only a few of the antennas in the sample are suitable for trapping of nanoobjects. We would like to note that our fabrication method does not yield control over the side-wall taper of our nanostructures, while we expect our nanostructures to be roughly straight walled resulting from the gold evaporation. Additional control over the side-wall taper would be advantageous, as this presents an extra degree of freedom (namely along the thickness of the gold film) that can be used to create additional hotspot confinement [32]. Ion beam milling strategies possess this feature and can be explored as an improved fabrication approach.

The optical response of the resulting plasmonic nanoantennas can be simulated directly using the TEM images (see Experimental Section 7.4). The use of the actual detailed shape deduced from the TEM images allows the antenna geometries to be simulated without the need for geometrical approximations to the average shape and gives a direct comparison between simulation and experiment. The results of the simulation of the optical transmission spectrum when excited in longitudinal polarization, are shown in Fig. 7.2B for the antennas #1 and #2 displayed in Fig. 7.2A. Both antennas show a clear resonance peak in the transmission, with an approximately 100 nm full-width-at-half-maximum, but a clear difference in resonance wavelength can be observed: Antenna #1 (Fig. 7.2B, left) has a resonance at  $\sim 1150$  nm, i.e. at a longer wavelength than the 1064 nm laser wavelength (indicated with a black solid line) whereas antenna #2 (Fig. 7.2B, right) has a resonance at  $\sim 970$  nm, i.e. to the blue of the laser line. Since the gap is smaller and the width is larger for antenna #1, a resonance at a longer wavelength is expected compared the resonance of structure #2 [29]. The position of the resonance peak with respect to the laser line will determine whether the presence of the analyte, which induces a redshift of the resonance, causes an increase or decrease in the OT [30]: a resonance to the blue of the excitation laser will show increases upon particle insertion in the antenna (i.e. structure #2), whereas a resonance to the red of the

excitation laser will show decrease (i.e. structure #1).

### 7.2.3. OPTICAL TRAPPING OF 20 NM POLYSTYRENE BEADS



**Figure 7.3: Optical transmission (OT) signals of 20 nm PS beads trapping in plasmonic nanopores.** (A) OT time trace of plasmonic nanopore trapping event at 10 mW of laser power. The event start is marked by the sharp increase in optical transmission. The zoom reveals that the signal displays two-level hopping, indicative of two PS beads trapped simultaneously, entering and escaping the plasmonic nanopore sequentially. (B) Histogram of the duration of all events and corresponding log-normal fit (solid black line), with an average event duration of  $20 \pm 8$  ms. (C) OT time trace of an extended plasmonic nanopore trapping event at 10 mW of laser power, displaying two-level fluctuations. After switching off the excitation laser, the particles are released.

We first demonstrate the optical nanotweezing capabilities of our inverted-bowtie nanostructures by successfully trapping 20 nm polystyrene (PS) beads. Figure 7.3 displays OT time traces during a trapping experiment, in the absence of any bias voltage. Figure 7.3A shows a typical  $\sim 1$  s trapping event and a zoom thereof (additional trapping traces can be found in the SI Section 7.5.4). The event is marked by a sudden increase of around 3% in the OT through the nanostructure and is characterized by an increase of the fluctuations in the OT intensity. As is clear from the zoom, these fluctuations arise from hopping between two different levels (see zoom Fig. 7.3A). This has been observed before in plasmonic nanotweezer experiments [28] and has been attributed to the trapping of two PS beads simultaneously, where the presence of one nanoparticle strengthens the optical trap for the other, thus creating a more stable trap for both

[28]. Indeed, single level events are observed, but generally last much shorter than the two-level events. The event sequences that we observe support the dual-trapping hypothesis. For example, the event in Fig. 7.3A starts at a lower level ( $\sim 1.184$ ) before the higher level of transmission is attained ( $\sim 1.199$ ), consistent with a sequential entering of two particles into the plasmonic nanopore. Correspondingly, the escape of the particles from the trap displays this sequence in reverse.

The majority of the trapping events are short-lived. 7.3B plots the trapping time histogram of all events. The distribution of event durations follows a log-normal distribution with an average trap time of  $20 \pm 8$  ms (solid-black line), with the short events often only attaining the shallow spike amplitude (see SI 7.5.5). Around 15% of all events have event durations of over 100 ms, the majority of which displays the dual trap behavior described in the previous paragraph.

Very long-lasting trapping events ( $> 1$  s) happen occasionally, in about 1% of all detected events. Figure 7.3C shows the OT time trace of such a dual-trapping event, which is terminated by turning off the excitation laser. Similar event characteristics as described in the previous paragraph are observed in these data, where two particles enter the trap producing  $\sim 4\%$  transmission increase and display two-level fluctuations. Upon turning off the incident laser, the OT returns to its baseline value, and the two-level fluctuations have disappeared. In the example of Fig. 7.3B, the noise in the baseline was significant after release, most likely due to a form of contamination entering the aperture. More trapping traces can be found in the SI Section 7.5.4, including some for different experiments and nanostructures. The results demonstrate that these plasmonic nanopores can be used to tweeze nanoobjects.

## 7

#### 7.2.4. INTERACTION-ASSISTED NANOTWEEZING OF BETA-AMYLASE

Plasmonic nanopores are ultimately aimed as a tool for the investigation of biologically relevant substrates, such as protein or DNA. To demonstrate the ability of the nanoantenna to investigate single proteins, we performed nanotweezing experiments using beta-amylase, a globular 200 kDa protein of around 10 nm in size [33]. Figure 7.4 shows two typical OT time traces from two different nanoantennas (nanoantennas #1 and #2 in Fig. 7.2) after adding beta-amylase at a concentration of 0.03% w/v to the flow cell. Short transients, discrete signals of a particular amplitude (0.7% of the OT baseline signal), can clearly be observed in both traces, which we attributed to the temporary trapping of single protein molecules in the plasmonic nanopore.

Figure 7.4A shows clear increases in the transmission upon protein entering the aperture. These increases are indeed expected, based on simulations of the optical response of the antenna (c.f. Fig. 7.2B, right): a red-shift of the resonance due to the presence of the protein in the antenna, shifts the resonance closer to the excitation wavelength, resulting an increased transmission. On the contrary, Fig. 7.4B shows clear decreases in the transmission, in agreement with simulations, where the antenna resonance is at a longer wavelength than the laser line, indicating that a protein-induced redshift will decrease the transmission through the nanoantenna. Additional traces of protein trapping can be found in the SI Section 7.5.8.

Most of the OT transients (Fig. 7.4B) are short lived (see SI Section 7.5.7), typically lasting less than 10 ms, with a few long-lived events lasting over 100 ms. This is

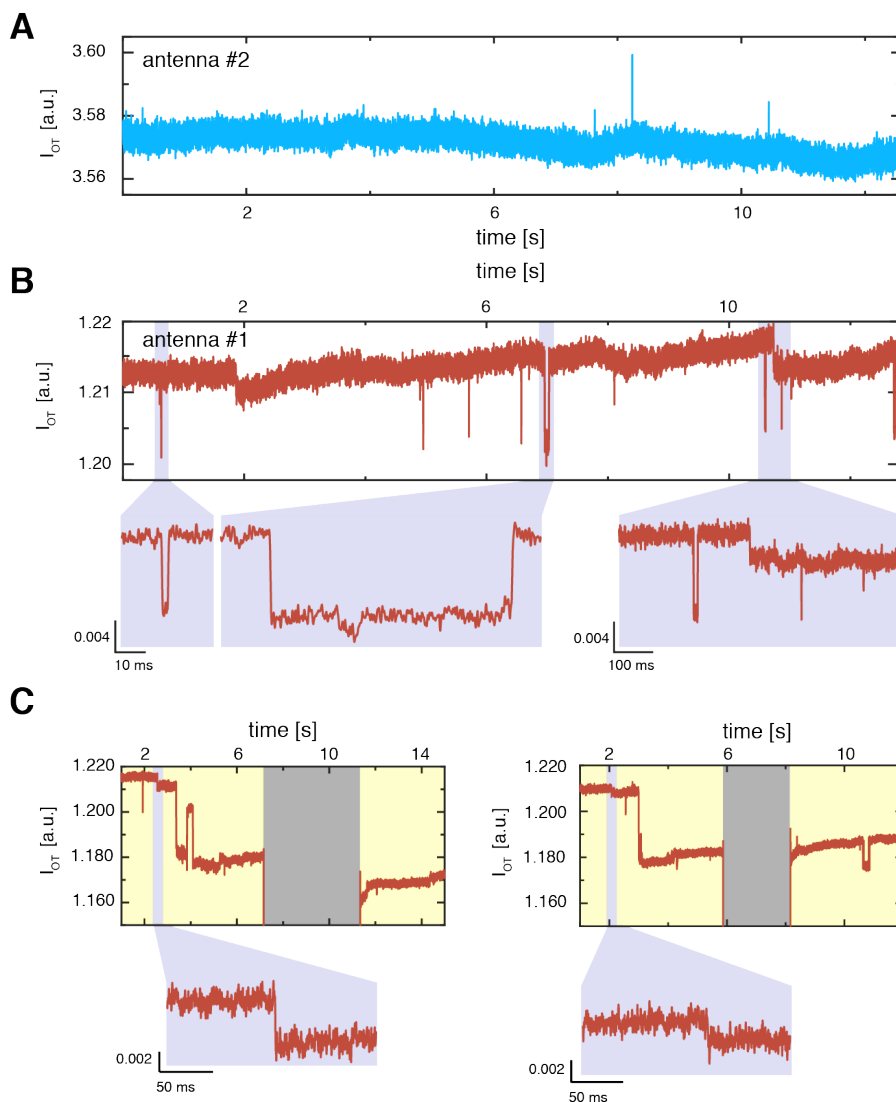


**Figure 7.4: Optical transmission (OT) signals of beta-amylase protein in plasmonic nanopores.** (A) OT time trace of beta-amylase protein temporarily residing in the plasmonic nanopore #2 (Fig. 7.2) at 15 mW of input laserpower. Signal are brief increases in OT, in accordance with the blue-detuned resonance of this antenna to the excitation laser. (B) OT time trace of beta-amylase protein temporarily residing in the plasmonic nanopore #1 (Fig. 7.2) at 15 mW of input laserpower. Signal are decreases in OT, in accordance with the red-detuned resonance of this antenna to the excitation laser. Zooms show short-lived (<10 ms) and long-lived (>100 ms) events, with varying amplitudes and event durations. (C) Two examples of protein molecules denaturing on the surface. The denaturing event is marked by the sudden deep OT decrease and is not released by switching off the excitation laser (black shaded region). The zooms show the protein molecule entering the plasmonic nanopore.

similarly behavior to the spikes observed after the addition of PS beads. However, in the case of the proteins, no clear two-step process is observed for the longer lasting events. Furthermore, no clear increase in noise fluctuations are observed (c.f. Fig. 7.4B, middle) for longer lasting events. An increase in fluctuations was reported before for single-protein trapping in double nanoholes [34], as caused by the Brownian motion of the protein in the nanotrap [34], and was used to identify the size and conformations of trapped particle [8, 24]. The absence of elevated noise levels in our data suggests that Brownian motion is suppressed during the long-lasting events and implies that the protein interacts with the surface, restricting the translational freedom of the protein in the trap. Indeed, unspecific binding of protein to gold surfaces is commonly observed [35] and has been used in plasmon resonance sensing to observe protein molecules and study protein-surface binding kinetics [10]. Moreover, very long-lasting events cannot be released by turning off the laser, indicating that the protein can remain permanently stuck to the surface of the antenna (see Fig. 7.4C and SI Section 7.5.6). We thus expect the surface interactions to play a major role in protein trapping in these structures. In case one would aim to observe trapping of proteins independent of surface interactions, surface passivation strategies can be employed to minimize protein-surface interactions.

Interestingly, some very long-lasting events display two steps, an initial step at a shallow level and a final much deeper OT level ( $\sim 3\%$ ). Figure 7.4C shows two examples of these events, with a zoom of the initial step. The events cannot be removed by switching off the excitation laser (shaded black region). We interpret these events as protein entering (initial shallow step) the plasmonic nanoantenna and subsequently denaturing on the surface of the antenna (deep final step). A denatured protein molecule will produce a larger signal, since it covers a larger part of the most sensitive region in the hotspot and will thus induces a larger resonance shift [21, 34]. Denaturing of the protein can be further enhanced by the elevated temperatures in the gap of the plasmonic antenna. In our case, simulations predict a temperature increase of  $22^\circ\text{C}$  [36], which is not enough to denature the protein fully, but yet can promote the denaturing process significantly [37]. The observation of protein denaturing in the plasmonic nanopore demonstrates that conformational changes of the molecules in the sensor can be monitored.

Further examination of the amplitude of the OT decreases (zooms of Fig. 7.4B) reveals that the spikes show single steps of  $0.8 \pm 0.3\%$  in amplitude, although shallower amplitude drops are also observed (see SI Section 7.5.7). These lower amplitude events can arise for two different reasons. First, the inhomogeneity of optical field distribution inside the antenna causes the signal produced by protein to be sensitive to the position of the protein inside the aperture [38, 39]. The largest signals are produced when the protein resides in the region of the hotspot with the largest local field intensity, exactly in the center of the gap at the surface of the antenna [7]. Optical forces will push protein molecules entering the nanopore towards this region, but surface interactions can occur in the periphery, where the protein molecule produces a lower signal. Second, traces are low-pass filtered at 1 kHz, implying that signals from molecules that spend less than 1 ms in the trap will be distorted by the filtering and will generate a smaller signal amplitude [11].

## 7.2.5. VOLTAGE DEPENDENCE OF BETA-AMYLASE TRAPPING

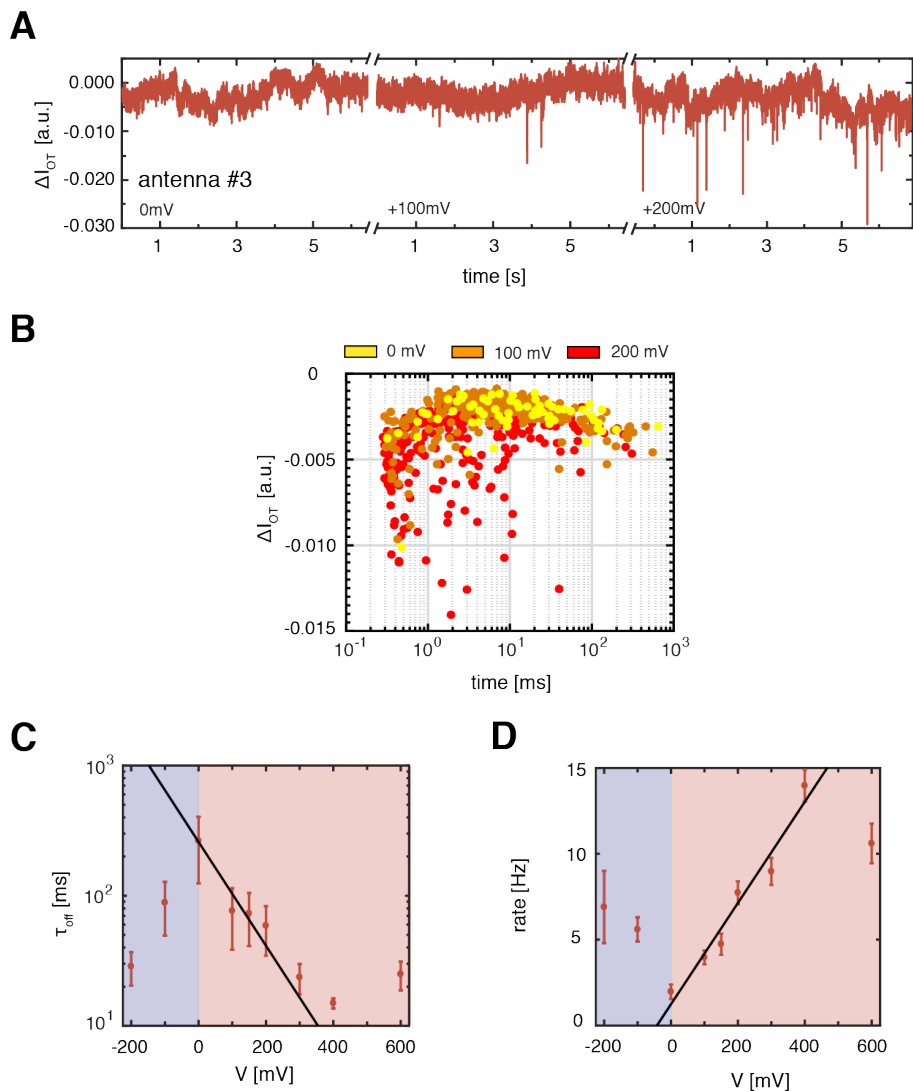


**Figure 7.5: Characterization of the voltage dependence of beta-amylose trapping in a plasmonic nanopore.**

(A) Typical OT time traces of beta-amylose trapping in plasmonic nanopores under 0, 100, and 200 mV bias and 30 mW laser power. (B) OT event amplitude versus dwell time scatter of beta-amylose trapping events at 0, 100 and 200 mV bias. (C) Characteristic dwell time, determined from single-exponential fits to the dwell-time histogram (see SI Section 7.5.9), versus bias voltage. A clear exponential decreasing trend (solid black line, characteristic voltage  $V_0 = 100 \pm 29$  mV,  $\chi^2_{red} = 2.1$ ) can be observed. (D) Event rate versus bias voltage. A clear linear increase (solid black line,  $29 \pm 9$  Hz/V,  $\chi^2_{red} = 1.8$ ) in event rate can be observed for increasing bias voltage. Error bars are standard errors of the histogram fits. All data is recorded on plasmonic nanopore #3, see SI Section 7.5.1.

Plasmonic nanopores allow for the application of electrophoretic forces to the biomolecules to influence their behavior inside the plasmonic nanopore and to facilitate transport of molecules towards it. Figure 7.5A shows OT time traces of beta-amylase trapping experiments under different transmembrane bias conditions in plasmonic nanopore #3 (see SI Section 7.5.1). Again, downward spikes are clearly discernable and become more frequent for larger transmembrane bias.

A detailed analysis of the events reveals that the signal amplitude and the event distribution remain similar at different voltages. Figure 7.5B shows the average event amplitude versus duration at 0, 100, and 200 mV. The scatter maps show significant overlap, indicating that the effect of the bias voltage is subtle. Interestingly, no striking disparity in the residence time population is observed, where a strong dependence of the residence time on voltage might have been expected. Typically, the depth of a potential well for a trapped dielectric nanoparticle is shallow, on the order of a few  $k_B T$  [40]. Even though beta-amylase has a small net charge of  $-2e$  [41], a weak transmembrane bias of 100 mV would already provide enough force on the protein molecule to push it out of the trap. Ignoring electroosmotic forces on the particle, the energy gain upon translocation of the beta-amylase molecule is already 8 kT, which is larger than the depth of the trapping potential. Hence, according to this crude approximation, an applied voltage should affect the trapping dynamics strongly. However, even at large membrane biases ( $> 200$  mV) long events are observed (see Fig. 7.5B), which furthermore indicates that interactions play a significant role in the beta-amylase trapping process.

Yet, the voltage does still affect the interaction-mediated trapping dynamics. Assuming the binding kinetics to dominate the residence time, residence time histograms can be fitted by a single exponential and the characteristic residence time can be extracted (see SI Section 7.5.9 for histograms and corresponding fits). Figure 7.5C shows the characteristic residence times  $\tau_{\text{off}}$  plotted versus bias voltage. A clear decrease in residence times can be observed for larger applied transmembrane bias voltages, showing that the transmembrane bias influences the interaction kinetics of the molecules present in the plasmonic nanopore. The characteristic residence time peaks at 0 mV, i.e. in absence of a transmembrane. An exponential fit of  $\tau_{\text{off}} \sim \exp\left(-\frac{V}{V_0}\right)$  to the data from 0 mV to 400 mV (solid black line, Fig. 7.5C,  $\chi^2_{\text{red}} = 2.1$ ), reveals a characteristic voltage  $V_0$  of  $100 \pm 29$  mV. Considering the binding process to be force dependent, this characteristic voltage can reveal information about the extent of the binding-potential well associated with the bound protein state [42]:  $x_\beta = k_B T / F_{E,0}$ , where  $F_{E,0}$  is the electrical force on the protein molecule at the characteristic voltage. Assuming that the voltage drop is uniform across the 120 nm length of the aperture and using a protein valence of  $2e$ , this translates to a characteristic potential well  $x_\beta = 15 \pm 4$  nm, which is similar to the size of the protein.

Additionally, a transmembrane bias will enhance the event rate as the electric field emanating from the nanopore will pull molecules towards the sensor [43, 44]. Figure 7.5D show the event rate as a function of voltage. A clear increase in event rate is observed for larger transmembrane biases, and a clear minimum is present again in absence of a bias voltage. Surprisingly, also an increase in rate is observed at negative transmembrane biases. This may arise as proteins that have passed the membrane into the trans container (either through the plasmonic nanopores or through the large

alignment apertures in the membrane), will be pulled back through the plasmonic pore. The dependence of the event rate on voltage appears to be linear and a fit on the data points from 0 mV to 400 mV (see Fig. 7.5D, solid black line) shows good agreement with the data ( $\chi_{ref}^2 = 1.8$ ). The linear dependence indicates that the transport towards the pore is diffusion limited [43], as can be expected [11].

### 7.3. DISCUSSION AND CONCLUSION

In summary, we have demonstrated label-free optical detection of single polystyrene beads and single beta-amylase proteins trapped in a plasmonic nanopore, and we characterized the trapping events under the application of a transmembrane bias. Inverted-bowtie plasmonic nanopores were made by electron-beam lithography and plasma etching on a freestanding SiN membrane and subsequent gold evaporation, resulting in through-hole nanoantennas. Characterization through TEM imaging and direct FDTD simulations of the nanoantennas showed sharp resonances near the 1064 nm excitation wavelength, but revealed significant variation ( $\pm 7$  nm) in geometrical parameters. We used the intensity of the optical light transmission (OT) through the nanoantenna, modulated by particle-induced plasmon resonance shifts, as all-optical read-out. First, we verified the optical trapping capabilities of the antenna by trapping 20 nm polystyrene beads. Signals from trapped analytes revealed that two nanoparticles were simultaneously present in the trap and that the particles could be held in the trap for seconds or longer, indicating our nanoantennas can be used as optical nanotweezers. Next, we demonstrated the ability of the nanoantennas to detect and hold single protein molecules, in particular beta-amylase, a 200 kDa protein. The globular protein produced optical transients in the OT through the plasmonic nanopores with a signal polarity, i.e. OT increases or decreases, in agreement with the resonance peak wavelength determined by simulations of the inverted-bowtie geometry. Absence of enhanced fluctuations in OT during long-lasting trapping events and the failure to release them by switching of the excitation laser, revealed strong protein-gold-surface interactions to aid the optical trapping. Moreover, signals of trapped protein molecules showed protein denaturing on the surface of the aperture, possibly promoted by the elevated temperature (about 20°C increase). This indicates that these nanoantennas can be used to monitor and investigate protein conformational changes. Finally, we characterized the behavior of the protein trapping events under the influence of a bias voltage. We revealed that the application of a bias voltage could increase the event rate by over an order of magnitude. We furthermore found the residence time to decrease weakly with increasing bias voltage, again indicating surface effects to play a role in the trapping process. Thus, we clearly demonstrated a functional application of an electrophoretic force onto a trapped protein, providing the experimenter with an extra control handle at the single-molecule level. Further work will focus on reducing protein-surface interactions to establish nanotweezing of free non-surface-bound proteins, improve field confinements using ion-beam milled nanostructures, and determine signatures in the read-out that are characteristic for each protein type.

## 7.4. EXPERIMENTAL METHODS

### 7.4.1. SAMPLE FABRICATION

Plasmonic nanopore devices are fabricated on a 20 nm thin freestanding SiN membrane of around  $40 \times 40 \mu\text{m}$  in size [45]. First, a 50 nm thick layer of PMMA 950K resist is spin coated onto the membranes and subsequently an array of inverted bowties is patterned into the resist using electron-beam pattern generator (EBPG5200, Raith) at an exposure dose of  $3000 \mu\text{C}/\text{cm}^2$ . Then, the pattern is developed in MIBK:IPA 1:3 for 1 min and transferred into the membrane using  $\text{CHF}_3$  plasma etching for 100 sec, with a flow rate of 50 sccm of  $\text{CHF}_3$  and 2.5 sccm of  $\text{O}_2$  and at a power of 40 W and a pressure of 8  $\mu\text{bar}$  (Leybold). The residual resist is stripped in an  $\text{O}_2$  plasma for 3 min at 100 W (Tepla) and, finally, 5 nm of Ti and 100 nm of Au is evaporated onto the membrane at a rate of 1  $\text{\AA}/\text{s}$  and 2  $\text{\AA}/\text{s}$  respectively, using an electron-beam evaporator (Temescal).

### 7.4.2. EXPERIMENTAL SETUP

Prior to the experiment, the sample is rinsed in ethanol and ddH<sub>2</sub>O and cleaned in  $\text{O}_2$  plasma for 30 sec (50 W). The sample is mounted in a custom-made PEEK flowcell that allows for plasmonic nanopore to be optically excited and the transmission light to be collected. The flow cell is filled with either 1X phosphate buffered saline (PBS) or ddH<sub>2</sub>O solution and a voltage is applied over the membrane using a pair of Ag/AgCl electrodes connected to a current amplifier (Stanford). Subsequently, the laser (M9-A64-0200 laser-diode, Thorlabs, operated in constant-current mode) is focused to a diffraction-limited spot on the sample using a 60x 1.2 NA water-immersion objective (Olympus) in an inverted microscope setup (see SI Section 7.5.3 for optical path schematic). The transmission light is collected using a 10x 0.3 NA objective (Nikon) and projected onto an Avalanche Photo Diode (APD410C/M, Thorlabs). Subsequently, the laser focus is positioned to a  $4 \times 4 \mu\text{m}$  aperture in the gold film and aligned to the detector by maximizing the signal on the APD. The plasmonic nanopore is aligned to the laser focus using a piezoelectric positioning stage (MadCity Labs, Inc) and maximizing the transmission through the plasmonic nanopore. Prior to the addition of analyte the light transmission through the antenna is monitored for 5 min to ensure absence of spikes in the transmission signal. Subsequently analyte is flushed in. 20 nm polystyrene beads (Thermofischer) are dispensed in 0.02% w/v SDS in ddH<sub>2</sub>O to a concentration of 0.02% w/v. Beta-amylase proteins (Sigma) are dispensed in 1X PBS to a concentration 0.03% w/v. Data acquisition is performed using custom made Labview software through a NI DAQ (NI USB-6251, National Instruments) at a sampling rate of 200 kHz.

### 7.4.3. EVENT DETECTION AND ANALYSIS

Event detection and analysis is performed using Tranzalyser [41], a custom-made MATLAB-based software package developed in our lab. All traces are low-pass filtered using a Gaussian filter with a cut-off at 1 kHz for analysis. Event detection is done using a 6 sigma threshold spike detection, using a baseline and sigma value calculated from a moving average window of 10000 data points.

#### 7.4.4. FDTD SIMULATIONS

We use FDTD Solutions (Lumerical Solutions, Inc., Canada) to model the optical properties of the inverted-bowtie plasmonic nanoantennas. The inverted bowtie is modeled a bowtie-shaped aperture in a 100 nm thick gold film with a side length of 60 nm, a width of 140 nm, a 20 nm gap, and 40 nm-in-radius in-plane tip rounding to best resemble the fabricated structures. The antenna is supported by a 20 nm thin silicon-nitride membrane with a refractive index (RI) of 2. The surrounding medium is modeled as water with a RI of 1.33. Symmetry is used to reduce the computational time. The plasmonic aperture is excited by a pulse from a total-field scattered-field source incident normal to the gold surface, and with the polarization in either the longitudinal or the transverse mode. The fractional light transmission through the nanostructure is calculated by integrating the far-field power flux through a screen placed 350 nm below the membrane and normalized to the total incident power at each frequency.

The optical response of the fabricated nanostructures is simulated by thresholding the planar geometry from a TEM image, using the image import function, and extruding it 100 nm perpendicular to the gold film to create an aperture in the film.

## 7.5. SUPPORTING INFORMATION

### 7.5.1. ADDITIONAL TEM IMAGES OF INVERTED-BOWTIE PLASMONIC NANOPORE SHAPES AND CORRESPONDING SIMULATED OPTICAL RESPONSE

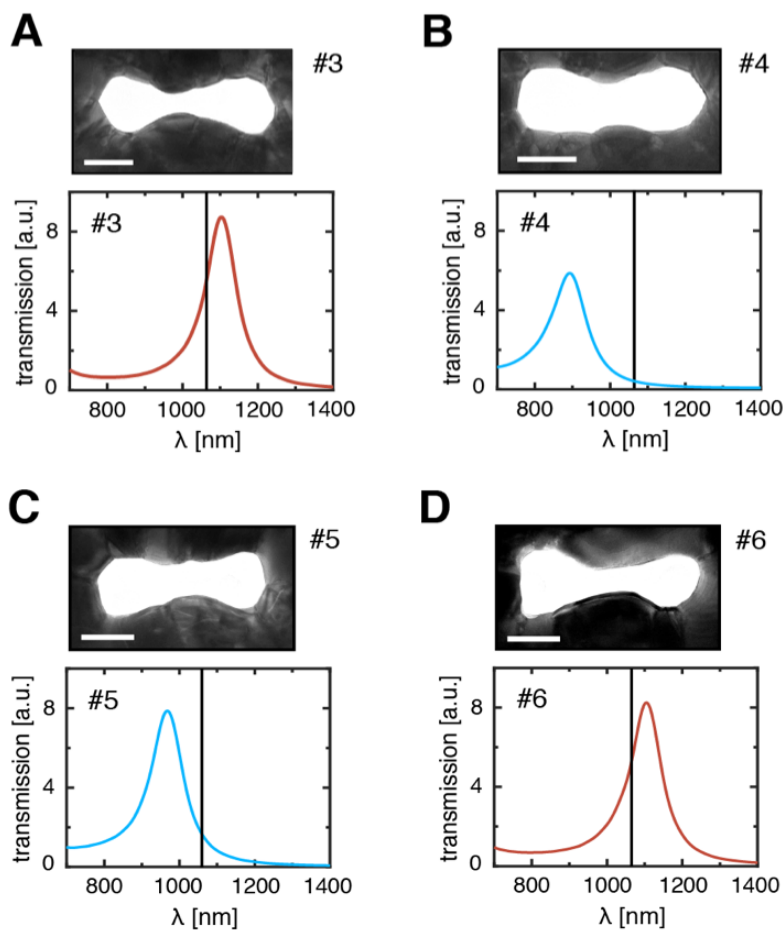


**Figure S7.6: Additional TEM images of resulting plasmonic nanopores shapes and the corresponding simulated optical response. Scale bars are 50 nm. Antennas are labeled and corresponding data sets to identify the antenna used to acquire the data set.**

### 7.5.2. SIMULATION OF IDEALIZED INVERTED-BOWTIE NANOANTENNA IN TRANSVERSE POLARIZATION

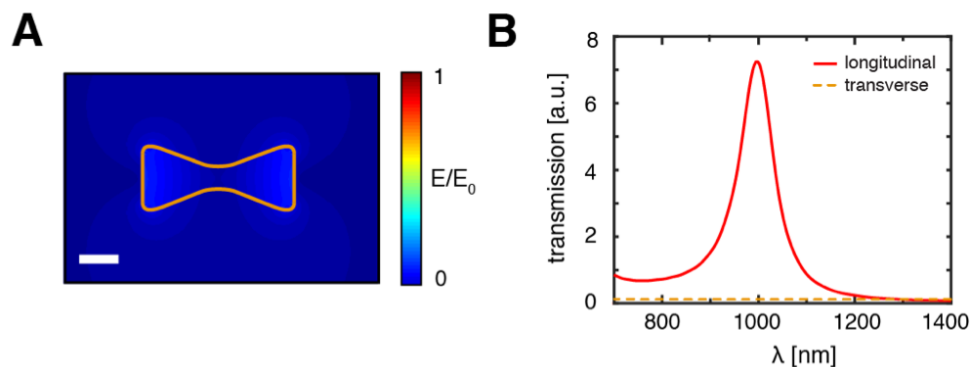


**Figure S7.7: Simulated optical response of the inverted-bowtie nanoantenna.** (A) normalized electric field density distribution under transverse illumination. No optical field enhancement is observed, and in a field density minimum can be found in the gap region. (B) simulated light transmission spectra of the nanostructure under longitudinal and transverse illumination.

### 7.5.3. SCHEMATICS OF OPTICAL SETUP

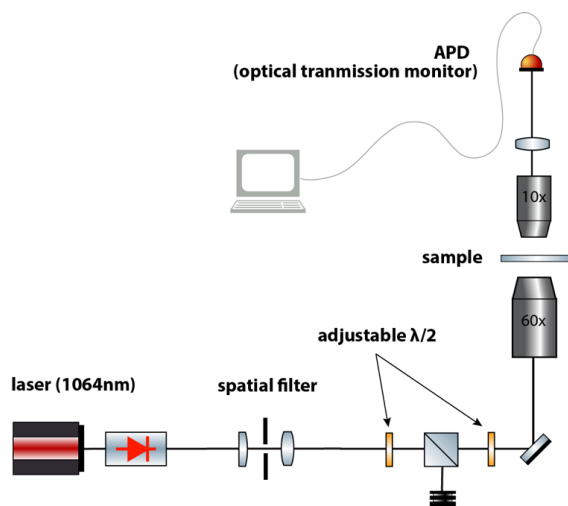


**Figure S7.8: Schematics of the optical setup.** A 1064 nm laser is passed through an optical isolator to prevent optical feedback into the diode laser. Subsequently, the beam is passed through a spatial filter to remove stray light from the laser beam and expand the beam. The beam is then passed through an adjustable half-wave plate ( $\lambda/2$ ) and a polarizing beam splitter to control the laser output power. The laser is put through another half-wave plate to control the polarization of the laser beam and focused onto the sample using a 60x 1.2 NA water-immersion objective. The light transmitted through the antenna is collected using a 10x 0.3 NA objective and monitored using an avalanche photo diode.

### 7.5.4. ADDITIONAL TRACES OF PS BEAD TRAPPING

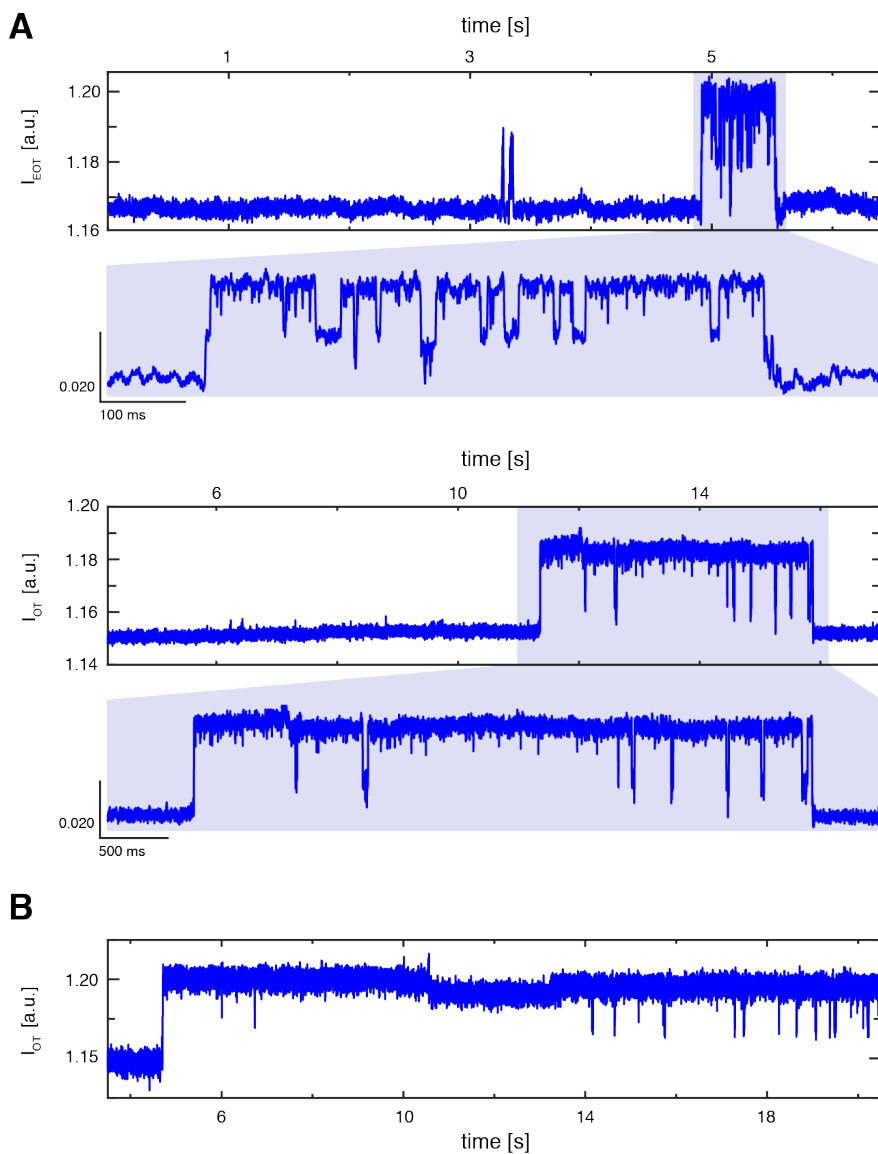


**Figure S7.9: Additional PS-bead trapping traces from the same data set as discussed in the main text (A) Dual PS bead trapping, where two beads subsequently enter and escape. (B) Indefinite PS bead trapping, lasting up to several seconds**

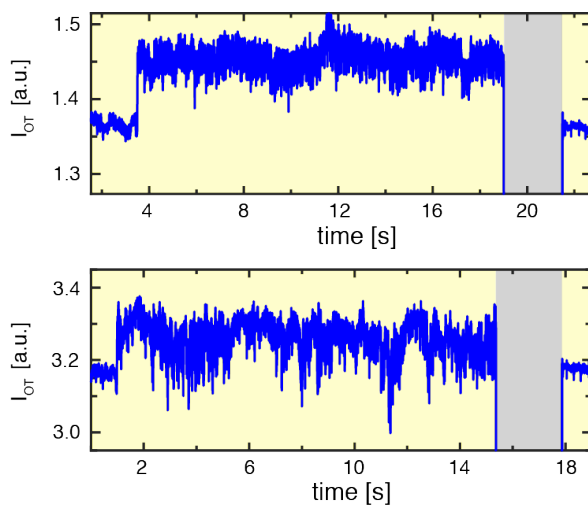


**Figure S7.10:** Additional PS-bead trap-and-release traces from different datasets.

### 7.5.5. AVERAGE EVENT AMPLITUDE VERSUS EVENT DURATION SCATTERPLOT OF PS BEAD TRAPPING

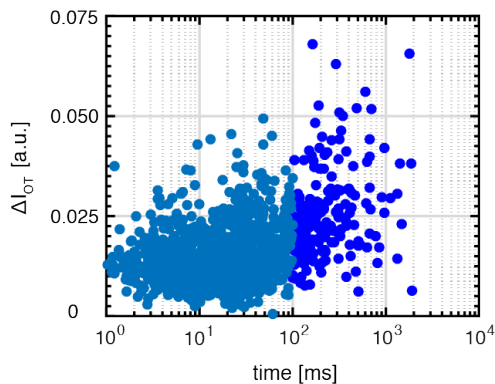


**Figure S7.11: Average event amplitude versus event duration scatter plot of PS bead trapping.** Out of all trapping events, 15% lasts longer than 100 ms (indicated dark blue). As can be observed from the scatterplot, most event are shallow and short lived.

### 7.5.6. EXAMPLE TRACE OF PROTEIN-GOLD-SURFACE BINDING

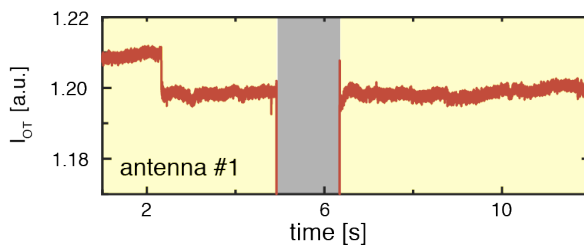


**Figure S7.12: Trap-and-stick trace during beta-amylase trapping.** The protein enters the trap, indicated by a characteristic drop in the OT. Subsequently switching off the laser (black shaded region) does not result in recovery of the OT baseline and indicates a molecule permanently stuck in the trap, bound to the surface of the gold antenna.

## 7.5.7. EVENT ANALYSIS OF BETA-AMYLASE TRAPPING EVENTS

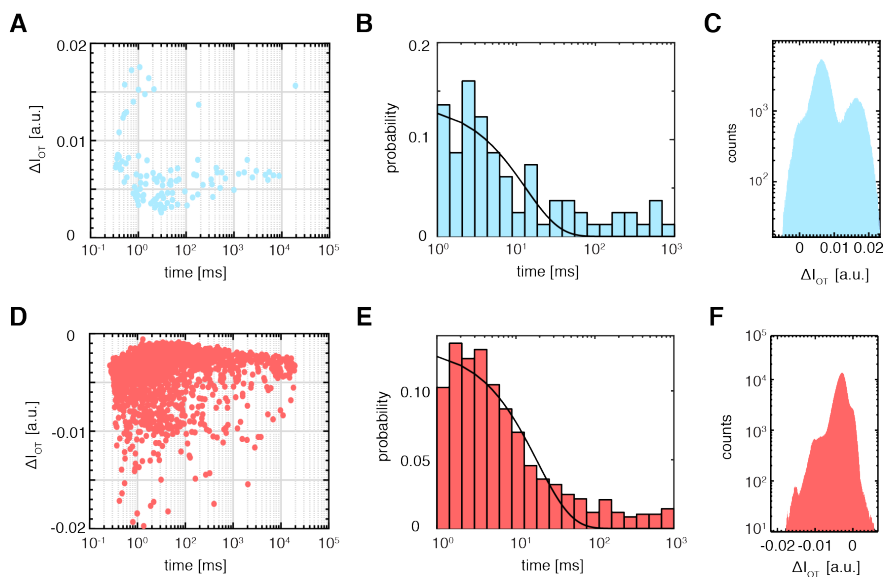


**Figure S7.13: Analysis of beta-amylase trapping** (A)-(C) Analysis of all trapping events in antenna #2 (OT increases upon trapping of a protein molecule). (A) Average event amplitude versus event duration. (B) Event duration histogram and corresponding single-exponential fit. (C) All-points histogram of all events. (D)-(F) Analysis of all trapping events in antenna #1 (OT decreases upon trapping of a protein molecule). (D) Average event amplitude versus event duration. (E) Event duration histogram and corresponding single-exponential fit. (F) All-points histogram of all events.

### 7.5.8. ADDITIONAL TIME TRACES OF BETA-AMYLASE TRAPPING IN DIFFERENT PLASMONIC NANOPORES

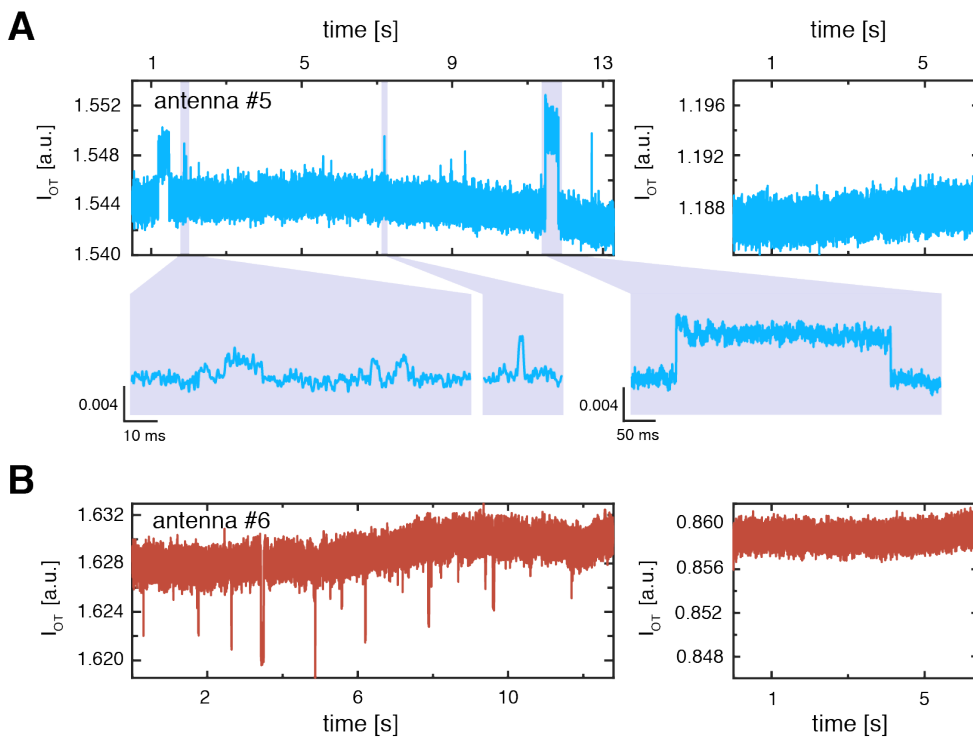


**Figure S7.14: Additional time traces of beta-amylase trapping in plasmonic nanopores. Inspection after the experiment showed severe contamination of the antennas. (A) trapping of beta-amylase in antenna #5. Clear OT increases can be observed in longitudinal polarization (left), but are absent in transverse polarization (right). Zoom of the events show, as discussed in the main text, signals with different amplitudes. (B) trapping of beta-amylase in antenna #6. Clear OT decreases can be observed in longitudinal polarization (left), but are absent in transverse polarization (right).**

### 7.5.9. DWELL TIME HISTOGRAMS OF BETA-AMYLASE TRAPPING

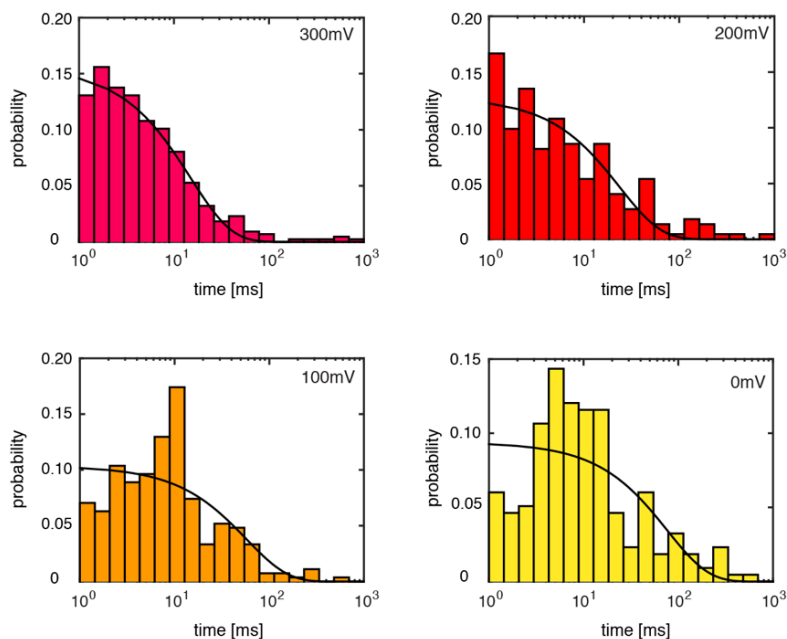


**Figure S7.15:** Dwell time histograms and corresponding exponential fits of beta-amylase trapping at (A) 100 mV, (B) 200 mV, (C) 300 mV, (D) 0 mV. The resulting fit values ( $\tau_{\text{off}}$ ) are plotted in main text Fig. 7.5C.

## REFERENCES

- [1] J. J. Gooding and K. Gaus, *Single-molecule sensors: Challenges and opportunities for quantitative analysis*, *Angewandte Chemie International Edition* **55**, 11354 (2016).
- [2] A. Ishijima and T. Yanagida, *Single molecule nanobioscience*, *Trends in biochemical sciences* **26**, 438 (2001).
- [3] M. Muthukumar, C. Plesa, and C. Dekker, *Single-molecule sensing with nanopores*, *Physics Today* **68**, 40 (2015).
- [4] A. A. Al Balushi, A. Kotnala, S. Wheaton, R. M. Gelfand, Y. Rajashekar, and R. Gordon, *Label-free free-solution nanoaperture optical tweezers for single molecule protein studies*, *Analyst* **140**, 4760 (2015).
- [5] S. Howorka and Z. Siwy, *Nanopore analytics: sensing of single molecules*, *Chemical Society Reviews* **38**, 2360 (2009).
- [6] C. Dekker, *Solid-state nanopores*, *Nature nanotechnology* **2**, 209 (2007).
- [7] A. B. Taylor and P. Zijlstra, *Single-molecule plasmon sensing: current status and future prospects*, *ACS sensors* **2**, 1103 (2017).

- [8] A. A. Al Balushi and R. Gordon, *Label-free free-solution single-molecule protein–small molecule interaction observed by double-nanohole plasmonic trapping*, ACS Photonics **1**, 389 (2014).
- [9] M. J. Levene, J. Korlach, S. W. Turner, M. Foquet, H. G. Craighead, and W. W. Webb, *Zero-mode waveguides for single-molecule analysis at high concentrations*, science **299**, 682 (2003).
- [10] A. B. Dahlin, *Sensing applications based on plasmonic nanopores: The hole story*, Analyst **140**, 4748 (2015).
- [11] C. Plesa, S. W. Kowalczyk, R. Zinsmeister, A. Y. Grosberg, Y. Rabin, and C. Dekker, *Fast translocation of proteins through solid state nanopores*, Nano letters **13**, 658 (2013).
- [12] L.-Q. Gu and J. W. Shim, *Single molecule sensing by nanopores and nanopore devices*, Analyst **135**, 441 (2010).
- [13] G. Huang, K. Willems, M. Soskine, C. Wloka, and G. Maglia, *Electro-osmotic capture and ionic discrimination of peptide and protein biomarkers with frac nanopores*, Nature communications **8**, 935 (2017).
- [14] J. Larkin, R. Y. Henley, M. Muthukumar, J. K. Rosenstein, and M. Wanunu, *High-bandwidth protein analysis using solid-state nanopores*, Biophysical journal **106**, 696 (2014).
- [15] H. Bayley, *Nanopore sequencing: from imagination to reality*, Clinical chemistry **61**, 25 (2015).
- [16] C. Plesa, D. Verschueren, S. Pud, J. van der Torre, J. W. Ruitenbergh, M. J. Witteveen, M. P. Jonsson, A. Y. Grosberg, Y. Rabin, and C. Dekker, *Direct observation of dna knots using a solid-state nanopore*, Nature nanotechnology **11**, 1093 (2016).
- [17] A. Squires, E. Atas, and A. Meller, *Nanopore sensing of individual transcription factors bound to dna*, Scientific reports **5**, 11643 (2015).
- [18] O. K. Dudko, J. Mathé, and A. Meller, *Nanopore force spectroscopy tools for analyzing single biomolecular complexes*, in *Methods in enzymology*, Vol. 475 (Elsevier, 2010) pp. 565–589.
- [19] S. A. Maier, *Plasmonics: fundamentals and applications* (Springer Science & Business Media, 2007).
- [20] I. Ament, J. Prasad, A. Henkel, S. Schmachtel, and C. Sönnichsen, *Single unlabeled protein detection on individual plasmonic nanoparticles*, Nano letters **12**, 1092 (2012).
- [21] P. Zijlstra, P. M. Paulo, and M. Orrit, *Optical detection of single non-absorbing molecules using the surface plasmon resonance of a gold nanorod*, Nature nanotechnology **7**, 379 (2012).
- [22] M. L. Juan, M. Righini, and R. Quidant, *Plasmon nano-optical tweezers*, Nature

- Photonics **5**, 349 (2011).
- [23] C. Genet and T. Ebbesen, *Light in tiny holes*, Nature **445**, 39 (2007).
- [24] S. Wheaton and R. Gordon, *Molecular weight characterization of single globular proteins using optical nanotweezers*, Analyst **140**, 4799 (2015).
- [25] S. Wheaton, R. M. Gelfand, and R. Gordon, *Probing the raman-active acoustic vibrations of nanoparticles with extraordinary spectral resolution*, Nature Photonics **9**, 68 (2015).
- [26] A. Kotnala and R. Gordon, *Double nanohole optical tweezers visualize protein p53 suppressing unzipping of single dna-hairpins*, Biomedical optics express **5**, 1886 (2014).
- [27] M. Belkin, S.-H. Chao, M. P. Jonsson, C. Dekker, and A. Aksimentiev, *Plasmonic nanopores for trapping, controlling displacement, and sequencing of dna*, ACS nano **9**, 10598 (2015).
- [28] C. Chen, M. L. Juan, Y. Li, G. Maes, G. Borghs, P. Van Dorpe, and R. Quidant, *Enhanced optical trapping and arrangement of nano-objects in a plasmonic nanocavity*, Nano letters **12**, 125 (2011).
- [29] H. Guo, T. P. Meyrath, T. Zentgraf, N. Liu, L. Fu, H. Schweizer, and H. Giessen, *Optical resonances of bowtie slot antennas and their geometry and material dependence*, Optics express **16**, 7756 (2008).
- [30] P. Mestres, J. Berthelot, S. S. Aćimović, and R. Quidant, *Unraveling the optomechanical nature of plasmonic trapping*, Light: Science & Applications **5**, e16092 (2016).
- [31] M. L. Juan, R. Gordon, Y. Pang, F. Eftekhari, and R. Quidant, *Self-induced back-action optical trapping of dielectric nanoparticles*, Nature Physics **5**, 915 (2009).
- [32] Y. Chen, A. Kotnala, L. Yu, J. Zhang, and R. Gordon, *Wedge and gap plasmonic resonances in double nanoholes*, Optics express **23**, 30227 (2015).
- [33] R. Lundgard and B. Svensson, *The four major forms of barley  $\beta$ -amylase. purification, characterization and structural relationship*, Carlsberg research communications **52**, 313 (1987).
- [34] Y. Pang and R. Gordon, *Optical trapping of a single protein*, Nano letters **12**, 402 (2011).
- [35] S. Choi and J. Chae, *Methods of reducing non-specific adsorption in microfluidic biosensors*, Journal of Micromechanics and Microengineering **20**, 075015 (2010).
- [36] F. Nicoli, D. Verschueren, M. Klein, C. Dekker, and M. P. Jonsson, *Dna translocations through solid-state plasmonic nanopores*, Nano letters **14**, 6917 (2014).
- [37] R. R. Ray, S. C. Jana, and G. Nanda, *Biochemical approaches of increasing thermostability of  $\beta$ -amylase from bacillus megaterium b6*, FEBS letters **356**, 30

- (1994).
- [38] T. J. Antosiewicz and M. Käll, *A multiscale approach to modeling plasmonic nanorod biosensors*, *The Journal of Physical Chemistry C* **120**, 20692 (2016).
- [39] J. Yang, H. Giessen, and P. Lalanne, *Simple analytical expression for the peak-frequency shifts of plasmonic resonances for sensing*, *Nano letters* **15**, 3439 (2015).
- [40] A. Zehtabi-Oskuie, H. Jiang, B. R. Cyr, D. W. Rennehan, A. A. Al-Balushi, and R. Gordon, *Double nanohole optical trapping: dynamics and protein-antibody co-trapping*, *Lab on a Chip* **13**, 2563 (2013).
- [41] C. Plesa and C. Dekker, *Data analysis methods for solid-state nanopores*, *Nanotechnology* **26**, 084003 (2015).
- [42] G. I. Bell, *Models for the specific adhesion of cells to cells*, *Science* **200**, 618 (1978).
- [43] A. Y. Grosberg and Y. Rabin, *Dna capture into a nanopore: interplay of diffusion and electrohydrodynamics*, *The Journal of chemical physics* **133**, 10B617 (2010).
- [44] M. Firnkes, D. Pedone, J. Knezevic, M. Doblinger, and U. Rant, *Electrically facilitated translocations of proteins through silicon nitride nanopores: conjoint and competitive action of diffusion, electrophoresis, and electroosmosis*, *Nano letters* **10**, 2162 (2010).
- [45] X. J. Janssen, M. P. Jonsson, C. Plesa, G. V. Soni, C. Dekker, and N. H. Dekker, *Rapid manufacturing of low-noise membranes for nanopore sensors by trans-chip illumination lithography*, *Nanotechnology* **23**, 475302 (2012)

# 8

## TEMPERATURE DEPENDENCE OF DNA TRANSLOCATIONS THROUGH SOLID-STATE NANOPORES

*In order to gain a better physical understanding of DNA translocations through solid-state nanopores, we study the temperature dependence of  $\lambda$ -DNA translocations through 10 nm-in-diameter silicon-nitride nanopores, both experimentally and theoretically. The measured ionic conductance  $G$ , the DNA-induced ionic-conductance blockades  $\Delta G$  and the event frequency  $\Gamma$  all increase with increasing temperature while the DNA translocation time  $\tau$  decreases.  $G$  and  $\Delta G$  are accurately described when bulk and surface conductances of the nanopore are considered and access resistance is incorporated appropriately. Viscous drag on the untranslocated part of the DNA coil is found to dominate the temperature dependence of the translocation times and the event rate is well described by a balance between diffusion and electrophoretic motion. The good fit between modeled and measured properties of DNA translocations through solid-state nanopores in this first comprehensive temperature study, suggest that our model captures the relevant physics of the process.*

---

This chapter has been published as: Daniel V. Verschuere, Magnus P. Jonsson, and Cees Dekker. Temperature dependence of DNA translocations through solid-state nanopores. *Nanotechnology*, 26(23):234004, 2015

## 8.1. INTRODUCTION

Solid-state nanopores are an emerging class of label-free, single-molecule biosensors, which are receiving great attention owing to their versatility and conceptual simplicity [1, 2]. At the heart of the nanopore sensor is a nanometer-sized hole, drilled in a thin silicon nitride membrane. Immersed between two containers filled with electrolyte, an ionic current can flow through this pore upon application of a bias voltage across the two containers. Charged biomolecules, such as DNA, are driven through the nanopore by the local electric field and partially obstruct the pore during passage. As a result, the current through the nanopore is reduced during this translocation, which provides the sensing signal for the single molecule. Nanopore devices have already found their way to a multitude of applications such as investigating DNA polymer physics [3, 4], anti-body binding kinetics [5], protein characterization [6–9], DNA depurination [10], and probing proteins bound on DNA [11–13].

Solid-state nanopore sensing systems have been integrated with laser optics in the past to affect DNA motion through the nanopore [14–16]. More recently, they have been combined with plasmonic optical antennas [17–21] to provide an alternative sensing method that complements the ionic current read-out. However, optical power concentration can lead to substantial local heating [22], most notably in plasmonic antennas [17, 23–26]. For such electro-optical nanopore systems, it is essential to understand how a temperature change affects the translocation process and nanopore conductance. A thorough understanding of the temperature dependence of the nanopore conductance will make it feasible to use the pore as a temperature probe with nanometer spatial resolution, for example, to quantify plasmonic heating from single nanostructures [25].

More generally, to extract biomolecular properties from a nanopore sensing experiment, it is vital to understand the fundamental physics that govern the translocation dynamics of the analyte. Previous investigations to elucidate these fundamentals have focused on voltage dependence [27, 28], DNA-length dependence [29], electrolyte ionic-strength dependence [30, 31] or a combination of those parameters [32], but the temperature dependence has remained largely uninvestigated. Some reports on DNA translocations through solid-state nanopores at different temperatures have been published [17, 32–34], including an extensive temperature analysis of DNA translocations through  $\alpha$ -hemolysin pores [35]. Surprisingly however, a comprehensive study on the temperature dependence of DNA translocations through solid-state nanopores has not been published to date.

Four translocation characteristics can be extracted for a translocation experiment, as indicated in Figure 8.1A: the pore conductance  $G$ , the conductance drop produced by a translocating biomolecule  $\Delta G$ , the translocation time  $\tau$ , and the event rate  $\Gamma$ . Here we report the temperature dependence of these characteristics experimentally and we describe a model to explain our observations.

## 8.2. MATERIALS AND METHODS

We fabricate nanopore devices as explained in [36]. Prior to measurements the chips were cleaned in an  $O_2$  plasma (50 W) for 1 minute. All experiments were performed

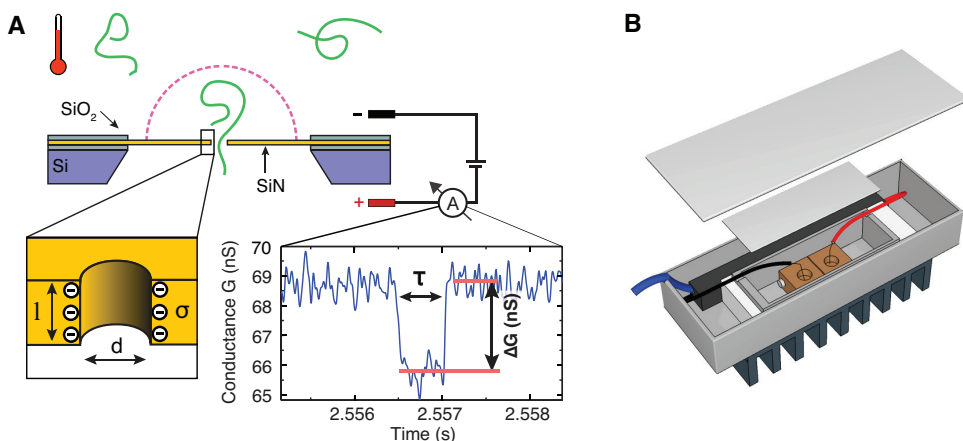


**Figure 8.1:** (A) schematics of a nanopore experiment. A nanometer-sized hole of diameter  $d$  is drilled into a thin silicon-nitride membrane of thickness  $l$ . During an experiment the conductance  $G$  of the nanopore is monitored and modulated by  $\Delta G$  upon passage of a DNA molecule.  $G$ ,  $\Delta G$ , the translocation time  $\tau$  and the event rate  $\Gamma$  (the capture radius is depicted as the pink dashed hemisphere) are investigated here as a function of temperature. (B) Experimental setup consisting of two Faraday cages and a peltier heater/cooler. The PEEK flow cell is located in the inner Faraday cage, the head-stage of the amplifier in the outer.

on 8 to 16 nm diameter pores in 1 M KCl, 10 mM Tris and 2 mM EDTA buffer. DNA translocations were done with  $\lambda$ -DNA (Promega) at  $\Delta V = 100$  mV bias. To heat or cool the flow cell, a Peltier heater/cooler was used, as shown in Figure 8.1B, with LABVIEW-controlled PID feedback. The temperature was monitored using two Pt100 thermistors, one directly placed on the flow cell and the other on the inner Faraday cage. For each newly set temperature, the flow cell was left to equilibrate for 20 min before acquisition. Acquisitions at different temperatures were carried out in random order and acquisition at room temperature (296 K) was always conducted at multiple occasions during an experiment, to prevent the convolution of changes due to temperature and residual temporal drifts in the system. Acquisition was done using an Axopatch 200B (Molecular Devices Ltd.) controlled by a custom-made LABVIEW program, and analysis of the data was done using a MATLAB-software package recently developed in our lab [37]. Pore diameters were obtained from TEM images (see Supporting Information (SI) Section 8.6.3) analyzed using ImageJ. All fitting is done by minimizing a  $\chi^2$  goodness-of-fit parameter using a simple weighted linear regression, where  $\chi^2 = \frac{1}{N-2} \sum_{i=1}^N \left( \frac{y_i - \bar{y}_i}{s_i} \right)^2$ . Here  $N$  is the number of data points,  $N - 2$  the degrees of freedom in the fit (single fit parameter),  $y_i$  is the experimental data point,  $\bar{y}_i$  the corresponding predicted value by the fitted model and  $s_i$  is the respective error.

## 8.3. RESULTS

### 8.3.1. OPEN PORE CONDUCTION

Understanding the origins of the current through a nanopore is crucial for any nanopore experiment, as this current underlies the signal of the sensor. Figure 8.2 shows the

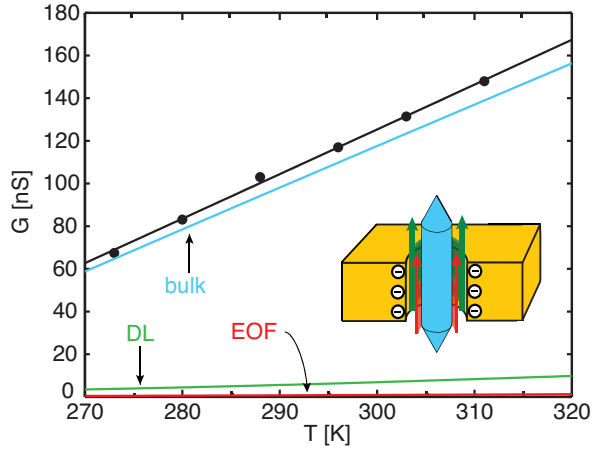


**Figure 8.2:** Temperature dependence of the conductance  $G$  of a  $d = 16$  nm nanopore in 1 M KCl. The black dots are experimental data points and the solid black line is a fit from equation 8.2. The inset shows the different contributions to the current. The bulk conductance is displayed in blue, and the surface conductances from the double-layer (DL) and electroosmotic flow (EOF) are displayed in green and red respectively.

experimental conductance (black dots) of a nanopore at different temperatures. The conductance of the pore is obtained from the slope of the linear  $I$ - $V$  curve taken between +200 mV and -200 mV. There is a strong linear increase in the conductance of the pore with increasing temperature, showing a high sensitivity  $\frac{dG}{dT} = 0.21$  nS/K of the pore conductance to temperature, which represents a doubling of the pore current over a range of only 35 K.

Several efforts have already been made to elucidate the contributions to the ionic pore current analytically [16, 30, 38]. None of these models have been specifically tested through the temperature dependence of the current. Here, we describe our model. A rigorous derivation of the ionic conduction of the nanopore and its temperature dependence is provided in SI Section 8.6.1.

Starting from the Poisson equation and the Nernst-Planck particle flux through a cylinder of diameter  $d$  and length  $l$  with a uniform surface charge density  $\sigma$ , one obtains (see SI Section 8.6.1) an expression for the pore conductance

$$G_{cyl} = \left[ \kappa_{bulk} \frac{\pi d^2}{4l} + \mu_K |\sigma| \frac{\pi d}{l} + \frac{\pi \sigma^2 r_D d}{\eta l} \right]. \quad (8.1)$$

Here  $\eta$  is the viscosity,  $d$  is the pore diameter,  $l$  is the pore length,  $\kappa_{bulk}$  is the bulk buffer conductivity of the electrolyte in the pore (1 M KCl in our case),  $\mu_K$  and  $\mu_{Cl}$  are the mobilities for the two major charge carriers  $K^+$  and  $Cl^-$  respectively, and  $r_D$  is the Debye length, which is the typical length scale over which the ion density significantly changes from the concentration in bulk.

Equation 8.1 shows the 3 main contributions to the nanopore conductance, as schematically indicated by the inset in Figure 8.2. By far the major contributor for these wide nanopores ( $d \gtrsim 10$  nm) is the first term, the bulk conductance. Ions within the electrolyte are mobile, giving rise to this bulk conductance. The second term is the

double-layer (DL) conductance. The electrolyte will act to screen surface charges of the silicon nitride by forming an excess layer of counterions at the pore surface [39]. Since the silicon-nitride surface charge density is negative, the (mobile) screening layer will be composed of potassium ions, which will move in the applied field, thus contributing a double-layer conductance. Finally, this net charge flow will set the background medium within the pore into motion. The flow that this creates, drags the charge of the double-layer, resulting in the electroosmotic flow (EOF) contribution to the pore conductance [16].

To model the conductance of a real nanopore, two more effects need to be accounted for: nanopores are in general not perfect cylinders and there is an access resistance that extends outside of the pore. Analogously to our previous work [40], we assume a total access resistance of  $G_{access}^{-1} = (\kappa_{bulk}d)^{-1}$  in series with a cylindrical pore resistance, and we use an effective pore length  $l_{eff}$  to correct for the non-cylindrical shape of the nanopore. By evaluating the potential drop over the cylindrical pore, one finds the conductance of the nanopore to be

$$G = \left[ \kappa_{bulk}(T) \frac{\pi d^2}{4} + \mu_K(T) |\sigma(T)| \pi d + \frac{\pi \sigma^2(T) r_D(T) d}{\eta(T)} \right] \frac{1}{l_{eff} (1 + \xi(T))}, \quad (8.2)$$

$$\xi(T) = \frac{G_{cyl}}{G_{access}}. \quad (8.3)$$

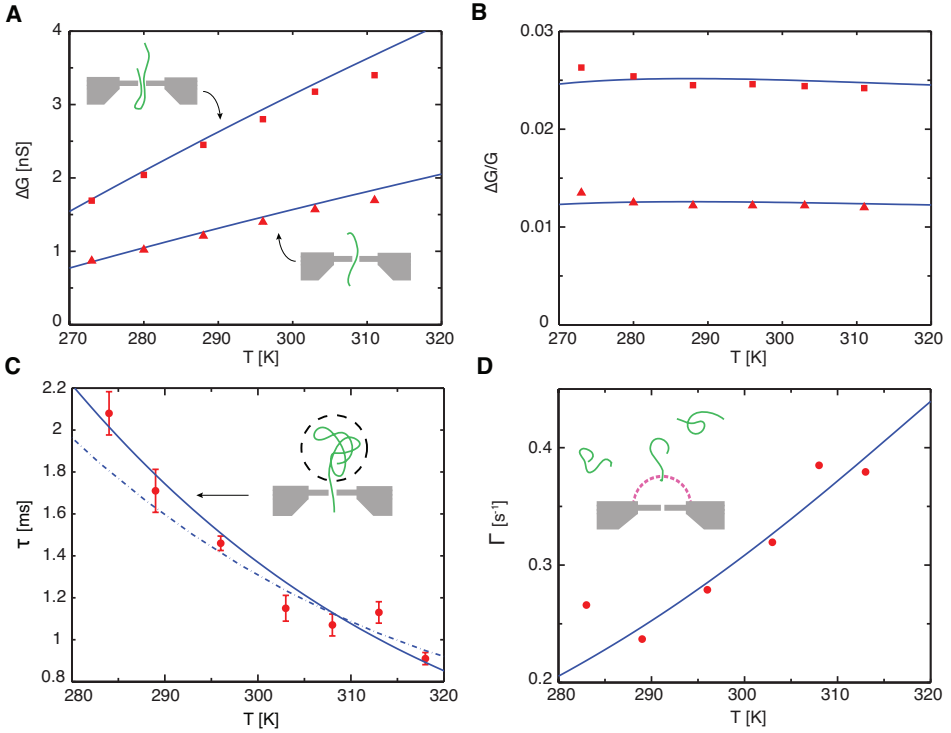
Here  $\xi(T)$  is a parameter that indicates the ratio of the total conductance of the cylinder  $G_{cyl}$  to the conductance of the access regions of the cylinder  $G_{access}$ . For a nanopore with  $d = 10$  nm in 1 M KCl,  $\xi(T) \sim 1.1$  and only weakly dependent on temperature.

Figure 8.2 shows a fit of equation 8.2 to the experimental data. The different temperature-dependent parameters  $\kappa_{bulk}(T)$ ,  $\mu_K(T)$ ,  $\sigma(T)$ ,  $r_D(T)$ , and  $\eta(T)$  are given in the SI Section 8.6.2. The effective length of the pore  $l_{eff}$  is fitted, yielding a value of 7.0 nm, which is very close to the value reported by [40] and in good agreement with the approximation by [41]. The model matches the experimental results well, considering that there is only a single fit parameter. Also shown are the three different components (bulk, double-layer and electroosmotic flow) that contribute to the nanopore conductance. It is clear that the bulk conductance constitutes the majority of the total pore conductance and that the EOF contribution is negligible.

### 8.3.2. BLOCKADE LEVELS

Biomolecules passing through the nanopore obstruct the pore partially and this volume exclusion produces a temporary reduction in the measured conductance. The magnitude of the conductance drops are the blockade levels  $\Delta G$ . A DNA molecule passing through a large nanopore will produce discrete blockade levels, depending on whether the molecule translocates in a linear fashion (only one double strand of DNA inside the pore) or in a folded fashion (two or more double strands of DNA in the pore simultaneously).

The blockade levels measured at various temperatures are fitted from a conductance histogram at each temperature and displayed in 8.3A, where the analysis was limited to only the first two blockade levels, one (red triangles) or two (red squares) double strands of DNA in the pore simultaneously. The blockade levels show a linear increase with



**Figure 8.3: Characteristics of DNA translocations as a function of temperature.** (A) Conductance blockades  $\Delta G$  for linear (triangles) and folded (squares) translocations in a  $d = 16$  nm pore. The blue lines are the predictions from equations 8.2 and 8.4 for a single blockade and a double blockade level, using  $l_{eff} = 7$  nm as obtained from the open pore conductance. (B) Relative conductance blockade levels  $\frac{\Delta G}{G}$  from the same pore as in A. Blue lines are obtained from the fits of  $G$  and  $\Delta G$ . (C) Translocation times  $\tau$  for  $\lambda$ -DNA in a  $d = 8.1$  nm pore. The solid line is a fit of equation 8.6 ( $\chi^2 = 2.3$ ), the dashed line is a fit to  $t_d \propto \eta$  ( $\chi^2 = 2.9$ ). (D) Event rate for  $\lambda$ -DNA in a  $d = 8.1$  nm pore. Solid line is a fit to equation 8.7 ( $\chi^2 = 60$ ). The symbols in this figure are larger than the errorbars.

temperature, doubling in size over about a 40 K range. Interestingly, this increase follows an almost identical trend as the open nanopore conductance, indicated by an almost constant  $\Delta G/G$  in Figure 8.3B, although a small decrease in  $\Delta G/G$  with temperature can be discerned.

The conductance blockade originates from the DNA molecule partly obstructing the nanopore and the access region. This reduces the conductance of the bulk of the nanopore by volume exclusion. However, the access resistance is determined by the convergence of electric-field lines near the nanopore [42] and the modification of this resistance due the presence of the DNA molecule in this region is less obvious. We can approximate this situation by assuming that a similar volume exclusion term applies to the access regions, as done by Carlsen *et al.* [27]. A double strand of DNA will reduce the conductance of each access region by  $\kappa_{bulk} \frac{\pi d_{DNA}^2}{2d}$ , where  $d_{DNA}$  is the diameter of a DNA strand and the approximate length of each access region is the radius of the pore  $d/2$ . This then gives a total conductance of the access regions in the presence of a double strand of DNA as  $G_{acc\ with\ DNA} = \kappa_{bulk} \left( d - \frac{\pi d_{DNA}^2}{4d} \right)$ .

Furthermore, a double-stranded DNA molecule is charged and this results in extra DL and EOF contribution due to ions flowing along the surface of the DNA molecule inside the nanopore, analogous to section 8.3.1. Contrary to [27], we do not include a DNA surface conductance term in the access regions. Measurements done at low salt concentrations show that molecules in access region produce conductance blockades [28], whereas conductance enhancements are expected if the surface conductance of the DNA is included in this region. The conductance of the pore with a double strand of DNA inserted into the pore then becomes

$$G_{with\ DNA} = \left[ \kappa_{bulk} \frac{\pi (d^2 - d_{DNA}^2)}{4} + (|\sigma|d + |\sigma_{DNA}|d_{DNA}) \pi \mu \kappa + (\sigma^2 d + \sigma_{DNA}^2 d_{DNA}) \frac{\pi r_D}{\eta} \right] \frac{1}{l_{eff} (1 + \xi_{with\ DNA}(T))}. \quad (8.4)$$

Here we have adopted a value of  $0.034\ \text{Cm}^{-2}$  as the effective surface charge density of the DNA  $\sigma_{DNA}$ , which is a factor 4 smaller than the bare DNA surface charge density to account for counterion condensation [43].

Note that  $\xi_{with\ DNA}(T)$  for the nanopore containing DNA is about 1.5% larger than  $\xi(T)$  for the open pore case, because the presence of the DNA strand affects the pore conductance and the access conductance differently. The conductance blockade that a single DNA duplex residing in the nanopore produces, is then given by  $\Delta G = G_{open\ pore} - G_{with\ DNA}$ . In the case two duplexes of DNA are present, the conductance blockade is almost exactly twice the blockade level for one double-strand of DNA.

Figure 8.3A shows the predicted conductance blockade levels  $\Delta G$  from equations 8.2 and 8.4 together with the experimental data, where we adopted a value of 7.0 nm for  $l_{eff}$ , as extracted from the open pore conductance. The model agrees well with the experimental values, given the simple approximation to the change in access resistance and the absence of fit parameters.

The relative conductance blockade  $\frac{\Delta G}{G}$ , i.e., the conductance blockade level divided by the open pore conductance, provides yet another measure to test the model. The

results for the two levels are shown in Figure 8.3B. The model predicts an almost constant value that approximates the experimental trend well, given that this involves no free fit parameters. The slight increase in the relative conductance blockades for lower temperatures is not well reproduced by the theoretical prediction, the small decrease of  $\frac{\Delta G}{G}$  with increasing temperatures is in qualitative agreement with our previous observation [17].

### 8.3.3. TRANSLOCATION TIMES

Translocation times of analytes through nanopores has been a major topic of interest and it is known that decreasing the temperature increases the translocation time of the molecule [33]. Figure 8.3C displays the translocation time  $\tau$  of 48.5 kbp  $\lambda$ -DNA molecules that pass through the nanopore in a linear fashion at different temperatures. There is a steep increase in translocation time for temperatures lower than room temperature and a slighter decrease in translocation times towards higher temperatures.

What sets the time it takes to translocate the molecule through a pore? Three main force contributions are at work during translocation [44]: (1) the electric field directly pulls on the charge on the DNA inside, (2) a viscous drag acts on the DNA inside the nanopore, and (3) a viscous drag exerts a force on the polymer blob outside the nanopore. The electric driving force acting on the DNA can be assumed to stay constant over the temperature range probed. The two retarding viscous forces couple to the molecule via the viscosity, which is strongly temperature dependent.

Inside the pore, the electroosmotic flow  $v_{EOF}$  determines the magnitude of the drag force, because the flow speed is typically an order of magnitude larger than the translocation velocity  $v_t$  of the DNA itself [45–47]. We assume a simple relation for the viscous drag  $f_d = \gamma\eta v$ , where  $v$  is the velocity of the object with respect to the viscous medium and  $\gamma$  is a drag coefficient depending on the size of the object the drag force acts on. By using  $v_{EOF} = \frac{r_D \sigma E_z}{\eta}$  [46] as the fluid velocity at the center of the pore, where  $E_z$  is a constant electric field in the nanopore, the drag force that acts on the DNA inside the pore scales as

$$f_d \propto \Delta V \sigma \frac{r_D}{l_{eff} + \frac{\pi d}{4}}. \quad (8.5)$$

Here  $\Delta V$  is the electric bias across the nanopore and the fraction  $\frac{1}{l_{eff} + \frac{\pi d}{4}}$  stems from the inclusion of access resistance in the analysis and from the non-cylindrical shape of the pore. Note that, importantly, this drag force contribution is independent of the viscosity [15, 45]. Since the remaining parameters in equation 8.5 all have a negligible dependence on temperature (see SI Section 8.6.2), this drag force is essentially independent of temperature. Hence the only force contribution that varies with temperature is the force on the polymer outside the nanopore.

Outside the pore, the conformation of the blob of the untranslocated DNA is important as it will determine the retention force. The exact shape of this untranslocated part during the translocation is debated and difficult to assess, even though models describing this have become increasingly more sophisticated [48]. We adopt a simple scaling model, as developed by Storm *et al.* [49], to fit to our results. Since in practice the Zimm relaxation time of the DNA coil is much slower than the translocation time

of the molecule, the coil does not have time to relax during the translocation process. Hence polymer conformation at the moment of DNA capture into the pore, determines the drag that dictates the translocation time. The size of this DNA molecule is roughly the hydrodynamic radius of the whole coil,  $R_g$ , and it will take  $\tau$  for this blob to travel over a distance equal to its own size  $R_g$  to reach the pore. Hence  $f_d \propto \eta \frac{R_g^2}{\tau}$  and since this drag balances the constant electrophoretic drive force, the translocation time is

$$\tau \propto R_g^2 \eta. \quad (8.6)$$

Both  $R_g$  and  $\eta$  are temperature dependent.  $R_g$  depends on temperature because the persistence length of the DNA  $a$  changes with temperature [50]. For a general coil,  $R_g \propto a^{1-\nu}$  with  $\nu$  the Flory exponent ( $\approx 0.6$  in our case).

Figure 8.3C shows excellent agreement of the model to the experimental data (solid line, goodness-of-fit (see section 8.2)  $\chi^2 = 2.3$ ), if we account for the temperature dependence of both  $\eta$  and  $R_g$ . When the temperature dependence of the hydrodynamic radius is neglected, the fit is slightly worse (dashed line,  $\chi^2 = 2.9$ ). It must be noted that the changes in persistence length are only moderate over the temperature range probed (ranging from 273 K to 313 K) and the effect it has on the translocation time is weak.

#### 8.3.4. EVENT RATE

One of the advantages of nanopores as single-molecule sensors is their ability to attract analytes, which increases the detection rate significantly compared sensors that rely on diffusion based transport. Figure 8.3D shows the event rate  $\Gamma$ , the rate at which molecules hit the pore and subsequently translocate through it. The event rate is observed to increase with increasing temperatures.

The rate at which DNA molecules pass through a nanopore is, for our experimental conditions, dictated by a balance between electrophoresis and diffusion [31]. The molecules diffusing within a region close to the pore will be attracted to the nanopore by an electrophoretic force that stems from the electric field emanating from the pore. Once the molecules enter this region, where the electrophoretic energy scale starts dominating over the diffusive energy scale, the molecules will be captured by the nanopore and will translocate through it. The size of this region determines the capture radius of the pore, which significantly exceeds the physical size of the pore, as shown by Grosberg and Rabin [31, 51]. If we include electrical access resistance and neglect surface charge effects such as electroosmotic flows, we arrive at an event rate

$$\Gamma = c\Delta V \mu_{DNA} \frac{\pi d^2}{l_{eff} + \frac{\pi d}{4}}, \quad (8.7)$$

where  $c$  is the concentration of DNA in the cis chamber and  $\mu_{DNA}$  is the electrophoretic mobility of the DNA.

The temperature dependence of the event rate is contained in the electrophoretic mobility  $\mu_{DNA}$  of DNA. Since the DNA coil is freely draining, i.e. the solvent molecules move through the DNA coil upon application of an electric force, the mobility is determined by a local balance between the electric pull and the viscous drag on the DNA. For a small Debye length  $r_D$ , appropriate for our high-salt conditions, this dependence

can be approximated by [52]

$$\mu_{DNA} \propto \frac{r_D}{\eta}. \quad (8.8)$$

Figure 8.3D shows the event rate changing with temperature and indicates a decent fit of the model. Because of fragmentation of long DNA polymers during handling, the concentration of  $\lambda$ -DNA molecules in the cis chamber is not accurately known and equation 8.7 is fitted, with  $c$  as a fit parameter. The normalized  $\chi^2$  value of the fit is 60, which is a large value, but it must be noted that the deviations in the trend are most likely set by small variations in pore diameter, which are not accounted for in the fitting error values. Using  $d = 8.1$  nm,  $l_{eff} = 7.0$  nm as appropriate for this data set, and  $\mu_{DNA} \approx 2.2 \cdot 10^{10}$  nm<sup>2</sup>/(V·s) [51], we find an effective concentration of  $\lambda$ -DNA of 0.4 ng/ $\mu$ L. This is lower than the 5 ng/ $\mu$ L of  $\lambda$ -DNA used in the initial sample and we attribute the discrepancy to fragmentation and the uncertainty in our numerical estimate for  $\mu_{DNA}$ .

## 8.4. DISCUSSION

Changing the temperature of the system affects many parameters. Because molecular interactions that give rise to collective properties, such as viscosity and permittivity, are in general temperature dependent, each of these features should be carefully inspected to explain the temperature dependence of DNA translocations. SI Section 8.6.2 contains a list of all parameters that exhibit or are expected to exhibit an appreciable temperature dependence. Even though the list is substantial, the main trends are captured by only considering the temperature dependence of the viscosity and the buffer conductivity.

In high-ionic-strength solutions, charges are in general not only screened by counterions, but also effectively reduced, by counterion condensation [43]. The degree of condensation can depend on temperature. Remarkably, however, the models reproduce the experimental trends very well while keeping the effective charge of the DNA constant. The results indicate that the counterion condensation on the DNA does not vary very much within the temperature range probed (273 - 318 K) in these high-ionic-strength solutions.

While all trends were measured in multiple experiments on multiple pores, the data displayed in each separate figure are taken from a single experiment, to prevent slight changes in experimental conditions. The translocation times and event rates of all experiments can be found in the SI Section 8.6.4.

## 8.5. CONCLUSION

We have presented here the first extensive study on the temperature dependence on DNA translocation through solid-state nanopores. We analyzed the characteristic features of these translocations, comprising the open pore conductance  $G$ , conductance blockade  $\Delta G$ , translocation times  $\tau$ , and event rate  $\Gamma$ . In order to explain the observed experimental trends in these features, we have extended existing theory by incorporating the access resistance in established models. The temperature dependence of  $G$  and  $\Delta G$  are well described when the conductance contributions from the bulk and the surface charges of the nanopore walls and the DNA inside the pore are taken into account. The

open pore conduction of the nanopore is very sensitive to local changes in temperature and can be used to determine heating from nanostructures. Additionally, the trends in event rate  $\Gamma$  could be accurately described by a balance between diffusion and electrophoretic motion [51]. Finally, for the translocation time  $\tau$  we obtained excellent agreement with a model developed by Storm *et al.* [49], where the untranslocated coil dictates the translocation velocity of the DNA molecule.

## 8.6. SUPPORTING INFORMATION

### 8.6.1. NANOPORE CONDUCTION MODEL

The electrical current through a nanopore is determined by a steady state flux of ions through the small orifice. This ion flux is governed by three fundamental equations. The Nernst-Planck flux (equation S8.9) describes the particle flux  $\mathbf{J}_i(\mathbf{r})$  of each species  $i$  directly. The ion density  $n_i(\mathbf{r})$  is not only determined by this equation, but also by the Poisson equation (equation S8.10), as the ions are charged. The background medium can in general support an incompressible Stokes flow  $\mathbf{u}(\mathbf{r})$  (equation S8.11), as the Reynolds number is small for flow at these dimensions.

$$\mathbf{J}_i(\mathbf{r}) = D_i \nabla n_i(\mathbf{r}) - \mathbf{u}(\mathbf{r}) n_i(\mathbf{r}) + \frac{D_i z_i e}{k_B T} n_i(\mathbf{r}) \nabla \phi(\mathbf{r}) \quad (\text{S8.9})$$

$$\nabla^2 \phi(\mathbf{r}) = -\frac{\rho(\mathbf{r})}{\epsilon} \quad (\text{S8.10})$$

$$\eta \nabla^2 \mathbf{u}(\mathbf{r}) = -\rho(\mathbf{r}) \nabla \phi(\mathbf{r}) \quad (\text{S8.11})$$

Here  $D_i$  is the diffusion constant of species  $i$ ,  $z_i$  is its valence,  $\epsilon$  is the electrical permittivity,  $\eta$  is the viscosity of the background medium,  $\rho(\mathbf{r}) = \sum_i z_i e n_i(\mathbf{r})$  is the volume charge density, and  $\phi(\mathbf{r})$  the electric potential.

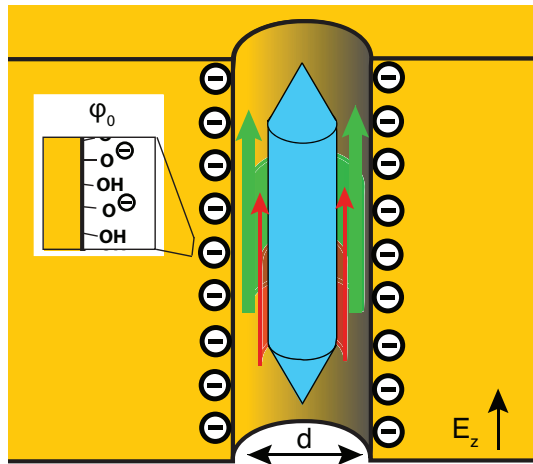


**Figure S8.4:** Schematic of cylinder of diameter  $d$ , filled with electrolyte embedded in silicon nitride. The cylinder has a uniform  $\zeta$ -potential  $\phi_0$  due to the deprotonated silanol groups at the surface and an axial electric field  $E_z$  is applied. The bulk conduction (blue arrow) and the surface conduction, double-layer (DL, green arrow) and electroosmotic flow conduction (EOF, red arrow) are indicated in the figure.

First we consider a simplified system, containing solely a perfect cylinder filled with electrolyte. The cylinder has a diameter  $d$ , the walls are at a uniform  $\zeta$ -potential of  $\phi_0$ , and a constant axial electric field  $\frac{\partial \phi(\mathbf{r})}{\partial z} = E_z$  is applied. A schematic of this is shown in Fig. S8.4. The cylinder contains a conductive electrolyte with two major charge carriers: potassium and chloride, each with mobility  $\mu_K$  and  $\mu_{Cl}$  respectively.

The symmetry in the radial direction dictates the flow and the net ion-flux to be zero in this direction. This simplifies the PNP equations to the Poisson-Boltzmann (PB) equation ,

$$\nabla^2 \phi(r) = -\frac{1}{\epsilon} \sum_i z_i n_0 \exp\left(-\frac{z_i e \phi(r)}{k_B T}\right). \quad (\text{S8.12})$$

For a single-valence binary electrolyte, the PB equation sets a typical length scale  $r_D = \sqrt{\frac{\epsilon k_B T}{2 n_0 e^2}}$ , the Debye length. This is the distance over which the ion density significantly changes from the bulk density  $n_0$ . In case the Debye length is small compared to the scale of the system ( $r_D \ll d$ ), we can linearize the exponential term in equation S8.9. The PB equation then simplifies to the Debye-Hückel limit, for which equation S8.9 can be solved analytically, invoking cylindrical symmetry [53]:

$$\phi(r) = \phi_0 \frac{I_0(r/r_D)}{I_0(d/2r_D)}. \quad (\text{S8.13})$$

Here,  $I_0(x)$  is the zero-order modified Bessel-function of the first kind.

With this solution to the electric potential, equation S8.11 can readily be solved. The symmetry restricts the net flow to be along the axis of the cylinder and only the  $z$  component of the flow is non-zero. With a no-slip condition on the wall of the cylinder,  $u_z(r)$  becomes [46]

$$u_z(r) = -\frac{\epsilon \phi_0 E_z}{\eta} \left[ 1 - \frac{I_0(r/r_D)}{I_0(d/2r_D)} \right]. \quad (\text{S8.14})$$

Using the Debye-Hückel approximation, the current density becomes:

$$J_{z,e} = \sum_{i=K,Cl} z_i e J_{z,i} = (\mu_K + \mu_{Cl}) e n_0 E_z - \mu_K \frac{\epsilon \phi(r)}{r_D^2} E_z - u_z(r) \frac{\epsilon \phi(r)}{r_D^2}, \quad (\text{S8.15})$$

where we used the Einstein relation  $\mu_i = \frac{e D_i}{k_B T}$ . Combining equations S8.13, S8.14, and S8.15, we have a complete analytic expression for the current density inside the cylinder. Fig. S8.5 shows the current density distribution due to the separate terms in this equation for a  $d = 10$  nm cylinder with an electric field density  $E_z = 5 \cdot 10^7$  V/m and a  $\zeta$ -potential of  $\phi_0 = -14$  mV, which corresponds to the silicon-nitride  $\zeta$ -potential at room temperature (see Fig. S8.8B)

We can assign a physical interpretation to each term in equation S8.15 if we identify  $\frac{\epsilon \phi(r)}{r_D^2}$  as an effective volume charge density. The first term represents the bulk current density. The second term is the double-layer (DL) current density as the volume charge density itself is mobile and affected by the electric field. The last term in this expression is the electroosmotic flow (EOF) current, which arises from a net charge flux due to the flow in the background medium  $u_z(r)$ .

A note must be made to the double-layer contribution, which arises from the screening of the surface charge density on the walls of the cylinder. The Debye-Hückel theory predicts, incorrectly, that the reduction of coion density near the charged cylinder wall is equal and opposite to the enhancement of counterion density. This is not true close to the charged surface and is borne out by the full Poisson-Boltzmann theory [39]. A common approximation is to neglect the reduction of coions entirely and attribute the screening exclusively to the counterions, as is done here in equation S8.15.

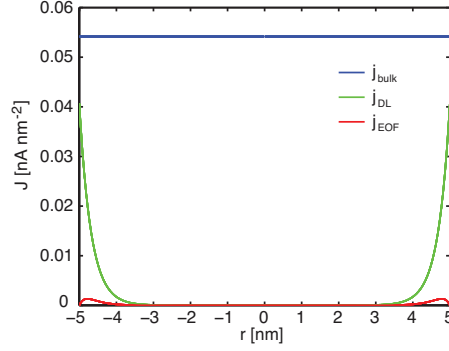


**Figure S8.5:** Current density distribution inside the cylinder. The bulk current density  $j_{bulk}$  is by far the dominant contribution over the surface currents, double-layer current density  $j_{DL}$  and EOF current density  $j_{EOF}$ .

Integrating the expression for the current density over the cylinder yields the total current through it. For this we need  $\int_0^x x' I_0(x') dx' = x I_1(x)$ , where  $I_1(x)$  is roughly equal to  $I_0(x)$  for large  $x$  ( $d/2r_D \gg 1$ ) and  $\int_0^x x' I_0^2(x') dx' = \frac{1}{2} x^2 (I_1^2(x) - I_0^2(x))$ , which approximates to 0 for large  $x$ . The resulting current in terms of  $\phi_0$  is then

$$I_{cyl} = \int_0^{\frac{d}{2}} J_{z,e}(r) 2\pi r dr = n_0 e (\mu_K + \mu_{Cl}) \frac{\pi d^2}{4} E_z + \mu_K e |\phi_0| \frac{\pi d}{r_D} E_z + \frac{\pi \epsilon^2 \phi_0^2 d}{\eta r_D} E_z. \quad (\text{S8.16})$$

A more familiar expression can be obtained by rewriting  $\phi_0$  to a surface charge density  $\sigma$ . The surface charge density is related to the  $\zeta$ -potential by the Grahame equation

$$\sigma(\phi_0) = \frac{2k_B T \epsilon}{r_D e} \sinh\left(\frac{e\phi_0}{2k_B T}\right). \quad (\text{S8.17})$$

In the case  $e|\phi_0|$  is small with respect to  $k_B T$ , this equation reduces to  $\sigma = \frac{\epsilon\phi_0}{r_D}$ . We can then rewrite equation S8.16,

$$I_{cyl} = \left[ \overbrace{n_0 e (\mu_K + \mu_{Cl})}^{\kappa_{bulk}} \frac{\pi d^2}{4} + \mu_K |\sigma| \pi d + \frac{\pi \sigma^2 r_D d}{\eta} \right] E_z. \quad (\text{S8.18})$$

When access resistance is neglected,  $E_z$  is simply  $\frac{\Delta V}{l}$  where  $\Delta V$  is the bias voltage applied across the cylinder of length  $l$ . The conductance of the cylinder then becomes

$$G_{cyl} = \left[ \kappa_{bulk} \frac{\pi d^2}{4l} + \mu_K |\sigma| \frac{\pi d}{l} + \frac{\pi \sigma^2 r_D d}{\eta l} \right]. \quad (\text{S8.19})$$

The first term in equation S8.19 is the bulk conductance  $G_{bulk}$  and the last two terms make up the surface conductance of the pore: the conductance due to the double-layer

$G_{DL}$  and the conductance due to the flow in the medium  $G_{EOF}$ . This equation is in agreement with other expressions for the pore current, derived with more heuristic methods [16, 30, 38], where only [16] takes the small EOF contribution into account.

In the case of a real nanopore, the shape deviates from that of a perfect cylinder and access effects need to be taken care of. Kowalczyk *et al.* [40] have shown that a nanopore is in general not a cylinder, but hourglass shaped and included access resistance in the conduction model. This implies that  $E_z$  is not just  $\frac{\Delta V}{l}$ , but that only part of the voltage drop is over the cylindrical pore, which now has a modified thickness  $l_{eff}$ . Assuming a total access resistance for both regions of  $G_{access} = d\kappa_{bulk}$ , the voltage drop over the pore becomes:

$$\Delta V_{pore} = \frac{G_{cyl}^{-1}}{G_{cyl}^{-1} + G_{access}^{-1}} \Delta V$$

and subsequently the electric field strength in the pore becomes

$$E_z = \frac{\Delta V}{l_{eff}(1 + \xi(T))}. \quad (S8.20)$$

Here,  $\xi(T) = \frac{G_{cyl}}{G_{access}}$  is roughly equal to 1.1 in our conditions, and depends weakly on temperature. Hence, the conductance of the pore is:

$$G_{pore} = \left[ \kappa_{bulk} \frac{\pi d^2}{4} + \mu_K |\sigma| \pi d + \frac{\pi \sigma^2 r_D d}{\eta} \right] \frac{1}{l_{eff}(1 + \xi(T))} \quad (S8.21)$$

### 8.6.2. TEMPERATURE DEPENDENCE OF PARAMETERS IN CONDUCTION MODEL

Many parameters in the model as described in section 8.6.1 are temperature dependent. This section lists all the temperature dependent parameters used in the model.

#### VISCOSITY $\eta$ , MOBILITY $\mu_K$ , AND CONDUCTIVITY $\kappa_{bulk}$

The temperature dependence on the viscosity  $\eta$  is fitted to data obtained from [54] with a second order polynomial in  $T^{-1}$ . The temperature dependence of the bulk conductivity of the electrolyte is obtained from [55] and fitted to a linear function of  $T$  [25].

The temperature dependence of the mobility of the potassium ions, which make up the double-layer conductance, is assumed to depend directly on the viscosity:

$$\mu_K(T) = \mu_K(T = 296 \text{ K}) \frac{\eta(T = 296 \text{ K})}{\eta(T)}, \quad (S8.22)$$

where  $\mu_K(T = 296 \text{ K}) = 7.9 \cdot 10^{-8} \text{ m}^2(\text{Vs})^{-1}$ .

#### DEBYE LENGTH $r_D$

To calculate the temperature dependence of the Debye length  $r_D = \sqrt{\frac{k_B T \epsilon}{2n_0 e^2}}$ , we used a temperature-dependent electric permittivity [56]. The change of  $r_D$  with temperature is actually minor, as shown in Fig. S8.7.

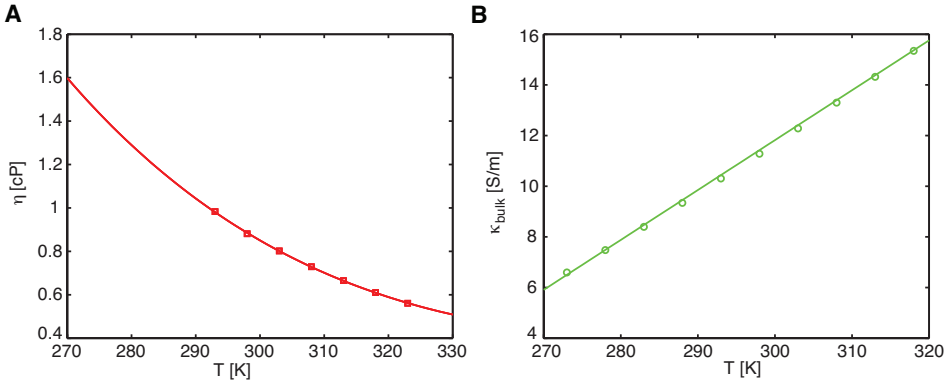


**Figure S8.6:** (A) Temperature dependence of viscosity of 1 M KCl and the respective fit. (B) Temperature dependence of the buffer conductivity of 1 M KCl and the respective fit.

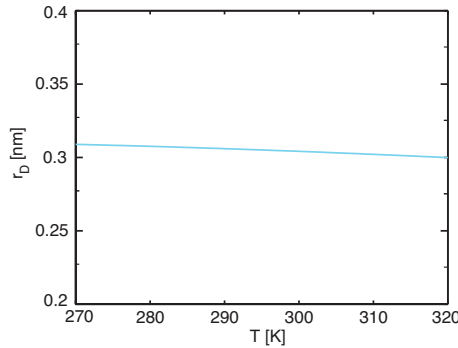


**Figure S8.7:** Temperature dependence of the Debye length  $r_D$  in 1 M KCl.

### SURFACE CHARGE DENSITY $\sigma$

The surface charge density in the pore is set by the silanol chemistry of the SiN [57]. The  $\zeta$ -potential is related to the surface charge density by the chemical equilibrium of the surface silanol groups, as described by the Behrens-Grier equation [58]

$$\phi_0(\sigma) = \frac{k_B T}{e} \ln \left( \frac{-\sigma}{e\gamma + \sigma} \right) - (\text{pH} - \text{pK}) \frac{k_B T}{e} \ln(10) - \frac{\sigma}{C}, \quad (\text{S8.23})$$

where  $\gamma$  is the site density of the surface silanol group ( $8 \text{ nm}^{-2}$ ), pK it's acid dissociation constant, and  $C$  the stern capacitance of the surface ( $0.3 \text{ Fm}^{-2}$ ) [59]. Together with the Grahame equation (equation 8.16), the surface charge density  $\sigma$  can be solved self-consistently, using an iterative method like, for example, MATLAB's `fsolve()`.

pK and pH values are in general temperature dependent. In this case, pK of the surface silanol groups is  $\text{pK} = -\frac{\Delta G^*}{2.3N_A k_B T}$ . Here  $\Delta G^* = 4.2 \text{ kJ/mol}$  [60] is the Gibbs free energy gain of the dissociation of a proton from a silanol surface group. In case of the pH

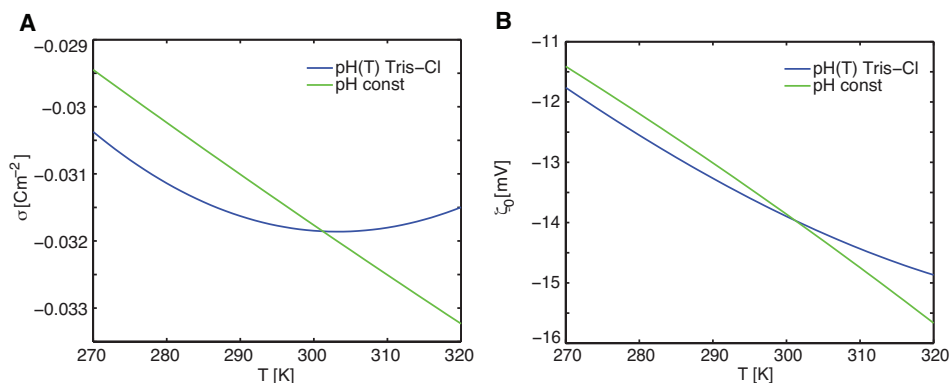


**Figure S8.8:** (A) Temperature dependence of the surface charge density  $\sigma$  on the silicon nitride according to the coupled Grahame, Behrens-Grier equations, with a constant pH (green) and a temperature dependent pH, as for Tris-Cl (blue). (B) Temperature dependence of the  $\zeta$ -potential  $\phi_0$ . Again the effect of changing the pH (blue) or keeping the pH constant with temperature (green) is shown.

of Tris-Cl, the temperature dependence is  $\text{pH}(T) = 8.0 - 0.03 \cdot (T - 296)$  [61].

Fig. S8.8 shows the temperature dependence of both the  $\zeta$ -potential and surface charge density  $\sigma$  of the pore's surface, where the pH is kept constant with temperature or allowed to vary as the pH of Tris-Cl. It is clear from this figure that the choice for Tris-Cl buffer causes very little change in the surface charge density.

### 8.6.3. TEM IMAGES OF NANOPORES

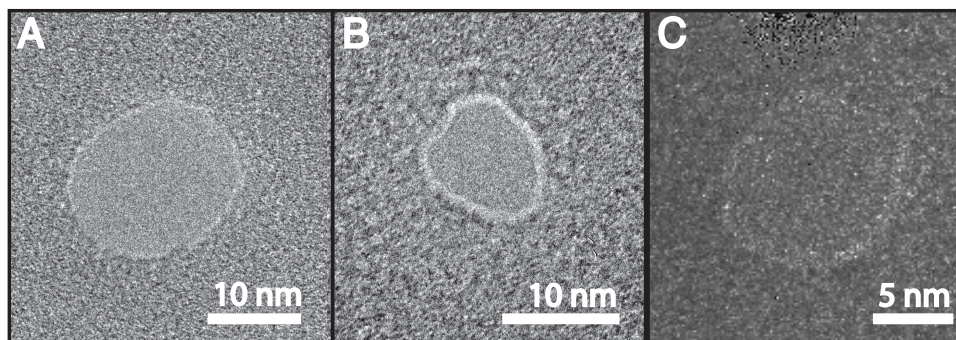


**Figure S8.9:** (A) pore TB4 12-9 ( $d = 16.0$  nm) (B) pore TB1A 3-9 ( $d = 8.1$  nm) (C) pore TB1B 1-9 ( $d = 8.9$  nm)

Figure 2 and figures 3A and B in the main text and Fig. S8.10A and C are data from pore TB4 12-9 (Fig. S8.9A), figures 3C and D in the main text are from pore TB1A 3-9 (Fig. S8.9B) and Fig. S8.10B and D are from pore TB1B 1-9 (Fig. S8.9C).

### 8.6.4. TRANSLOCATION TIMES AND EVENT RATES FROM DIFFERENT EXPERIMENTS

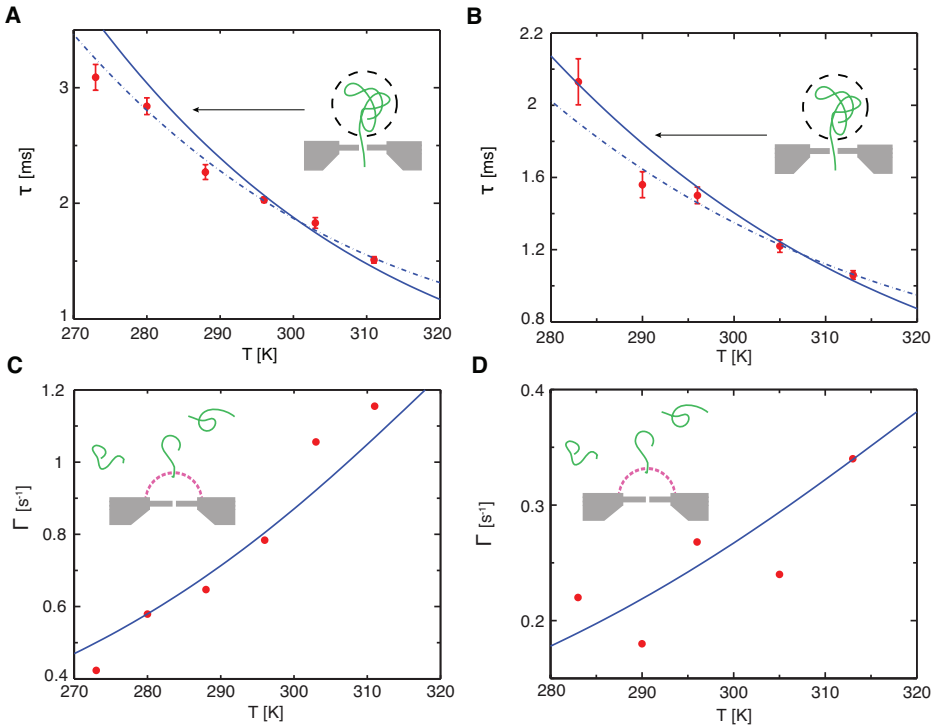


**Figure S8.10:** Event rate  $\Gamma$  and translocation time  $\tau$  of  $\lambda$ -DNA translocations as a function of temperature. **(A)** Translocation times  $\tau$  for TB4 12-9.  $\chi^2 = 9.1$  (solid line) from fit of equation 6 in the main text,  $\chi^2 = 1.7$  (dashed line) from fit of viscosity only. **(B)** Translocation times  $\tau$  for TB1B 1-9.  $\chi^2 = 2.9$  (solid line),  $\chi^2 = 1.7$  (dashed line). **(C)** Event rate  $\Gamma$  for TB4 12-9. The solid line is a fit of equation 7 in the main text,  $\chi^2 = 480$ . The symbol size is large than the error bars. **(D)** Event rate  $\Gamma$  for TB4 12-9,  $\chi^2 = 640$ . The symbol size is large than the error bars.

## REFERENCES

- [1] C. Dekker, *Solid-state nanopores*, Nat Nano **2**, 209 (2007), 1748-3387 10.1038/nnano.2007.27 10.1038/nnano.2007.27.
- [2] M. Wanunu, *Nanopores: A journey towards dna sequencing*, Physics of Life Reviews **9**, 125 (2012), 1571-0645.
- [3] C. Plesa, L. Cornelissen, M. W. Tuijtel, and C. Dekker, *Non-equilibrium folding of individual dna molecules recaptured up to 1000 times in a solid state nanopore*, Nanotechnology **24**, 475101 (2013).
- [4] M. Mihovilovic, N. Hagerty, and D. Stein, *Statistics of dna capture by a solid-state nanopore*, Physical Review Letters **110**, 028102 (2013), 1079-7114.

- [5] R. Wei, V. Gatterdam, R. Wieneke, R. Tampe, and U. Rant, *Stochastic sensing of proteins with receptor-modified solid-state nanopores*, *Nat Nano* **7**, 257 (2012), 1748-3387 10.1038/nnano.2012.24 10.1038/nnano.2012.24.
- [6] C. Plesa, S. W. Kowalczyk, R. Zinsmeister, A. Y. Grosberg, Y. Rabin, and C. Dekker, *Fast translocation of proteins through solid state nanopores*, *Nano Letters* **13**, 658 (2013).
- [7] M. Firnkes, D. Pedone, J. Knezevic, M. Döblinger, and U. Rant, *Electrically facilitated translocations of proteins through silicon nitride nanopores: conjoint and competitive action of diffusion, electrophoresis, and electroosmosis*. *Nano Letters* **10**, 2162 (2010).
- [8] G. V. Soni and C. Dekker, *Detection of nucleosomal substructures using solid-state nanopores*, *Nano Letters* **12**, 3180 (2012).
- [9] E. C. Yusko, J. M. Johnson, S. Majd, P. Prangkio, R. C. Rollings, J. Li, J. Yang, and M. Mayer, *Controlling protein translocation through nanopores with bio-inspired fluid walls*. *Nat Nano* **6**, 253 (2011).
- [10] M. M. Marshall, J. A. Ruzicka, E. W. Taylor, and A. R. Hall, *Detecting dna depurination with solid-state nanopores*, *PLoS ONE* **9**, e101632 (2014).
- [11] S. W. Kowalczyk, A. R. Hall, and C. Dekker, *Detection of local protein structures along dna using solid-state nanopores*, *Nano Letters* **10**, 324 (2009), doi: 10.1021/nl903631m 1530-6984 doi: 10.1021/nl903631m.
- [12] C. Raillon, P. Cousin, F. Traversi, E. Garcia-Cordero, N. Hernandez, and A. Radenovic, *Nanopore detection of single molecule rnap-dna transcription complex*, *Nano Letters* **12**, 1157 (2012).
- [13] D. Japrun, A. Bahrami, A. Nadzeyka, L. Peto, S. Bauerdick, J. B. Edel, and T. Albrecht, *Ssb binding to single-stranded dna probed using solid-state nanopore sensors*, *The Journal of Physical Chemistry B* **118**, 11605 (2014).
- [14] U. F. Keyser, B. N. Koeleman, S. van Dorp, D. Krapf, R. M. M. Smeets, S. G. Lemay, N. H. Dekker, and C. Dekker, *Direct force measurements on dna in a solid-state nanopore*, *Nat Phys* **2**, 473 (2006), 10.1038/nphys344.
- [15] S. van Dorp, U. F. Keyser, N. H. Dekker, C. Dekker, and S. G. Lemay, *Origin of the electrophoretic force on dna in solid-state nanopores*, *Nat Phys* **5**, 347 (2009), 10.1038/nphys1230.
- [16] N. Di Fiori, A. Squires, D. Bar, T. Gilboa, T. D. Moustakas, and A. Meller, *Optoelectronic control of surface charge and translocation dynamics in solid-state nanopores*, *Nat Nano* **8**, 946 (2013).
- [17] F. Nicoli, D. Verschuere, M. Klein, C. Dekker, and M. P. Jonsson, *Dna translocations through solid-state plasmonic nanopores*, *Nano Letters* (2014), 10.1021/nl503034j.
- [18] M. P. Cecchini, A. Wiener, V. A. Turek, H. Chon, S. Lee, A. P. Ivanov, D. W. McComb, J. Choo, T. Albrecht, S. A. Maier, and J. B. Edel, *Rapid ultrasensitive single particle*

- surface-enhanced raman spectroscopy using metallic nanopores*, Nano Letters **13**, 4602 (2013).
- [19] Y. Li, C. Chen, S. Kerman, P. Neutens, L. Lagae, G. Groeseneken, T. Stakenborg, and P. Van Dorpe, *Harnessing plasmon-induced ionic noise in metallic nanopores*, Nano Letters **13**, 1724 (2013).
- [20] S. Nam, I. Choi, C.-c. Fu, K. Kim, S. Hong, Y. Choi, A. Zettl, and L. P. Lee, *Graphene nanopore with a self-integrated optical antenna*, Nano Letters **14**, 5584 (2014).
- [21] J. Larkin, M. Foquet, S. W. Turner, J. Korfach, and M. Wanunu, *Reversible positioning of single molecules inside zero-mode waveguides*, Nano Letters **14**, 6023 (2014).
- [22] U. F. Keyser, D. Krapf, B. N. Koeleman, R. M. M. Smeets, N. H. Dekker, and C. Dekker, *Nanopore tomography of a laser focus*, Nano Letters **5**, 2253 (2005).
- [23] N. Harris, M. J. Ford, and M. B. Cortie, *Optimization of plasmonic heating by gold nanospheres and nanoshells*, The Journal of Physical Chemistry B **110**, 10701 (2006).
- [24] Z. J. Coppens, W. Li, D. G. Walker, and J. G. Valentine, *Probing and controlling photothermal heat generation in plasmonic nanostructures*, Nano Letters **13**, 1023 (2013).
- [25] M. P. Jonsson and C. Dekker, *Plasmonic nanopore for electrical profiling of optical intensity landscapes*, Nano Letters **13**, 1029 (2013).
- [26] J. B. Herzog, M. W. Knight, and D. Natelson, *Thermoplasmonics: Quantifying plasmonic heating in single nanowires*, Nano Letters **14**, 499 (2014).
- [27] A. T. Carlsen, O. K. Zahid, J. Ruzicka, E. W. Taylor, and A. R. Hall, *Interpreting the conductance blockades of dna translocations through solid-state nanopores*, ACS Nano **8**, 4754 (2014).
- [28] S. W. Kowalczyk and C. Dekker, *Measurement of the docking time of a dna molecule onto a solid-state nanopore*, Nano Letters **12**, 4159 (2012).
- [29] A. J. Storm, J. H. Chen, H. W. Zandbergen, and C. Dekker, *Translocation of double-strand dna through a silicon oxide nanopore*, Physical Review E: Statistical, Nonlinear, and Soft Matter Physics **71**, 051903 (2005), pRE.
- [30] R. M. M. Smeets, U. F. Keyser, D. Krapf, M.-Y. Wu, N. H. Dekker, and C. Dekker, *Salt dependence of ion transport and dna translocation through solid-state nanopores*, Nano Letters **6**, 89 (2006), doi: 10.1021/nl052107w 1530-6984 doi: 10.1021/nl052107w.
- [31] M. Wanunu, W. Morrison, Y. Rabin, A. Y. Grosberg, and A. Meller, *Electrostatic focusing of unlabelled dna into nanoscale pores using a salt gradient*, Nat Nano **5**, 160 (2010), 10.1038/nnano.2009.379.
- [32] M. Wanunu, J. Sutin, B. McNally, A. Chow, and A. Meller, *Dna translocation governed by interactions with solid-state nanopores*, Biophysical Journal **95**, 4716 (2008).

- [33] D. Fologea, J. Uplinger, B. Thomas, D. S. McNabb, and J. Li, *Slowing dna translocation in a solid-state nanopore*. Nano Letters **5**, 1734 (2005).
- [34] Y. Zhang, G. Wu, J. Ma, Z. Yuan, W. Si, L. Liu, J. Sha, and Y. Chen, *Temperature effect on translocation speed and capture rate of nanopore-based dna detection*, Science China Technological Sciences, **1** (2014).
- [35] A. Meller, L. Nivon, E. Brandin, J. Golovchenko, and D. Branton, *Rapid nanopore discrimination between single polynucleotide molecules*, Proceedings of the National Academy of Sciences **97**, 1079 (2000).
- [36] X. J. A. Janssen, M. P. Jonsson, C. Plesa, G. V. Soni, C. Dekker, and N. H. Dekker, *Rapid manufacturing of low-noise membranes for nanopore sensors by trans -chip illumination lithography*, Nanotechnology **23**, 475302 (2012), 0957-4484.
- [37] C. Plesa and C. Dekker, *Data analysis methods for solid-state nanopores; submitted*, (2014).
- [38] T. Albrecht, T. Gibb, and P. Nuttall, *Chapter 1 - ion transport in nanopores*, in *Engineered Nanopores for Bioanalytical Applications*, edited by J. B. Edel and T. Albrecht (William Andrew Publishing, Oxford, 2013) pp. 1–30.
- [39] R. B. Schoch, J. Han, and P. Renaud, *Transport phenomena in nanofluidics*, Reviews of Modern Physics **80**, 839 (2008), rMP.
- [40] S. W. Kowalczyk, A. Y. Grosberg, Y. Rabin, and C. Dekker, *Modeling the conductance and dna blockade of solid-state nanopores*, Nanotechnology **22**, 315101 (2011), 0957-4484.
- [41] M. Wanunu, T. Dadosh, V. Ray, J. Jin, L. McReynolds, and M. Drndic, *Rapid electronic detection of probe-specific micrnas using thin nanopore sensors*, Nat Nano **5**, 807 (2010), 10.1038/nnano.2010.202.
- [42] J. E. Hall, *Access resistance of a small circular pore*, The Journal of general physiology **66**, 531 (1975).
- [43] G. S. Manning, *The molecular theory of polyelectrolyte solutions with applications to the electrostatic properties of polynucleotides*, Quarterly Reviews of Biophysics **11**, 179 (1978).
- [44] L. Chen and A. T. Conlisk, *Forces affecting double-stranded dna translocation through synthetic nanopores*, Biomedical Microdevices **13**, 403 (2011).
- [45] S. Ghosal, *Electrokinetic-flow-induced viscous drag on a tethered dna inside a nanopore*, Physical Review E **76**, 061916 (2007), pRE.
- [46] C. T. A. Wong and M. Muthukumar, *Polymer capture by electro-osmotic flow of oppositely charged nanopores*, The Journal of Chemical Physics **126**, (2007).
- [47] B. Luan and A. Aksimentiev, *Electro-osmotic screening of the dna charge in a nanopore*, Physical Review E **78**, 021912 (2008), pRE.
- [48] P. Rowghanian and A. Y. Grosberg, *Force-driven polymer translocation through a*

- nanopore: An old problem revisited*, The Journal of Physical Chemistry B **115**, 14127 (2011).
- [49] A. J. Storm, C. Storm, J. Chen, H. Zandbergen, J.-F. Joanny, and C. Dekker, *Fast dna translocation through a solid-state nanopore*, Nano Letters **5**, 1193 (2005), doi: 10.1021/nl048030d 1530-6984 doi: 10.1021/nl048030d.
- [50] S. Geggier, A. Kotlyar, and A. Vologodskii, *Temperature dependence of dna persistence length*, Nucleic Acids Research **39**, 1419 (2011).
- [51] A. Y. Grosberg and Y. Rabin, *Dna capture into a nanopore: Interplay of diffusion and electrohydrodynamics*, The Journal of Chemical Physics **133**, (2010).
- [52] P. Rowghanian and A. Y. Grosberg, *Electrophoresis of a dna coil near a nanopore*, Physical Review E **87**, 042723 (2013), pRE.
- [53] F. Booth, *The solution of some potential problems in the theory of electrolytes*, The Journal of Chemical Physics **19**, 821 (1951).
- [54] M. Afzal, M. Saleem, and M. T. Mahmood, *Temperature and concentration dependence of viscosity of aqueous electrolytes from 20.degree.c to 50.degree.c chlorides of (sodium(1+), potassium(1+), magnesium(2+), calcium(2+), barium(2+), strontium(2+), cobalt(2+), nickel(2+), copper(2+) and chromium(3+)*, Journal of Chemical & Engineering Data **34**, 339 (1989).
- [55] K. W. Pratt, W. F. Koch, Y. C. Wu, and P. A. Berezansky, *Molality-based primary standards of electrolytic conductivity (iupac technical report)*, (2001).
- [56] G. C. Malmberg and A. A. Maryott, *Dielectric constant of water from 0c to 100c*, Journal of Research of the National Bureau of Standards **56** (1956).
- [57] N. Jaffrezic-Renault, A. De, P. Clechet, and A. Maaref, *Study of the silicon nitride/aqueous electrolyte interface on colloidal aqueous suspensions and on electrolyte/insulator/semiconductor structures*, Colloids and Surfaces **36**, 59 (1989).
- [58] S. H. Behrens and D. G. Grier, *The charge of glass and silica surfaces*, The Journal of Chemical Physics **115**, 6716 (2001).
- [59] F. H. van der Heyden, D. Stein, and C. Dekker, *Streaming currents in a single nanofluidic channel*, Physical review letters **95**, 116104 (2005).
- [60] A. Revil, P. A. Pezard, and P. W. J. Glover, *Streaming potential in porous media: 1. theory of the zeta potential*, Journal of Geophysical Research: Solid Earth **104**, 20021 (1999).
- [61] I. New England BioLabs, *ph vs temperature for tris buffer*, (2014)

# 9

## MECHANICAL TRAPPING OF DNA IN A DOUBLE-NANOPORE SYSTEM

*Nanopores have become ubiquitous components of systems for single-molecule manipulation and detection, in particular DNA sequencing where electric field-driven translocation of DNA through a nanopore is used to read out the DNA molecule. Here, we present a double-pore system where two nanopores are drilled in parallel through the same solid-state membrane, which offers new opportunities for DNA manipulation. Our experiments and molecular dynamics simulations show that simultaneous electrophoretic capture of a DNA molecule by the two nanopores mechanically traps the molecule, increasing its residence time within the nanopores by orders of magnitude. Remarkably, by using two unequal-sized nanopores, the pore of DNA entry and exit can be discerned from the ionic current blockades and the translocation direction can be precisely controlled by small differences in the effective force applied to DNA. The mechanical arrest of DNA translocation using a double-pore system can be straightforwardly integrated into any solid-state nanopore platform, including those using optical or transverse-current read-outs.*

---

This chapter has been published as: Sergii Pud, Shu-Han Chao, Maxim Belkin, Daniel V. Verschueren, Tuen Huijben, Casper van Engelenburg, Cees Dekker and Aleksei Aksimentiev. Mechanical trapping of DNA in a double-nanopore system. *Nano Letters*, 16(12):8021-8028, 2016

## 9.1. INTRODUCTION

The physical properties of biopolymers like DNA are of fundamental interest as these long molecules are the principal information carriers in all living systems [1, 2]. Single-molecule force spectroscopy techniques such as optical and magnetic tweezers have been the tool of choice for investigating the mechanical properties of polymers, and their interaction with molecular motors at the single-molecule level [3–5]. These techniques allow for exquisite control over the tension and extension of the biopolymers, but do require handles and anchor points to be chemically engineered onto the biomolecules, increasing complexity and limiting the versatility of these techniques [6]. Alternative label-free methods to manipulate biopolymers in novel ways at the single-molecule level would be much welcome.

Nanopores are single-molecule force manipulators that not only can exert controlled forces onto biopolymers without the need for handles or labels, but also provide read-out of the biological information encoded in the sequence [7, 8]. The principle of nanopore sequencing [9], where an individual DNA molecule is passed in a head-to-tail fashion through a pore while its sequence is locally read, allows for long uninterrupted read-lengths at low copy number and its feasibility has recently been demonstrated by the introduction of a commercial sequencer based on protein nanopores [10]. Solid-state nanopores [11] are promising for improving such sequencing technology, as they offer benefits in robustness, manufacturing, parallelization, and device integration [12, 13]. However, the typical residence time of a DNA molecule in a solid-state nanopore is too short to be used for force manipulation studies, let alone to sequence DNA. Although salt gradients [14], unconventional electrolyte conditions [15–17], DNA-nanopore interactions [18, 19], opto-electronic surface-charge modulation [20] and plasmonic excitations [21, 22] have been shown to increase the residence time of DNA in a solid-state nanopore, there is a clear need for a more radical approach to control the DNA in the nanopore. Previous studies have attempted to achieve this goal with some success. For example, attaching a molecular roadblock to the DNA polymer was shown to transiently halt nanopore translocation [23, 24] whereas single-molecule force probes, such as single-molecule tweezers and scanning probes, could balance the force driving the DNA translocation and move the DNA through a nanopore at arbitrary low speed [25–29]. However, these techniques for controlling DNA in a nanopore lack throughput, do not allow parallelization, and require DNA labelling, eliminating the advantage the nanopore force spectroscopy techniques has over other conventional techniques.

Here, we present a novel and label-free mechanistic approach for DNA manipulation based on a double-nanopore system, that can slow down and even fully arrest the motion of a single DNA molecule. The key element of our system is two parallel nanopores that are drilled in close proximity (less than  $1\ \mu\text{m}$ ) from each other within the same solid-state membrane (Fig 9.1A and B). During the electrophoretically driven passage of a DNA molecule through one of the nanopores, the untranslocated part of that molecule can be captured by the second nanopore, leading to mechanical entrapment of the molecule, see Fig. 9.1. The two nanopores exert opposite forces on the DNA that connects them and thus perform a nanoscale tug-of-war on the molecule. This tug-of-war vastly increases the molecule's residence time within the nanopore sensor,

with some molecules being trapped indefinitely (i.e. escaping only when the bias voltage is reversed). Furthermore, by using nanopores of unequal size, we show that the pore of DNA entry and exit can be experimentally discerned, unveiling new insights into the physics of DNA transport.

## 9.2. RESULTS AND DISCUSSION

Upon application of a transmembrane bias, an ionic current flows through both nanopores, which permits detection of DNA inside the pores [30]. Fig 9.1C illustrates typical DNA translocation events recorded using a double-pore system containing two 15 nm pores separated by 550 nm. Almost without exception, double-pore events last much longer, from 10 ms to  $10^4$  ms or even longer than regular DNA translocations (1 – 3 ms). The double-pore events can be discriminated from regular translocations by the pattern of the ionic current trace at the beginning of the event, the level of the long-duration blockade and, most distinctively, the event ending. A double-pore event begins with multiple changes of a baseline current as the DNA enters each of the nanopores, see the example trace in Fig. 9.1D. (For additional examples see Fig. S9.6 and S9.7 of the Supporting Information (SI).) First, the DNA molecule enters one of the nanopores with its leading end folded (Fig. 9.1D I), as is common for large pores (>5 nm), resulting in two strands of DNA residing in one of the nanopores, whilst the other pore remains open. This produces a double blockade of the current compared to the single blockade level. Subsequently, the DNA fold is pulled through (Fig. 9.1D II), similar to normal DNA translocation. Then, however, the lagging end of the DNA polymer blob is captured into the other nanopore in a folded conformation (Fig. 9.1D III), temporarily leading to a triple blockade level until also this fold is pulled through (Fig. 9.1D IV) resulting in a double current blockade. At this stage, the DNA becomes trapped between the two nanopores, which is topologically similar to the type of stalling that a long DNA molecule experiences during gel electrophoresis [31]. In this phase, the DNA folds are pulled out until the DNA is stretched taut between the two pores, and consequently a tug-of-war is set up between the two nanopores. Eventually one of the nanopores wins the nanoscale tug-of-war and DNA escapes from both nanopores sequentially. After escaping from the first nanopore, there is a short period where DNA resides in only one of the nanopores. The current trace reflects this in a brief single-level blockade (see Fig. 9.1D V), after which the current value reaches the baseline again. The duration of this ending was found to increase with nanopore distance (see Fig. S9.8), as expected. The presence of this brief single-blockade-level end signature serves as perhaps the clearest identifier of double-pore events.

Figure 9.2A shows the dwell time distribution of all events recorded using a double-nanopore setup, where the double-pore events are highlighted as black lines underneath the histogram. Long events are found to be almost exclusively associated with double-pore events. Note also the occurrence of very long events, lasting several seconds, which were only released upon switching off the bias voltage and hence can be considered as indications of indefinitely trapped DNA molecules. The contribution of double-pore events to the total number of observed events is small, about 0.5%, showing that regular translocations make up the vast majority of the population of events. Note that though occurrence of double pore trapping events is very low, it

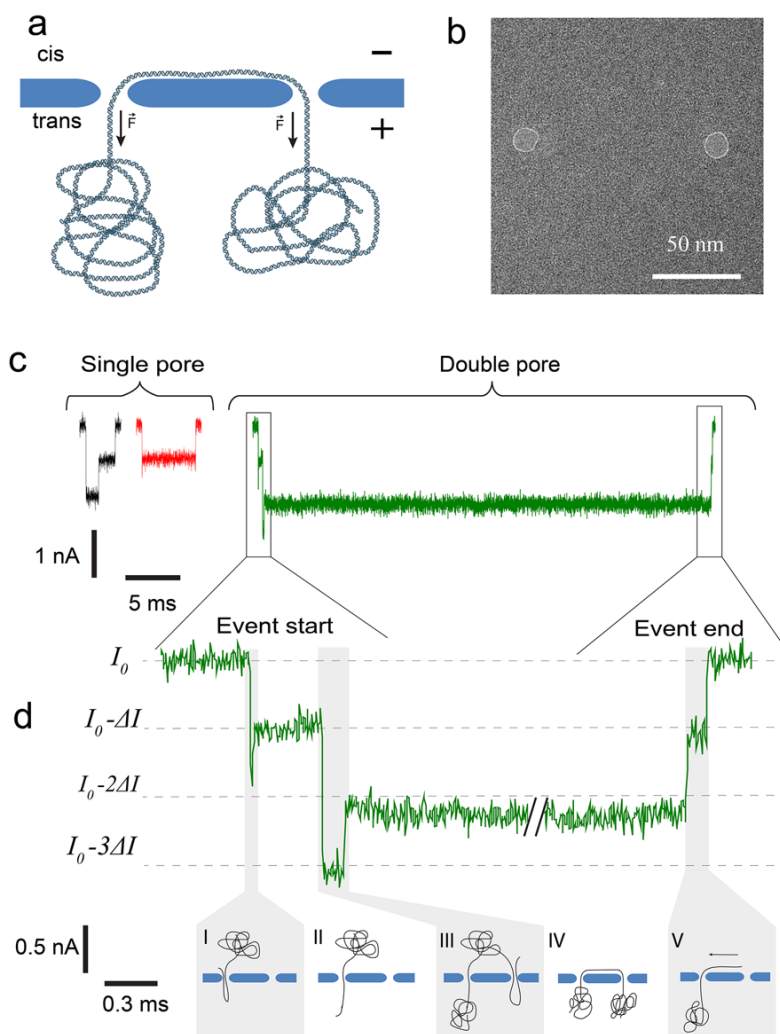


**Figure 9.1: Concept of trapping DNA in a double-nanopore system.** (A) Side-view sketch of a single DNA molecule that is trapped in two nanopores. In a tug-of-war fashion, the forces in the two nanopores cancel out, thus arresting the translocation of the DNA. (B) TEM image of two 10 nm nanopores drilled in a freestanding SiN membrane, separated by 100 nm. (C) Typical examples of single-nanopore and double-nanopore events at a bias voltage of 300 mV, pore diameter of 15 nm, and the pore-to-pore distance of 550 nm. (D) Expanded view of the beginning and ending of the double-pore event. The DNA molecule enters the first nanopore in a folded conformation (I), subsequently traverses it in single-file fashion (II), whereupon a different part of the molecule is captured by the second pore (III) in a folded fashion. Finally, the DNA reaches the trapped state (IV), and eventually slides out (V).

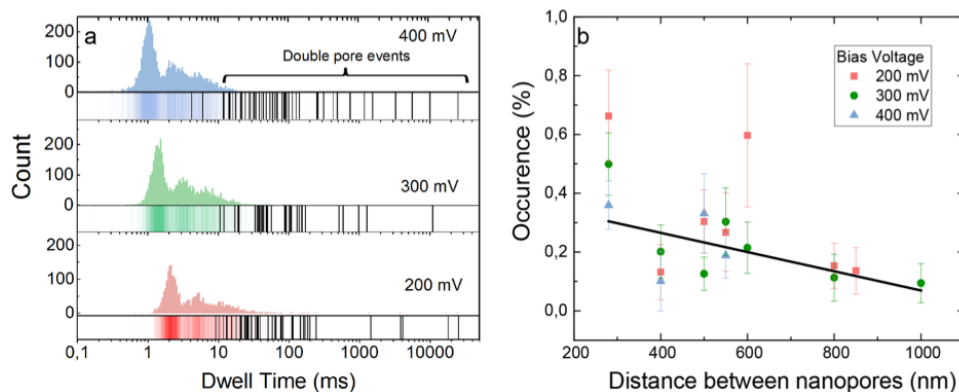


**Figure 9.2: Experimental event characteristics of the double-pore events.** (A) Dwell time distribution of DNA translocations in two 15 nm pores separated by 280 nm. The black lines in the histogram represent the double-pore events. (B) Occurrence rate of double-pore events as a function of distance between nanopores. The black line is a linear fit to the data. Error bars are standard errors.

is still enough to record tens of these events within half an hour of measurements (Fig. 9.2A). The likelihood of observing double-nanopore events decreases with the distance between the pores, see Fig. 9.2B. A control measurement performed using 5  $\mu\text{m}$ -spaced nanopores did not show any double-pore events within the observation time of 30 minutes, during which over 10000 free translocations were registered. The escape velocity of the DNA molecule, deduced from the duration of the end signatures (see Fig. S9.8), is in agreement with measurements of DNA translocation velocity reported previously in literature [32]. The end velocity is found to decrease with increasing distance between the nanopores (see Fig. S9.9), which suggests that interactions between DNA and the membrane surface influence the escape speed.

Coarse-grained (CG) molecular dynamics (MD) simulations provided insights into the mechanics of double-pore trapping. In our CG simulations, a single DNA molecule was initially placed at one side (*cis*) of a solid-state membrane that contained two circular nanopores, with one of the DNA ends entering one of the nanopores (Fig 9.3A). 2000 independent simulations were run for 2400  $\mu\text{s}$  each in the absence of a transmembrane bias to produce 2000 random DNA conformations. Subsequently, transmembrane bias was turned on and each system was simulated until the entire DNA molecule escaped to the *trans* side of the membrane (see Experimental Section 9.4 for a complete description of the MD simulation protocols.)

In the large majority of the simulations, the DNA molecules were observed to translocate in the normal fashion where they moved through the nanopore that they were initially threaded in, without having any of the coil interacting with the other nanopore (Fig. 9.3B, top). Double-nanopore events were however observed in a small number of cases, where a part of the DNA molecule was seen to enter the second nanopore, leading to the threading of the lagging part of the DNA into the second nanopore, thus causing the double-pore trapping (Fig. 9.3B, bottom). Plots of the local density of the DNA as a function of the simulation time characterize the ensemble of

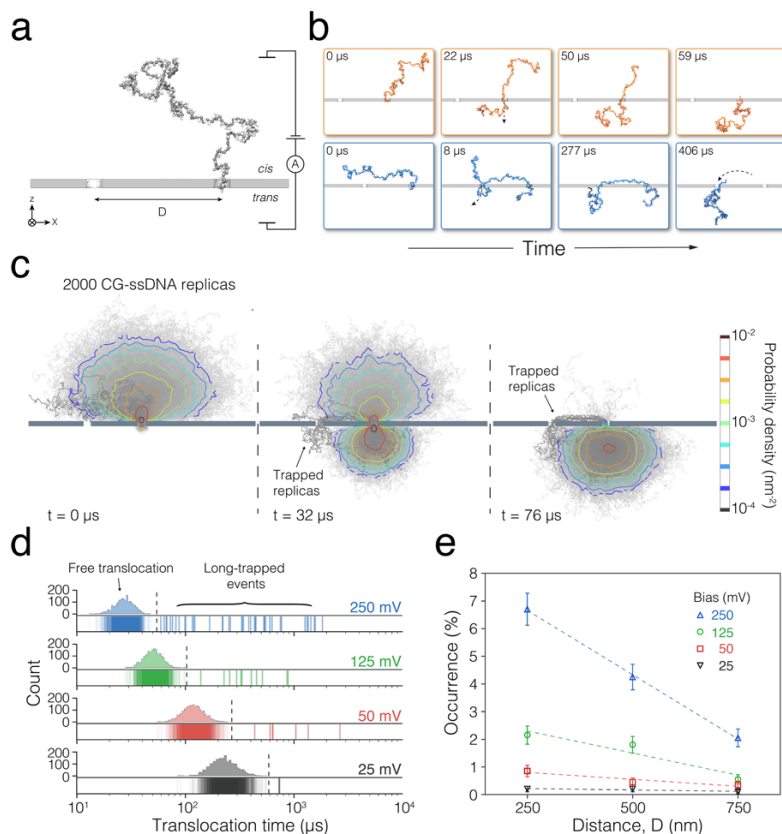


**Figure 9.3: Coarse-grained molecular dynamics simulations of DNA capture and translocation in a double-pore system.** (A) Setup of the CG simulation. The system consists of two compartments (*cis* and *trans*) divided by a solid-state membrane (grey). Two nanopores of equal dimensions are separated by a distance  $D$ . A DNA molecule (dark grey) is initially placed in the *cis* compartment, with one of its ends entering one of the nanopores. A voltage bias is applied across the membrane. (B) Snapshots from two CG MD simulations illustrating a typical single-pore translocation event (top, orange) and a double-pore capture (bottom, blue). (C) Ensemble of DNA conformations observed in double-pore capture and translocation simulations. Shown in grey are the 2000 instantaneous conformations of DNA overlaid with each other. The DNA molecules simultaneously captured by the two pores are highlighted using a darker shade of grey. The color contours specify the density of the CG beads at several stages of the DNA translocation process averaged over the 2000 replica systems. The density was computed by projecting the DNA beads coordinates onto the XZ plane (the plain passing through both pores normal to the membrane) over  $1 \text{ nm}^2$  grid. (D) Simulated distributions of the DNA translocation time. The DNA translocation time was defined as the time elapsed from the beginning of the simulation (when one end of the DNA was already threaded through one of the pores) until the entire DNA molecule moved to the *trans* compartment. The translocation times from individual replicas are shown as overlaid vertical bars. The histograms illustrate the distribution of the single-pore translocation times; each histogram contains 40 bins. Dashed lines indicate the time threshold for distinguishing long-lasting events, which is defined as the average translocation time plus 5-fold of the standard deviation of the single-pore translocation durations. The duration of the long-lasting events is show using darker colors. In this particular set of simulations, the scaled-up distance between the nanopores  $D = 750 \text{ nm}$ . (E) Occurrence of the long-lasting events under different pore separations and transmembrane biases. The occurrence is defined as the percentage of long-trapped events among all 2000 replicas for each simulation condition.

conformations explored by DNA in the 2000 independent translocation simulations, see Fig. 9.3C. At the beginning, the DNA conformations form the expected mushroom-like average configuration centered at the nanopore that contains one end of the DNA [33]. As the simulations progress, a mushroom-like cloud of DNA conformations grows at the *trans* side as the one at the *cis* side shrinks. Eventually, most of the DNA exits to the *trans* side while a small number of DNA molecules remain trapped with their two ends threaded through the two nanopores.

The distributions of the simulated DNA translocation times, Fig. 9.3D, exhibit features that are remarkably close to those measured in experiments, cf. Fig. 9.2A. At each transmembrane bias, the individual DNA translocation times histogram form a well-defined cluster, where the cluster's center shifts toward longer translocation times as the bias decreases, which is the expected behavior for single pore translocations. At the same time, a small but significant number of translocation events last considerably longer than the average. To quantitatively assess the occurrence rate of long-lasting DNA translocation events, we computed the mean and the standard deviation of the single-pore events histograms and defined the long-lasting events as those exceeding the mean single pore translocation time plus five times the standard deviation (see Fig. S9.10 for details). Analysis of the DNA translocation trajectories confirmed that double-pore trapping occurred in all of the long-lasting events. The occurrence of the long-lasting events, Fig. 9.3E, is found to be of order a few percent, to increase with the transmembrane bias, and to decrease with distance between the nanopores, similar to the trends observed in experiments. The numerical difference between the simulated and experimentally measured occurrence can be attributed to the differences between the initial conformations realized in the simulations and experiments, the length of the DNA fragments, and approximations that went into the construction of the CG model (see Experimental Section 9.4). Overall, MD simulations verify that double-pore trapping can increase the dwell time of DNA in the nanopore by at least two orders of magnitude in comparison to that produced by single-nanopore translocations.

The tug-of-war produced by the double-pore capture of DNA not only slows down the overall DNA translocation process but also offers a means to control the direction of DNA translocation. To demonstrate such control, we considered a situation where a DNA molecule is symmetrically partitioned between the two nanopores, Fig. 9.4A. In contrast to our previous simulations of DNA translocation (Fig. 9.3), the effective forces applied to DNA in the left and right nanopores,  $F_L$  and  $F_R$ , are now independently controlled. Experimentally, such a force differential can arise from the differences in the nanopore geometry [34, 35] and/or surface charge [36, 37], and can potentially be externally controlled by optical [20, 22] or electrical [38] means. When the forces in the two nanopores are exactly equal, the DNA escape process is determined by the diffusive motion of the DNA (Fig. 9.4A, and the differential entropic forces of the two polymer coils [39, 40] that develop when the symmetric partitioning of the DNA in the double-pore trap is broken. Hence, the likelihood of DNA exiting from the left or the right nanopore is equal (Fig 9.4B,i). However, we find that even a very small (0.5 pN) imbalance of the forces considerably affects the direction of the overall DNA motion within the double-pore trap and thus determines the pore from which the DNA exits (Fig. 9.4B,ii). Increasing the force imbalance makes the DNA motion through the double-pore system

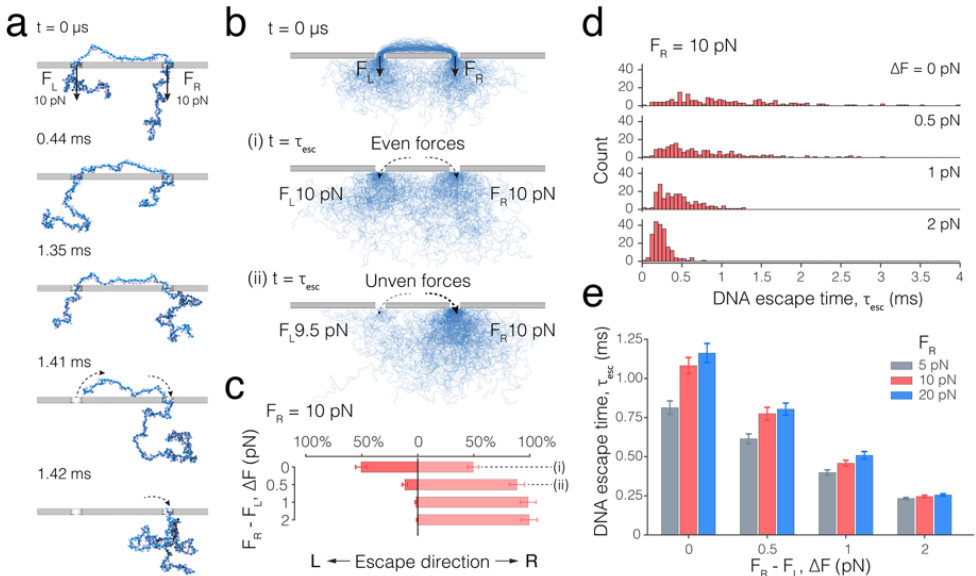


**Figure 9.4: Force-differential control over DNA escape from a double-pore trap.** (A) Sequence of snapshots illustrating escape of a DNA molecule from a symmetric double-pore-trapped conformation. At  $t = 0$ , a DNA molecule (blue) is threaded through both pores such that the DNA fragments that extend from the two pores to the *trans* side are of equal length. The backbone beads of the DNA residing within the left and right nanopores experience total net forces  $F_L$  and  $F_R$ , respectively, directed from *cis* to *trans* side, normal to the membrane. In this particular simulation,  $F_L = F_R = 10$  pN. (B) Ensembles of DNA conformations observed during CG MD simulations of DNA escape from a double-pore trap. Shown in blue are 200 instantaneous conformations of DNA overlaid with each other. At  $t = 0$ , the DNA molecules are symmetrically threaded through the two pores, similar to the conformation shown in the top snapshot in panel (A). (i) Ensemble of conformations adopted by DNA right after escaping (at  $t = \tau_{\text{esc}}$ ) to the *trans* compartment in the case the driving forces in the two nanopores are equal ( $F_L = F_R = 10$  pN). Note that individual escape times vary from one replica to the other, see panel (D). DNA escape through either left or right nanopore is equally likely. (ii) Same as above, except that the driving force in the right nanopore is 0.5 pN larger than in the left nanopore. The majority of the DNA now escapes through the right pore. (C) The percentage of 200 replica simulations where DNA is seen to escape through either right or left nanopore as a function of the nanopore force differential,  $\Delta F$ . The force at the right pore was fixed to 10 pN. (D) Distribution of the DNA escape times. The DNA escape time is defined as the time elapsed from the beginning of the simulation until the moment the entire DNA molecule moves to the *trans* side of the system. The force at the right pore was 10 pN. Bin size of the histograms is 50  $\mu\text{s}$ . (E) Average DNA escape time versus the force differential. The force at the right pore equals 5 pN (grey bar), 10 pN (red bar), and 20 pN (blue bar).

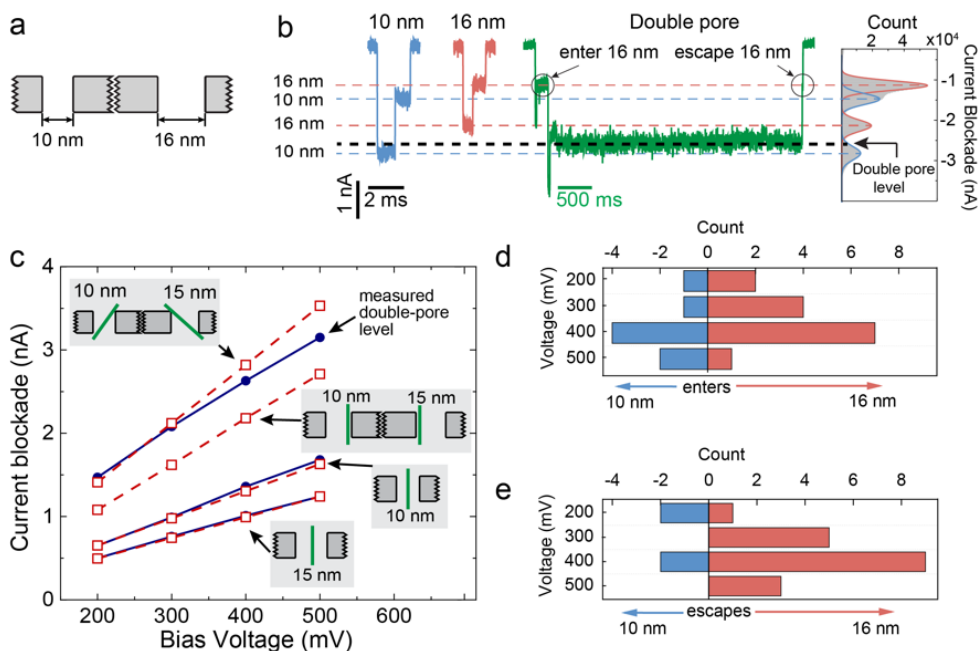


**Figure 9.5: DNA translocations through asymmetric double nanopores.** (A) Schematic of an asymmetric double-nanopore system with two pores of 10 and 16 nm diameters. (B) Example events at 400 mV of freely translocating DNA molecules through the 10 nm and 16 nm nanopores, and a double-pore event. The average current blockade levels (dashed lines) are derived from the peaks in the current histogram of all events, displayed on the far right. (C) Experimental (blue) and theoretical (red) ionic current blockades as a function of bias voltage of the free translocations (bottom two curves) and double-nanopore events (top curves), indicating a voltage-dependent tilted conformation of the DNA when DNA is trapped in the double nanopore. The schematics indicate the orientation of the DNA inside the nanopore for each respective theoretical prediction. (D) Histogram of pore of entry for double-nanopore events. (E) Histogram of the escape directions for double-pore events, showing a clear bias for escape from the larger pore.

more unidirectional (Fig. 9.4C) and the DNA escapes faster (Fig. 9.4D). At a 2 pN force differential, which corresponds to only a 20% change of the 10 pN force acting on the DNA in each pore, the DNA was observed to exit through the nanopore of the higher effective force in 199 out of the 200 independent simulations.

We experimentally created a force imbalance in a double-nanopore system by fabricating two nanopores of different diameters: 10 nm and 16 nm, see Fig. 9.5A (see Fig. S9.12 for a TEM image). As there is a weak dependence of the electrophoretic force and electroosmotic drag on the pore diameter [34, 35, 41], we expect the trapped events to end with DNA escaping preferentially from one of the two nanopores. In such an asymmetric double-pore system, double-pore events are clearly observed and constitute about 0.4% of all recorded translocations. Figure 9.5B shows examples of single and double-pore events and the current blockade histogram of all, single and double-pore, translocations taken at 400 mV (for the histograms of current blockades at other voltages, see Supporting Information Fig. S9.11). Interestingly, the difference between current blockades produced by DNA in either 10 nm or 16 nm nanopores can

clearly be distinguished, since the DNA current blockade has a weak dependence on the nanopore size [42]. The DNA current blockade in a 10 nm nanopore is higher than in a 16 nm nanopore and this difference increases linearly with bias voltage. These current blockade differences enable us to discriminate whether DNA is translocating through either the 10 nm or 16 nm nanopore (Fig. 9.5B). Notably, the DNA captured simultaneously by both nanopores produces a current blockade, which is not equal to the doubled blockades produced by DNA in either the 10 or the 16 nm pore. The double-pore current blockade is found to be systematically larger than the sum of the current blockades from the single-pore translocations. We can attribute this effect to a difference in the orientation of the DNA helix within the nanopore. As a DNA molecule trapped in the double-pore is pulled taut onto the membrane and because of its high stiffness (with a persistence length of about 50 nm), we expect it to adopt a tilted orientation in the nanopores, which is different from the freely translocating molecule (see the top inset in Fig. 9.5C). To investigate this, we developed a theoretical model that describes the conductance blockades without any adjustable fit parameters (see SI Section 9.5.7) and explicitly accounts for the orientation of the DNA molecule in the nanopore. Note that our theoretical model does not take into account the surface charge of the nanopore as its effect on the conductance blockade amplitude is minimal in the case of a high-ionic strength electrolyte used in this work. For freely translocating molecules, the model is in excellent agreement with the measured current blockades in both nanopores (bottom 2 lines in Fig. 9.5C), assuming the DNA molecules translocate through the center of the nanopores. Figure 9.5C shows upper (maximally inclined) and lower (straight hugging of the pore wall) bound estimates for the double-pore blockade level as predicted by the model. At bias voltages below 300 mV, the measured double-pore blockade level is consistent with the resident DNA maximally inclined, as expected. Interestingly however, above 300 mV the observed double-pore level starts to deviate from the model's predictions, implying a voltage-mediated change in DNA orientation inside the pores. The lower observed double-pore current blockade level indicates a less tilted conformation of the DNA inside the pore, which can be interpreted as voltage-induced bending of DNA that aligns the molecule with the pore axis.

The current signatures produced by DNA translocating through differently sized pores allowed us to determine the order in which the DNA entered and escaped during the double-pore events (see SI Section 9.5.8). In most cases, DNA molecules first entered the 16 nm nanopore (roughly 60% of observed double-nanopore events, see also Fig. 9.15 for an independent second experiment), as is shown in Fig. 9.5D, which is the expected behavior [33]. Interestingly, we also observed the DNA molecule to preferentially escape from the 16 nm nanopore (Fig 9.5E). This is a nontrivial result that, at first sight, appears to contradict the expectation that the larger electrophoretic force inside the 10 nm pore would force the DNA to exit through the smaller pore. A careful consideration of the forces on the DNA in the double-pore system explains the result however. The critical point is that the electric field distribution in the access region near a 10 nm nanopore is different from that of a 16 nm nanopore (See Fig. 9.17). For these relatively large nanopores, the potential drop over the access region can dominate the potential drop over the nanopore itself (see SI Section 9.5.10). Hence, even though the electric field and thus the electrophoretic force inside the 10 nm nanopore is larger

compared to the 16 nm one [34], the forces exerted on the DNA by the electric field in the access region are significantly larger for the 16 nm nanopore (see SI Section 9.5.11), such that the force differential pushes the DNA towards the 16 nm pore. Note that, because DNA is highly bent in the double-pore-trapped conformation, the total force on the DNA molecule is not solely determined by the transmembrane bias [25]. For the asymmetric double-pore system, our observations (Fig. 9.5E) indicate that such force imbalance indeed determines the tug of war and results in preferred escape through the 16 nm nanopore. The asymmetric double nanopore system thus enabled us to determine and control the entry and escape direction of a DNA molecule trapped in a double nanopore.

## 9.3. CONCLUSION

To conclude, we developed a novel approach to mechanical trapping of DNA in solid-state nanopores, which can vastly increase the residence times of the molecules, with some molecules being trapped indefinitely. The double nanopore platform not only allows for slowing down DNA molecule translocations, but also unveils interesting physics of this nanoscale tug-of-war on DNA, that we corroborate with MD simulations and theoretical modelling. We show that, for differently sized nanopores, we can monitor the entry and escape direction of the stalled DNA molecule, which are dictated by the size asymmetry between the two pores. The purely mechanical stalling of the DNA translocation with the double-pore approach holds great potential for future biophysics experiments and nanopore applications. The approach is straightforward to upscale and is easily incorporated in any solid-state nanopore platform, where the slowed down molecule allows the long integration times required for optical [22] or transverse [43] read-out of its sequence. The control over the translocation direction by applying minute force differences between the pores may permit re-addressing the same DNA fragment multiple times, for example for re-sequencing when generalized to single-stranded DNA. Ultimately, the sliding speed of the DNA molecule past the nanosensor can be controlled at will by the experimenter by addressing each of the nanopores independently, which will be the focus of our future work.

## 9.4. EXPERIMENTAL DETAILS

### 9.4.1. DOUBLE-PORE EXPERIMENTS

Double nanopores were fabricated by drilling two nanopores in close proximity within the same freestanding membrane, made of 20 nm-thick low-stress SiN. A TEM image of the typical double-pore device is shown in Fig. 9.1B. During the experiments DNA is placed into the *cis* compartment and it is dragged through the nanopore by biasing the Ag/AgCl electrode on the *trans* side. Throughout all the experiments we used  $\lambda$ -DNA (48 kbp, contour length 16.3  $\mu\text{m}$ ) in 2M LiCl buffers with 20mM Tris and 2mM EDTA. Most of the experiments were carried out using 15 nm nanopores, unless specified otherwise. The distances between the nanopores were chosen to be roughly smaller than the diameter of gyration of the  $\lambda$ -DNA coil, which is approximately 800 nm [39]. The double-pore events were extracted from ionic current traces using Tranzalyser [44] and analysed using a custom-made software.

### 9.4.2. COARSE-GRAINED MD SIMULATIONS

All CG MD simulations were performed using a previously described custom CG model [45]. Although this CG model was originally developed to describe the behaviour of unstructured single-stranded DNA, it can also describe the behaviour of much larger dsDNA molecules through scaling of the simulation length scales with the ratio of the persistence lengths of the molecules, i.e., by a factor of 50. The time scale of the CG simulations was calibrated by matching the experimental [46] and simulated electrophoretic mobility of DNA. The electrolyte conditions were taken into account implicitly through calibration of the CG model to MD simulations and experiments [45]. All distances and time intervals reported in the manuscript have been scaled to describe the behavior of dsDNA. The steric forces from the inorganic membrane and the forces produced by the transmembrane bias were applied through grid-force potentials [47] using a method described previously [22] and the solvent was modelled implicitly via a Langevin thermostat. SI Section 9.5.3 provides a complete description of the simulation protocols. Theoretical model of the conductance blockade. To theoretically compute the blockade-current amplitude for a given orientation of the DNA in a nanopore, the nanopore volume was divided into cylindrical slabs of the same height arranged perpendicular to the nanopore axis. The resistance of each slab was computed by integrating the local resistance of the solution within the slab, which in turn was computed using a previously established dependence of the ion mobility and ion number density on the distance from the DNA molecule [48]. The total resistance of the nanopore volume was computed by summing up the resistances of all slabs. The ionic current blockades were computed by taking into account both the resistance of the nanopore volume and the access resistance of the solution. SI Section 9.5.7 provides a complete description of the theoretical model.

## 9.5. SUPPORTING INFORMATION

### 9.5.1. ADDITIONAL EXAMPLES OF DOUBLE-NANOPORE EVENTS

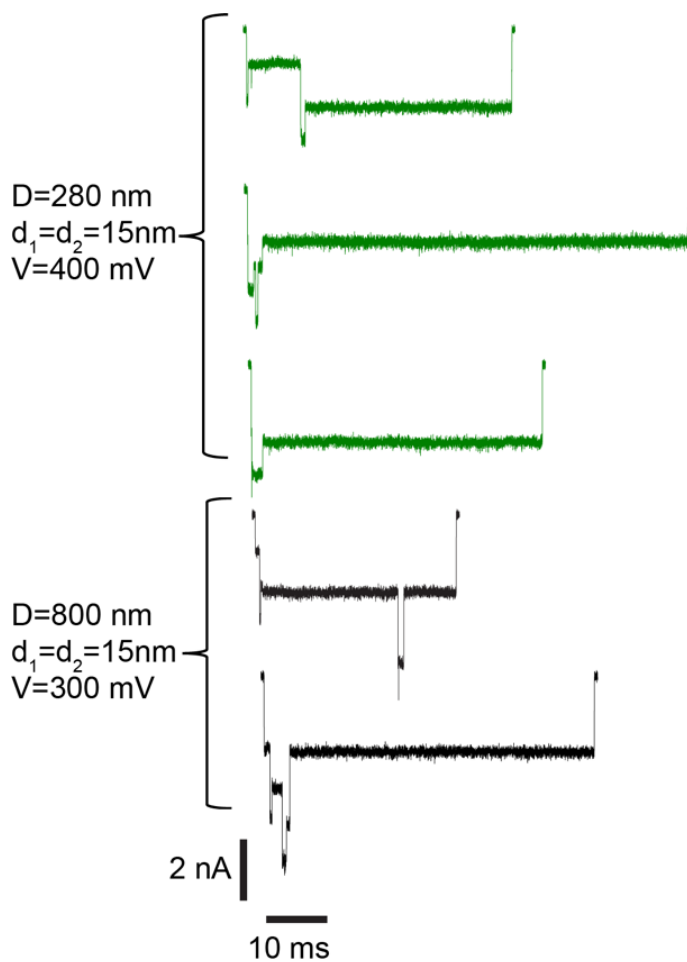


**Figure S9.6:** Examples of double-nanopore trapped events recorded using a system of two 15 nm-diameter nanopores separated by 280 (top) and 800 nm (bottom).



### 9.5.2. CHARACTERISTICS OF THE END SIGNATURES OF DOUBLE-NANOPORE EVENTS

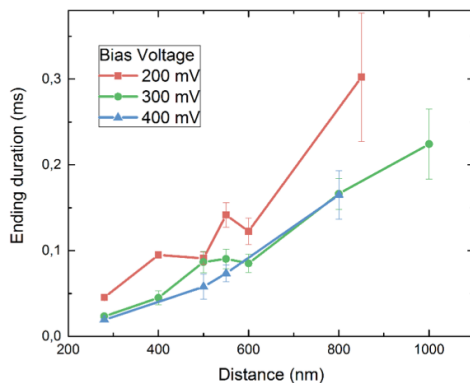


**Figure S9.8:** Duration of the ending signature of double-nanopore events (i.e., the brief single-blockade-level right before the final escape) as a function of distance between nanopores in a double-nanopore system. The end-signature duration increases with increasing pore to pore distance, as the latter increases the length that the lagging end of the DNA molecule has to traverse before exit.

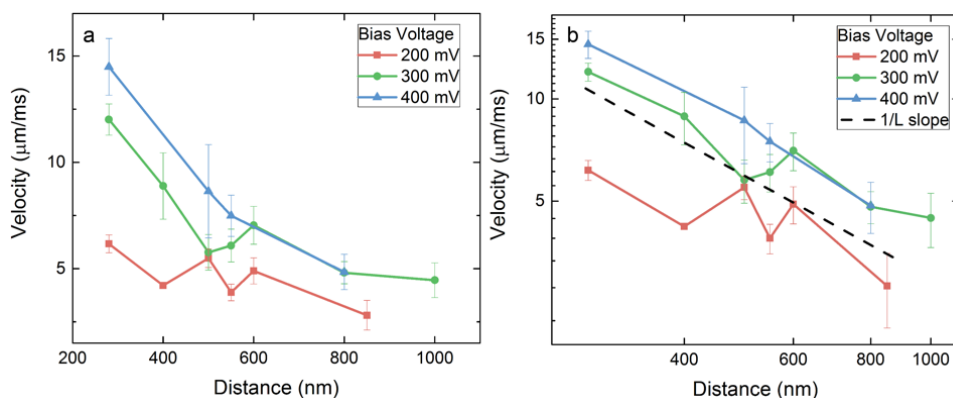


**Figure S9.9:** End velocity calculated using the end signature of the double-nanopore events, shown in normal scale (A) and in double-logarithmic scale (B). Black dashed line in (B) indicates a 1/L slope. The 1/L dependence of the escape velocity on distance suggests non-specific interactions between the DNA and the membrane surface where the friction force increases linearly with DNA-surface interaction length.

### 9.5.3. COARSE-GRAINED MD SIMULATIONS

The coarse-grained MD simulations were performed using a custom version of NAMD2 [45, 49]. Each ensemble simulation contained 2000 replicas in the double-nanopore trapping study and 200 replicas in the translocation control study. Each simulation system contained a 150-nucleotide ssDNA molecule described using our two-beads-per-nucleotide coarse-grained model 2 and a grid potential representing the steric interaction between DNA and the membrane. Given that the ratio of the persistence lengths of dsDNA and ssDNA is approximately 50, the 150 nucleotide fragment of ssDNA employed in our CG MD simulations corresponds to a ~4500 base pair fragment of dsDNA, a molecule ten times shorter than the one employed in our experiments. The steric potential was defined to have values of 0 and 5.85 kcal/mol assigned to the region of space occupied by the solution and the membrane, respectively. The grid spacing was 1 Å in each dimension. The membrane was 1 nm thick and each nanopore was 2 nm in diameter. The distance between the centers of the two pores was 5, 10 or 15 nm in the double-pore trapping study and 15 nm in the translocation control study. The distances reported in the main text reflect the 50-fold scaled up values, deduced by the 50:1 ratio of dsDNA/ssDNA persistence lengths. The simulation unit cell was a cube 105 nm on each side. Periodic boundary conditions and a nominal time step of 20 fs were employed. The tabulated nonbonded interactions were computed using a 34–35 Å cutoff. Stochastic forces from the solvent were introduced via a Langevin thermostat set to a temperature of 295 K and a nominal damping coefficient of  $1.24 \text{ ps}^{-1}$ . The trajectories were recorded every 10000 simulation steps. The time scale of the coarse-grained simulations was calibrated by matching the simulated electrophoretic mobility of a 150-nt CG ssDNA ( $5.8 \cdot 10^{-4} \text{ cm}^2/(\text{V}\cdot\text{s}) = 6.44 L_{\text{ss}}^2/(\text{V}\cdot\text{ns})$ , where  $L_{\text{ss}}$  is the persistence length of ssDNA) and the experimental free-draining mobility of dsDNA ( $4.2 \cdot 10^{-4} \text{ cm}^2/(\text{V}\cdot\text{s}) = 1.58 \cdot 10^{-2} L_{\text{ds}}^2/(\text{V}\cdot\text{ns})$ , where  $L_{\text{ds}}$  is the persistence length of dsDNA) [46], yielding 1 to 408 conversion factor between the ssDNA and dsDNA time scales. The time intervals reported in the main text already reflect the time scale calibration.

To set up initial conditions for DNA trapping simulations, one end of the DNA molecule was threaded through one of the nanopores. The terminal bead of the threaded end was restrained to remain at the center of the *trans* side exit of the nanopore. 2000 copies of the system were equilibrated for  $3 \cdot 10^8$  simulation steps each (2.4 ms scaled time), producing 2000 random conformations of the polymer. During the equilibration, the terminal three beads threaded through one of the two nanopores were subject to a cap grid potential (defined to have values of 11.7 kcal/mol at the *cis* region and 0 kcal/mol at the *trans* region and inside the nanopore) that prevented that end of the DNA molecule from escaping the nanopore; a 10 pN force pointing toward +z direction (the *cis* region) was applied to any bead of the DNA molecule that entered the volume of the other pore, preventing accidental double-nanopore trapping.

The double-nanopore trapping simulations were carried out starting from 2000 random conformations of DNA each having one end of the DNA threaded through one nanopore. The simulations were carried out in the presence of a grid potential that represented the effect of the transmembrane bias. Such transmembrane bias potentials were computed using the COMSOL Multiphysics program (version 4.4) for the double-nanopore geometry over a 2 Å-spaced grid; the details of the procedures

are described in our previous study [22]. Subject to a transmembrane bias potential, each backbone bead of coarse-grained DNA experienced an electric force equal to the product of the local electric field and  $0.25 q^*$ , where  $q^*$  is the nominal charge of a DNA nucleotide. To prevent the end of the DNA initially threaded through the nanopore from escaping, the terminal three beads at the threaded end were subjected to a cap grid potential defined to have values 11.7 and 0 kcal/mol at the *cis* region and inside the nanopore, respectively. The size of the cap grid was  $7 \times 7 \times 0.3 \text{ nm}^3$ . The cap potential was applied only for the first  $10^7$  steps ( $80 \mu\text{s}$  scaled time) of each DNA capture simulation. The forces on the beads produced by the steric, transmembrane bias and cap potential grids were calculated using the grid forces feature [47] of NAMD2. Each simulation was run until the DNA fully translocated from *cis* to *trans* side of the membrane.

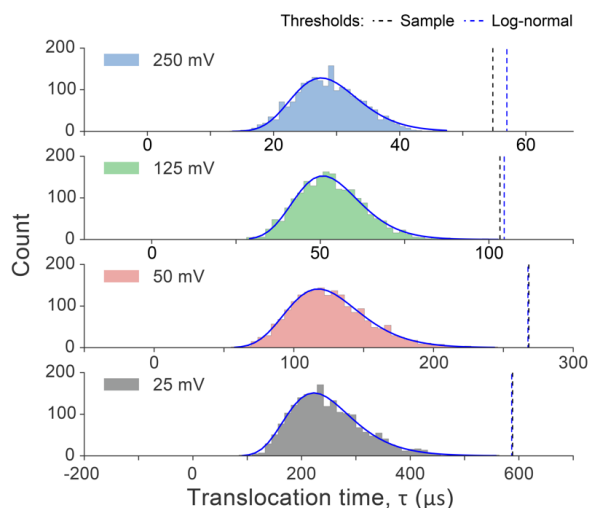


**Figure S9.10: Distribution of single-pore DNA translocation times.** The data shown are the same as in the main text Fig. 9.4D, but now plotted on a linear time scale. Each histogram contains 40 bins. Blue solid lines show the log-normal fit (i.e. a Gaussian on a log scale) to each of the histograms. The thresholds, shown as dashed lines, were defined as the sample mean plus 5-fold sample standard deviation (black, same as in main text Fig. 9.4D) or log-normal distribution mean plus 5-fold distribution standard deviation (blue).

For the study of force-differential control over DNA escape from a double-nanopore trap, both ends of the DNA molecule were initially threaded through both pores, one of each. One backbone bead was restrained to the center of each pore such that the lengths of the DNA fragments extending to the *trans* compartment from each pore were equal. The length of the middle portion, i.e. the segment exposed to the *cis* compartment, was chosen to approximately match the expected extension of the molecule at the target force on the DNA in the nanopores. The actual tension in the DNA fragment at the *cis* side of the nanopore computed from the displacement of the restrained beads was  $4.1 \pm 1.1$ ,  $8.4 \pm 1.1 \text{ pN}$  and  $17.0 \pm 1.2$  for the 5, 10 and 20 pN target force, respectively. The systems were equilibrated for  $5 \cdot 10^7$  steps ( $400 \mu\text{s}$  scaled time), producing 200 random conformations for each target force. The translocation control simulations were carried out applying a constant external force to each backbone bead of DNA confined within

the nanopore volume via a custom tcl script. The total force on the beads in one of the nanopores was set to either 5, 10 or 20 pN, whereas the total force on all beads in the other pore was either equal to or 0.5, 1 or 2 pN less than the force in the first pore. Each simulation was run until the DNA fully translocated from *cis* to *trans* side of the membrane.

#### 9.5.4. CURRENT BLOCKADE HISTOGRAMS RECORDED USING AN ASYMMETRIC DOUBLE-NANOPORE SYSTEM

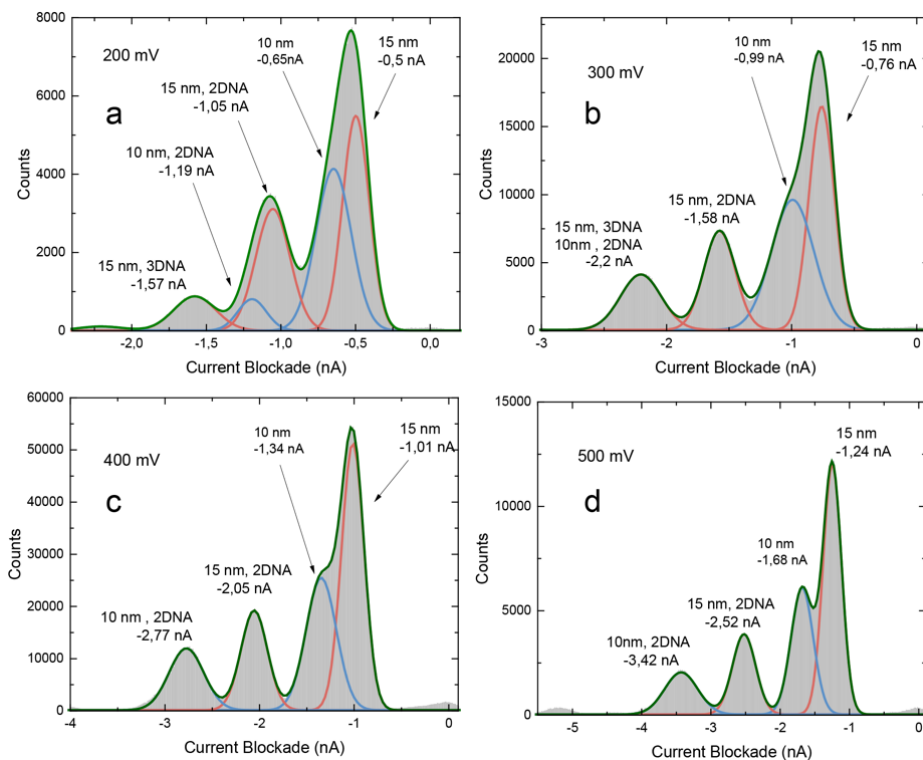


**Figure S9.11: Histograms of experimental ionic current blockades produced by all DNA translocations through an asymmetric double-nanopore system and respective Gaussian fits.** The diameters of the individual pores were 10 and 16 nm (see Fig. S9.12). Data in panels (A), (B), (C), and (D) correspond to a transmembrane bias of 200, 300, 400 and 500 mV, respectively. The fitted peak values and the corresponding pore diameters are indicated on the graphs.

### 9.5.5. TEM IMAGE OF THE ASYMMETRIC DOUBLE-NANOPORE SAMPLE

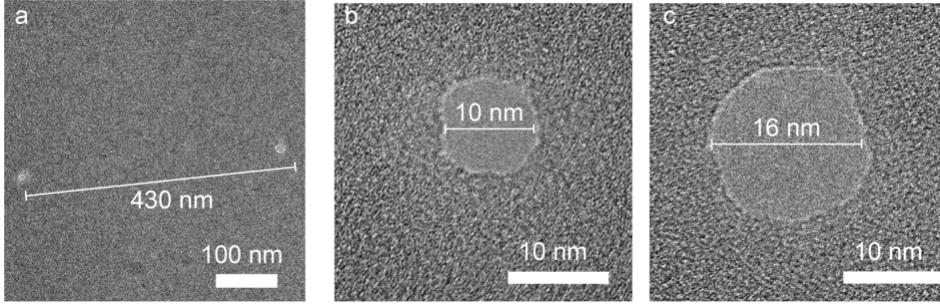


**Figure S9.12: DTEM image of an asymmetric double-nanopore system.** (A) The distance between nanoparticles is 430 nm. The pore diameters are (B) 10 and (C) 16 nm.

### 9.5.6. CURRENT BLOCKADE ESTIMATION USING THE MODEL OF CARLSEN *et al.* [42]

We estimated the current blockade values for single pore DNA translocations using the model published by Carlsen *et al.* [42], where DNA is inserted in the middle of the nanopore. The conductance of each access region is

$$G_{\text{acc}} = 2\sigma d_p$$

where  $d_p$  is the nanopore diameter and  $\sigma$  is the conductivity of the electrolyte, which in our case was taken as 13.2 S/m (measured value) for 2M LiCl solution. Taking into account the bulk and surface conductivity contributions, the conductivity of the pore region is defined as:

$$G_{\text{pore}} = \frac{\pi d_p^2}{4L_{\text{eff}}} \left( \sigma + \frac{4S\mu_{\text{cation}}}{d_p} \right)$$

where  $L_{\text{eff}}$  was taken as a fitting parameter close to  $L/3$  (see Ref. [50, 51]). In our case of a 20 nm membrane it was taken as 5 nm,  $S$  is the surface charge density on SiN in LiCl solution, which was taken as [21]  $0.03 \text{ C/cm}^2$ ,  $\mu_{\text{cation}}$  is cation mobility of lithium, which was taken as  $4 \cdot 10^{-8} \text{ cm}^2/(\text{V}\cdot\text{s})$ . The total nanopore conductance can be evaluated as [51]:

$$G_{\text{total}} = \left( \frac{1}{G_{0,\text{pore}}} + \frac{2}{G_{0,\text{acc}}} \right)^{-1}$$

The DNA blocks the access region of nanopore and also occludes volume of the nanopore. We can calculate access and bulk conductance of the pore with DNA in it:

$$G_{\text{acc,DNA}} = G_{0,\text{acc}} - G_{\text{DNA,acc}} = G_{0,\text{acc}} - \sigma \frac{\pi d_{\text{DNA}}^2}{2d_p}$$

$$G_{\text{pore,DNA}} = G_{0,\text{pore}} - G_{\text{DNA,pore}} = G_{0,\text{pore}} - \sigma \frac{\pi d_{\text{DNA}}^2}{4L_{\text{eff}}}$$

where  $d_{\text{DNA}} = 2.2$  nm. Note we have neglected DNA surface currents, as the effective charge of the DNA in high concentration LiCl buffers is small [15]. The conductance blockade can be then evaluated as the difference between the conductance of the bare pore and that of a pore with DNA:

$$\Delta G_{\text{DNA}} = \left( \frac{1}{G_{\text{pore,DNA}}} + \frac{2}{G_{\text{acc,DNA}}} \right)^{-1} - G_{\text{total}}$$

Using the last equation we evaluated the conductance blockades for DNA translocations through 10 nm and 16 nm nanopores and voltages ranging from 200 mV to 500 mV. Figure S8.8 shows the results of the calculations along with the experimentally obtained values.

### 9.5.7. THEORETICAL MODEL OF A BLOCKADE CURRENT

To explain the observed difference in conductance blockades that DNA produces in individual solid-state nanopores and when trapped simultaneously by the two pores, we developed a theoretical model that is schematically illustrated in Fig. S9.13. In this model, the space is divided into three compartments: *cis*, *trans*, and the nanopore volume. Total resistance of the system is, therefore, the sum of resistances of the compartments:  $R_{\text{total}} = R_{\text{cis}} + R_{\text{pore}} + R_{\text{trans}}$ . Ionic current that flows through the pore under an applied bias  $U$  can be readily computed as  $I = U/R_{\text{total}}$ . To estimate the three components of the total resistance, we consider neutral nanopores of a cylindrical shape. In doing so we neglect the change in ion behavior near the charged membrane surfaces.

We start by noting that resistances of *cis* and *trans* compartments in the absence of DNA can be estimated according to the classical formula for access resistance of a cylindrical pore:  $R_{\text{acc}} = (2D\sigma_{\text{bulk}})^{-1}$ , where  $D$  is the diameter of a pore, and  $\sigma_{\text{bulk}}$  is conductivity of bulk electrolyte solution. When DNA translocates through the pore, it occludes both of these compartments (*cis* and *trans*) and changes their resistances. To estimate access resistance in the presence of DNA, we use the approach of Carlsen *et al.* [42]

$$R_{\text{acc,DNA}} = \frac{1}{G_{\text{acc,DNA}}} = \frac{1}{G_{\text{acc}} - \Delta G_{\text{DNA}}} = \frac{1}{2D\sigma_{\text{bulk}} - \sigma_{\text{bulk}} \frac{\pi d_{\text{DNA}}^2}{2D}}$$

The open pore resistance can be computed based on the geometrical expression for the nanopore volume resistance and access resistance in the absence of DNA ( $R_{\text{acc}}$ ) [52]:

$$R_{\text{openpore}} = R_{\text{pore}} + 2R_{\text{acc}} = \frac{L}{\sigma_{\text{bulk}}S} + \frac{L}{\sigma_{\text{bulk}}S} = \frac{L/S + 1/D}{\sigma_{\text{bulk}}}$$

where  $L$  and  $S$  are the pore length and cross-sectional area. To calculate resistance of the middle compartment (nanopore) in the presence of DNA, we split the nanopore volume into thin “slabs” perpendicular to the nanopore axis, see Fig. S9.13B. As these slabs are connected in series (see the equivalent electrical diagram in Fig. S9.13C), the overall resistance of the nanopore volume  $R_{\text{pore}}$  is, therefore, the sum of resistances of these slabs:  $\sum_i R_i$ . Resistance of an individual slab can be calculated according to the definition as:

$$R_i = \frac{\Delta l}{\langle \sigma_i \rangle s_i}$$

where  $\langle \sigma_i \rangle$  is the average conductivity, and  $\Delta l$  and  $s_i$  are the thickness along the pore axis and cross-sectional area of the slab, correspondingly, see Fig. S9.13B. To compute the average conductivity  $\langle \sigma_i \rangle$  of a slab, we recall that local current density  $\vec{J}$  can be written as:

$$\vec{J} = \sum_{\text{iontypes}} nq\vec{v} = \sum_{\text{iontypes}} nq\mu\vec{E} = \sigma\vec{E}$$

where  $n$ ,  $q$ ,  $\vec{v}$ , and  $\mu$  are number density, charge, velocity, and mobility of ions,  $\sigma$  is local conductivity of the medium, and  $\vec{E}$  is the local electric field. From here it follows that local conductivity at the position defined by a radius vector  $\vec{r}$  can be computed as  $\sigma(\vec{r}) = \sum_{\text{iontypes}} qn(\vec{r})\mu(\vec{r})$ . Therefore, average conductivity of  $i$ -th slab can be computed as:

$$\sigma(\vec{r}) = \frac{1}{s_i} \sum_{\text{iontypes}} \int_{s_i} qn(\vec{r})\mu(\vec{r}) dS$$

where summation is performed across all types of ions in the solution, and integration is performed across the cross-sectional area of a slab  $s_i$ . The only assumption we made while arriving at this expression was that local ion velocity is linearly proportional to the local electric field, i.e.  $\vec{v} = \mu\vec{E}$ , which should be valid for such a small species as ions. When the above expression is substituted into the expression of the resistance of a slab, cross-sectional area terms  $s_i$  cancel out and we arrive at the following expression:  $R_i = \Delta l \left( \sum_{\text{iontypes}} \int_{s_i} qn(\vec{r})\mu(\vec{r}) dS \right)^{-1}$ . Finally, the total nanopore resistance can be written as:

$$R_{\text{total}} = 2R_{\text{acc,DNA}} + \sum_{i(\text{slabs})} \Delta l \left( \sum_{\text{iontypes}} \int_{s_i} qn(\vec{r})\mu(\vec{r}) dS \right)^{-1}$$

In our model, we approximate the DNA conformation inside the pore with a straight line, Fig. S9.13A and B. For simplicity and clearness, we use two points,  $\vec{M}$  and  $\vec{N}$ , to define the conformation of the DNA molecule. To perform numerical integration using the above equation each slab is discretized into rectangular parallelepiped bins  $(\Delta x, \Delta y, \Delta z)$  and integration  $\int_{s_i} dS$  is replaced by a double summation  $\sum_x \sum_y \Delta x \Delta y$ . Contribution of a particular bin to average conductivity of a slab is determined by the distance  $d$  from the center of the bin,  $\vec{P}$ , to DNA, see Fig. S9.13B. Within our model, this distance is set by a simple expression for the distance from a point to a line  $d = |(\vec{P} - \vec{N}) \times (\vec{M} - \vec{N})|$ . Distance from the DNA is then used to find number density  $n$  and mobility  $\mu$  for all types of ions in that bin using the profiles reported in [48]. Obtained distributions of  $\mu(\vec{r})$  and  $n(\vec{r})$  across all bins in a slab are then used to compute the integral  $\int_{s_i} qn(\vec{r})\mu(\vec{r}) dS$  numerically as  $\sum_x \sum_y q\mu(x, y, z_i) n(x, y, z_i) \Delta x \Delta y$ . Resistance of a slab is then computed as:

$$R_{\text{slab}} = \frac{\Delta l}{\sum_{\text{iontypes}} \sum_x \sum_y q\mu(x, y, z_i) n(x, y, z_i) \Delta x \Delta y}$$

The final expression for the total resistance of a nanopore with DNA can be written as:

$$\begin{aligned} R_{\text{total}} &= 2R_{\text{acc,DNA}} + \sum_{\text{slabs}(z_i)} \frac{\Delta l}{\sum_{\text{iontypes}} \sum_x \sum_y q\mu(x, y, z_i) n(x, y, z_i) \Delta x \Delta y} \\ &= \frac{1}{D\sigma_{\text{bulk}} - \sigma_{\text{bulk}} \frac{\pi d_{\text{DNA}}^2}{4D}} + \sum_{\text{slabs}(z_i)} \frac{\Delta l}{\sum_{\text{iontypes}} \sum_x \sum_y q\mu(x, y, z_i) n(x, y, z_i) \Delta x \Delta y} \end{aligned}$$

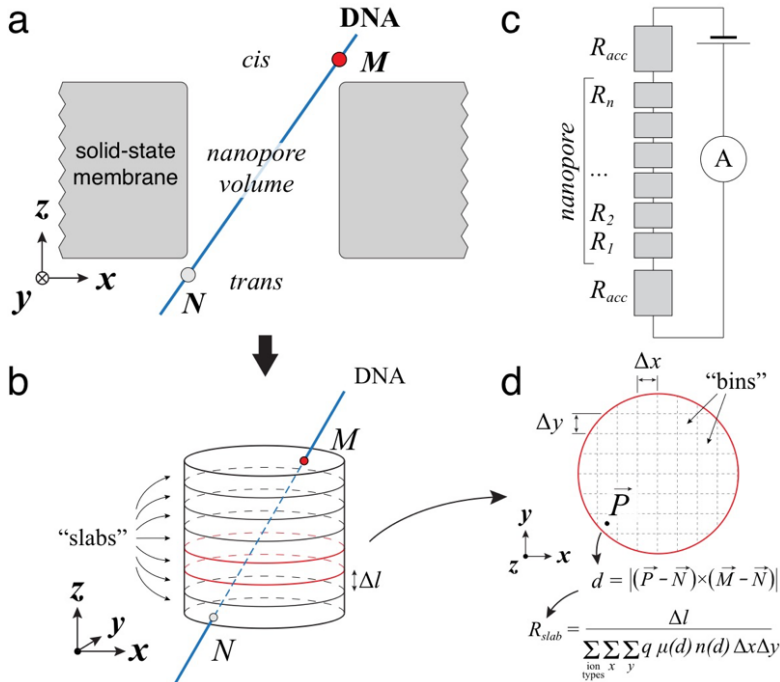


**Figure S9.13: Theoretical model of the nanopore resistance.** (A) Schematic representation of the overall model. The DNA molecule is shown as a blue line, solid-state membrane – as a gray surface. Points  $M$  and  $N$  define the orientation of DNA with respect to the nanopore. (B) Schematic representation of the nanopore volume containing a straight DNA molecule. The nanopore volume is split into horizontal slabs that are perpendicular to the nanopore axis ( $z$ ). Each slab has the same height  $\Delta l$  along the  $z$  axis. (C) An equivalent electrical diagram of the employed theoretical model. (D) Top view of a slab and its discretization into bins. Shortest distance from the center of a bin (point  $\vec{P}$ ) to DNA is computed as  $d = |(\vec{P} - \vec{N}) \times (\vec{M} - \vec{N})|$ . This distance is then used to determine mobility and number density of ions in that bin, which are then used to compute average conductivity of the slab. Resistance  $R_{slab}$  of a slab is calculated as an inverse average conductivity of a slab  $\sigma$  scaled by ratio of the slab's thickness  $\Delta l$  and its cross-sectional area  $S$ .

#### VERIFICATION OF THE THEORETICAL MODEL

We verified our theoretical model for two simple scenarios. First, we considered the case when no DNA was present in the nanopore, so that conductivity and mobility in each bin of every slab was equal to those of the bulk solution. The calculated resistance of the nanopore volume was found to closely follow the classical geometry-based expression  $R = \frac{\Delta l}{\sigma S}$ . Then, we considered the case of DNA is placed in the pore center along the nanopore axis and computed the changes in the conductance, resistance, and ionic current for various diameters of the pore, Fig. 9.14A-C. As it follows from the figure, DNA changes the conductance of a nanopore volume by the same amount if the nanopore radius exceeds 25 Å, see Fig. 9.14A, blue circles. At the same time, the effect of DNA on the conductance of access regions depends on the pore radius, which results in the overall non-trivial dependence of conductance blockade on the pore diameter. The

change in the resistance of a nanopore due to the presence of the molecule depends on the radius of the nanopore, Fig. 9.14B. For example, the molecule increases the resistance by 0.718 M $\Omega$  in a 10 nm pore, but only by 0.167 M $\Omega$  in the 15 nm pore. As it follows from Fig. 9.14A, the model predicts conductance blockades of 3.26 nS and 2.48 nS for 10 and 15 nm nanopores, correspondingly. These values are in excellent quantitative agreement with experimentally obtained values of 3.35 nS and 2.50 nS.

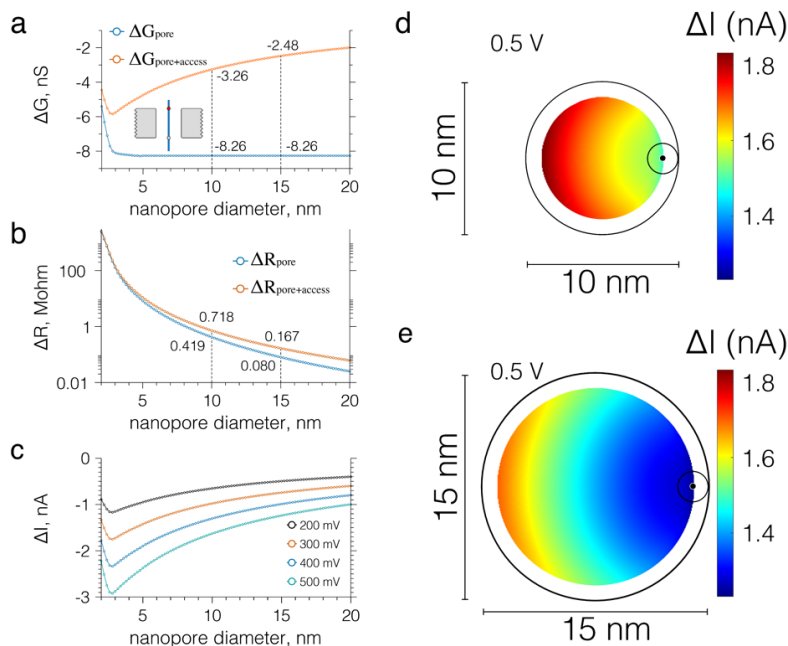


**Figure 9.14: Nanopore blockade currents according to the theoretical model.** Changes in nanopore conductance (A), resistance (B), and ionic current (C) as a function of the nanopore radius produced by a DNA molecule positioned in the middle of the nanopore and parallel to its axis. Panels (A) and (B) also show corresponding changes for conductance and resistance of the nanopore volume only (blue circles). Vertical dashed lines indicate the values obtained for the nanopores 10 and 15 nm in diameter. For pores larger than 5 nm in diameter, DNA decreases conductance of the nanopore volume by the same amount. At the same time, the increase of the nanopore resistance caused by the presence of DNA depends on the pore radius. (D-E) Example of the 2-D maps of ionic current blockades. Point *M* (defined in Fig. S9.13) is shown as a black dot with a circle around it; the circle indicates the cross-section of DNA. The highest current blockade is achieved when DNA spans across the pore, whereas the lowest one corresponds to DNA positioned near the nanopore surface and oriented parallel to its axis.

#### CALCULATION OF THE CONDUCTANCE BLOCKADE FOR OBLIQUELY ORIENTED DNA IN A NANOPORE

Using the described model for the nanopore resistance, we computed 2-D current blockade maps shown in Fig. 9.14D and E. For this purpose, we performed a series of calculations in which we varied the position of the point *N*, while keeping position of the point *M* fixed. Point *M* was positioned in such a way that DNA was touching the corner of the cylindrical nanopore. Such a position of point *M* corresponds to the case

when DNA is trapped by both pores in the double-nanopore system and is stretched between them. For each position of  $N$  we computed the nanopore resistance using the above expression and Li and Cl ion mobility and number density profiles reported in Fig. S8.3 and S8.6, respectively, of Ref. [48]. Bulk conductivity of the solution was calculated as  $\sigma_{bulk} = q_{Li}\mu_{Li,bulk}n_{Li,bulk} + q_{Cl}\mu_{Cl,bulk}n_{Cl,bulk} = 18.2$  S/m, and DNA diameter  $d_{DNA}$  was set to 2.2 nm. Following that we computed the open pore resistance,  $R_{open\ pore}$ . To directly compare the results of our calculations to experiment, all resistance values were scaled by the ratio of bulk electrolyte conductivities in simulations and experiment, i.e.:  $\frac{\sigma_{bulk}}{\sigma_{exp}}$ , where  $\sigma_{exp}$  is the experimental value of solution conductivity equal to 13.2 S/m. Using the obtained resistance values, we computed the resistance increase,  $\Delta R = R_{total} - R_{pore\ open}$ , and the conductance blockade,  $\Delta G = \frac{1}{R_{total}}$ . Corresponding current blockade  $\Delta I$  was then calculated as a product of the conductance blockade  $\Delta G$  and the applied bias voltage  $V$ .

Using the obtained maps, Fig. 9.14D and E, we compute the limits on the ionic current blockade reported in main text Fig. 9.5C. As expected, the highest current blockade corresponds to the scenario when DNA spans across the pore in an oblique orientation, while the lowest current blockades correspond to the scenario in which DNA is oriented parallel to the nanopore axis and located near the nanopore wall ('hugging the nanopore').

### 9.5.8. CRITERIA FOR DETERMINING ESCAPE DIRECTION IN A DOUBLE-NANOPORE EVENT

Using Fig. S9.12 we determined  $\Delta I_{10}$  or  $\Delta I_{16}$ , which are current blockades produced by single linear dsDNA molecule translocating through either 10 or 16 nm pores, respectively. The observed blockade levels at the end signature (the region of the current trace where DNA escapes the double-nanopore event and thus resides only in one of the nanopores) was without exception, close to but slightly larger than the blockade levels observed from single-pore translocations. We suggest that this is caused by the DNA still being partly in the tilted orientation (see SI Section 9.5.7) after exiting the first pore, thus producing a larger blockade (cf previous section). Hence, we used the following criteria to assign the escape direction. If the blockade level of the end signature was between  $\Delta I_{16}$  and  $\Delta I_{10}$ , the DNA final exit was ascribed to the 16 nm pore. For all end signature blockade levels larger than  $\Delta I_{10}$ , DNA exit was ascribed to the 10 nm pore. No blockades smaller than  $\Delta I_{16}$  were observed in the experiment.

### 9.5.9. ADDITIONAL SET OF EXPERIMENTS CHARACTERIZING THE ENTRANCE AND EXIT OF DNA FROM AN ASYMMETRIC DOUBLE-NANOPORE SYSTEM

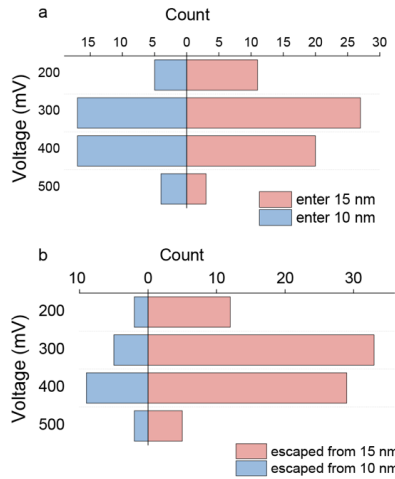


**Figure 9.15:** The number of double-nanopore events that (A) started with DNA entering the 15 nm pore (red) or the 10 nm pore (blue); (B) ended with DNA escaping the 15 nm pore (red) or the 10 nm pore (blue). This set of experiment was performed using a system of two pores, 10 and 15 nm in diameter, separated by 300 nm. The data are in agreement with the behaviour observed for the 10 nm/16 nm asymmetric double-nanopore system characterized in Fig. 9.5 of the main text.

### 9.5.10. EQUIVALENT CIRCUIT FOR THE ASYMMETRIC DOUBLE-NANOPORE SYSTEM

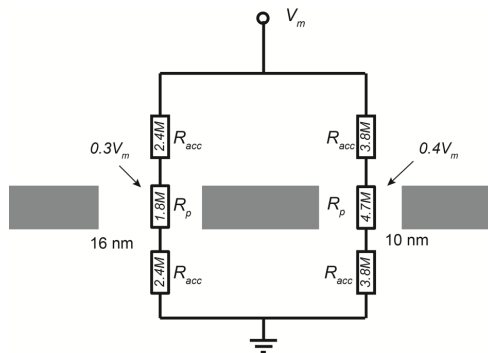


**Figure 9.16:** Equivalent circuit of the asymmetric double-nanopore system. The resistances were calculated based on the model described in Section 9.5.6.

### 9.5.11. CALCULATION OF THE FORCES ACTING ON THE DNA IN THE ACCESS REGION

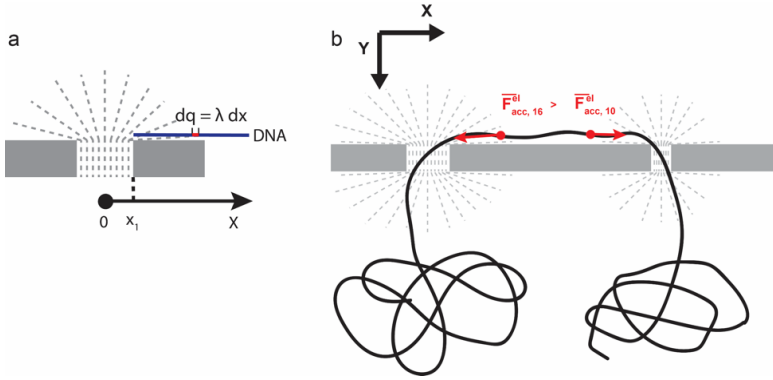


**Figure 9.17:** (A) Sketch of the model used for the calculation of the electric forces exerted on DNA by the transmembrane bias in the access region. The DNA molecule is shown as a blue line; the electric field lines as grey dashed lines. (B) Sketch of the forces exerted by access regions on DNA

The force of the transmembrane bias exerted on DNA in the access resistance region was estimated using the electrostatic model (Fig. 9.17A) built on the following assumptions:

1. The electric field near a nanopore can be approximated by the potential of a point-like charge [33]:

$$V(r) = \frac{d^2}{8lr} V_m$$

$$E(r) = -\frac{dV}{dr} = \frac{d^2}{8lr^2} V_m$$

where  $d$  is the pore diameter,  $l$  is the effective pore length,  $r$  is the distance from the pore and  $V_m$  is the transmembrane voltage

2. DNA is treated as a charged rod with the surface charge density [39]  $\sigma = 10.5 \text{ mC/m}^2$ , allowing for an increased effective screening [15]. This corresponds to a linear charge density of  $\lambda = 2\pi r_{\text{DNA}}\sigma$  of  $0.073 \cdot 10^{-9} \text{ C/m}$ .
3. DNA is stretched along the  $x$  axis (see Fig. 9.17B). The charge of a DNA fragment of length  $dx$  thus equals to  $dq = \lambda dx$ .

The force acting on each infinitesimal partition of DNA can thus be evaluated as:

$$dF = dq \times E = \frac{d^2}{8lx^2} \lambda dx$$

$$F = \int_{x_1}^{x_D} dF = \frac{d^2 \lambda}{8l} \left( \frac{1}{x_1} - \frac{1}{x_D} \right)$$

where  $x_D$  is the distance between two pores, and  $x_1$  is the coordinate of the nanopore wall. This leads to the result displayed in Fig. S10.5, which shows the forces exerted on DNA as a function of nanopore distance (Fig. S10.5A) and voltage (Fig. S10.5B) by each of the pores and the difference of the two forces. The essential point is that the force pulling the DNA toward the 16 nm pore is much larger (by 3–8 pN) than the force pulling the DNA toward the 10 nm pore. The difference of the two forces explains the preference for the DNA to exit through the 16 nm-diameter pore.

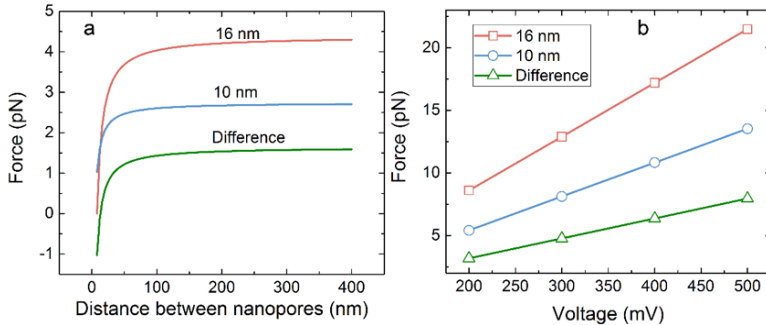


**Figure 9.18:** Force exerted on DNA by the electric field in the access region (A) plotted as a function of distance between nanopores (at  $V_m = 100$  mV) and (B) as a function of transmembrane voltage (at 400 nm distance between the nanopores).

## REFERENCES

- [1] J. Record, M. T., S. J. Mazur, P. Melancon, J. H. Roe, S. L. Shaner, and L. Unger, *Double helical dna: conformations, physical properties, and interactions with ligands*. *Annu. Rev. Biochem.* **50**, 997 (1981).
- [2] G. E. Joyce, *The antiquity of rna-based evolution*. *Nature* (London, U. K.) **418**, 214 (2002).
- [3] J. R. Moffitt, Y. R. Chemla, S. B. Smith, and C. Bustamante, *Recent advances in optical tweezers*. *Annu. Rev. Biochem.* **77**, 205 (2008).
- [4] M. D. Wang, H. Yin, R. Landick, J. Gelles, and S. M. Block, *Stretching dna with optical tweezers*, *Biophysical journal* **72**, 1335 (1997).
- [5] I. De Vlaminck and C. Dekker, *Recent advances in magnetic tweezers*. *Annu. Rev. Biophys.* **41**, 453 (2012).
- [6] K. C. Neuman and A. Nagy, *Single-molecule force spectroscopy: optical tweezers, magnetic tweezers and atomic force microscopy*. *Nat. Methods* **5**, 491 (2008).
- [7] S. Goodwin, J. D. McPherson, and W. R. McCombie, *Coming of age: ten years of next-generation sequencing technologies*. *Nat. Rev. Genet.* **17**, 333 (2016).
- [8] D. Branton, D. W. Deamer, A. Marziali, H. Bayley, S. A. Benner, T. Butler, M. Di Ventra, S. Garaj, A. Hibbs, X. Huang, S. B. Jovanovich, P. S. Krstic, S. Lindsay,

- X. S. Ling, C. H. Mastrangelo, A. Meller, J. S. Oliver, Y. V. Pershin, J. M. Ramsey, R. Riehn, G. V. Soni, V. Tabard-Cossa, M. Wanunu, M. Wiggin, and J. A. Schloss, *The potential and challenges of nanopore sequencing*. *Nat. Biotechnol.* **26**, 1146 (2008).
- [9] J. J. Kasianowicz, E. Brandin, D. Branton, and D. Deamer, *Characterization of individual polynucleotide molecules using a membrane channel*. *Proc. Natl. Acad. Sci. U. S. A.* **93**, 13770 (1996).
- [10] M. Jain, I. T. Fiddes, K. H. Miga, H. E. Olsen, B. Paten, and M. Akeson, *Improved data analysis for the minion nanopore sequencer*. *Nat. Methods* **12**, 351 (2015).
- [11] J. Li, D. Stein, C. McMullan, D. Branton, M. J. Aziz, and J. A. Golovchenko, *Ion-beam sculpting at nanometer length scales*. *Nature (London, U. K.)* **412**, 166 (2001).
- [12] C. Dekker, *Solid-state nanopores*. *Nat. Nanotechnol.* **2**, 209 (2007).
- [13] M. Wanunu, *Nanopores: A journey towards dna sequencing*, *Physics of life reviews* **9**, 125 (2012).
- [14] M. Wanunu, W. Morrison, Y. Rabin, A. Y. Grosberg, and A. Meller, *Electrostatic focusing of unlabelled dna into nanoscale pores using a salt gradient*. *Nat. Nanotechnol.* **5**, 160 (2010).
- [15] S. W. Kowalczyk, D. B. Wells, A. Aksimentiev, and C. Dekker, *Slowing down dna translocation through a nanopore in lithium chloride*. *Nano Lett.* **12**, 1038 (2012).
- [16] D. Fologea, J. Uplinger, B. Thomas, D. S. McNabb, and J. Li, *Slowing dna translocation in a solid-state nanopore*. *Nano Lett.* **5**, 1734 (2005).
- [17] M. Waugh, A. Carlsen, D. Sean, G. W. Slater, K. Briggs, H. Kwok, and V. Tabard-Cossa, *Interfacing solid-state nanopores with gel media to slow dna translocations*. *Electrophoresis* **36**, 1759 (2015).
- [18] U. Mirsaidov, J. Comer, V. Dimitrov, A. Aksimentiev, and G. Timp, *Slowing the translocation of double-stranded dna using a nanopore smaller than the double helix*. *Nanotechnology* **21**, 395501/1 (2010).
- [19] M. Wanunu, J. Sutin, B. McNally, A. Chow, and A. Meller, *Dna translocation governed by interactions with solid-state nanopores*. *Biophys. J.* **95**, 4716 (2008).
- [20] N. Di Fiori, A. Squires, D. Bar, T. Gilboa, T. D. Moustakas, and A. Meller, *Optoelectronic control of surface charge and translocation dynamics in solid-state nanopores*. *Nat. Nanotechnol.* **8**, 946 (2013).
- [21] F. Nicoli, D. Verschueren, M. Klein, C. Dekker, and M. P. Jonsson, *Dna translocations through solid-state plasmonic nanopores*. *Nano Lett.* **14**, 6917 (2014).
- [22] M. Belkin, S.-H. Chao, M. P. Jonsson, C. Dekker, and A. Aksimentiev, *Plasmonic nanopores for trapping, controlling displacement, and sequencing of dna*. *ACS Nano* **9**, 10598 (2015).
- [23] V. Tabard-Cossa, M. Wiggin, D. Trivedi, N. N. Jetha, J. R. Dwyer, and A. Marziali, *Single-molecule bonds characterized by solid-state nanopore force spectroscopy*. *ACS*

- Nano **3**, 3009 (2009).
- [24] Q. Zhao, G. Sigalov, V. Dimitrov, B. Dorvel, U. Mirsaidov, S. Sligar, A. Aksimentiev, and G. Timp, *Detecting snps using a synthetic nanopore*. Nano Lett. **7**, 1680 (2007).
- [25] U. F. Keyser, B. N. Koeleman, S. Van Dorp, D. Krapf, R. M. M. Smeets, S. G. Lemay, N. H. Dekker, and C. Dekker, *Direct force measurements on dna in a solid-state nanopore*. Nat. Phys. **2**, 473 (2006).
- [26] H. Peng and X. S. Ling, *Reverse dna translocation through a solid-state nanopore by magnetic tweezers*. Nanotechnology **20**, 185101/1 (2009).
- [27] A. Spiering, S. Getfert, A. Sischka, P. Reimann, and D. Anselmetti, *Nanopore translocation dynamics of a single dna-bound protein*. Nano Lett. **11**, 2978 (2011).
- [28] C. Hyun, H. Kaur, R. Rollings, M. Xiao, and J. Li, *Threading immobilized dna molecules through a solid-state nanopore at >100  $\mu$  s per base rate*. ACS Nano **7**, 5892 (2013).
- [29] A. Sischka, C. Kleimann, W. Hachmann, M. M. Schaefer, I. Seuffert, K. Tonsing, and D. Anselmetti, *Single beam optical tweezers setup with backscattered light detection for three-dimensional measurements on dna and nanopores*. Rev. Sci. Instrum. **79**, 063702/1 (2008).
- [30] A. J. Storm, J. H. Chen, H. W. Zandbergen, and C. Dekker, *Translocation of double-strand dna through a silicon oxide nanopore*. Phys. Rev. E: Stat., Nonlinear, Soft Matter Phys. **71**, 051903/1 (2005).
- [31] S. Gurrieri, S. B. Smith, and C. Bustamante, *Trapping of megabase-sized dna molecules during agarose gel electrophoresis*. Proc. Natl. Acad. Sci. U. S. A. **96**, 453 (1999).
- [32] C. Plesa, N. van Loo, P. Ketterer, H. Dietz, and C. Dekker, *Velocity of dna during translocation through a solid-state nanopore*. Nano Lett. **15**, 732 (2015).
- [33] A. Y. Grosberg and Y. Rabin, *Dna capture into a nanopore: Interplay of diffusion and electrohydrodynamics*. J. Chem. Phys. **133**, 165102/1 (2010).
- [34] B. Lu, D. P. Hoogerheide, Q. Zhao, and D. Yu, *Effective driving force applied on dna inside a solid-state nanopore*. Phys. Rev. E: Stat., Nonlinear, Soft Matter Phys. **86**, 011921/1 (2012).
- [35] S. Van Dorp, U. F. Keyser, N. H. Dekker, C. Dekker, and S. G. Lemay, *Origin of the electrophoretic force on dna in solid-state nanopores*, Nature Physics **5**, 347 (2009).
- [36] B. Luan and A. Aksimentiev, *Control and reversal of the electrophoretic force on dna in a charged nanopore*. J. Phys.: Condens. Matter **22**, 454123/1 (2010).
- [37] S. Ghosal, *Effect of salt concentration on the electrophoretic speed of a polyelectrolyte through a nanopore*. Phys. Rev. Lett. **98**, 238104/1 (2007).
- [38] Y. He, M. Tsutsui, C. Fan, M. Taniguchi, and T. Kawai, *Controlling dna translocation through gate modulation of nanopore wall surface charges*. ACS Nano **5**, 5509 (2011).

- [39] L. Chen and A. T. Conlisk, *Forces affecting double-stranded dna translocation through synthetic nanopores*. Biomed. Microdevices **13**, 403 (2011).
- [40] M. Muthukumar, *Polymer escape through a nanopore*. J. Chem. Phys. **118**, 5174 (2003).
- [41] S. Ghosal, *Electrophoresis of a polyelectrolyte through a nanopore*. Phys. Rev. E: Stat., Nonlinear, Soft Matter Phys. **74**, 041901/1 (2006).
- [42] A. T. Carlsen, O. K. Zahid, J. Ruzicka, E. W. Taylor, and A. R. Hall, *Interpreting the conductance blockades of dna translocations through solid-state nanopores*. ACS Nano **8**, 4754 (2014).
- [43] S. J. Heerema and C. Dekker, *Graphene nanodevices for dna sequencing*. Nat. Nanotechnol. **11**, 127 (2016).
- [44] C. Plesa and C. Dekker, *Data analysis methods for solid-state nanopores*. Nanotechnology **26**, 84003 (2015).
- [45] C. Maffeo, T. T. M. Ngo, T. Ha, and A. Aksimentiev, *A coarse-grained model of unstructured single-stranded dna derived from atomistic simulation and single-molecule experiment*. J. Chem. Theory Comput. **10**, 2891 (2014).
- [46] A. E. Nkodo, J. M. Garnier, B. Tinland, H. Ren, C. Desruisseaux, L. C. McCormick, G. Drouin, and G. W. Slater, *Diffusion coefficient of dna molecules during free solution electrophoresis*. Electrophoresis **22**, 2424 (2001).
- [47] D. B. Wells, V. Abramkina, and A. Aksimentiev, *Exploring transmembrane transport through  $\alpha$ -hemolysin with grid-steered molecular dynamics*. J. Chem. Phys. **127**, 125101/1 (2007).
- [48] M. Belkin and A. Aksimentiev, *Molecular dynamics simulation of dna capture and transport in heated nanopores*. ACS Appl. Mater. Interfaces **8**, 12599 (2016).
- [49] J. C. Phillips, R. Braun, W. Wang, J. Gumbart, E. Tajkhorshid, E. Villa, C. Chipot, R. D. Skeel, L. Kale, and K. Schulten, *Scalable molecular dynamics with namd*, Journal of computational chemistry **26**, 1781 (2005).
- [50] M. Wanunu, T. Dadosh, V. Ray, J. Jin, L. McReynolds, and M. Drndić, *Rapid electronic detection of probe-specific micrnas using thin nanopore sensors*, Nature nanotechnology **5**, 807 (2010).
- [51] S. W. Kowalczyk, A. Y. Grosberg, Y. Rabin, and C. Dekker, *Modeling the conductance and dna blockade of solid-state nanopores*, Nanotechnology **22**, 315101 (2011).
- [52] J. E. Hall, *Access resistance of a small circular pore*. The Journal of general physiology **66**, 531 (1975)

# 10

## TOWARDS FLOW-DRIVEN ROTATION OF A DNA ORIGAMI NANOMOTOR

*Much like the intricate and elusive motor proteins in cell biology, synthetic man-made motors at the nanoscale might enable to influence biological and chemical process at the single-molecule level. Essential to such motor function is the demonstration of directed rotary motion by the consumption of a local source of free energy. This chapter presents a progress report on the demonstration of directed rotation of such a nanomotor. Using the electroosmotic flow from a solid-state nanopore, we aim to drive a nanomotor that is made out of DNA origami. After docking the motor into a nanopore, the motor can in principle be driven using the flow generated in the nanopore by applying a bias voltage over the nanopore. Using dark-field imaging, rotation can be observed by tracking a gold nanorod attached to the end of a crank lever that is connected axle. We demonstrate the successful assembly of the DNA nanomotor consisting of two bearing halves and an axle that is extended with a propeller blade made of DNA and a 215 nm long crank lever. We furthermore show the fabrication of nanopore arrays and labeling of the end of the crank lever with a gold nanorod coated with DNA oligos. We characterize our dark-field imaging system and show that we can observe moving gold nanoparticles up to a 1 kHz frame rate. Finally, we discuss the further challenges and potential pitfalls in this project that need to be addressed to carry this exciting, but currently unfinished project to fruition.*

---

This chapter has not yet been published. Contributions to the work were made by Daniel V. Verschuereen, Philip Ketterer, Mart G. F. Last, Hendrik Dietz, and Cees Dekker.

## 10.1. INTRODUCTION

Biological rotary motors are nanomotors that can interconvert free energy and directed rotational motion to drive the cell's essential processes [1]. These motors either consume chemical energy to perform active transport, such as the bacterial flagella motor [2], or catalyze the synthesis of chemical constituents, such as the  $F_1F_0$ -ATP synthase that produces ATP in cells [3]. The intricate structure of these molecular machines tied with their high efficiencies of operation in noisy environments remains elusive, which has ensured that these biological motors are a major subject of fascination and study [4]. The sheer excitement about nanomotors [5] has propelled extensive efforts to mimic and recreate rotary machines at the nanoscale [6]. Creating nanoscale motors by rational design might enable us for example to interfere directly with chemical and cellular processes [7]. But whereas complex biological nanomotors arose in evolution over millions of years, the quest for man-made artificial mimics has started only recently. The most common route to create synthetic molecular machines has been through fundamental organic chemistry [8, 9]. However, challenges remain in the applicability of these devices in biological conditions and the very limited size and complexity of these assemblies make it difficult to approach the impressive functionality of their biological counterparts [4]. Scaffolded DNA origami nanotechnology is a new promising alternative that could make molecular motors on the size scale and playing field of naturally occurring ones. By using a single-stranded DNA scaffold, base-pairing, and base-stacking interactions [10] the scaffold can be folded into complex rationally designed three-dimensional nanostructures that can well be  $\sim 100$  nm in size [11]. The simple programmability and flexibility of the DNA backbone allows functional and spinning nanostructures to be designed. Previous works have demonstrated movable nanostructures fueled by DNA strand displacement [12, 13], molecular docking and diffusive rotation [14], and computer-controlled switching of a robotic arm [15]. However, pure motor action, where solely a local source of free energy drives a perpetuate cyclic motion, has not been demonstrated to date for these DNA assemblies, or any other biomimetic rotary motor.

Here we present a progress report on an effort to demonstrate directional rotary motion of a DNA origami nanomotor driven by a local viscous flow in a solid-state nanopore. First, the working principle of our DNA origami nanomotor, the design of the motor, and the motor-nanopore docking strategy are discussed. Subsequently, we report the realization of fully assembled DNA structures, successful fabrication of nanopore arrays, successful labeling of a gold nanorod to the motor's crank lever, and we describe and characterize the dark-field observation setup. Finally, we will discuss further challenges and potential pitfalls that need to be addressed to carry this exciting project to fruition. This chapter will present the status of this currently unfinished work.

## 10.2. RESULTS

### 10.2.1. ELECTROSMOTIC-FLOW (EOF) DRIVEN ROTATION OF A DNA ORIGAMI NANOMOTOR

All directed motion fundamentally requires the consumption of free energy and synthetic nanomotors are no exception. We propose to use water flow as a source

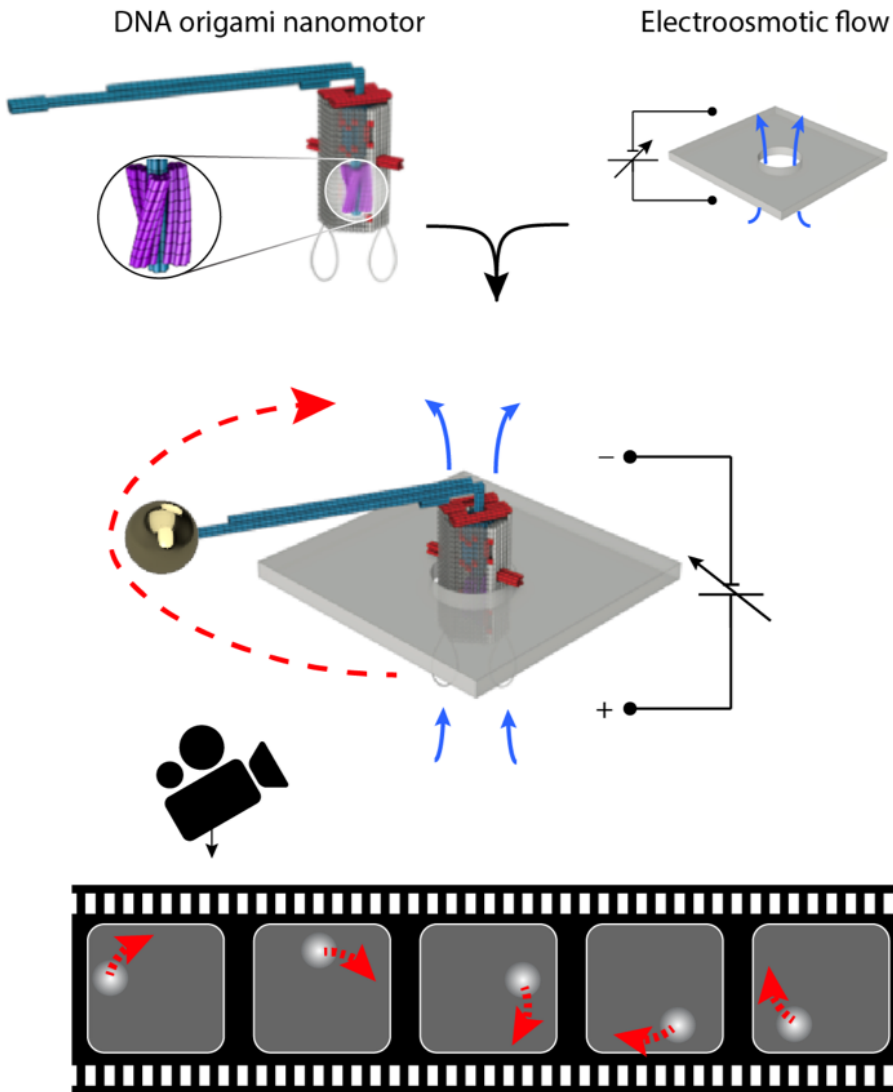


**Figure 10.1: Schematic of experimental observation of an electroosmotic flow driven rotation of a DNA origami nanoturbine.** A DNA origami nanomotor, with a propeller blades consisting of twisted DNA helices, is docked into a nanopore. The electroosmotic flow (blue arrows) set up through the nanopore by an electric field drives the directed rotation of the arm that can be observed by tracking the position of a gold nanoparticle using dark-field microscopy.

of power for our nanoscale motor, using a DNA-based propeller blade that drives the motor's axle. The motor consists of an axle extended by a blade designed with tilted DNA bundles, as shown in the top left in Fig. 10.1 and a capped bearing to retain the axle inside. The blade on the axle redirects the water flow, creating a torque on the blade that causes the axle and crank lever to spin, analogous to a propeller in a turbine. Water flows at the nanoscale are highly viscous in nature and, as a result, couple extremely well to nanoobjects [16].

Strong flows can locally be generated in a solid-state nanopore, a small constriction at a thin membrane interface between two chambers. A pressure difference between the two chambers, for example, will force liquid through the nanopore, creating a viscous flow. Viscous flows can also be set up by other means, such as a difference in composition of the solutions (osmosis) or by electrically biasing the chambers (electro-osmosis), see top right Fig. 10.1. The latter can easily and rapidly be controlled by tuning the bias voltage and would be ideal for driving the nanomotor at a desired speed, but it requires the presence of an electrolyte and a charged surface, e.g. the nanopore wall, for a flow to develop. Screening of the surface charge in the solution creates an excess layer of mobile counterions that move under the influence of an electric field. The motion of these ions couples viscously to the solution, leading to a flow of liquid [17].

Electroosmotic flow (EOF) speeds can be very large inside a nanopore. The flow velocity at the center of the pore ( $r = 0$ ) is, to first order (see SI Section 10.4.1), dependent on the bias voltage  $\Delta V$ , the thickness of the membrane  $l$ , the surface charge density of the nanopore wall  $\sigma$ , and the viscosity  $\eta$  as:

$$u_{\text{EOF}}(r) = -\frac{r_D \sigma \Delta V}{\eta l}. \quad (10.1)$$

Here  $r_D$  is the Debye length that depends on the concentration of ions in the bulk solution  $n_0$ ,  $r_D = \sqrt{\frac{\epsilon k_B T}{2n_0 e^2}}$ , where  $\epsilon$  the electrical permittivity of the solution. A typical membrane material such as silicon nitride will have a negatively charged surface and flow speeds of several mm per second are not uncommon in typical conditions (see SI Section 10.4.1). Hence large forces [18] and torques can be generated on the axle. Although the large flow speeds will likely break the no-slip condition on the blades, which would reduce the effective torque on the axle, the force from the flow will still bias the motor to rotate directionally.

It should be noted that the flow of ions itself does not exert significant forces on the origami object. DNA origami has been shown to be remarkably permeable to ions [19, 20]. Fortunately, the presence of DNA strands in the nanopore does not block the EOF, but even generates it [18]. Furthermore, molecular dynamic simulations have shown that EOF still develops when a DNA origami plate is docked onto a nanopore and that it exerts a force on the object [20]. Although the complex DNA motor will affect the flow pattern, it should not inhibit the formation of a flow. This could be different for pressure-driven flows, as the bearing cap might serve as a barrier for these flows.

The DNA origami motor must be correctly placed inside the nanopore. Positioning the DNA origami machine can be done by electrically biasing the nanopore. DNA is negatively charged, and, assisted by a long guiding leash, will be pulled into the

nanopore if the *trans*-chamber is positively biased (see Fig. 10.1). To prevent the object from translocating, protruding flaps are embedded in the bearing (red flaps in Fig. 10.1), which will cause the motor to dock onto the nanopore when pulled into the pore [19]. The retention of a bias voltage during the experiment is essential to keep the DNA motor in place and will prevent ejection of the motor out of the nanopore.

Finally, we aim to observe directed rotation of the axle by tracking the motion of the crank lever arm. The tracking should be able to resolve the position of the arm and the time-lapse imaging should be significantly faster than the rotation of the arm, since directed motion can only be confirmed if the full motion of the crank lever can be traced. Dark-field microscopy using light scattered from gold nanoparticles attached to an axle has been used in the past to observe fast movements of biological motors at sub-millisecond timescales [21, 22]. Here, we plan to implement a similar detection scheme, where we use laser dark-field microscopy [23] to track a gold nanoparticle conjugated to the cranklevers arm (see bottom Fig. 10.1).

### 10.2.2. THE DNA ORIGAMI NANOMOTOR

The core of the DNA nanomotor is based on a design of a DNA Brownian rotor published before [14]. The nanomotor design used here consists of an axle extended with a propeller (Fig. 10.2A) and two bearing clamps (Fig. 10.2B). The axle has a length of 85 nm including the propeller (purple) and has a 22 nm in diameter hexagonal central core consisting of 54 parallel DNA helices. The core is essential to ensure proper assembly of the bearing halves and the axle: base stacking interactions of the red extrusions at the axle's central core click into the bearing during assembly. The zoom in Fig. 10.2A shows the propeller which made out of three sets of 6 DNA helix bundles twisted around the axle. Finally, the axle is extended with a perpendicularly mounted 215 nm long crank lever that serves both to prevent the axle from escaping the bearing and to create an arm that traces the rotation of the axle.

The bearing, shown in Fig. 10.2B, is hexagonal and has an outer diameter of 42 nm and an inner diameter of 27 nm [14]. The long bearing extends all the way into the nanopore. This prevents the propeller from interacting with the pore's surface and creates a beneficial highly-charged DNA wall from which additional EOF can develop. Each bearing half contains one pocket for base stacking interactions (red) with the axle and two pockets in the side of the bearing for ensuring connection with the complementary bearing clamp, as indicated by the arrows in Fig. 10.2B. The clamps furthermore contain a hatch that can be sealed in the final assembly step by addition of a DNA staple strand to lock the bearing around the axle. To dock the complex onto the nanopore 10 nm long protrusion of 6 helix bundles are added to the bearing (red, pointing outwards from the bearing). Finally, the bearing contains a 400 bp leash that assists guiding the docking of the motor and that ensures it assumes the correct orientation upon docking [19].

The motor is one of the biggest mobile DNA origami designs fabricated to date [24]. With its molecular weight of approximately 30M Dalton, its much larger than the biological  $F_1F_0$ -ATP synthase motor, with a molecular weight of 550k Dalton. The design of such a large unit requires the use of 6 single-stranded DNA scaffolds in three separate folding reactions, i.e. the two bearing clamps and the axle unit. A newly developed

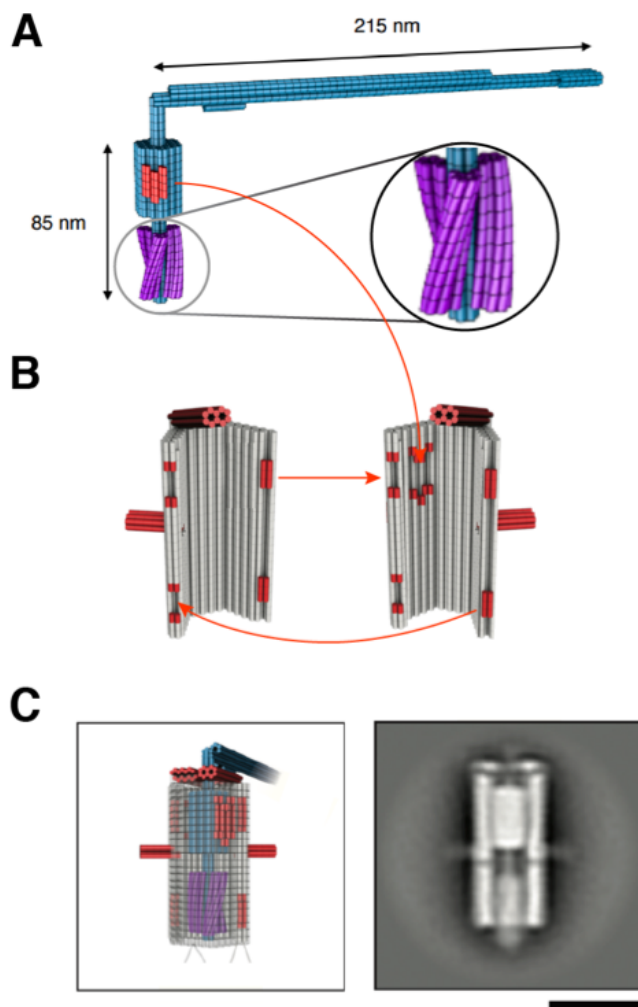


**Figure 10.2: DNA origami nanomotor design.** (A) Schematic rendering of the design of the DNA origami axle. The axle consists of a core unit used for docking into the bearing clamp (indicated by the red arrow), a 215 nm long crank lever, and a propeller. The zoom shows the propeller, which consists of three sets of 6 twisted DNA helix bundles, more clearly. (B) Schematic rendering of the two bearing clamps. The clamps and the axle assemble as a trimer through DNA base stacking interactions at the locations indicated by the red marks and red arrows. (C) Schematic rendering of the complete nanoturbine. TEM class average of negative-stained fully assembled trimer. The propeller blades and core unit of the axle are clearly visible. Scale bar is 50 nm.

single-stranded DNA scaffold by the Dietz lab at Munich allows the use two scaffolds in one reaction [24]. Essentially, the two scaffolds are orthogonal, meaning that no sequence of 7 consecutive bases occurs twice within the scaffolds.

Successful assembly of the DNA origami motor was realized, as displayed in Fig. 10.2C which shows a transmission electron microscope class-average image of a side view of the assembled motor. The bearing, the rotors central core, and the propeller are clearly visible. The image also shows the protruding flaps designed for docking and demonstrates that the hatch retaining the axle has been closed successfully. The full assembly protocol for creating the complete motor from the 3 separate units can be found in SI Section 10.4.3.

### 10.2.3. NANOPORE ARRAYS

To increase throughput, we developed a strategy to make nanopore arrays using electron-beam lithography and reactive-ion etching, as described in earlier work [25]. An array of  $42 \pm 3$  nm diameter nanopores, tuned to fit the nanomotors, is shown in SI Section 10.4.4. The use of arrays allows us to image multiple motors in one field of view. Upon using a  $40 \times 40 \mu\text{m}$  large freestanding membrane and a spacing of  $1.5 \mu\text{m}$  between the nanopores to prevent overlapping point-spread functions in our imaging system, approximately 700 nanopores can be fit onto one membrane.

### 10.2.4. GOLD NANOPARTICLE LABELING OF THE CRANK LEVER

To observe rotation, the end of the arm of the crank lever must be labeled preferable at its end. Our strategy to trace the motor using dark-field scattering requires us to label the end of the arm with a strongly scattering nanoparticle. We decided to use a gold nanorod (AuNR) of 12 nm in diameter by 39 nm in length (Nanopartz, Inc) for this purpose (see Fig. 10.3A), a small rod with defined dimensions that scatters visible light, in particular light of 637 nm in wavelength, extremely well [26]. The rods are anisotropic and the scattering properties of the rods will hence depend strongly on the orientation of the rod with respect to the polarization of the light used to image the rod. Using circularly polarized light and ensuring that the attachment of the rod is parallel to the arm will provide conditions for uniform excitation of the rod throughout its rotation.

To attach the AuNR to the end of the crank lever's arm, we again use DNA basepairing. The end of the arm contains 6 single-stranded DNA molecules that are complementary to strands that are coated on the nanoparticle using thiolated DNA oligos. This couples the nanoparticle to the arm at the correct location and orientation. The coating of the AuNR also prevents the nanorods from aggregating, as the highly charged DNA oligos cause the rods to repel each other, thus minimizing their mutual interactions in solution.

DNA coating of AuNRs is however not straightforward, since the bases of single-stranded DNA can interact with the gold surface. Moreover, the high charge density of a DNA oligo inhibits a high loading density of oligos on the rod's surface. Incomplete or insufficient coating will cause the AuNRs to aggregate in the presence of magnesium ions, which are required for DNA origami motor assembly and stability. To increase the loading density and stability of the AuNRs in solutions containing magnesium, we use a modified salt-aging protocol for nanorod coating [27–29]. This involves coating the DNA nanorods with mix of the target DNA sequence strands and

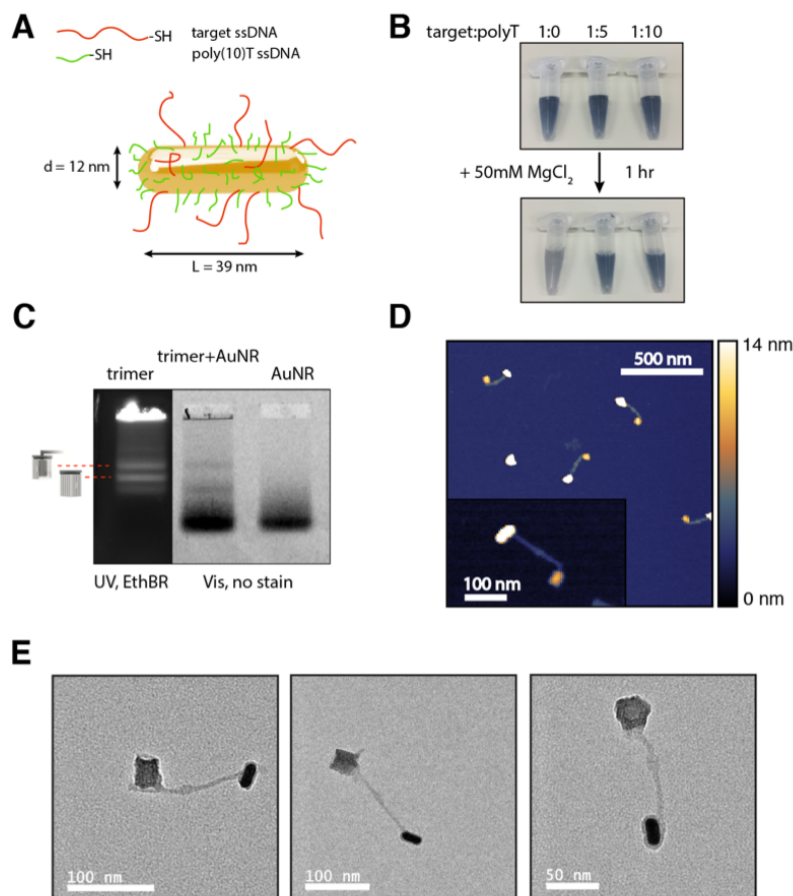


**Figure 10.3: Labeling DNA origami motor with a gold nanorod (AuNR).** (A) Coating strategy for gold nanorod (AuNR) of 12x39 nm. A mix of thiolated DNA complementary (target) to DNA binding sites on the crank lever and thiolated poly(10)T (polyT) functionalizes the gold surface. (B) Photos of 1nM AuNR solutions functionalized with DNA oligos at different target:polyT ratios: 1:0, 1:5, 1:10. The incubation of each solution with 50mM  $\text{MgCl}_2$  for 1 hours gives aggregation for the target only coating (1:0), but leaves the other samples unaffected. (C) UV (EthBR stained) and visible image of an electrophoresis gel. From left to right: complete diffusion rotor (stained), rotor + coated AuNR, coated AuNR only (no stain). A thick and two faint bands are visible in the middle lane. The thick band (bottom) contains free coated AuNR and the top faint band roughly colocalizes with the full rotor band in the EthBr stained lane (left), indicating the top band contains labeled trimers. (D) AFM image of a band cut-out of labeled rotor trimers labeled with AuNRs. The inset shows a zoom of a single labeled trimer. (E) Negative-stain (Uranyl acetate) TEM images of AuNR labeled diffusion motor. The left two images are a side view of the motor, the right most image is a top view of the motor. The hexagonal bearing halves are clearly visible in the latter.

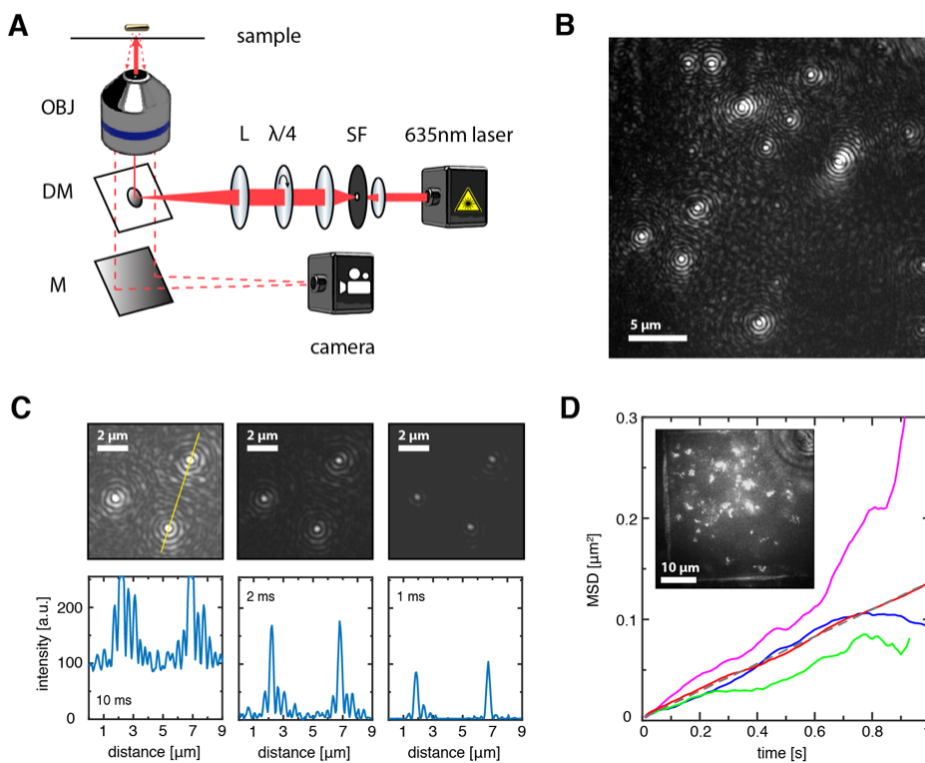
poly(10)T (thymine) strands whilst steadily increasing the ionic strength of the solution and the full protocol can be found in SI Section 10.4.2. Thymine bases are known to interact least strongly with the gold surface and have been previously used to coat AuNRs [30].

Figure 10.3B shows the AuNR rods coated with different ratios of poly(10)T strands and target strands before and after incubation with  $\text{MgCl}_2$ . Before the addition of  $\text{MgCl}_2$ , all particles are freely suspended, giving the solution a dark blue color. After the addition of 50mM  $\text{MgCl}_2$  and incubation for 1 hour, the particles that are solely coated with the target strands have aggregated, as indicated by the loss of color in the solution. When coated with a mix of polyT and target oligos, the particles are still freely suspended. This indicates that the coating with solely target oligos does not yield a complete coating of the AuNR surface and that the use of additional polyT sequence oligos is essential. It also reveals that there is a significant sequence dependence on the DNA loading efficiency.

Using the 1:5 target:polyT oligo coating, we tested the attachment of the AuNR to the arm of the diffusion rotor (Brownian rotor), using a 1:5 rotor:AuNR excess. Figure 10.3C shows the results of an electrophoretic mobility gel used to separate nanorotors labeled with AuNRs from free AuNRs. The left lane shows the DNA nanomotor, stained with ethidium-bromide in UV illumination. Two clear bands can be discerned, which contain fully assembled rotors (trimers) and empty bearing halves (dimers). The right two lanes contain labeled nanorotors and free AuNRs and are imaged in visible light. A strong thick band in both of these lanes indicates the free coated AuNR. Two more faint dark bands can be seen in the middle lane. One band lines up with a band in the UV image, indicating that this band contains successfully labeled trimers, while the other band most likely contains labeled axles that are not fit in their bearing clamps. We note that the labeling does not produce a large shift in the electrophoretic mobility assay because the AuNR's size is small compared to the rotor's extent. Thus we cannot separate labeled from unlabeled rotors using this method.

Analysis of the band intensities reveals that only 1.3% of the total number of particles attaches to the nanomotor, which, because of the 1:5 rotor:AuNR excess, means that only 6.5% of the rotors have particles attached to them. The large number of unlabeled DNA origamis is also observed for DNA origami plates (see SI Section 10.4.5). One of the reasons for the low yield might be that the bases of the DNA target oligos still interact with the gold surface, blocking the base pairing of the oligo to the motor's arm and thus reducing the labelling yield.

Figure 10.3D shows an AFM image of the band cut-out from the electrophoretic mobility gel. Rotor trimers can be clearly seen with particles attached to their arms, confirming attachment of the particles to the arms. The inset shows a zoom of a rotor. In this case, the number of labeled trimers compared to non-labeled trimers is roughly 20%, which is similar to the low labeling efficiency of 6.5% determined from the gel. Figure 10.3E shows three TEM images of diffusion rotors labeled with AuNRs after gel purification. The three images show two side views and one top view of a labeled rotor, illustrating more clearly that these trimers are labeled with a single gold nanorod.



**Figure 10.4: Dark-field imaging setup.** (A) schematic of optical layout. A 637 nm laser beam is collimated and filtered using a spatial filter (SF), passed through a quarter-wave plate ( $\lambda/4$ ), and focused on the back-focal plane of a 60x 1.2 NA water immersion objective (OBJ) using a lens (L), via a dot mirror (DM). The dot mirror filters the reflected and scattered light, creating a dark-field type contrast, which is focused onto camera via a mirror (M). (B) Typical image at 10 ms exposure time and a laser power of  $\sim 1 \mu\text{W}/\mu\text{m}^2$  of uncoated AuNR attached onto the surface of a glass slide. (C) Zoom of 3 AuNRs from (B) attached onto a surface of a glass slide at different exposure times: 10 ms, 2 ms, and 1 ms. The signal and noise clearly drops with decreasing exposure time. The profile along the yellow line is plotted below for each image. The particles show strong satellite peaks, indicating spherical aberrations. (D) The mean-square-displacement (MSD) versus time plot for the first 1 second of 4 selected 60 nm gold nanoshells diffusing on a membrane in 3:2 glycerol:water. A linear fit to the MSD of the red line is also plotted in the figure as the grey dashed line, with a diffusion constant of  $3 \cdot 10^{-13} \text{ m}^2/\text{s}$ . The inset shows an overlay of all 2031 frames. The membrane edge is visible by bright edges in the left and bottom side of the image.

### 10.2.5. DARK-FIELD IMAGING OF GOLD NANOPARTICLES

For the observation of the rotation, we plan to use a laser-based dark-field imaging system, as shown in Fig. 10.4A, which is based on the approach reported in Ref. [23]. The system employs a 637 nm laser (Thorlabs, laser diode HL63142DG) focused on the back focal plane of a 60x 1.2 NA water immersion objective using a dot mirror (DM, Fig. 10.4A), an elliptical custom-made gold mirror of 3x4.24 mm. The dot mirror has a much smaller diameter than the aperture size of the objective, under filling the lens. Since the dot mirror is in both the illumination as in the imaging path, the mirror works as a filter to reject specular reflections from the sample. Light scattered under a large angle, however, will still be collected by the imaging system, as the dot mirror is designed to transmit light off the optical axis. Light scattered from strong scatterers, like gold nanoparticles, will thus be imaged, whereas background light will be filtered out, creating a dark-field imaging effect.

The remaining components of the imaging system serve to create the correct illumination of the dot mirror and the sample. We use a spatial filter (SF), with a 1:3 beam expander and a 40  $\mu\text{m}$  pinhole, to clean the laser spot from stray light generated by the laser diode. The expanded beam is passed onto a quarter-wave plate ( $\lambda/4$ ) to create circularly polarized light, which allows uniform scattering from the nanorods at different in-plane orientations. Using a 125 mm focal length lens, the beam is focused on the back focal plane of the objective via the dot mirror. Scattered light is then passed through the dot mirror again and collected onto a CMOS camera (Mikrotron, MC1362) with a maximum frame rate of 10 kHz. The camera is read out using 8-bit binning and a custom made Labview program via a camera-link acquisition card (NI, PCIe-1342). Benchmarking by a marker of known size, we determined that the 14x14  $\mu\text{m}$  pixel size of the camera corresponds to a 56x56 nm area on the image. This gives a 250x magnification, where the objective magnifies the image 60x and the remaining imaging path does another 4x. Note that we did not use a tube lens in the imaging system. The choice for imaging without a tube lens allows a larger magnification. This allows accurate sampling of the diffraction-limited Airy-disk spot of 320 nm (using an NA of 1.2 and 637 nm wavelength of light), but it comes at the expense of severe spherical aberrations [31].

Figure 10.4B shows a typical image of AuNRs fixed on a glass slide by dropcasting. The image shows several bright spots on a dark background. The spots are not all of equal intensity. This might be caused by non-uniform illumination, inhomogeneity in nanoparticle sizes, or out-of-plane orientation of the nanorods. Moreover, the background is not completely dark, which can be a result of reflections of stray light in the imaging system. Finally, the spots show very pronounced satellite rings. The spots from the nanorods are Airy disks that have side rings. However, for a true Airy pattern, these side bands should only be around 1.7% of the maximum main peak intensity but they are clearly stronger here. These are spherical aberrations that are caused by the absence of a tube lens and this should be corrected for. Using 4x beam expansion in the imaging path and a proper tube lens should correct for these aberrations, whilst retaining the correct magnification.

Figure 10.4C shows a zoom of three spots from the image in Fig. 10.4B, at different exposure times. Initially, decreasing the exposure time from 10 to 1 ms decreases both

the background and the signal intensity. The signal-to-noise ratio (see SI Section 10.4.6) initially increases from  $SNR = 8$  at 10 ms to 17 at 2 ms and 12 at 1 ms, as the peak intensity at 10 ms exposure saturates the camera and the background is severely reduced at the shorter exposure times. A line scan, as shown below the images, reveals this more clearly and also shows the intense side bands from the spots. The middle line scan, where the peak intensity of the spot can be read, reveals these side bands have an intensity of around 20-30% of the main peak intensity, much stronger than the theoretical 1.7%. The distance from the peak maximum to the first minimum is 310 nm, which agrees well with the size of the diffraction-limited point-spread function of 320 nm, using an NA of 1.2 and 637 nm wavelength of light. Imaging at even faster time resolutions should be possible, by increasing the incident laser power and removing the spherical aberrations by using a correct tube lens.

To demonstrate the ability of the imaging system to do particle tracking, we tracked the location of 60 nm nanoshells (40 nm SiO<sub>2</sub> core, 10 nm Au shell, scattering peak at 635 nm) on a membrane in 3:2 glycerol:water mixture. To determine the position and track the nanoparticles, we used centroid fitting and TrackMate, a plugin in ImageJ. Figure 10.4D shows the resulting mean-square displacement (MSD) versus accumulated time of 4 selected tracked shells, with an overlay of all 2031 frames shown in the inset. Linear fits yield a diffusion constant of  $\sim 3 \cdot 10^{-13} \text{ m}^2/\text{s}$ , which agrees well with the expected diffusion constant of  $2.85 \cdot 10^{-13} \text{ m}^2/\text{s}$  for 60 nm particles in a solution with a viscosity of 0.025 Pa·s [32].

This characterization shows that the system can be used for tracking nanoparticles, which should be straightforwardly extended to track the rotating of our nanomotor. Unfortunately, we have not yet managed to test the latter yet. Such measurements are now being planned.

### 10.3. CONCLUSION AND OUTLOOK

In this chapter we have presented the current status of a project to observe the rotation of a DNA origami nanomotor driven by electroosmotic flow. We have discussed the operational principle of the nanomotor, where the viscous flow induced by electroosmosis in a nanopore drives a DNA origami propeller that is incorporated in the axle. Through TEM imaging we demonstrated successful folding of our 42 nm-in-diameter DNA nanomotor design, which is based on Ref. [14]. We successfully fabricated nanopore arrays using electron-beam lithography. Observation of the nanomotor rotation will be done by tracking of a gold nanoparticle at the end of a 215 nm crank lever attached to the axle by dark-field microscopy. We demonstrated that coating of gold nanorods with a mix of polyT and target sequence DNA using thiol chemistry and salt aging provides nanorods that are stable in solutions containing high concentrations of magnesium ions. We confirmed the attachment of the gold nanorod on the arm, albeit with a low yield. Furthermore, we characterized our dark-field imaging system and showed it can be used for tracking AuNR up to 1 kHz. This endeavor, however, is not yet completed and a few challenges will still need to be addressed, as we will discuss below.

First, proper orientation of the motor when docked is critical and this will be tested first. To ensure correct docking, the two bearing halves contain each a 400 bp leash. The

rationale behind the leash is that a long leash will be able to probe a larger space than the motor itself and will insert first when the motor approaches the nanopore. The current leash size is unlikely to be long enough to achieve this effect, as the motor arm is already longer than the leashes. Attaching a much longer leash, for example with a 5 kb fragment of DNA, will fix this.

Second, interactions of the crank lever with the surface might inhibit rotation. DNA is known to interact with solid-state surfaces, in particular in the presence of divalent ions like magnesium, required for DNA origami stability. The interactions can be reduced significantly by replacing the magnesium ions with a high concentration of sodium, in which the origami nanostructures also retain their integrity. Alternatively, interactions can be mitigated by using a surface passivation strategy, for example by coating the surface with polyethylene glycol (PEG) molecules. This was used in Ref. [14] to successfully observe rotational diffusion of the Brownian DNA origami rotor. Care must be taken when coating, however, because long PEG molecules will also coat the nanopore interior and might impede docking of the motor.

Third, the low yield of the crank lever labeling with the gold nanoparticle currently hinders progress. Initial tries to observe rotor diffusion of previously published rotor [14] in our dark-field imaging system have not yet been successful due to the low AuNR labelling yield. Obtaining labeled rotors in large enough quantities has proven difficult, making it hard to observe diffusive rotor action on a coverslip. Two approaches can be taken to overcome this issue. One reason that the attachment yield of the nanoparticles is low can be the interactions of the target oligo with the gold surface, possibly mediated by the presence of magnesium. Using sodium chloride to replace the magnesium chloride could prevent this issue, increasing the attachment yield. Another approach would be to abandon the gold nanoparticle labeling all together, and use fluorescence to observe nanomotor rotation. The current sites for AuNR attachment can be used to bind fluorescently labeled DNA oligos, alternatively creating a bright arm tip that can be observed in epi-fluorescence. Placing multiple fluorophores at the crank lever's end will alleviate effects of photobleaching of the dye, and will create a spot bright enough to be seen in epi illumination conditions.

Fourth, it is yet unclear if the current design of the propeller on nanomotor will be able provide enough torque to drive the entire crank lever. Molecular dynamics simulations done by Aleksei Aksimentiev (University of Illinois) on a few different propeller designs have shown that rotation of the propeller in a flow is possible, even in an electroosmotic flow (personal communication). However, the propeller needs to maintain its shape in the presence high electric fields and the same simulations show that the flaps in the current design might collapse under the influence of the electrophoretic forces in the pore. Other designs are more resilient, but are more complex to implement into the DNA origami design and these will be tested only at a later stage.

Fifth, the structural integrity of the motor as a whole in the strong electric fields in the nanopore can be a concern. The strong electric field might significantly deform the bearing, the DNA origami flaps to keep the motor docked could fail, or the axle might be pulled out of the bearing. Structural deformation of DNA origami plates can happen on a nanopore [33], but this only occurs at increased bias voltages. The freedom to be able

to choose the bias voltage at will should allow us to stay clear from conditions that can lead to structural failure of the motors during the experiment. Even though there thus are a number of challenges that will have to be tackled, every one of these challenges separately seems well addressable experimentally. This stems us hopeful and we are confident that we will succeed in mounting all of them, so that we can complete our quest to realize a driven rotation of a DNA origami nanomotor.

## 10.4. SUPPORTING INFORMATION

### 10.4.1. ELECTROSMOTIC FLOW SPEED IN A NANOPORE

Electroosmotic flow (EOF) is the flow of a solution induced by an external electric field. Flow at the nanoscale is viscous in nature and is then entirely determined by the viscous contribution in the Navier-Stokes equation, which describes general flows of liquid solutions,

$$\eta \nabla^2 \mathbf{u}(\mathbf{r}) = \rho(\mathbf{r}) \mathbf{E}(\mathbf{r}). \quad (\text{S10.2})$$

Here  $\eta$  is the viscosity,  $\mathbf{u}(\mathbf{r})$  the flow velocity,  $\rho(\mathbf{r})$  the charge density in the solution, and  $\mathbf{E}(\mathbf{r})$  in this case the external electric field.  $\rho(\mathbf{r})$  can be written as  $\sum_i n_i(\mathbf{r}) z_i e$ , where  $n_i(\mathbf{r})$  is the ion density,  $z_i$  is the ion valence,  $e$  is the electron charge, and the summation runs over all ion species  $i$  in the solution.  $n_i(\mathbf{r})$  must be determined if the flow profile needs to be calculated. It is clear that if the net charge density in the solution  $\rho(\mathbf{r})$  is zero, there can be no fluidic flow induced by an electric field. Ions in an electrolyte solution must obey the Poisson-Nernst-Planck (PNP) equations, which describe the spatial distribution of charged molecules, subject to diffusion, in the presence of an arbitrary electric field. The PNP equations can be significantly simplified by invoking the symmetry of a simplified nanopore geometry, in which the nanopore is modeled as infinite cylinder of radius  $a$ , with a fixed potential  $\phi_0$  at the wall of the nanopore. If the external electric field does not disturb the ion distribution inside the nanopore  $n_i(\mathbf{r})$ , the ion distribution will only have a radial dependence and the PNP equations simplify to the Poisson-Boltzmann equation:

$$\nabla^2 \phi(r) = -\frac{1}{\epsilon} \sum_i z_i e n_i(r), \quad (\text{S10.3})$$

with

$$n_i(r) = n_0 \exp\left(\frac{z_i e \phi(r)}{k_B T}\right),$$

where  $\phi(r)$  is the electric potential that needs to be solved,  $\epsilon$  is the electric permittivity of the solution,  $n_0$  is the bulk density of ions. Typically, only the dominant ion contribution is considered, usually from sodium and chloride. Identifying  $r_D = \sqrt{\frac{\epsilon k_B T}{2 n_0 e^2}}$  as the Debye length and the characteristic length over which the ion density significantly changes, this equation can be linearized if the Debye length is significantly smaller than the typical length scale of the system,  $r_D \ll a$ . The electrostatic potential can then be solved for analytically using Eqn. S10.3 in a cylindrical geometry using the boundary condition on the nanopore wall as discussed:

$$\phi(r) = \phi_0 \frac{I_0(r/r_D)}{I_0(a/r_D)}, \quad (\text{S10.4})$$

where  $I_0(r)$  is the zero-order modified Bessel function of the first kind.

The electroosmotic flow profile inside the nanopore can now be solved, invoking a no-slip boundary condition on the wall. Using  $\mathbf{E}(\mathbf{r}) = E_z = \frac{\Delta V}{l}$ , where  $l$  is the thickness of the membrane and  $\Delta V$  is the bias voltage, Eqn. S10.2 can be solved for :

$$u(r) = -\frac{\epsilon \phi_0 \Delta V}{\eta l} \left[ 1 - \frac{I_0(r/r_D)}{I_0(a/r_D)} \right], \quad (\text{S10.5})$$

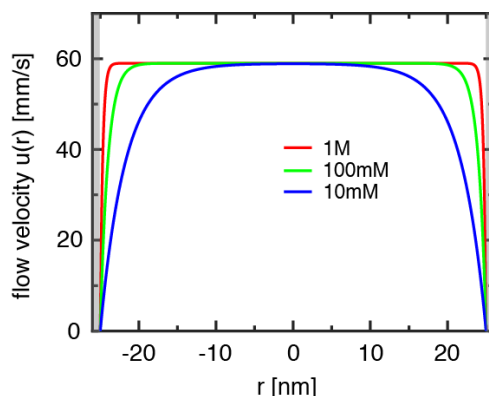


**Figure S10.5:** Electroosmotic flow profile inside the nanopore as a function of distance from the center of the nanopore for  $a = 25$  nm,  $l = 20$  nm,  $\phi_0 = -15$  mV, and  $\Delta V = 100$  mV, and different electrolyte concentrations (monovalent, e.g. NaCl).

For small surface potentials  $\phi_0$  compared to  $k_B T/e$ , the surface charge density  $\sigma$  on the pore walls is related to the surface potential as  $\sigma = \frac{c\phi_0}{r_D}$ , and at the center of the nanopore the expression is recovered as written in Eqn. 10.1 in the main text. Again, if there is no surface charge density on the nanopore wall, there will be no net charge density in the pore, and hence there will be no flow.

Equation 10.5 is plotted in Fig. S10.5 for a nanopore with  $a = 25$  nm,  $l = 20$  nm,  $\phi_0 = 15$  mV, and  $\Delta V = 100$  mV, for different bulk concentrations  $n_0$ : 10mM NaCl, 100mM NaCl, and 1M NaCl. Clearly the flows are strong, on the order of several mm/s, and the flow reaches its maximum at the center of the pore. For higher bulk ion concentrations  $n_0$ , the flow speed is more uniform across the nanopore. This is related to the smaller Debye length for higher bulk ion concentrations, which causes the net charge density in the solution to be more concentrated near the nanopore wall.

#### 10.4.2. PROTOCOL FOR AUNR COATING WITH SSDNA

##### MATERIALS:

- Monothiol polyT oligos 100 $\mu$ M (iDT; thiol-5'-TTTTTTTTTT-3')
- Monothiol target oligos 100 $\mu$ M (iDT; thiol-5'-TTTGGGACGGCCAAAAATGCTTTGG-3')
- 500mM pH 2.5 trisodium citrate-HCl buffer
- 5M NaCl
- 1M NaOH
- G50 desalting column (Illustra)
- 100OD-mL 39x12 nm nanorods (AuNR, 90nm) citrate stabilized (Nanopartz, Inc)

**PROTOCOL:**

1. Mix 100  $\mu\text{M}$  monothiolated poly(10)T and 100  $\mu\text{M}$  target oligos in a 5:1 ratio, to a final volume of 50  $\mu\text{L}$ . Add 1  $\mu\text{L}$  500 mM TCEP, vortex and spin briefly, then leave for >1 hour.
2. Remove TCEP from the oligo solution using one G50 desalting column at 735 g spin speed, collecting solution in a 1.5 mL low-retention tube.
3. Increase the volume of the solution to 1 mL by adding MilliQ. Place the tube in a shaker at 37°C and 1200 rpm for 2 min.
4. Add 11  $\mu\text{L}$  of 100OD-mL AuNR solution to obtain 1nM AuNR (oligo:AuNR 1:5000). The color of the solution should be blue-green. Place the tube immediately back in the shaker and leave for 2 min.
5. Add 33  $\mu\text{L}$  of 500mM trisodium citrate-HCl pH 2.5 and place the tube back immediately in the shaker and leave for 1 min.
6. Add 10  $\mu\text{L}$  of 5M NaCl and place the tube back immediately in the shaker and leave for 1 min. Repeat this step 18 times. During these steps, the color of the solution should not change.
7. Add 50  $\mu\text{L}$  of 1M NaOH and place the tube back immediately in the shaker and leave for 1 min.
8. Take the tube out of the shaker and let them cool down for 10 min.
9. Remove excess oligos. Spin the tube down at 8000 g for 20 min. and carefully remove supernatant. Redissolve the pellet in 1 mL 0.5x TBE + 0.02% SDS by shaking. Vortex briefly. Repeat this step 4 times. Redissolve the supernatant in 0.5x TBE at the last step.
10. Spin the tube down at 8000 g for 20 min and carefully remove supernatant. Increase the volume to 50  $\mu\text{L}$  by adding 0.5x TBE, yielding a final particle concentration of ~20nM.

**10.4.3. PROTOCOL FOR MOTOR ASSEMBLY AND AUNR ATTACHMENT****MOTOR ASSEMBLY AND AND AUNR ATTACHMENT:**

1. Incubate 50nM of clamp A with the axle (R) 1:1 at 30°C in the presence of 20mM MgCl<sub>2</sub> overnight.
2. First adjust the MgCl<sub>2</sub> concentration of the clamp B solution to 20mM, before adding. Add equal part of clamp B and incubate at 45°C in the presence of 20mM MgCl<sub>2</sub> for 6 hours.
3. Add bracket closing oligonucleotides in excess at a ratio of 5:1 per binding site (4) and incubate at room temperature for 24 hours.

**AUNR ATTACHMENT LABELED ORIGAMI PURIFICATION USING BAND EXCISION FROM GEL ELECTROPHORESIS:**

1. Add 1:5 excess of ssDNA coated AuNRs to DNA origami sample (trimer or plates), reducing the final concentration of  $\text{MgCl}_2$  to 5mM and leave overnight.
2. Run the sample on ice in a 1% agarose gel in 0.5xTBE buffer and 11mM  $\text{MgCl}_2$  for 2 hours at 70 V. Replace buffer solution every 45 min.
3. Cut out the respective band, visible in white light (see main text). This purifies the labeled trimers from the free AuNR.
4. Extract the sample from the cut out using an adjusted freeze and squeeze protocol. Crush the gel cut out in an 0.5 mL Eppendorf tube.
5. Cut the tube and fit the tube onto a freeze'n squeeze column (Biorad). Spin 3 min at 13000 g and collect the filtered solution.

#### 10.4.4. EXAMPLE TEM IMAGES OF NANOPORE ARRAY

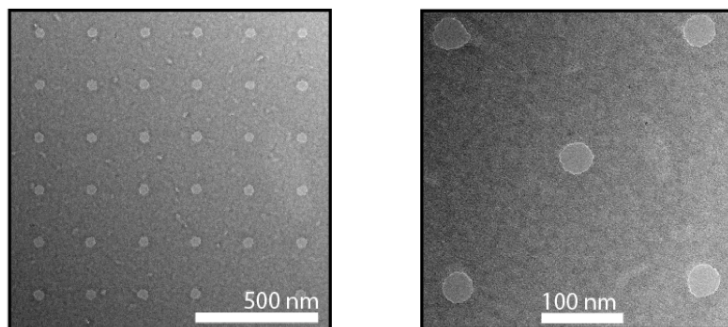


**Figure S10.6:** Example TEM images of a nanopore array with an average nanopore diameter of  $42 \pm 3$  nm at different zooms.

#### 10.4.5. GEL ELECTROPHORESIS AND AFM IMAGE OF DNA ORIGAMI PLATES LABELED WITH AuNR

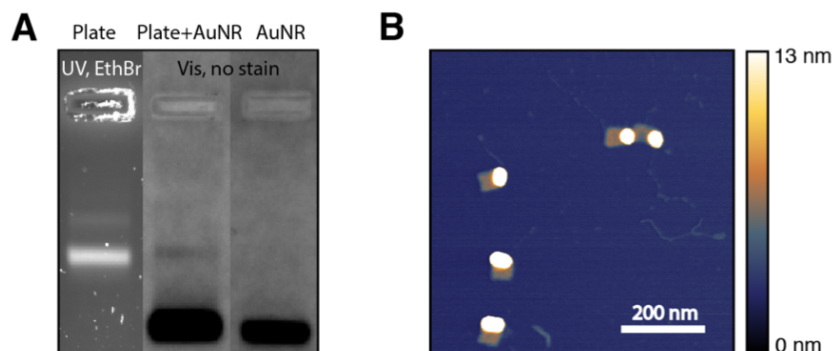


**Figure S10.7: Labeling of DNA origami plates.** (A) Gel electrophoresis image of gel purification of AuNR-labeled DNA origami plates, as described in SI Section 10.4.2. A clear band in the EthBr-stained lane aligns with a faint band in the visible gel image from the lane containing AuNR-labeled plates. Free AuNR make up the thick band in the visible image, the faint band illustrates the low yield. (B) AFM image after purification, as described in SI Section 10.4.2. The square plates are labeled with a particle.

### 10.4.6. DETERMINATION OF SIGNAL-TO-NOISE RATIO IN IMAGING SYSTEM

The signal-to-noise ratio was determined [34] by measuring the mean intensity  $I_s$  in an area of 12x12 pixels (0.65x0.65 $\mu\text{m}$ ) and determining the average background intensity  $I_b$  in a 12x12 pixel area adjacent to the spot:

$$SNR = \frac{I_s - I_b}{\sqrt{\sigma_i^2 + \sigma_b^2}} \quad (\text{S10.6})$$

where  $\sigma_i^2$  is the variance of the signal intensity and  $\sigma_b^2$  is the variance of the background region.

## REFERENCES

- [1] M. Yoshida, E. Muneyuki, and T. Hisabori, *Atp synthase—a marvellous rotary engine of the cell*, Nature Reviews Molecular Cell Biology **2**, 669 (2001).
- [2] T. Minamino, K. Imada, and K. Namba, *Molecular motors of the bacterial flagella*, Current opinion in structural biology **18**, 693 (2008).
- [3] W. Junge and N. Nelson, *Atp synthase*, Annual review of biochemistry **84**, 631 (2015).
- [4] G. Oster and H. Wang, *Rotary protein motors*, Trends in cell biology **13**, 114 (2003).
- [5] R. Feynman, *There's plenty of room at the bottom*, Engineering and Science **23**, 14 (1960).
- [6] E. R. Kay, D. A. Leigh, and F. Zerbetto, *Synthetic molecular motors and mechanical machines*, Angewandte Chemie International Edition **46**, 72 (2007).
- [7] G. A. Ozin, I. Manners, S. Fournier-Bidoz, and A. Arsenault, *Dream nanomachines*, Advanced Materials **17**, 3011 (2005).
- [8] W. R. Browne and B. L. Feringa, *Making molecular machines work*, Nature nanotechnology **1**, 25 (2006).
- [9] S. Erbas-Cakmak, D. A. Leigh, C. T. McTernan, and A. L. Nussbaumer, *Artificial molecular machines*, Chem. Rev **115**, 10081 (2015).
- [10] F. Kilchherr, C. Wachauf, B. Pelz, M. Rief, M. Zacharias, and H. Dietz, *Single-molecule dissection of stacking forces in dna*, Science **353**, aaf5508 (2016).
- [11] P. Wang, T. A. Meyer, V. Pan, P. K. Dutta, and Y. Ke, *The beauty and utility of dna origami*, Chem **2**, 359 (2017).
- [12] C. Zhou, X. Duan, and N. Liu, *A plasmonic nanorod that walks on dna origami*, Nature communications **6**, 8102 (2015).
- [13] A. E. Marras, L. Zhou, H.-J. Su, and C. E. Castro, *Programmable motion of dna origami mechanisms*, Proceedings of the National Academy of Sciences **112**, 713 (2015).
- [14] P. Ketterer, E. M. Willner, and H. Dietz, *Nanoscale rotary apparatus formed from tight-fitting 3d dna components*, Science advances **2**, e1501209 (2016).

- [15] E. Kopperger, J. List, S. Madhira, F. Rothfischer, D. C. Lamb, and F. C. Simmel, *A self-assembled nanoscale robotic arm controlled by electric fields*, *Science* **359**, 296 (2018).
- [16] E. Purcell, *Life at low reynolds number*, *American Journal of Physics* **45**, 3 (1977).
- [17] R. B. Schoch, J. Han, and P. Renaud, *Transport phenomena in nanofluidics*, *Reviews of modern physics* **80**, 839 (2008).
- [18] S. Van Dorp, U. F. Keyser, N. H. Dekker, C. Dekker, and S. G. Lemay, *Origin of the electrophoretic force on dna in solid-state nanopores*, *Nature Physics* **5**, 347 (2009).
- [19] C. Plesa, A. N. Ananth, V. Linko, C. Gülcher, A. J. Katan, H. Dietz, and C. Dekker, *Ionic permeability and mechanical properties of dna origami nanoplates on solid-state nanopores*, *ACS nano* **8**, 35 (2013).
- [20] C.-Y. Li, E. A. Hemmig, J. Kong, J. Yoo, S. Hernández-Ainsa, U. F. Keyser, and A. Aksimentiev, *Ionic conductivity, structural deformation, and programmable anisotropy of dna origami in electric field*, *ACS nano* **9**, 1420 (2015).
- [21] R. Yasuda, H. Noji, M. Yoshida, K. Kinosita Jr, and H. Itoh, *Resolution of distinct rotational substeps by submillisecond kinetic analysis of f1-atpase*, *Nature* **410**, 898 (2001).
- [22] H. Ueno, T. Suzuki, K. Kinosita, and M. Yoshida, *Atp-driven stepwise rotation of fof1-atp synthase*, *Proceedings of the National Academy of Sciences of the United States of America* **102**, 1333 (2005).
- [23] H. Ueno, S. Nishikawa, R. Iino, K. V. Tabata, S. Sakakihara, T. Yanagida, and H. Noji, *Simple dark-field microscopy with nanometer spatial precision and microsecond temporal resolution*, *Biophysical journal* **98**, 2014 (2010).
- [24] P. Ketterer, *Rotary mechanisms and scientific devices based on DNA*, Thesis (2017).
- [25] D. V. Verschuere, W. Yang, and C. Dekker, *Lithography-based fabrication of nanopore arrays in freestanding sin and graphene membranes*, *Nanotechnology* **29**, 145302 (2018).
- [26] P. K. Jain, K. S. Lee, I. H. El-Sayed, and M. A. El-Sayed, *Calculated absorption and scattering properties of gold nanoparticles of different size, shape, and composition: applications in biological imaging and biomedicine*, *The journal of physical chemistry B* **110**, 7238 (2006).
- [27] S. J. Hurst, A. K. Lytton-Jean, and C. A. Mirkin, *Maximizing dna loading on a range of gold nanoparticle sizes*, *Analytical chemistry* **78**, 8313 (2006).
- [28] F. N. Gür, F. W. Schwarz, J. Ye, S. Diez, and T. L. Schmidt, *Toward self-assembled plasmonic devices: high-yield arrangement of gold nanoparticles on dna origami templates*, *ACS nano* **10**, 5374 (2016).
- [29] R. Schreiber, N. Luong, Z. Fan, A. Kuzyk, P. C. Nickels, T. Zhang, D. M. Smith, B. Yurke, W. Kuang, and A. O. Govorov, *Chiral plasmonic dna nanostructures with*

- switchable circular dichroism*, Nature communications **4**, 2948 (2013).
- [30] V. V. Thacker, L. O. Herrmann, D. O. Sigle, T. Zhang, T. Liedl, J. J. Baumberg, and U. F. Keyser, *Dna origami based assembly of gold nanoparticle dimers for surface-enhanced raman scattering*, Nature communications **5**, 3448 (2014).
- [31] C. J. Sheppard and M. Gu, *Aberration compensation in confocal microscopy*, Applied Optics **30**, 3563 (1991).
- [32] N.-S. Cheng, *Formula for the viscosity of a glycerol-water mixture*, Industrial & engineering chemistry research **47**, 3285 (2008).
- [33] S. Hernández-Ainsa, K. Misiunas, V. V. Thacker, E. A. Hemmig, and U. F. Keyser, *Voltage-dependent properties of dna origami nanopores*, Nano letters **14**, 1270 (2014).
- [34] M. K. Cheezum, W. F. Walker, and W. H. Guilford, *Quantitative comparison of algorithms for tracking single fluorescent particles*, Biophysical journal **81**, 2378 (2001)

# SUMMARY

Grabbing a single molecule and inspecting its contents is far from easy. Apart from the small size of the objects, biomolecules shake, shimmer, and bounce around a tremendous amount. How can one gently control something that small (without squashing or destroying it) and still be able to tell what it is? The work in this thesis is exactly aimed to develop a practical solution to that problem: creating a plasmonic nanopore sensor to investigate and manipulate single biomolecules. The plasmonic nanopore is constructed from two single-molecule sensing devices merged into one: a solid-state nanopore, a tiny hole in a thin membrane that confines a static electric field, and a plasmonic nanoantenna, a gold nanostructure that concentrates light into nanoscale volumes (hotspots). Using these localized static and optical fields, biomolecules can be captured, trapped, perturbed, manipulated, and probed in a variety of ways. All controlled at will by the experimenter, one single molecule at the time.

**Chapter 1** provides a brief introduction to the concepts used in this thesis. It aims to sketch the scene encountered at the nanoscale and briefly discusses the concepts of the plasmonic nanopore sensor. It explains how nanopores work and how optically driven electron oscillations, or plasmons, can be used to act optical forces on single molecules and detect their presence. The tools of top-down nanotechnology are shortly introduced and the chapter finishes with a short overview of the plasmonic nanopore field.

Before one can do anything interesting with plasmonic nanopores, they will have to be made first. Creating robust nanostructures at these length scales is challenging, and two works that describe the creation of nanopores are presented in the two subsequent chapters. They present alternatives to conventional transmission-electron-microscopy (TEM) drilling of the nanopores, which is a little slow in throughput and expensive.

**Chapter 2** describes a novel fabrication method to create regular nanopore arrays in a simple and scalable manner using electron-beam lithography on freestanding SiN and graphene membranes. By controlling the dose of the single-shot electron-beam exposure, circular nanopores of any size down to 16 nm in diameter can be fabricated in both materials at high accuracy and precision. We demonstrate the sensing capabilities of these nanopores by translocating dsDNA through pores fabricated using this method and find their performance on par with TEM-drilled nanopores.

Not only expensive nanotechnology tools can be used to create plasmonic nanopores. **Chapter 3** describes a novel cost-efficient method for the fabrication of self-aligned plasmonic nanopores by means of optically controlled dielectric breakdown. This can, in principle, be employed by just using a 9 V battery and a simple laserpointer. Through the excitation of a plasmonic bowtie nanoantenna, a high-voltage-driven breakdown of the membrane material is localized to the hotspot of the antenna, resulting in a self-aligned plasmonic nanopore. This principle can also be used to optically localize breakdown to create non-plasmonic nanopores. We show that the approach provides precise control over the nanopore size and that these plasmonic

nanopores can be used as single-molecule DNA sensors with a performance matching that of TEM-drilled nanopores.

Plasmonic nanopores have a variety of handles that can be employed to study molecules. The next four chapters will describe how the plasmonic nanopores can be used for sensing single molecules.

Our initial adventure into plasmonic nanopores resulted in characterizing the effects from the local heating of the antenna. **Chapter 4** investigates DNA translocations through a plasmonic nanopore based on a gold bowtie nanoantenna integrated with a nanopore. The plasmonic excitation is found to influence the nanopore ionic signal from translocating DNA translocation, but does not affect their translocation times. Furthermore, a striking plasmon-induced enhancement of the DNA translocation event rate is observed in lithium chloride (LiCl), but absent in potassium chloride (KCl) buffers. We propose a mechanism based on plasmon-induced local heating and thermophoresis as explanation of our observations.

Second, in **Chapter 5** we demonstrate that the plasmonic nanopore can not only locally heat the nanopore sensor, but also provide an additional read-out through plasmon resonance sensing. By monitoring the backscattered light intensity from the plasmonic nanoantennas, single DNA molecules can be detected in a label-free manner at sub-millisecond acquisition rates. The nanopore then allows for efficiently delivery of molecules to the plasmonic hotspot. Our method realizes an event detection rate of 10 molecules per second with better than 200  $\mu$ s temporal resolution, both orders of magnitude better than for any reported plasmonic single-molecule sensing method. Furthermore, the DC electric field applied to the nanopore can, in contrast to previous surface-binding-based plasmonic biosensors, both capture and release biomolecules from the hotspot, allowing efficient reuse of the sensor for subsequent molecules.

Moreover, plasmon resonance sensing can be done in transmission mode, where light transmitted through the antenna is collected and used as read out. In **Chapter 6** we demonstrate concurrent detection of DNA translocations of single DNA molecules in both the ionic current and transmitted light intensity through an inverted-bowtie plasmonic nanoantenna integrated with a nanopore. Additionally, the antenna design results in reduced temperature increase caused by the plasmon excitation compared to the regular bowtie antenna. We discuss the noise characteristics of the optical read-out and demonstrate DNA translocation event detection at various driving voltages and buffer conditions where traditional ionic current sensing fails.

Lastly, in **Chapter 7**, we show that plasmonic nanopores can also be used to trap and manipulate single molecules. Using an inverted-bowtie shaped plasmonic nanopore we trap single molecules to provide ample measurement time. We first characterized our plasmonic nanoantennas, defined by electron-beam lithography, using transmission electron microscopy and FDTD simulations. Employing enhanced light transmission through the nanoantenna as the read-out signal, we verified the optical trapping ability of the plasmonic nanopore by tweezing 20 nm-in-diameter polystyrene nanoparticles for seconds or longer. To prove that the plasmonic nanopore can function as a single molecule biosensor, we furthermore trapped single beta-amylase protein molecules in the nanoantenna. Analysis of the trapping events revealed that trapping was assisted by protein-surface interactions and indicated that some trapped protein denatured on

the surface. The application of an electrical bias voltage increased the event rate over an order of magnitude and shortened the residence time of the molecules in the plasmonic nanopore.

But it's not only plasmonic nanopores that are useful. Conventional nanopores can also be helpful, for example to understand polymer physics or to use polymer properties to control the speed of translocation. To gain a better physical understanding of the DNA translocation process, we investigate in **Chapter 8** the temperature dependence of  $\lambda$ -DNA translocations through 10 nm-in-diameter silicon-nitride nanopores, both experimentally and theoretically. The measured ionic conductance  $G$ , the DNA-induced ionic-conductance blockades  $\Delta G$  and the event frequency  $\Gamma$  all increase with increasing temperature while the DNA translocation time  $\tau$  decreases.  $G$  and  $\Delta G$  are accurately described when bulk and surface conductances of the nanopore are considered and access resistance is incorporated appropriately. Viscous drag on the untranslocated part of the DNA coil is found to dominate the temperature dependence of the translocation times and the event rate is well described by a balance between diffusion and electrophoretic motion.

In **Chapter 9**, we use the long DNA polymer to control the DNA residence times in the nanopore. By capturing either end of the coil in two in-plane nanopores simultaneously, we show that an extra nanopore can be used to control the translocation of the DNA molecule. Our experiments and molecular dynamics simulations show that simultaneous electrophoretic capture of a DNA molecule by the two nanopores mechanically traps the molecule, increasing its residence time within the nanopores by orders of magnitude. Remarkably, by using two unequal-sized nanopores, the pore of DNA entry and exit can be discerned from the ionic current blockades and the translocation direction can be precisely controlled by small differences in the effective force applied to DNA.

Studying biomolecules is a fascinating adventure. The efficiency, precision, and grand variety of these macromolecular complexes still puzzles us. But nanotechnology is progressing beyond the mere position of bystander and we are starting to engage in the nanoscale world with our own rationally designed molecules. **Chapter 10** describes an initial attempt to create a nanoscale motor that converts energy into rotation much like an engine. The chapter presents a progress report towards the demonstration of directed rotation of such a DNA origami nanomotor using an electrically controlled electroosmotic flow from a solid-state nanopore. Using dark-field imaging, rotation can be observed by tracking a gold nanorod attached to the end of a crank lever that is connected to the axle. We demonstrate the successful assembly of the DNA nanomotor consisting of two bearing halves and an axle that is extended with a propeller blade made of DNA and a 215 nm long crank lever. We furthermore show the fabrication of nanopore arrays and labeling of the end of the crank lever with a gold nanorod coated with DNA oligos. We characterize our dark-field imaging system and show that we can observe moving gold nanoparticles up to 1 kHz frame rate. Finally, we discuss the further challenges and potential pitfalls in this project that need to be addressed to carry this exciting, but currently unfinished project to fruition.

Where will nanopores in general take us in the future? Protein based nanopores have already demonstrated their use in applications, as a commercial DNA sequencing

device is already on the market. Moreover, commercial ventures to employ biological nanopores for small molecule sensing are well on their way. Still, solid-state nanopores have the advantage over their biological counterparts that they are truly versatile single-molecule sensors: their size can easily be adjusted. Hence, there is no doubt these little guys will be at the core of many biomedical sensors and diagnostic devices in the future. But their main selling point, their versatility, actually also comes with a drawback. Solid-state nanopores currently do not have a very selective read-out and molecular transit times are currently too short to allow for useful information to be extracted; in particular the nucleotide sequence of a DNA molecule or the amino acid sequence of a protein molecule.

We have tried to address these issues with plasmonic nanopores, but this is only one way to improve the nanopore sensor. For example, improved current amplifiers, tunneling current read-out, and double nanopores all attempt to improve nanopores such that sufficient sensitivity is reached at the appropriate bandwidth. Currently, plasmonic nanopores have not managed yet to show a platform-wide advantage over conventional solid-state sensors. In particular, the prospect of plasmonic nanopores towards sequencing is not great. Whereas I do believe that with further hotspot engineering optical forces can be boosted sufficiently to increase residence times and allow for the physical characterization of whole molecules, I do not think that the plasmonic hotspot can be made small enough for read-out of a nucleotide sequence. Some applications do not require this level of miniaturization though, such as the investigation of DNA-protein binding at physiological conditions, and these could give the sensor an application. However, it remains to be seen if the plasmonic nanopore strategy will really be better than other (nanopore) techniques. If plasmonic nanopores are to be made great, significant improvements will have to be made, in particular in hotspot engineering and surface passivation. I do not think that the current prospects this sensor class possesses will justify the required investments. Nonetheless, development of plasmonic nanopores is certainly interesting from an engineering perspective and I have no doubt that challenges that have been surmounted in the sensor development here will benefit other scientific areas.

# SAMENVATTING

Een enkel molecule vastpakken en onderzoeken is ongelofelijk moeilijk. Behalve dat objecten op deze schaalgrootte natuurlijk ongelofelijk klein zijn, wiebelen, stuiten en bewegen ze ook nog eens extreem veel. Hoe kan je zoiets kleins voorzichtig vastpakken (zonder het te verpletteren of kapot te maken) zodat men kan vertellen wat het precies is? Het werk dat wordt gepresenteerd in dit proefschrift probeert precies voor dit probleem een praktische oplossing te geven: door het maken van een plasmonisch nanogaatje (plasmonic nanopore, in normaal taalgebruik) dat individuele moleculen kan manipuleren en onderzoeken. Het plasmonische nanogaatje is gemaakt uit twee afzonderlijke sensoren, die ieder afzonderlijk individuele moleculen kunnen detecteren: een nanogaatje geboord in een rigide membraan van een vaste stof dat een statisch elektrisch veld in zich focust, en een plasmonische antenne, een gouden nanostructuurtje dat licht kan concentreren tot nanoschaal volumes (hotspots). Door gebruik te maken van deze gelokaliseerde statische en optische velden kunnen biomoleculen worden gegrepen, vastgehouden, verstoord, gemanipuleerd, en onderzocht op verschillende manieren. Allemaal gecontroleerd door de onderzoeker, een molecule per keer.

**Hoofdstuk 1** introduceert kort de concepten die aan bod komen in dit proefschrift. Het poogt een situatie schets te geven van de processen op de nanoschaal en zal kort het concept van het plasmonisch nanogaatje toelichten. Er wordt kort uitgelegd hoe nanogaatjes werken en optisch aangedreven elektronen oscillaties (plasmon oscillaties) gebruikt kunnen worden om optische krachten uit te oefenen op individuele moleculen. Het gereedschap van de nanotechnologie wordt kort toegelicht en het hoofdstuk sluit af met een summier overzicht van het vakgebied van plasmonische nanogaatjes.

Voordat iemand ook maar iets interessants kan doen met plasmonische nanogaatjes, zullen ze eerst gemaakt moeten worden. Het creëren van robuuste nanostructuurtjes op deze schaalgrootte is een uitdaging en de volgende twee hoofdstukken presenteren twee nieuwe methodes voor het creëren van deze nanoapparaten. Ze rapporteren alternatieven voor de conventionele fabricage van nanogaatjes waarbij gaatjes worden geboord door middel van de transmissie elektronen microscoop (TEM), wat nogal tijdrovend en duur werk is.

**Hoofdstuk 2** beschrijft een nieuwe fabricage techniek om regelmatige roosters van nanogaatjes te maken op een simpele en schaalbare manier, door gebruik te maken van elektronen bundel lithografie op vrijstaande silicium-nitride en grafeen membraantjes. Door middel van het controleren van de dosis van een enkel schot van de elektronen bundel tijdens de belichting kunnen circulaire nanogaatjes gemaakt worden van iedere grootte groter dan 16 nm in diameter. We testen of deze nanogaatjes goede sensoren zijn door dubbel strengs DNA door de gaatjes te halen en we laten zien dat de sensor kwaliteit vergelijkbaar is met de TEM gemaakte nanogaatjes.

Niet alleen dure nanotechnologische apparaten kunnen worden gebruikt om

plasmonische nanogaatjes te creëren. **Hoofdstuk 3** beschrijft een nieuwe kosten efficiënte techniek voor de fabricage van zelf-uitgelijnde plasmonische nanogaatjes door middel van een optisch gecontroleerde diëlektrische doorslag. Dit kan, in principe, worden uitgevoerd door gebruik van een 9 V batterij en een laserpointer. Via de excitatie van een plasmonische vlinder nano-antenne kan een met een elektrische hoogspanning aangedreven diëlektrische doorslag in het membraan materiaal worden gelokaliseerd in de hotspot van de antenne. Hierdoor ontstaat een zelf-uitgelijnd plasmonische nanogaatje. Het principe kan ook worden toegepast om de diëlektrische doorslag voor het maken van normale, niet-plasmonische nanogaatjes optisch te lokaliseren. We laten zien dat deze techniek precieze controle geeft over de grootte van het nanogaatje. Daarnaast demonstreren we dat deze plasmonische nanogaatjes vergelijkbaar presteren als TEM geboorde plasmonische nanogaatjes voor de detectie van individuele DNA moleculen.

Plasmonische nanogaatjes hebben verscheidene eigenschappen die gebruikt kunnen worden om moleculen te bestuderen. De volgende vier hoofdstukken beschrijven hoe plasmonische nanogaatjes gebruikt kunnen worden om individuele moleculen te bekijken.

Ons eerste avontuur met plasmonische nanogaatjes leidde tot een karakterisatie van de lokale opwarming van de het nanostructuurtje. **Hoofdstuk 4** onderzoekt hoe DNA zich transporteert door een plasmonisch nanogaatje bestaande uit een plasmonische vlinder antenne geïntegreerd met een nanogaatje. Excitatie van de plasmonische antenne beïnvloedt het signaal in de ionenstroom dat de DNA moleculen produceren, maar heeft geen effect op de translocatie tijd. Bovendien zien we een sterke verhoging in het aantal moleculen dat de sensor bereikt per seconde slechts wanneer we lithiumchloride buffers gebruiken, en niet wanneer we kaliumchloride buffers gebruiken. We stellen een mechanisme voor, gebaseerd op lokale verwarming en thermoforese, dat een verklaring biedt voor de waarnemingen.

Ten tweede, in **Hoofdstuk 5**, laten we zien dat een plasmonisch nanogaatje meer kan doen dan alleen zijn directe omgeving verwarmen, maar ook gebruikt kan worden als optische uitlees methode die gebaseerd is op molecule detectie via de plasmon resonantie van de antenne. Door het terugverstrooide licht van de antenna te monitoren kunnen individuele DNA moleculen zonder label worden gedetecteerd met sub-milliseconde datavergaringsnelheden. Het nanogaatje kan worden gebruikt om efficiënt DNA moleculen in de plasmonische hotspot te krijgen. Onze methode heeft een detectie snelheid van 10 moleculen per seconde met 200  $\mu$ s tijdsresolutie, beide ordes van grootte beter dan andere gepubliceerde plasmon resonantie detectiemethodes van individuele biomoleculen. Bovendien kan het statische elektrische veld in de nanopore, in contrast met eerdere plasmon resonantie detectiemethodes gebaseerd op oppervlakte binding, gebruikt worden om moleculen in de sensor te vangen en ze ervan te verwijderen, zodat de sensor efficiënt herbruikt kan worden.

Daarnaast kan plasmon resonantie detectie ook worden gedaan in transmissie modus, waarbij het licht dat door een plasmonische antenna komt, wordt opgevangen en wordt gebruikt als uitlees strategie. In **Hoofdstuk 6** beschrijven we gelijktijdige detectie van individuele DNA moleculen in zowel de ionenstroom als de licht transmissie door de inverse-vlinder antenne die is geïntegreerd met een nanopore. Bijkomend

zorgt het antenne-ontwerp ervoor dat de omgeving een stuk minder opwarmt door de plasmon excitatie vergeleken met de plasmonische vlinder antenne. We bespreken de ruis karakteristieken van de optische waarneming en laten zien dat DNA translocaties optisch kunnen worden gedetecteerd bij verschillende spanningsverschillen en buffercondities waarbij de traditionele ionenstroom meting niks detecteert.

Tenslotte, in **Hoofdstuk 7**, demonstrenen we dat de plasmonische nanogaatjes gebruikt kunnen worden om individuele moleculen te kunnen vasthouden en te manipuleren. Door gebruik te maken van een inverse-vlinder-vorm plasmonisch nanogaatje, kunnen we individuele moleculen vasthouden wat ons voldoende tijd geeft om ze te waarnemen. Eerst karakteriseren we onze nano-antennes, gemaakt met behulp van elektronen bundel lithografie, via elektronen microscopie en FDTD simulaties. Door gebruik te maken van de verhoogde licht transmissie door de nano-antenne als signaal drager, bevestigen we dat de nano-antenne kan worden gebruikt om optisch nanodeeltjes van 20 nm in diameter voor secondes of langer vast te houden. Om aan te tonen dat het plasmonisch nanogaatje gebruikt kan worden om biomoleculen te detecteren, houden we het eiwit beta-amylase vast in de nano-antenne. Analyse van de signalen laat zien dat het vasthouden van de eiwitten wordt geassisteerd via interacties tussen het eiwit en goud oppervlak en laat zien dat sommige eiwitten denatureren op het oppervlak van de antenne. Door een spanningsverschil aan te leggen over het nanogaatje kan het aantal moleculen dat de sensor bereikt per seconden worden verhoogd en de residentie tijd van een molecule in de antenne worden verkort.

Maar niet alleen plasmonische nanogaatjes zijn nuttig. Conventionele nanogaatjes kunnen ook gebruikt worden om bijvoorbeeld polymeerfysica te bestuderen of polymeer eigenschappen te gebruiken. Om een beter begrip te krijgen van het DNA translocatie proces, bestuderen we in **Hoofdstuk 8** de temperatuurafhankelijkheid van DNA translocaties door 10 nm in diameter silicium-nitride nanogaatjes, beide experimenteel en theoretisch. De gemeten ionische conductie van het nanogaatje  $G$ , de door het DNA geïnduceerde ionenconductie blokkades  $\Delta G$  en de snelheid waarmee de moleculen de sensor bereiken  $\Gamma$  gaan allemaal omhoog wanneer de temperatuur wordt verhoogd.  $G$  en  $\Delta G$  worden accuraat beschreven wanneer bulk en oppervlakte conductanties en de toegangsweerstand van het nanogaatje in beschouwing worden genomen. Viscouse weerstand op het deel van het DNA molecule dat zich nog niet door het gaatje heeft bewogen domineert de temperatuurafhankelijkheid van de translocatie tijd. Tenslotte wordt de snelheid waarmee moleculen de sensor bereiken goed beschreven door een balans tussen diffusie en elektroforetische beweging van het DNA molecule.

**Hoofdstuk 9** maakt gebruik van het lange DNA polymeer om de residentie tijd van het DNA in het nanogaatje te controleren. Door beide einden van het DNA simultaan in twee nanogaatjes te stoppen, die zijn gemaakt in hetzelfde vlak, kan het translocatie proces gecontroleerd worden door het extra nanogaatje. Onze experimenten en moleculaire dynamiek simulaties laten zien dat het molecule mechanisch kan worden vastgehouden door het gelijktijdig in twee verschillende nanogaatjes te vangen. Hierdoor wordt de residentie tijd van het molecule in beide nanogaatjes met verschillende ordes in grootte verlengd. Verrassend genoeg kan, door gebruik te maken van twee nanogaatjes met verschillende grootte, het nanogaatje waarin het molecule zich eerst begeeft en waaruit het als laatste ontsnapt worden

bepaald via de ionenstroom. De translocatie richting kan exact worden gecontroleerd door middel van kleine verschillen in de effectieve krachten die werken op het DNA.

Het bestuderen van biomoleculen is een fascinerend avontuur. De efficiëntie, precisie, en grote variëteit van de macromoleculaire complexen blijft ons nog steeds verbazen. Maar voortgang in de nanotechnologie heeft ons nu gebracht voorbij het punt waar we slechts kunnen observeren. We beginnen nu zelf ook deel te nemen in de nanowereld met onze eigen ontworpen moleculen. **Hoofdstuk 10** beschrijft het begin van een poging om een apparaatje te maken op nanoschaal dat energie kan omzetten in rotatie, net als een motor. Het hoofdstuk presenteert een voortgangsrapport over het realiseren van een dergelijke DNA origami nanomotor die draait met behulp van een elektrisch gecontroleerde, elektro-osmotische waterstroom uit een nanogaatje. Met behulp van donker-veld microscopie kan de rotatie van de motor worden waargenomen, via het traceren van een gouden nanostaafje dat is bevestigd aan de as van de motor. We laten succesvolle constructie zien van de DNA origami nanomotor, die bestaat uit twee lager helften en een as die is verlengd met een propeller blad en een 215 nm lange arm. We laten bovendien succesvolle fabricage van nanogaatje roosters zien en beschrijven de labeling van het einde van de arm met een goud nanostaafje dat is bekleed met korte stukjes DNA. We karakteriseren onze donker-veld microscoop en laten zien dat we gouden nanodeeltjes kunnen bekijken met een snelheid van 1 kHz. Tenslotte, zetten we de toekomstige uitdagingen en potentiële valkuilen in het project uiteen die moeten worden verholpen om dit boeiende, maar op dit moment onafgesloten project tot een succes te maken.

Waar brengen nanogaatjes ons naar toe in de toekomst? Nanogaatjes uit eiwitten hebben op dit moment al een slag gemaakt op de markt, en zijn al geïntegreerd in een commercieel DNA sequentie analyse apparaat. Bovendien zijn er al bedrijfjes druk bezig biologische nanogaatjes te gebruiken om kleine moleculen te detecteren. Toch hebben nanogaatjes in vaste stof membraantjes een groot voordeel omdat ze breed kunnen worden toegepast op de detectie van verschillende soorten individuele moleculen: de grootte is eenvoudig te controleren. Daarom ben ik er van overtuigd dat we deze kleine jongens terug gaan zien in biomedische sensoren en diagnostische apparaten in de toekomst. Maar hun grootste voordeel, die brede inzetbaarheid, komt ook met een groot nadeel. Vaste stof nanogaatjes zijn momenteel niet selectief genoeg in hun uitlees strategie en moleculaire passeertijden door de sensor zijn te kort om interessante informatie te kunnen vergaren van het molecuul. Dat betekent in het specifiek de nucleotide sequentie van een DNA molecuul of de aminozuur sequentie van een eiwit.

We hebben gepoogd met dit werk deze problemen aan te pakken door gebruik te maken van plasmonische nanogaatjes, maar dit is slechts een van de ondernemingen die proberen nanogaatjes beter te maken. Beter elektronische versterking van de ionenstroom, tunnelstroom detectie en dubbele nanogaatjes hebben allemaal hetzelfde doel voor ogen om genoeg resolutie in het signaal te verkrijgen. Op dit moment hebben plasmonische nanogaatjes niet laten zien dat ze algeheel beter zijn dan conventionele nanogaatjes. In het specifiek, het vooruitzicht van het uitlezen van een DNA sequentie via plasmonische nanogaatjes is niet heel hoopvol. Ik ben er zeker van dat de optische krachten dusdanig kunnen worden versterkt dat moleculen in hun geheel fysiek kunnen worden gekarakteriseerd. Maar ik geloof niet dat

de plasmonische hotspot dusdanig verkleind en verbeterd kan worden zodat een nucleotide sequentie kan worden uitgelezen. Niet alle toepassingen vereisen dit overigens, bijvoorbeeld het bestuderen van DNA-eiwit interacties bij fysiologische condities, en die kunnen de sensoren een applicatie geven. Het blijft dan echter nog de vraag of plasmonische nanogaatjes echt een betere strategie zijn dan andere (nanogaatje gebaseerde) technieken. Als plasmonische nanogaatjes groots gemaakt willen worden, moeten er nog significante verbeteringen worden gemaakt, in het specifiek in hotspot ingenieurswerk en oppervlakte passivatie. Ik denk niet dat de potentie die deze klasse van sensoren heeft de benodigde investeringen kunnen verantwoorden. Desalniettemin blijft de ontwikkeling van plasmonische nanogaatjes zeker interessant vanuit een ingenieursperspectief en ik ben er dan ook van overtuigd dat de problemen die zijn overwonnen in de ontwikkeling van de sensor andere onderzoeksgebieden zal sterken.



# ACKNOWLEDGEMENTS

Here, I would like to take a moment to thank the great many and the many great people who have been instrumental in bringing the work reported in this dissertation to fruition. I have had a truly wonderful time here in Delft, which has brought me indispensable experiences both on a professional and personal level. I feel particularly fortunate to have been submerged in such an open, vibrant, and welcoming atmosphere that the department harbors. At every point in the past 5 years, I have felt the support from so many of you, in some way or another. And all of you deserve at least a special mention.

First and foremost, I would like to begin with expressing my gratitude to prof. **Cees Dekker**, my advisor, mentor, and promotor. Your excitement and enthusiasm about science is just contagious. I have always felt your full support throughout my scientific adventures and your encouragements to pursue my own ideas have been very valuable to me. Your to the point and critical scientific remarks often impressed me, as did your swift communication: there are few people I know that use their email so effectively as an instant messaging service. Thank you for all the lively discussions and eagerness to engage in them. I feel I have been very fortunate to have you as a supervisor early on in my career, it has been a lot of fun working with you.

The wonderful world of plasmonic nanopores would not have been there for me to explore without dr. **Magnus Jonsson**. A daily supervisor in my early days in Delft and a plentiful source of knowledge, you have been inspiring to me. I can honestly say that I have never met anyone who exhibits more patience and composure. I very much enjoyed the discussions we had and I really appreciate we kept in close contact after you, inevitably, moved back to Sweden. I am grateful that you are part of my committee and I am going to make a big effort to keep in touch (whether you like that or not).

As the final great grandfather of plasmonic nanopores (next to Cees and Magnus), I would like to extend my gratitude to prof. **Aleksei Aksimentiev**. From Illinois (USA), you (together with Maxim and Jim) supplied us with interesting ideas for experiments and many, many results from your MD simulations. It was a great pleasure to meet you.

I would also like to thank prof. **Hendrik Dietz** and dr. **Philip Ketterer**, some of the best DNA origami architects in the world, for their shared excitement and effort to kickstart the DNA origami motor project. I admire your drive and efficiency and I cherish the great time I had in Munich.

Furthermore, I am grateful to prof. **Kobus Kuipers** and **Lorenzo De Angelis** for their assistance in the optical characterization of our nanostructures. In particular, Lorenzo, it was been great to work together with you. Thanks for all the uplifting conversations and your contagious laughter.

Special thanks are extended to my remaining committee members: prof. **Romain Quident**, prof. **Ulrich Keyser**, prof. **Serge Lemay**, dr. **Jacob Hoogenboom** and prof.

**Nynke Dekker**, each top experts in the fields of either nanophotonics or nanofluidics. Thank you for devoting your time to evaluate the work in this thesis.

All the hard work in the lab could really not have been done without my colleagues of the Plasmonics Team. We really had a lot of fun and I owe so much to you! I could rely unconditionally on you, always ready to help out when needed.

First of all: **Sergii**, thank you for all the time we shared in the cleanroom playing metal storm, brainstorming on new ideas to prevent plasmonic nanopores from sinking, and fighting groundloops in the setup. I have learned a lot from you and we had some great times together, both inside as well as outside of the lab, and always as professionals! I am sure you will make a great professor.

**Xin**, you joining the team has been a true blessing from the sky. Your critical knowledge and can-do attitude in the lab have really managed to get things in the lab going. Moreover, you are really a great guy to collaborate with, you have a powerful work ethic, yet are always ready to go for coffee. I admire your perseverance and patience, you are a great person. Thanks for all the dinners and beers we had at the department and for sharing your views on the world (I think I agree with most of them), I am sure you are going to do well where-ever you will go!

**Wayne**, always up for a good joke or silly comment. Your presentations are first class informative and entertaining and it has been a pleasure to work with you in the lab side-by-side (although not *on* your side of the lab, you are very messy). You are a very bright young man, but you will never be as buff as Kuba.

Finally, **Nils**, our most recent addition to the team. In the short time we worked together, I have noticed your relaxed but sharp attitude and I am sure you are going to do great in your PhD. Also I'm very jealous of your command of the Chinese language.

The plasmonics team has also seen many great student researchers without whom this thesis would have been a lot less fat. **Francesca**, thank you for helping me getting started in the lab. Your tips and tricks have been indispensable for me during those early day experiments. **Misha**, thank you for all the chats and discussions. Your work has been really helpful for us. I'm glad you stayed around as a PhD student with Martin, good luck with those last bits! **Illias**, thanks for your help in the lab and the relaxing chats. It wasn't easy reviving that old setup, but you managed! **Charlotte**, it was really great to have you around in the lab. Despite that your laptop got stolen and the piezo stage that zapped you, you have always held a really positive attitude. **Tim**, those experiments on the fd-virus were tricky, but you made a nice piece of work out of it. **Sofieke**, thank you for your work on motor docking. It was good to see you always kept a low-stress attitude. **Jacintha**, thank you for all that very tough work on getting those last transmission experiments done. You have a very proactive attitude and that is very pleasant to work with! Finally, **Mart**, thank you for all your work on the motor. I really had a great time working with you in the lab. You are keen to get working and always come up with inventive solutions. Although you did outstanding work in setting up the dark-field and labeling, your greatest achievements are, amongst others, the timer trimer, your AFMart, and the 0 euro coin. But I am sure plenty more will follow.

I'd also give a special mention to the secretaries and support staff: **Amanda**, **Jolijn**, **Diana**, **Emmylou**, **Esther**, **Marije**, **Angela**, and **Sacha** who have always helped me with

all the admin. I only wished you would have told me more gossip!

My particular gratitude goes out to all the members of the CD lab. I have been very fortunate to be surrounded by so many great minds and friendly folks. We had many great times, from dancing in the lab, to beers in Klooster, to tubbing in Ireland, and I am going to miss those for sure.

I have had a real blast with my office mates from F068. **Adi**, you are a wonderful guy, your stories always made me crack up. Your happy face is something I can have around all the time. Thank you for all the coffee breaks and rockets. But I am not too happy that you got this good at squash... **Kuba** no matter what I ask you, you always manage to come up with a funny reply. I have many fond memories of our chats about adventurertime or FMVG awareness day. Thank you for all that, and I hope we can go skiing together again (with Adi this time, tricks, tricks)! And some time after I joined, there was **Anthony!** You are a great office mate who has always littered the entire office with pictures. Your magnificent voice and nestor-like attitude will bring you far, no doubt about that. Thank you for all the times you have gone for second coffee with me.

Also I would like to thank my current (and past) F0.150 office mates of course for keeping such a friendly atmosphere around: **Eugene**, thanks for always listening to my random chats / **Allard**, thanks for accepting all our bad pranks at face value. And a big thanks of course for fixing my self-found bike! / **Paola**, keep up that engaging attitude and that eagerness to learn! / **Ana**, thanks for the diners and Ray the dog / **Kevin**, thanks for your relaxed attitude and sharp commentary.

And of course the rest of the lab; **Jorine**, It was great fun making those Christmas presentations (we needed your decisiveness), without you they would have never been funny! / **Fede**, thank you for all your kind thoughts and emotional help, it meant a lot to me. Also, I really had a great time in Milan! / **JK** Don't forget, you are the best! Keep moonwalking! / **Stephanie** You really showed me how to soldier on. And thanks for all the IO-biertjes! / **Jaco**, I very much enjoyed our chats in and outside the lab. I always really enjoyed helping you clear out those boxes! / **Jelle** bedankt voor al je inzichten en tijd die je hebt vrijgemaakt voor mij! / **Jacob**, don't worry, you'll never get old! / **Yoonos**, keep up the skiing! / **Laura**, thanks for showing me reggaeton (I still don't like it) / **Calin**, the smartest man I know, but that's mainly because I like random facts / **Siddharth**, I miss bumping into you on the train! / **Alessio** I have great memories of our random 2am stroll through The Hague / **Sonja** for all the interesting and direct discussions, I feel I can learn a lot from you / **Dimitri** Thanks for all your workshop assistance, and I am sorry for all the times I have called you Jelle. My happy mood in the lab has also been greatly indebted to **Michel, Sabina, Eli, Greg, Sandro, Alberto, Yaron, Ganji, Fabai, Felix, Erwin, Dan Burnham, and Sung-Hyun.**

Furthermore, the bionanoscience department consists of many inspiring and friendly characters and I would like to thank you all for the chats. Special thanks go to the group leaders **Chirlmin, Christophe, Bertus, Timon, Martin, Nynke** and department head **Marileen** for all the great discussions and time you created to listen to my stories. I'd also like to extend my gratitude to **Sam, Helena, Mike, Mehran, Louis, Carsten, Viktorija, Theo, Essengül, Sumit, Maarten, Bojk, Ilja.**

One of my most favorite days was Mondays, as then we would get cracking with

BN/QN's Real RKC/KavliWarriors. Thank you for those great times, **Ruben, Afshin, Fokko, Bas, Mo** and others. The same holds true now on some other random day in the week, because then there is BN squash club! I really enjoyed those squashy days, and I think the best I can do for that here is provide a little advertizement: if you want to join, please email/whapp Sergii.

Outside of the department I'd like to thank the cleanroom staff for the excellent support and eagerness to take my bribes: thank you for the great help and chat: **Ewan, Marc, Marco 2x, Anja, Eugene, Arnold, and Roel**. The same holds for true **Meng-Yue**; thanks for drilling all those pores and being so flexible. I would also like to express my gratitude to our HIM collaborators from TNO: **Tom, Arnold, Elfi** and **Roger**, TU Delft: **Gaurav** and dr. **Paul Alkemade**, and Wake Forest: dr. **Adam Hall**. I'm sure you guys will keep that HIM working!

Finally, I am gratefully honoured that my wonderful thesis cover has been made by **Selma van Tartwijk**. Thank you for your efforts (and **Marijke** for putting me in touch with her), I really admire your artwork!

Also on a personal level I would like to thank a few people. **Attila** and **Casper** for all the great times after work. **Joey** and **Tijn** for all the great parties and holidays. There are many more I should thank, but I feel a private thank you would be more appropriate.

Finally, I would like to thank my family. For all the exceptional support that you have given me all those years. **Mama**, bedankt voor al die keren dat je vroeg hoe het ging. Jij bent echt extreem sterk en ik ben blij dat ik daar ook een beetje van heb meegekregen. **Papa**, al je enthousiaste verhalen hebben mij veel goed gedaan. Ik heb zoveel van jou geleerd en ik weet zeker dat ik dat blijf doen! **Rudy & Marijke** voor al jullie steun op zoveel manieren, de wordfeud spelletjes en straffe wandelingen. Ook will ik **Henk & Maarten** bedanken voor hun luisterende oor, en **Simon & Julie** omdat jullie natuurlijk juist niet zo goed luisterden. Ook **Oma Kitty, Oma Loes** en **Opa Eddie** wil ik graag hartelijk bedanken voor de mooie diner avonden en al het volstoppen. En natuurlijk ook **Leo** en **Ana** die altijd voor mij klaar stonden en staan! Als laatste wil ik mijn zussen bedanken, **Suzanne** en **Marjon**, tevens ook mijn paranimfen. Bedankt voor alles in alle afgelopen jaren, jullie zijn echt mijn grote voorbeelden geweest. Jullie werken zo hard, maar zijn ook altijd in voor een gezellig uitje, waarvan we er samen meerder hebben genoten. Dat gaan we in de toekomst zeker blijven doen!

Maar de allerlaatste die ik wil bedanken is natuurlijk **Iris**! Je hebt zo veel voor mij betekend in de afgelopen 10 jaar! Ik heb extreem veel lol beleefd met je, vooral op al die keren dat je me op vakantie hebt gesleept: Madagascar, Bolivia, Suriname, Noorwegen. Alle moeilijke tijden die ik tijdens dit proces heb doorgemaakt, en dat zijn er een heel aantal geweest, heb jij hoofdzakelijk moeten ondervinden. Maar je hebt me altijd gesteund en me een schop onder de kont gegeven waar nodig, mij laten zien dat er zoveel meer is dan werken. Ik ben ongelofelijk blij dat ik de keuze heb gemaakt om na mijn studie terug te keren naar Nederland om met jou te zijn. Het is geen overdrijving als ik zeg dat jij het beste bent dat mij is overkomen en ik kijk uit naar het avontuur met je in London!

Daniel Verschueren, August 2018

# CURRICULUM VITÆ

## **Daniel Vincent VERSCHUEREN**

- 13-02-1991      Born in Nijmegen, The Netherlands
- 2003–2009      Secondary school  
Stedelijk Gymnasium Nijmegen, Nijmegen
- 2009–2013      MPhys. Physics (with distinction)  
University of Oxford, Oxford, United Kingdom
- 2010–2013      BSc. Chemistry (with distinction)  
Radboud University, Nijmegen, The Netherlands
- 2013–2018      Ph.D. Bionanoscience  
Delft University of Technology, Delft, The Netherlands  
*Thesis:*            Plasmonic nanopores for single molecule sensing  
*Promotor:*        Prof. dr. C. Dekker



# LIST OF PUBLICATIONS

10. Daniel V Verschueren, Xin Shi, and Cees Dekker. *Nano-optical tweezing of single proteins in plasmonic nanopores*. manuscript in preparation
9. Xin Shi, Daniel V Verschueren, and Cees Dekker. *Active delivery of single DNA molecules into a plasmonic nanopore for label-free optical sensing*. submitted
8. Daniel V Verschueren, Sergii Pud, Xin Shi, Lorenzo De Angelis, L Kuipers, and Cees Dekker. *Label-free optical detection of DNA translocations through plasmonic nanopores*. submitted
7. Daniel V Verschueren<sup>\*</sup>, Wayne Yang<sup>\*</sup>, and Cees Dekker. *Lithography-based fabrication of nanopore arrays in freestanding SiN and graphene membranes*. **Nanotechnology**, 29(14):145302, 2018
6. Xin Shi, Daniel V Verschueren, Sergii Pud, and Cees Dekker. *Integrating sub-3 nm plasmonic gaps into solid-state nanopores*. **Small**, 14(18):1703307, 2018
5. Sergii Pud<sup>\*</sup>, Shu-Han Chao<sup>\*</sup>, Maxim Belkin, Daniel V Verschueren, Teun Huijben, Casper van Engelenburg, Cees Dekker, and Aleksei Aksimentiev. *Mechanical trapping of DNA in a double-nanopore system*. **Nano Letters**, 16(12):8021–8028, 2016
4. Calin Plesa, Daniel V Verschueren, Sergii Pud, Jaco van der Torre, Justus W Ruitenbergh, Menno J Witteveen, Magnus P Jonsson, Alexander Y Grosberg, Yitzhak Rabin, and Cees Dekker. *Direct observation of DNA knots using a solid-state nanopore*. **Nature Nanotechnology**, 11(12):1093, 2016
3. Daniel V Verschueren, Magnus P Jonsson, and Cees Dekker. *Temperature dependence of DNA translocations through solid-state nanopores*. **Nanotechnology**, 26(23):234004, 2015
2. Sergii Pud<sup>\*</sup>, Daniel V Verschueren<sup>\*</sup>, Nikola Vukovic, Calin Plesa, Magnus P Jonsson, and Cees Dekker. *Self-aligned plasmonic nanopores by optically controlled dielectric breakdown*. **Nano Letters**, 15(10):7112–7117, 2015
1. Francesca Nicoli, Daniel V Verschueren, Misha Klein, Cees Dekker, and Magnus P Jonsson. *DNA translocations through solid-state plasmonic nanopores*. **Nano Letters**, 14(12):6917–6925, 2014

---

<sup>\*</sup> denotes equal contribution

